TRANSPORT PROPERTIES AND NANOSENSORS OF OXIDE NANOWIRES AND NANOBELTS

A Dissertation
Presented to
The Academic Faculty

by

Changshi Lao

In Partial Fulfillment
of the Requirements for the Degree
Doctor of Philosophy in the
School of Materials Science and Engineering

Georgia Institute of Technology
December, 2007

TRANSPORT PROPERTIES AND NANOSENSORS OF OXIDE NANOWIRES AND NANOBELTS

Approved by:

Dr. Zhong Lin Wang, Advisor
School of Materials Science & Engineering
Georgia Institute of Technology

Dr. Robert Snyder
School of Materials Science & Engineering
Georgia Institute of Technology

Dr. C. P. Wong
School of Materials Science& Engineering
Georgia Institute of Technology

Dr. Yulin Deng
School of Chemical & Biomolecular Engineering
Georgia Institute of Technology

Dr. Peter Hesketh
School of Mechanical Engineering
Georgia Institute of Technology

Date Approved: 10/22/2007

ACKNOWLEDGEMENTS

I would like to express my greatest thankfulness and appreciations to all the people that help with my PhD research and help me make through my graduate study, especially my advisor, Professor Zhong Lin(ZL) Wang.

I would never have made through my graduate school without the help, encouragement, and guidance from Dr. Wang. Dr. Wang has provided me with a lot of precious advice, encouragement, and unlimited support throughout my graduate career. He has shown me the value of being an energetic scientist, the importance of keeping an innovative brain in your research, the real meaning of hard work and productive, and a lot of other invaluable experience and brilliant ideas. All these precious inheritance I obtained from Dr. Wang helps to define my identity of being such a researcher I am today and encourage me pursuing for my future development in my travel of being a successful scientist.

I would also like to extend my appreciation and admiration to the other members of my defense committee, Prof. Robert Snyder, Prof. C.P. Wong, Prof. Yulin Deng, and Prof. Peter Hesketh for their help and their insightful instruction they provided for my research.

Also, I would like to thank all my group members for their constantly support and help with my research. More specifically, to Qin Kuang for his help with my research projects and making my most 2 recent paper possible in the past year, to Dr. Xudong Wang for his constantly advice and discussion with my research, to Ben Weintraub for introducing me a lot of pop culture in US and helping me get further exposure to

American culture, to Dr. Jun Zhou for showing the actually way of doing research, and again to all my group members for their consistent and non-reserved help with my work and my life.

Most importantly, I would like to express my deepest love and appreciation to my family for their consistent support throughout the years no matter how I did and where I am. Their expectation, support and encouragement is the endless power for me to inspire myself to work harder and harder and to pursue for the next step of advancement.

TABLE OF CONTENTS

LIST OF TABLES

LIST OF FIGURES

LIST OF ACRONYMS AND ABBREVIATION

0D	Zero Dimensional
1D	Quasi One Dimensional
2D	Two Dimensional
LED	Light Emitting Diodes
(HR)TEM	(High-Resolution) Transmission Electron Microscope
SEM	Scanning Electron Microscope
AFM	Atomic Force Microscopy
FIB	Focused-Ion Beam
XRD	X-Ray Diffraction
SWNT	Single-Wall Carbon Nanotube
FET	Field Effect Transistor
NW	Nanowire
NB	Nanobelt
VS	Vapor-Solid
VLS	Vapor-Liquid-Solid
EDS	Energy-Dispersive X-ray Spectrum
NPGS	Nanometer Pattern Generation System
PMMA	Polymethyl Methacrylate

SUMMARY

In the current extensive research interests in nanotechnology, ZnO are one of the materials that attract the most of research efforts. ZnO is a II-VI semiconducting-oxide material with great importance in the applications of optoelectronics, sensors, and transistors. It has a wide band gap of 3.4eV with an exiton binding energy of 60meV, which makes ZnO 1D nanostructures ideal for optical device applications. It is also a high piezoelectricity material with applications in nanogenerators, which is a result of semiconductor and piezoelectricity coupling effect.

Also, due to the non-central symmetric crystallographic structure and spontaneous surface polarization characteristics make ZnO one of the most exciting oxide nano- structures for investigating the synthesis of nanostructures. Recently, utilizing its unique crystal structure and the three major fastest growth directions, various single-crystal/crystalline nanostructures of ZnO have been synthesized, such as nanobelts, nanorings, and nanohelices. From the abundance of the surface morphologies, ZnO offers the most diverse nanostructures of any material known today.

The research work conducted in this theis mostly focused on the synthesis study, electric transport properties study, and surface functionalization study of ZnO, which is listing as follows: (1) Success synthesis of different ZnO nanostructures, such as nanocombs, nanonetworks, nanodiskettes. (2) Detail electric transport properties investigation of ZnO nanobelts, which provide a better understanding of different device fabrication criteria and performances. (3) Surface functionalization of ZnO by polymers and different molecules to achieve giant improvement in its electric transport and different device properties.

In the first chapter, a brief overview of the current progress in ZnO synthesis and device applications is presented. The second chapter covers my research work on the synthesis of ZnO nanostructures, which includes nanobelts, nanonetworks, nanocombs, nanodiskettes. Then, a detailed study of the basic transport study of oxide nanowires/nanobelts is discussed in chapter 3. The research work on the surface functionalization study of ZnO nanowire devices is presented in chapter 4. Chapter 5 is about some current proposal of potential research might carried out on the further investigation of ZnO nanobelt based devices.

Chapter 1

INTRODUCTION

Nanotechnology has become very prevalent research area in recent years.[1-10] It is a subject investigating the effect of functional materials, devices and systems when the critical sized is scaled down to nanometer length (1-100 nanometers).[11-18] It is now a common theme that is prevalent over all physical and materials sciences and is of great significance in both science and technology known as nanotechnology. It covers many conventional areas of physics, chemistry, biology and medicine and becomes an interdisciplinary subject.[19-31] Presently, the most significant aspects of nanotechnology are focused in basic sciences and mainly within physics and chemistry.[32-35] With development of nanotechnology, it is worthwhile and promising to expect its research and applications on applied sciences, including biology,[36] nanomedicine[37] and other potential areas[38]. The research and development in nanomaterials involved three viewpoints: synthesis of nanomaterials,[39] characterization of their properties,[40] and realization of their applications.[41] The large research interests in nanotechnology and nanoscale materials is inspired by the enormous economical, technological and scientific advantages of several areas: (a) With the exponential growth of the processing speed of semiconducting chips, the crucial components that virtually enable all modern technology, the fabrication technique is quickly approaching its

limit of functions and demands new technology and new materials science on the nanometer scale. (b) Novel nanoscale materials and devices hold great promising potentials in energy, environmental, biomedical applications. They have supreme properties for more efficient use of energy source, effective treatment of environmental hazards, rapid and accurate detection and diagnosis of human sicknesses and improved treatment of such diseases. (c) When a material is reduced to nanoscale, its properties can be extremely different from those of the bulk materials that we can see and touch even through the composition is essentially the same. Many of the evolutions in this field arise from the requirements of the increasing integration density with nanometer scale structures. Those requirements have driven scientists to develop advanced fabrication processes in nanotechnology. There are two kinds of methods for manufacturing nano-scale building blocks which can be characterized as top-down and bottom-up. In the top-down approach, lithography methods are used to facilitate the device fabrication. Processing speeds and critical structure size are limited with this processing method. For the bottom-up method: nanostructures are grown at spatially defined positions and then automatically followed by device fabrication around the grown nanostructures.

The nanostructures, having at one dimension between 1 and 100 nm, exhibit special physical and chemical properties which is a bridge between atomistic scale properties and the extended states of the bulk and result in

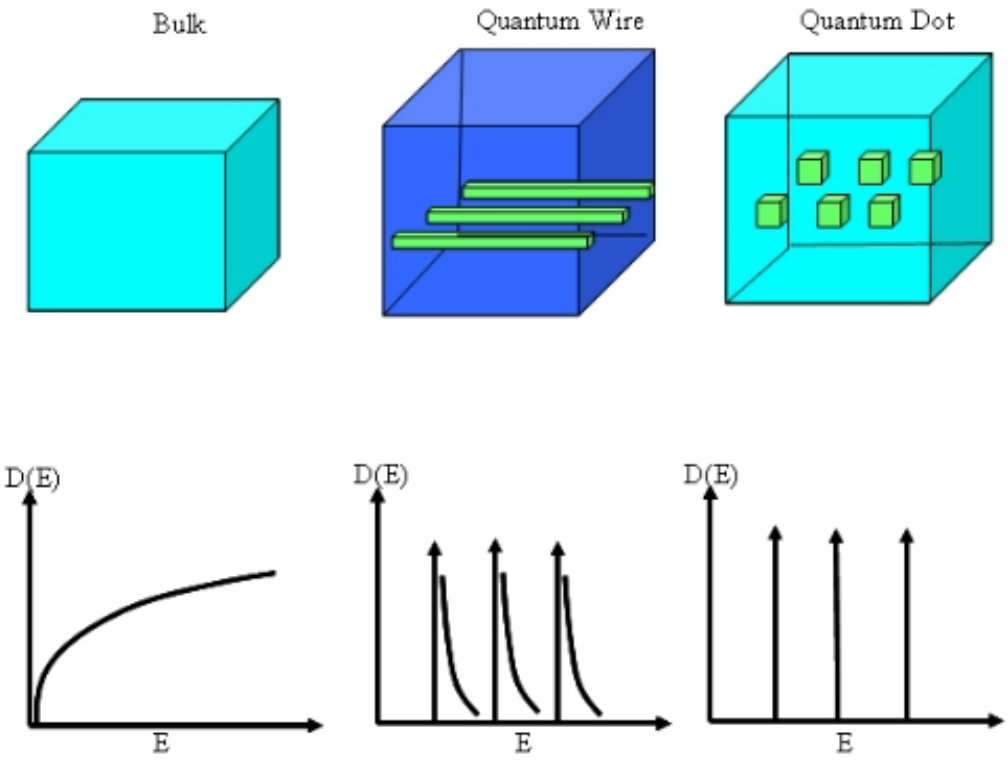

Fig. 1.1 Change in the density of states with the dimensionality of the system.

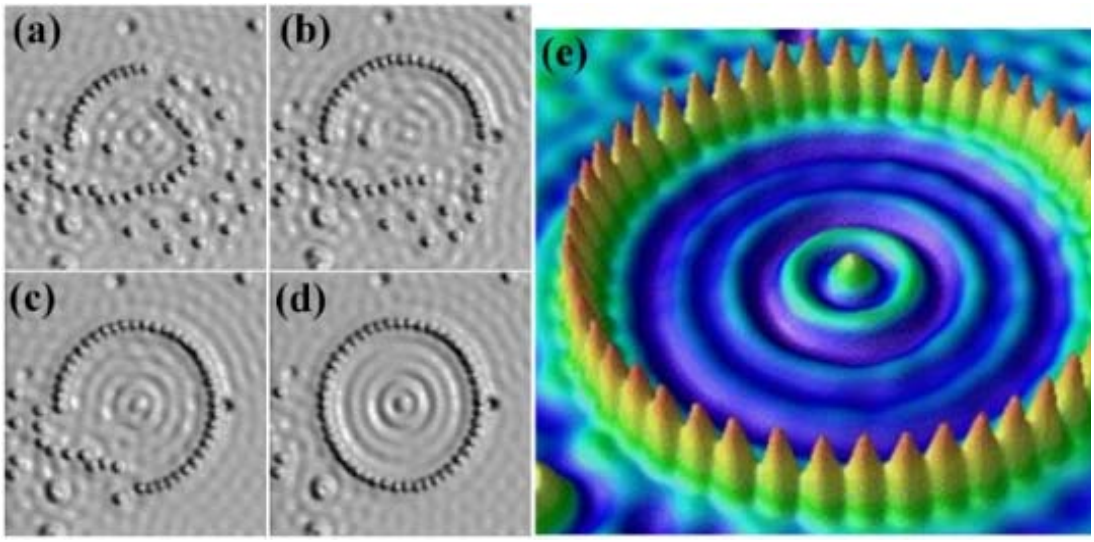

Fig. 1.2 The process of creating a quantum corral on a copper (111) surface by manipulating iron adatoms using an STM.

peculiar and fascinating properties and applications superior to their bulk counterparts. Nanostructures in such low-dimensional systems present the novel fundamental properties (Fig. 1.1) and the stimulating prospect for

utilizing these nanostructures in nanotechnology-enabled electronic and photonic applications. For example, a great amount of interesting and new phenomena is associated with nanometer-sized structures, with size-dependent excitation or emission,[42, 43] quantized conductance,[11, 27, 44, 45] and optoelectronics[46]. The particular example of nanostructures is the ubiquitous quantum corral as shown in Fig. 1.2.[47]

1.1 One-Dimensional Building Blocks

The interest in the nanostructures has been stimulated by the fact that, owing to the small size of the building blocks (particles, grains or phases) and the high surface-to-volume ratio, these nanostructures are supposed to demonstrate unique mechanical, optical, electronic and magnetic properties.[48-56] Up-to-date studies in low-dimensional semiconductor materials have been stimulated by the development for miniaturization of electronic and optoelectronic devices and curiosity to the fundamentals of nanoscale chemistry and physics. Traditional fabrication methods adopt a combination of thin film growth, lithography and etching approaches to define nanoscale features.[57] This methodology is typically labeled as a "top-down" approach in that one starts with bulk materials and sculpts downward to get to the nanoscale. This "top-down" technology has been progressed at a rate such that the amount of transistors per chip has been

doubling every 18-24 months over the last to four decades. This tendency is known as Moore's Law.[58]

The amazing rate of progress will be difficult to continue in the next decade, owing to a combination of technological and economic reasons. As the incapability of photolithography to define extremely small patterns and the exponentially increasing costs associated with upgrading fabrication facilities are both crucial factors impelling researchers to look for substitute strategies to nanoscale fabrication. Miniaturization also exhibits the tendency in a range of other technologies, for example, in information storage there are many efforts to develop magnetic and optical storage components with critical dimensions as small as tens of nanometers.[59] Top-down approach also could be administered to the nanostructured materials or nanoscopic particles and nanocrystals by sculpting it from the macroscopic piece of unstructured material (bulk). Common techniques used for this intention are lithography, etching, mechanical milling, engineering using atomic force microscope (which can be used to 'scratch' the surface leaving nanoscopic channels and structures behind).

A different approach to nanofabrication is the so-called "bottom-up" or "nano-assembly" approach similar to molecular engineering, the synthesis are employed to fabricate nanoscale building blocks that are subsequently assembled into nanoscale devices and architectures. Low-dimensional building blocks, such as zero-dimensional nanocrystals (C_{60} [60], Sc_3NC_{80}

metallofullene) and one-dimensional carbon nanotubes,[52, 61, 62] nanowires[63, 64] and nanocables,[65] are attractive candidates to develop a bottom-up method for nanotechnology-enabled architectures. Individual molecules and quantum dots, which can be classified as zero dimension structures, are attractive building blocks for bottom-up assembly of nanoscale electronics. These 0D structures have been intensively chased over the past decade since they present the smallest building blocks with corresponding high potential for integration. Much effort has been made to zero-dimensional nanocrystals and a rich variety of chemical approaches have already been developed for fabricating quantum dots with well-controlled dimensions, morphology, phase purity, and chemical composition. However, the use of individual molecules or quantum dots in integrated system has been restricted by challenges in establishing dependable electrical contacts to individual molecules and quantum dots. It has thus been difficult to demonstrate and amplify on realistic schemes for scalable interconnection and integration of 0D devices into functional architectures.[66, 67] One-dimensional nanostructures such as wires, rods, belts, tubes and cables have no persecution in electrical contact and can act both as interconnects for the transport of charge carriers as well as functional units in fabricating electronic, optoelectronic, electrochemical and electromechanical nano-devices.

One-dimensional nanostructures have been the focus of expansive studies worldwide due to their unique physical properties and promising to

revolutionize broad areas of nanotechnology. First, 1D nanostructures illustrate the smallest dimension structure that can efficiently transport electrical carriers, and thus are ideally suited to the critical and ubiquitous task of moving charges in integrated nanoscaled systems. Second, 1D nanostructures can also exhibit device functions, and thus can be exploited as both the wiring and device elements in architectures for functional nanosystems. 1D nanostructures and devices can be synthesized and fabricated using a number of developed nano-lithogrphic technologies[68] such as electron-beam or focused-ion-beam writing,[69] proximal-probe patterning[70] and X-ray or extreme-UV lithography.[71] These technologies need to further explore into practical methods to high-volume production of nanodevices from a various kinds of materials, rapidly and at reasonably low costs.

1.2 Synthesis of 1D Nanostructures

As discussed previously, vapor phase evaporation represents the most widely studied method for nanowire synthesis due to its simplicity in operation and variety in the as fabricated nanostructures. In this chapter, we will mostly focused on nanowires synthesis through vapor phase evaporation, more specifically, physical vapor deposition (PVD).[72] Briefly reviewed, PVD describes the solidification of a vapor directly onto a surface.

Direct deposition implies that no chemical reactions are permitted to occur in the vapor, with the vapor, and/or with the surface to be deposited. If a chemical reaction does occur, then the process is not PVD, but rather (CVD). [73]

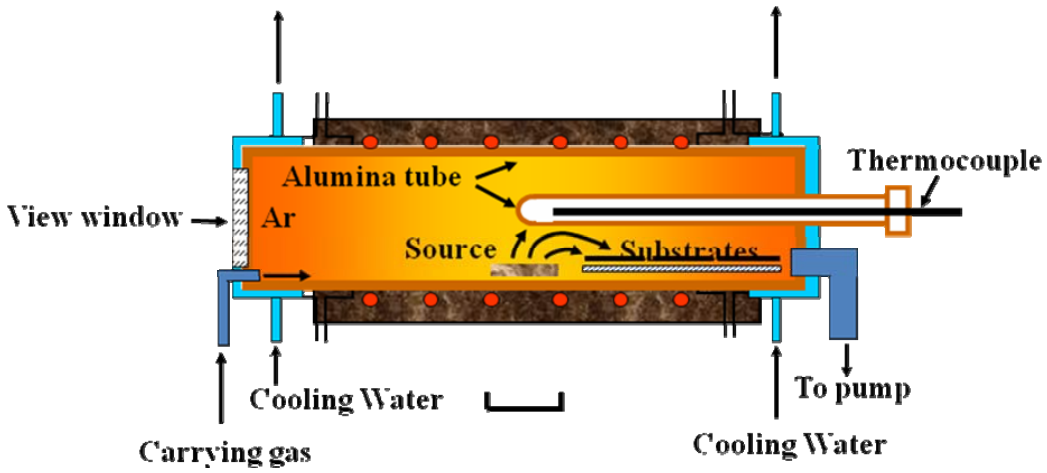

Fig. 1.3 Schematically illustration of entire furnace synthesis system.

Variety nanostructures with different composition and different morphologies were successfully synthesis. Examples of 1D nanostructures grown with PVD are rather diverse, such as nanowires of ZnO, In_2O_3, SiO_2, SnO_2, Ga_2O_3, and etc.[74-78] A typical furnace system used in the PVD synthesis method is comprised of two components: the furnace and the vacuum system. A schematic of the entire system is given in Figure 1.3.[39] The experimental apparatus includes a horizontal high temperature tube furnace, an enclosed alumina tube, a rotary pump, and a gas controlling system (Figure 1.3). By carefully controlling of the growth conditions such as temperatures, pressure, processing period, and substrate location, different sorts of semiconducting oxide nanostructures can be synthesized.

In crystal nanostructure synthesis, ZnO has three types of fast growth directions: <0001>, <01 $\bar{1}$ 0> and <2 $\bar{1}$ $\bar{1}$ 0>, together with the ± (0001) polar-surfaces, various unusual structural configurations have been reported for the fabrication of ZnO, such as nanobelts, nanosprings, nanorings and nanocombs. By studying the intrinsic growth mechanism of different sorts of ZnO nanostructures, a lot of useful and informational knowledge can be obtained from this. In this section, we will mainly focus on the synthesis methods and growth mechanisms of different ZnO nanostructures to elaborate the basic physics in the nanostructure synthesis and most recent development in this area.

The synthesis of nanostructures of ZnO is based on the high-temperature solid-vapor deposition process.[79] The experimental apparatus included a horizontal high temperature tube furnace, an enclosed alumina tube, a rotary pump, and a gas controlling system as shown in Figure 1.3. In the experiments, usually a certain amount of reactants is loaded on a substrate and placed in the center of the tube as the source material. Several pieces of collecting substrates are positioned downstream to collect the products. With the source and other prerequisite conditions are satisfied, the furnace system is pumped to around $1x10^{-3}$ Torr by a mechanical pump, which is critical in the ZnO nanostructure synthesis. Afterwards, the furnace system is heated up to a very high temperature (around 1200 ^{o}C) at programmed ramping pace. At the same time, Ar working as a carrier gas flows, with a certain flow rate

through the tube furnace at pressure of pre-selected value. This carrier gas will transport the source vapor to the downstream region. With a constant pressure and gas flow rate, the evaporation process was kept running for a certain amount of time. The grown nanostructures are collected at a lower temperature zone on the collecting substrate. The as-synthesized structures are characterized with Scanning Electron Microscopy (FE-SEM, field emission LEO 1530 FEG) and Transmission Electron Microscopy (TEM, field emission TEM Hitachi HF-2000).

By controlling of the synthesis conditions, such as reaction temperature, pressure, source materials, temperature ramp rate, and catalyst, we can get a variety of as-fabricated ZnO nanostructures. For example, ZnO nanobelts are normally obtained at a higher temperature which is around 1400 ^{o}C. ZnO nanowires are normally synthesized at a lower temperature of around 1100 ^{o}C.

1.2.1 Crystal Structure of ZnO

ZnO is one of the common II-VI compounds with wurtzite crystal structure. Schematically illustration of wurtzite structure is shown in Figure 1.4. Generally, wurtzite structure is a tetrahedral lattice site in a compound AB each A atom is surrounded symmetrically by four nearest neighboring B. If we look at the wurtzite structure in a large scale, the A and B atoms form two interpenetrating close-packed hexagonal lattices as illustrated in Figure 1.

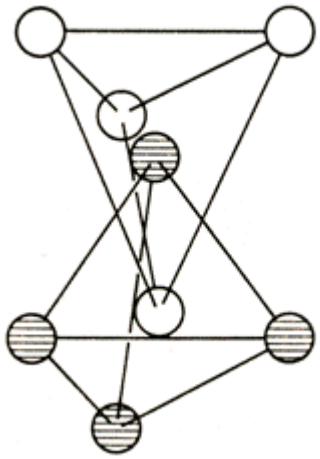

Fig. 1.4 Tetrahedra configurations for the II-VI compounds corresponding

5. In a more simplicity and straight forward way, the wurtzite structure is composed of a number of alternating planes which are formed by the tetrahedrally coordinated O^{2-} and Zn^{2+} ions. These two O^{2-} and Zn^{2+} ion planes stacked alternatively along C axis. This crystal structure configuration is shown in Figure 1.6. For crystal structures without any defects, this alternative stacking positive charged Zn^{2+} planes and negatively charged O^{2-} planes results in polar surfaces in C axis. This generates a dipole moment along top and bottom surface of C axis which results in spontaneous polarization and surface energy divergence. This specific property of ZnO wurtzite structure plays a significant role in the formation of different nanostructure of ZnO. Structurally, ZnO has three-types of fast growth directions: <0001> (±[0001]), <01$\bar{1}$0> (±[01$\bar{1}$0], ±[10$\bar{1}$0], ±[1$\bar{1}$00]), and <2$\bar{1}$$\bar{1}$0> (±[2$\bar{1}$$\bar{1}$0], ±[$\bar{1}2\bar{1}$0], ±[$\bar{1}$$\bar{1}$20].[80, 81] For 1D nanowires or other nanostructures grown along <0001> direction, the polar surface is the top and bottom surface of the nanowire. Consequently, the polarization effect is minimized and will

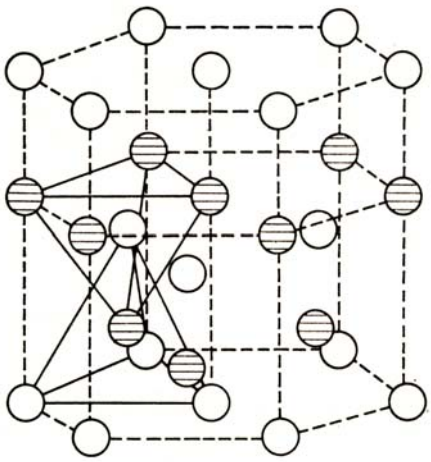

Fig. 1.5 Schematic demonstrating how the interpenetrating tetrahedra form the wurtzite crystal structure.

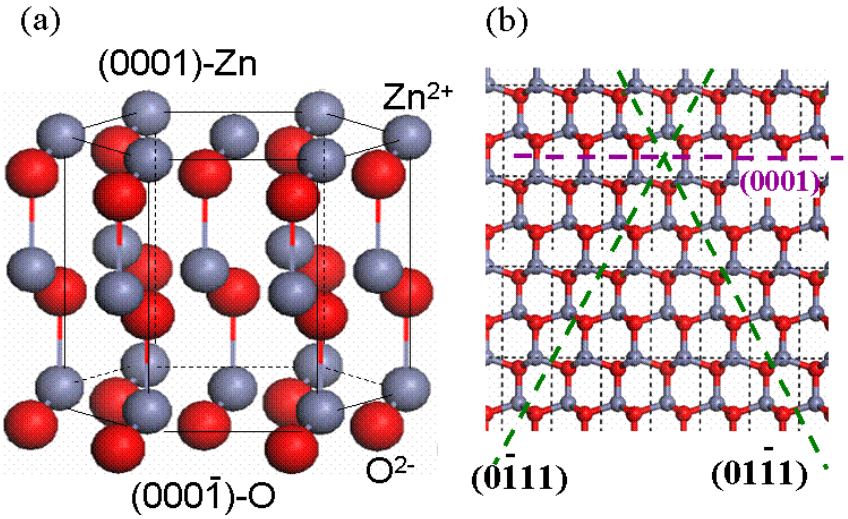

Fig. 1.6 ZnO crystal structure illustration

have little influence on the growth mechanism of these nanowires. For nanostructures grown along <01 $\bar{1}$ 0> or <2 $\bar{1}$ $\bar{1}$ 0>, the polar surfaces are on the relatively thinner dimensions of the nanowire, the polarity effect will affects the growth of nanowire significantly, which results in a group of special structures dominated by the polar surfaces. In the following sections, we

will first introduce the nanostructures fabricated with the polar surface effects. Then non-polar surface nanowires and other structures will be discussed.

1.2.2 ZnO Nanobelts

Nanobelt is a new category of 1D nanostructure as a complementary to nanowire and nanotube.[82] The most significant difference of a nanobelt to a nanowire is that the cross session of a nanobelt is rectangular, with a size of around several nanometers by several tens of nanometers. A nanobelt is more like a nanowire other than a nanotube because it is solid with crystal lattice extending along the cross section. Figure1. 7 is a typical image of nanobelt.

The synthesis of ZnO nanobelts is a typical PVD. For details of the experiment parameters, with the set up of previous mentioned synthesis apparatus, we set the reaction temperature to a very high standard, around 1400-1500 ^{o}C. This high temperature will help to form the energy unfavorable polar surface dominated nanobelts. Other experiment parameters inclues: 2 grams of commercial (Alfa Aesa) ZnO powder, 300 torr ambient pressure, 50 sccm (standard cubic centimeters per minute) carrier gas flow rate, 2 hours reaction time, and collecting substrates are polycrystalline Al_2O_3 plates at temperature region of around 700 ^{o}C. This results in a woollike synthesis product on the collecting substrates.

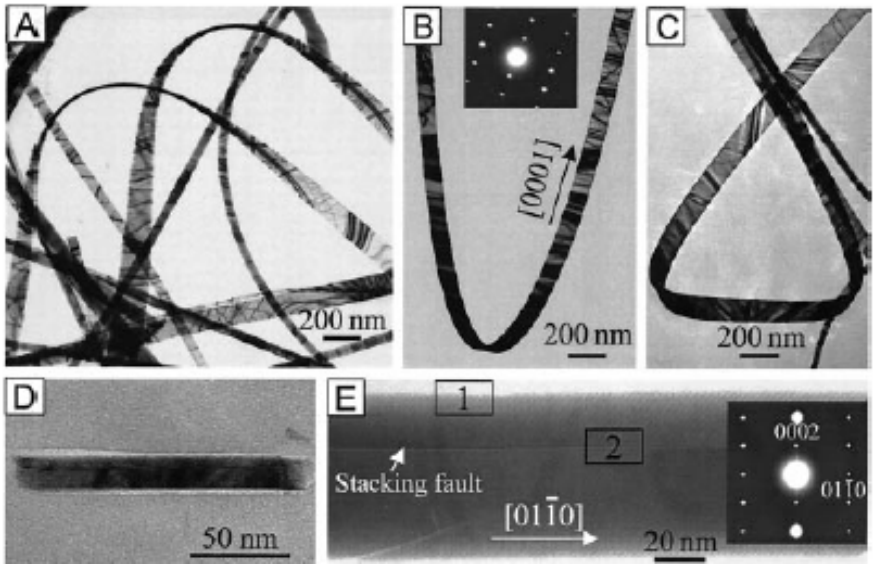

Fig. 1.7 typical image of nanobelt.

These as-fabricated products are characterized with SEM and TEM. SEM image in Figure 1. 7 (a) shows the large scale and high purity of these woollike nanostructures. The length of these nanostructures ranges from several micometers to as long as several millimeters. Energy-dispersive x-ray spectroscopy (EDS) and x-ray diffraction (XRD) measurements prove that the crystal structure of these synthesized products is wurtzite structure, consistent with the parameters of bulk ZnO, with lattice constant of a=3.249Å and c=5.206Å. Magnified images under TEM reveal that the cross section of these products is rectangular, as shown in Figure 1.7 (b). This is a significant distinction with previous studied 1D nanostructures such as nanotubes and nanowires. As shown in the figures, the nanostructure, named nanobelt, has a uniform width and thickness along its entire length. Typical thickness of nanobelts is of around 10 – 30nm. Typical width is of around 50 nm - 300 nm. The aspect ratio is 5 to 10. According to the High Resolution TEM

(HRTEM) images, the nanobelts are structurally uniform and single crystalline. There are two growth directions of these nanobelts. One is [0001], enclosed by $\pm(2\bar{1}\bar{1}0)$ and $\pm(01\bar{1}0)$. The other growth direction is $[01\bar{1}0]$. The enclosing surfaces of this kind of nanobelts are $\pm(0001)$ and $\pm(2\bar{1}\bar{1}0)$. As discussed previously, the polar surface $\pm(0001)$ and the consequently polarization effects plays a significant role in determining the physical and chemical properties of the nanobelts. This will be demonstrated in the following session of this chapter. We will show the effect of polar surface on different nanostructure synthesis.

Besides ZnO nanobelts, this rectangular cross section morphology is also observed on the 1D nanostructure synthesis on some other semiconducting oxides with similar experiment conditions, such as SnO_2, In_2O_3, CdO, Ga_2O_3, and PbO_2.[83, 84] As demonstrated for ZnO nanobelts, these semiconducting nanobelts all process a perfect geometry, high crystallinity. This perfect and well control geometry make semiconducting oxide nanobelts an ideal candidate for the optical, electrical and mechanical application of 1D nanostructures.

1.2.3 ZnO Nanorings

The morphology of a ZnO nanoring[84] is straight forward from the nomenclature. It is a ring formed by coiling of ultrathin polar ZnO nanobelts. A typical ring is a circular coil of nanobelts with diameter of around 1-4 μm.

The coiled nanobelt form a thin, uniform and wide shell with thickness of around 10 – 30 nm.

ZnO nanoring is single crystal structure. The synthesis condition is about the same as that of ZnO nanobelts, except that the source materials is a mixture of ZnO, indium oxide and lithium carbonate powders at a weight ratio of 20:1:1. During the synthesis process, ZnO powder is decomposed into Zn^{2+} and O^{2-}. This decomposition step is very critical for controlling of the anisotropic growth of the nanobelts and finally facilitates the formation of ZnO nanorings.

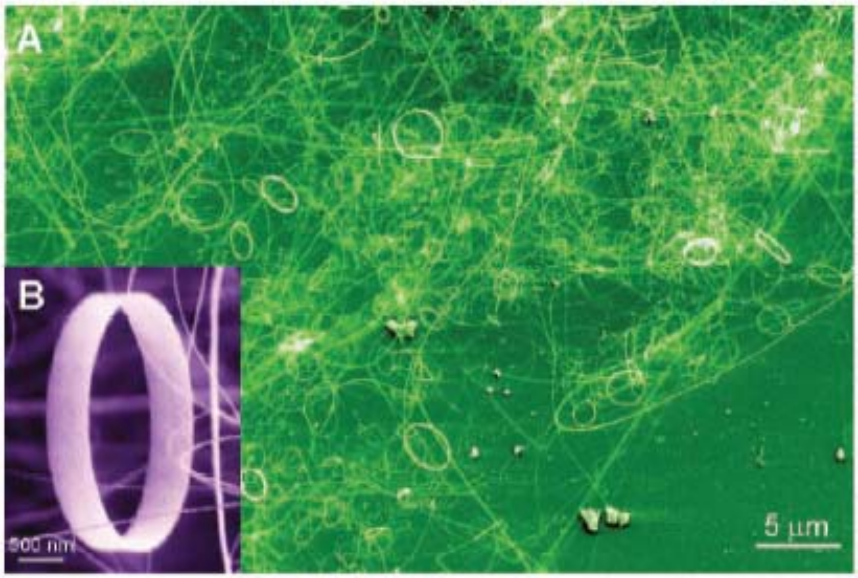

Fig. 1.8 SEM image of nanoring.

Characterization of ZnO nanorings shows that these nanorings are formed with a single crystal ZnO nanobelt bended evenly along the circular circumstance of the nanoring. The entire nanoring is almost a single crystal structure, although the crystallinity varies slightly across the width of the

nanoring due to the coiling mismatch of the nanobelt, as shown in the enlarged SEM image Figure 1.8.

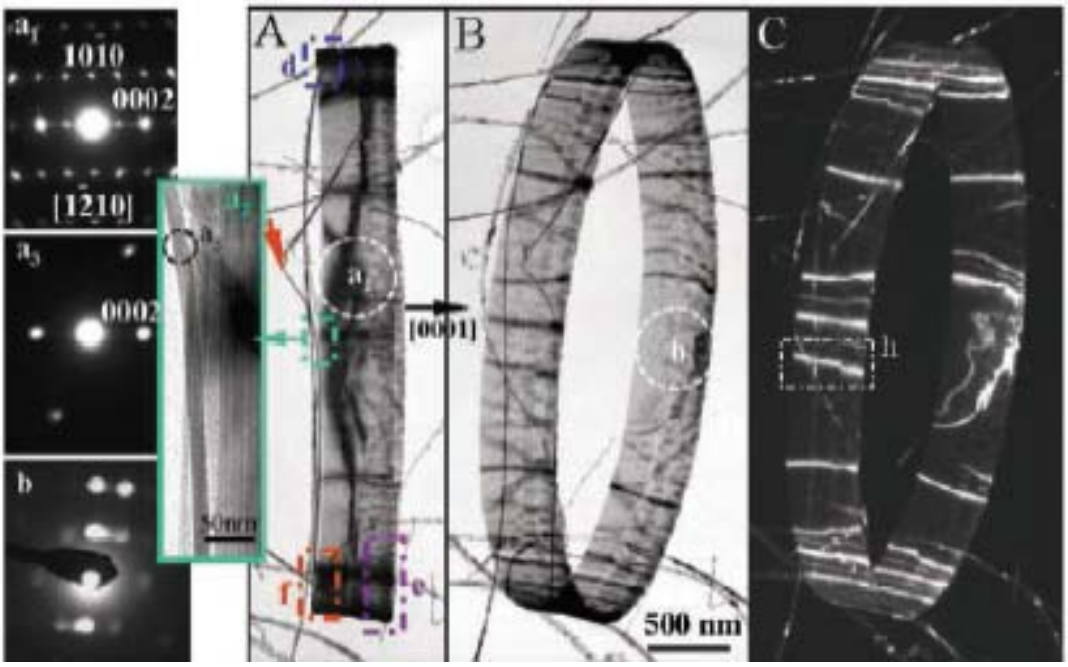

Fig.1.9 TEM analysis of ZnO nanoring.

Typical structure of a nanoring is that the radial direction of a ring is $[1\bar{2}10]$, then tangential direction is $[10\bar{1}0]$ and the axis is [0001]. With further TEM analysis (Figure 1.9), the nanoring structure is determined by the growth direction of the nanobelt. Generally, the nanobelt grow along $[10\bar{1}0]$ with side surfaces of $\pm(1\bar{2}10)$ and top/bottom surfaces of ±(0001). The coiling of the ZnO nanobelt is realized by interfacing its (0001)-Zn and $(000\bar{1})$-O planes at the same crystallographic orientation. This reason that introduces this automatic coiling effect is the most important factors in the growth mechanism of the nanoring. The wurtzite structure ZnO nanobelt has a top and bottom surfaces of ±(0001). So the side surface of this nanobelt is terminated with oppositely charged ion surfaces, positively charged (0001)-Zn

and negatively charged $(000\bar{1})$-O polar surfaces. So, during the growth progress of the nanobelt, the polar surfaces introduce a polarity which will increase the energy and instability of the nanobelt during the growth. To compensate the energy diverse effect of the polar surface, the nanobelt may tend to fold itself along its growth direction to minimize the area of the polar surface, consequently the electrostatic energy. By self coiling of the nanobelt, the positively charged (0001)-Zn polar surface stacks on the top of the negatively charged $(000\bar{1})$-O polar surface. This neutralized the local polar charges, thus forming a nanoring. However, the radius of the loop may be a relative arbitrary result of how the nanobelt bends during its initial growth. However, due to the minimization of the total energy of this nanoring, the radius of the nanoring cannot be too small to reduce the elastic deformation energy. Hence, the total energy, including the polarity effect of the polar charges, surface area and elastic deformation introduced energy, play a significant role in determination of the formation of a nanoring.

As the first discovered single crystal nanoscale circular system, ZnO nanoring is of great importance for investigation of the fundamental physics phenomenon, such as optics trapping effects in a close loop and Aharonov-Bohm excitations in exciton luminescence.[85]

1.2.4 ZnO Nanohelices

The ZnO nanohelix is another sort of nanostructures formulated by the polar surface effects of the ZnO nanobelts.[86, 87] Generally, it is a rigid helical structure of zinc oxide with superlattice-structured nanobelt. The superlattice nanobelt is a periodic, coherent, epitaxial and parallel assembly of two types of long-stripes of zinc oxide crystals oriented with c-axis perpendicular with each other.

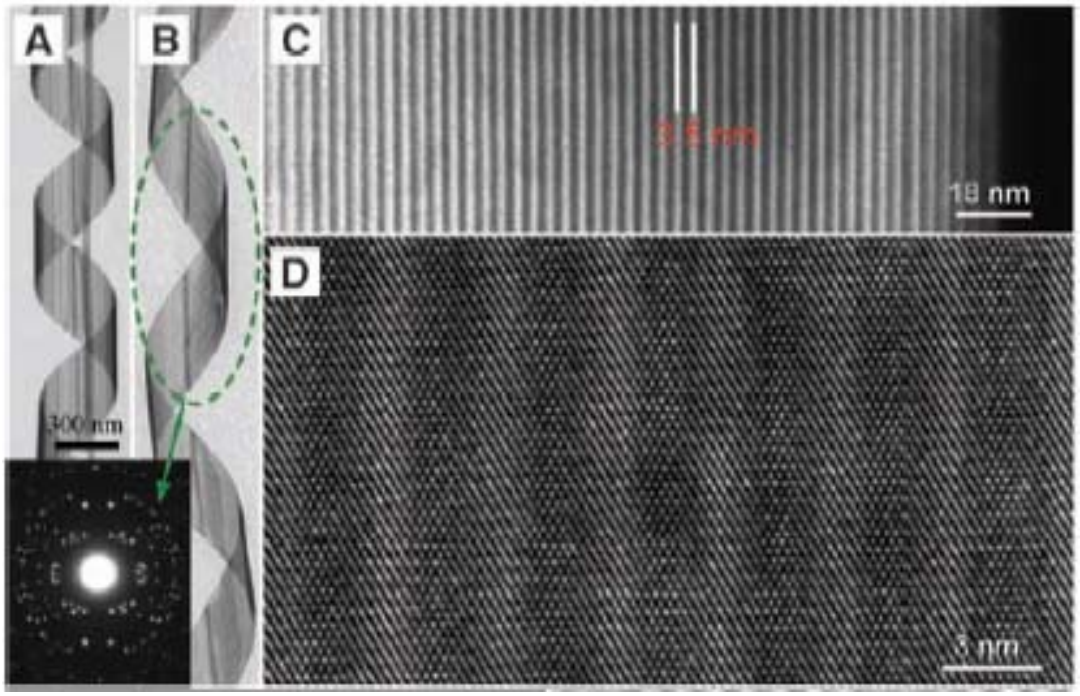

Fig. 1.10 Image of ZnO nanohelices.

The ZnO nanohelix can be synthesized at a high reproducibility and a relatively high yield with solid-vapor evaporation process. With similar experiment apparatus set-up as the ZnO nanoring synthesis, pure ZnO powder is used as the source material, only slightly changes on the pressure

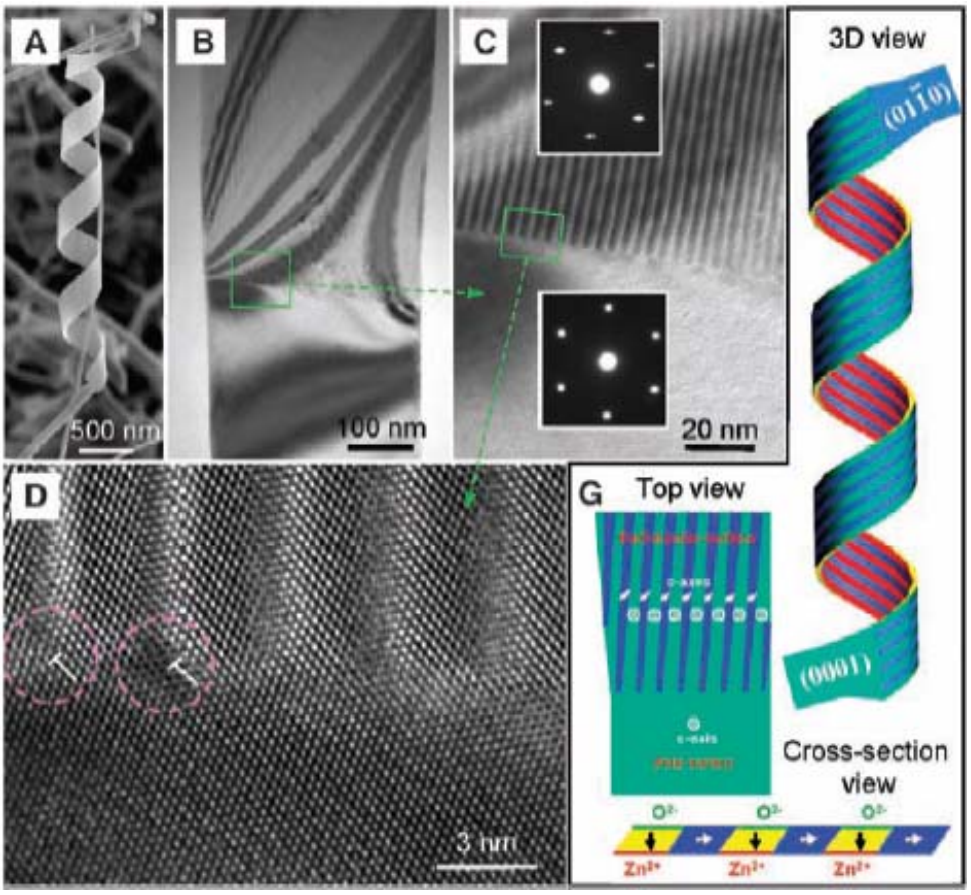

Fig. 1.11 Detail structure analysis of the as-growth ZnO nanoring.

and deposition area. The as-synthesized sample is composed of a significant percentage of freestanding nanohelixes. Morphologies of these nanohelixes are shown in the SEM images. ZnO nanohelix has perfect shape and superior uniformity the spring structure. The nanohelix can be left-handed and right-handed with product ratio of around 1:1. The sized of the nanobelt that forms the nanohelixes are typical nanobelt features with length in the range of 300-1000 nm and widths in the range of 100-500 nm. The pitch distances of the helix spread over a large range from 500 – 3000 nm, as seen from a few typical images presented in Figure 1.10. From the Energy

dispersive X-ray spectroscopy analysis, the ZnO nanohelixes are demonstrated to have uniform crystal structures without detectable impurity.

Detail HRTEM analysis on this sample reveals that the nanohelix is composed of superlattice-structured nanobelt stripes, as shown in Figure 1.10 . The superlattice of the nanohelix is made of two different crystalline nan-stripes: Stripe I: growth direction $[0\bar{1}10]$, top and bottom surfaces $\pm(0001)$ (polar-surfaces), and side surfaces $\pm(\bar{2}110)$; Stripe II: growth direction [0001], top and bottom surfaces $\pm(01\bar{1}0)$ (non-polar-surfaces), and side surfaces $\pm(\bar{2}110)$. The stripes line along with each other and extend almost parallel to the growth directions of the nanobelts through the whole length of the nanohelix.

The growth mechanism of the nanohelix is also an effect of polarity of the polar surface. As shown in the SEM image (Figure 1.11), at the initial stage of the nanohelix formation, a straight stiff-nanoribbon is transformed to the superlattice nanoribbons. The superlattice is formed spontaneously and abruptly across the entire width of the nanoribbon. The stripes hold the same orientation and orientation relationship as defined previously. The superlattice formation on the entire ribbon directly results in the nanohelix, which is also likely to be a polar charge induced structural transformation. For superlattice stripe I, which is composed of positively charged (0001)-Zn and negatively charged $(000\bar{1})$-O polar-surfaces (c-planes), the polar charges

on the stripe are preserved on the surface during the growth under conditions of high temperature and inert environment, which will cause the energy divergence on the nanostructure. Due to the requirement of energy minimization, the same mechanism in the formation of ZnO nanoring, a possible way of reducing the electrostatic energy is to transform the polar-surface into a non-polar-surface, provided the interface mismatch energy is reasonably low. A possible way is to form superlattice-structured stripes almost parallel to the growth direction of the nanobelt, one of which preserves the same orientation of the stiff-nanoribbon with c-plane dominated surfaces (stripe I), and the other has $(01\bar{1}0)$ (a-plane) non-polar-surfaces (stripe II). The two stripes have a coherent and epitaxial interface possibly with low mismatch energy: the mismatch between $(0\bar{1}10)$ of stripe I with (0002) of stripe II is 2.9%, and $(\bar{1}010)$ of stripe I with 2x$(\bar{2}112)$ of stripe II is 2.15%. This is proved with our TEM analysis. An important fact is that the width of the nanobelt increases after the structural transformation from a single-crystal c-plane dominated stiff-nanoribbon into a superlattice-structured flexible nanobelt; the stripes may not be exactly parallel to the growth direction of the nanobelt but at a small angle of ~ 5^{o}, and a small in-plane rotation of ~ 4^{o} exists between the orientation of the two adjacent stripes, which may induce the geometrical curvature required for rigidly twisting its shape. The polar charges remaining on the surfaces of stripe I also helps to bend the nanobelt into a ring structure especially with

the reducing of the nanobelt thickness. Thus, a continuous growth of the stripes along the length of the nanobelt may result in the formation of a helical structure, which could be left-handed or right-handed.

With further study by Focused Ion Beam (FIB) system, the nanohelix is cut into different pieces. The sectioned pieces of nanohelix retain its original curved shape, which means that the nanohelix is a rigid structure with little stored elastic energy.

The nanohelix structure presented here displays a new formation mechanism about crystalline helical coils, and it is a new structural configuration of ZnO that is distinctly different from the nanosprings and nanorings. The perfect helix shape is of great interest not only for understanding the growth behavior of polar-surface driven growth process, but also for investigating fundamental physical phenomena

1.2.5 ZnO Nanowires

There are quite a few reported synthesis methods for ZnO nanowire synthesis, such as aqueous solution based synthesis, and vapor-liquid-solid (VLS) deposition. Here, we will focus on the VLS deposition process reported by Yang et al. [88-91]

Unlike vapor solid deposition, the general method used in previous reported polar surface induced growth nanostructures, the VLS process normally requires a low melting point metal working as catalytic material.

For ZnO nanowire synthesis, Gold is the most common used catalyst. First, a thin layer of Au (several nanometers) is thermal evaporated onto colleting substrates. As the Au particle is heated up to a certain temperature, this thin

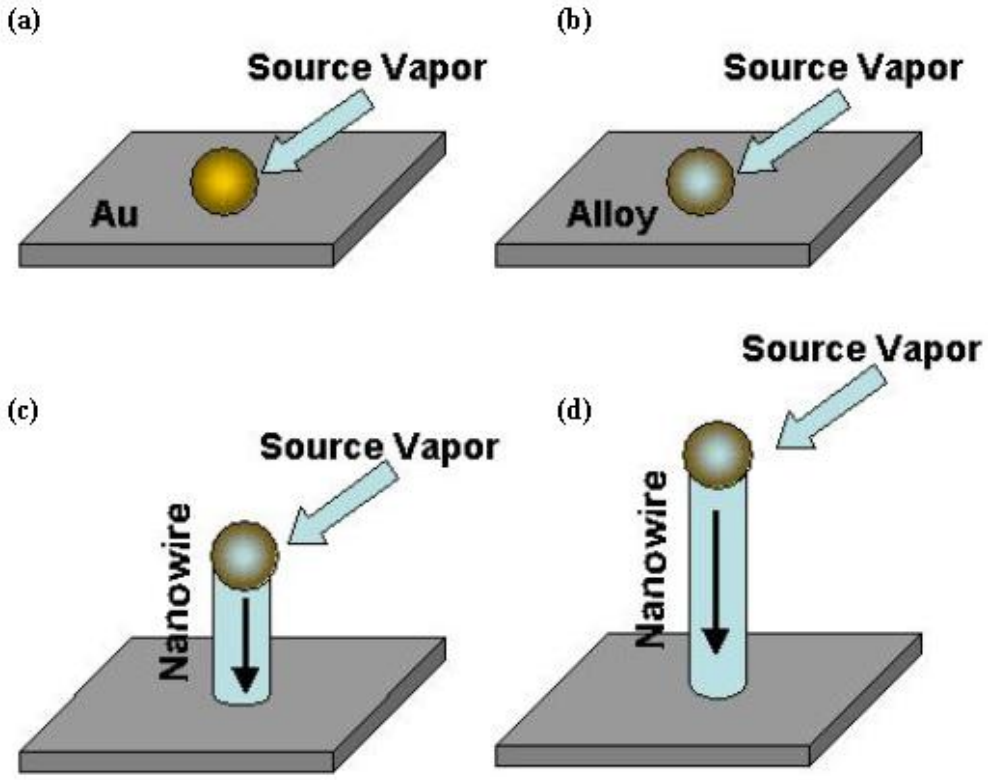

Fig 1.12: Schematic illustrating the various stages of the VLS process**.**

Au layer will be molten to form liquid droplet equally distributed on the substrate. The carrier gas transports the source material vapor to the Au catalyst droplet. Subsequently, the vapor source diffuses into the metal catalyst to form an alloy. With the reaction process going on, the concentration of the vapor material will exceed the solubility of the metal catalyst. The supersaturated metal and source material alloy precipitates out a solid with source material chemical components. This supersaturation and precipitation process continues until the source material is run out or the

growth conditions are no longer preserved, such as lowering the pressure and temperature. With VLS growth process, metal particles are frequently observed at the growth tip of the ZnO nanowire. This whole process is illustrated in Figure 1.12.

Similar furnace system is used for the VLS growth of ZnO nanowires. Equal amount of ZnO power and graphite powder are used as the source materials. And the collecting substrates are coating with a layer of Au thin film. The reaction temperature of ZnO nanowire synthesis is of around 800-1000 ^{o}C. The reaction temperature is much lower than that of ZnO nanobelts. The reason is that the catalyst facilitate the accumulation and precipitation of ZnO vapor, this lower the temperature requirement. Typical synthesis ZnO nanowire samples are shown in Figure 1.13.

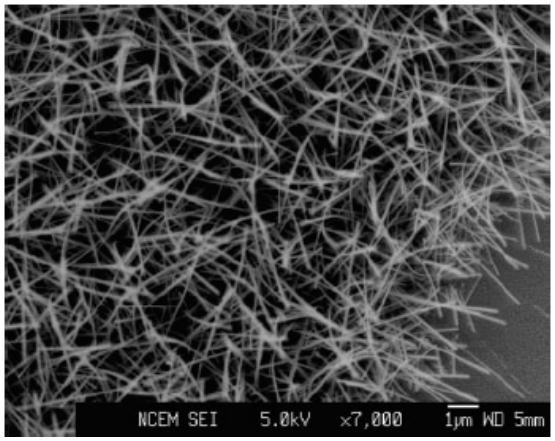

Fig. 1.13 . Typical synthesis ZnO nanowire samples

With SEM, TEM and EDS analysis, these nanostructures are wurtzite structured ZnO materials. TEM analysis shows that the preferential growth direction is <0001>. The (0001)-Zn and $(000\bar{1})$-O polar-surfaces locate on the

top and bottom surface across the entire length of nanowire, which means that the polarity effect is greatly minimized.

1.2.6 Aligned ZnO Nanowire Arrays

Because of the supreme physical and chemical properties of devices based on single nanowires, it is attracting more and more research interests. One of the major topics is how to increase the output signal magnitude of these devices. Aligned nanowire arrays can be one of the options to increase the output signal strength, at the same time, maintaining the intrinsic properties of the nanosized structures.[88, 92-95]

To obtain the synthesis of aligned ZnO nanowire arrays, one of the most important concerns is the substrate selection. ZnO nanowires grow along <0001> direction, which is the c axis of ZnO. Zinc and oxygen ions are six-fold symmetric about the growth axis. A possible method to control the growth direction is to select substrate with similar lattice constant so that the ZnO nanowires can grow epitaxially on the substrate. GaN is one of these ideal substrates for ZnO nanowire array synthesis because of the similar lattice constant with little mismatch of GaN and ZnO (1.9%). Growing ZnO nanowire arrays on the GaN substrate has been thoroughly investigated. In the experiment, GaN plates coated with a thin layer of Au (7-8nm) are used as the collecting templates. With similar experiment set up as the ZnO nanowire growth and adjusting the reaction temperature and other

parameters a little bit, well aligned ZnO nanowires are synthesized, as shown in Figure 1.14. These aligned nanowires have similar length and diameters. Detail TEM analysis (Figure 1.14) reveals that the growing direction of these nanowires is (0001), which is consistent with the lattice orientation of the GaN

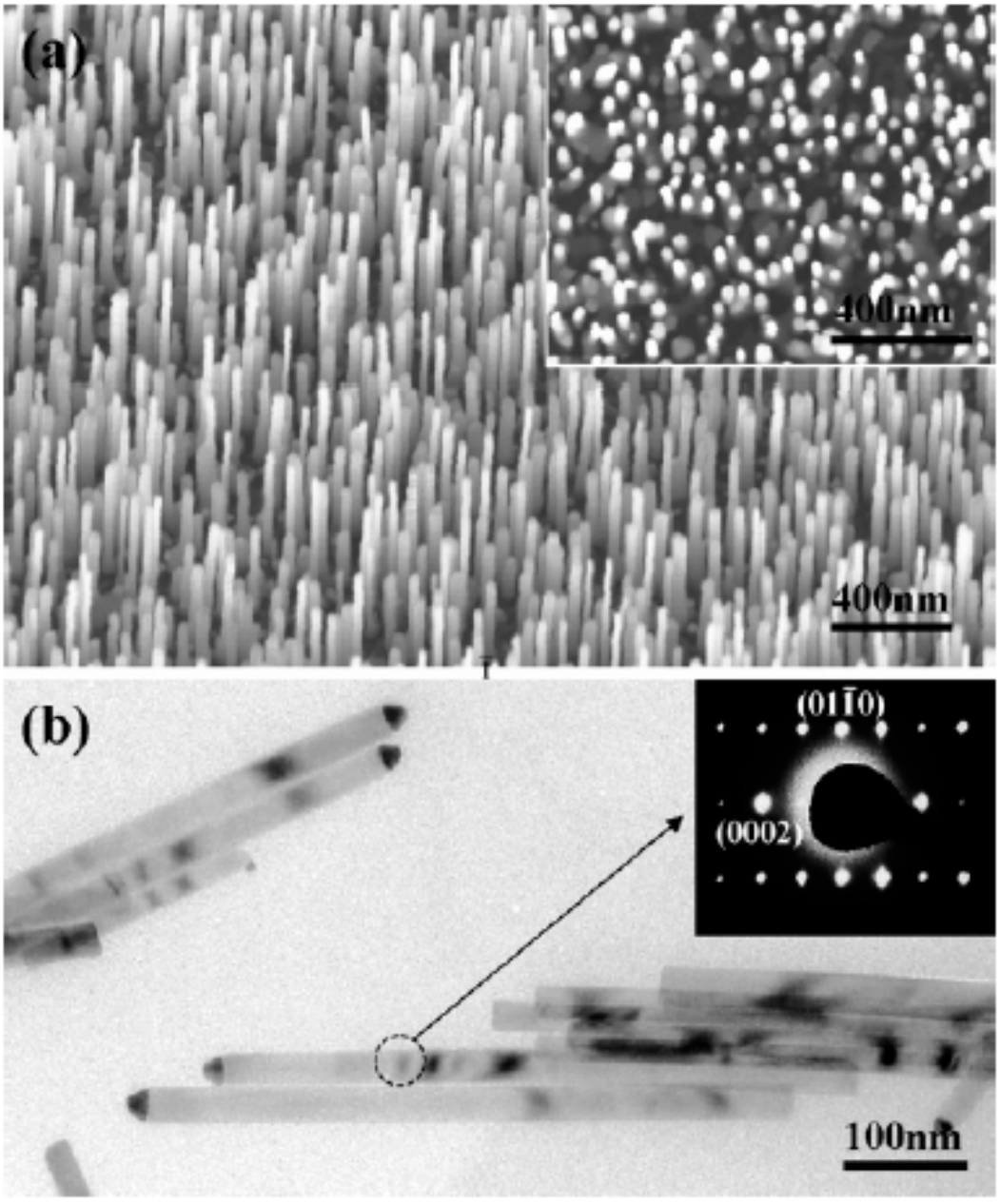

Fig. 1.14 SEM and TEM image of aligned ZnO nanowires.

substrate.

Other than the random growth of aligned nanowires on the substrate, scientists also try to explore the possibility of controlling the patterned growth of ZnO nanowire arrays to meet the specific requirement in the application. Wang et al. demonstrated an effective method for large scale, hexagonal patterned, and aligned ZnO nanowires in their recent research work. Here, a monolayer of self-assembled submicron poly-styrene spheres was used as the patterned mask on the single-crystal Al_2O_3 substrates. This close packed monolayer spheres will generate a hexagonal pattern when a layer of gold is deposited on the substrate. Finally, aligned ZnO nanowires can be grown on the substrate with the same synthesis method. These synthesis patterns and grown ZnO nanowires are shown in Figure 1.14. The growth direction is the same as previous result, along (0001) direction.

1.2.7 ZnO Mesoporous Nanowires

Besides the single crystal solid nanowires, porous ZnO nanowires are also fabricated. Most interestingly, these mesoporous nanowires have also a single crystal structure, which guarantee their advanced electrical and optical properties.[65, 80, 89, 91, 92, 95-133]

In the experiment, a silicon substrate was used as the collecting plates. In the synthesis process, the furnace was heated up to 1300 ^{o}C. This is another different experiment conditions with previous ZnO nanowire synthesis. With the SEM analysis, as shown in Figure 1.15, the nanowires

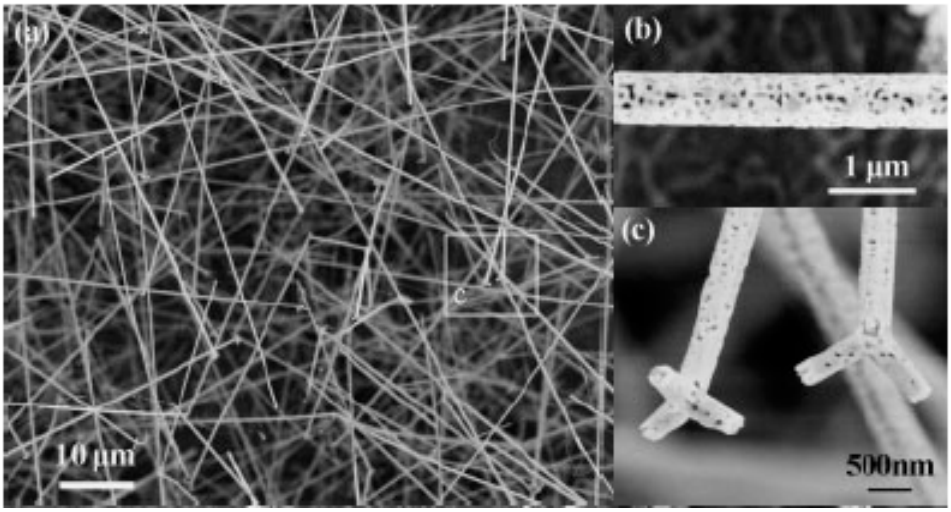

Fig. 1.15 SEM images of mesoporous ZnO nanowires

are around several hundred μm in length, with diameter of 50-500 nm. Magnified SEM images shows that these as-synthesized nanowires are craved on its side surface and forming a unique porous structured nanowire. These porous nanowires are proved to be single crystal structure with TEM analysis.

It is proposed that because of the high reaction temperature, Si-O vapor will be sublimated from the silicon subsrate together with the Zn vapor and O_2. So, during the formation of the ZnO nanowires, the Si-O vapor deposited on the nanowire surface and formed a new product on the surface layer of nanowire, Zn_2SiO_4. This Zn_2SiO_4 layer has a big lattice mismatch with the ZnO nanowire (14%), so Zn_2SiO_4 layer forms textured islands on the surface of nanowire, leaving some area of ZnO nanowires exposed to ambient. The newly form Zn_2SiO_4 is more stable than ZnO. So the relatively high reaction temperature used here may result in evaporation of Zn-O from the open areas. This helps the formation of the holes in the volume of the

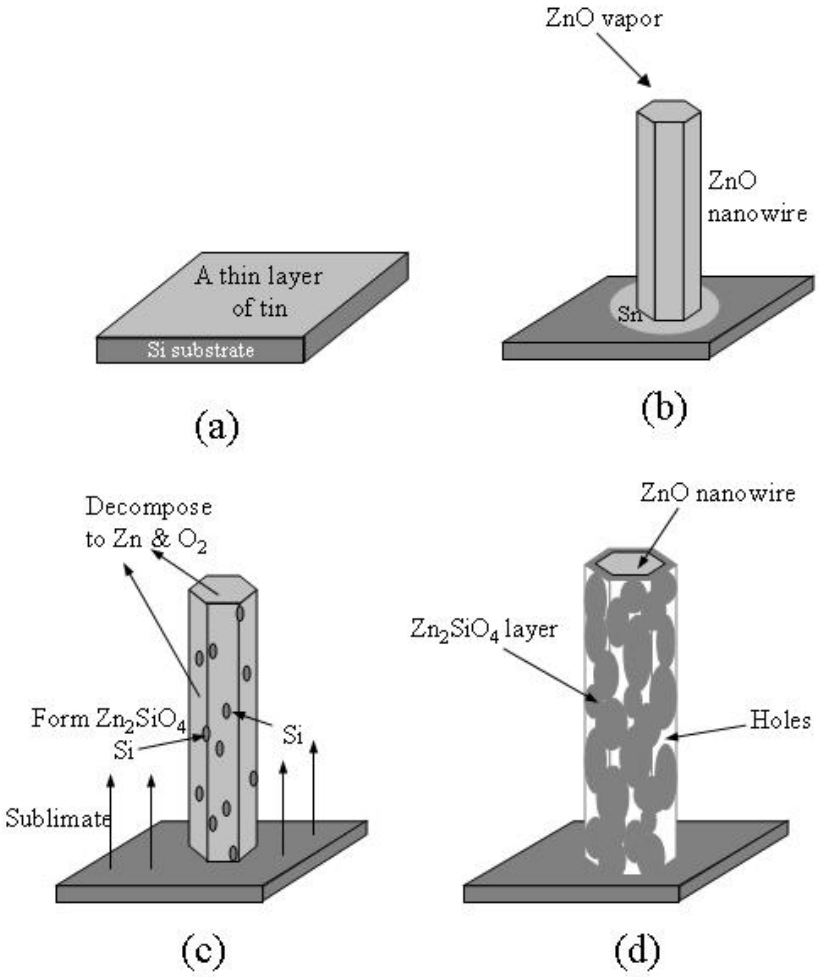

Fig. 1.16 Growth mechanism of ZnO mesoporous nanowire.

nanowire. The sublimation of ZnO and growth of Zn_2SiO_4 proceed simultaneously and finally end with a high-porosity ZnO nanostructure. This growth mechanism is shown in Figure 1.16.

1.2.9 Summary

Semiconducting oxides have been successfully employed as materials for chemical and biological sensing in bulk and thin film materials. This section includes the synthesis of different nanostructures of semiconducting oxides,

especially ZnO. ZnO nanobelts, nanorings, nanohelix, nanocombs, nanowires, nanowire arrays, etc. has been successfully fabricated. A large portion of these nanostructures mostly demonstrated are synthesized in our laboratory. Among these newly reported nanostructures, a specific group of polar-surface dominated nanostructures is of great importance to illuminate the complex growth mechanism and the perfect art of the combination of physical effect, chemical effect and mechanical effect. Also, these semiconducting oxides nanostructures have been demonstrated and proposed to process significant application in electronics, optics, and nanopiezotronics, which will be reviewed in the next part of this book chapter.

1. 3 Device Applications of ZnO Nanowires/Nanobelts

Semiconducting oxide one-dimensional nanostructures exhibit unique and novel size-dependent chemical and physical properties.[80, 89, 91, 92, 95-133] With a reduction in size, new electrical, mechanical, chemical and optical properties are introduced. The electrical conductivity of nanowires depends strongly on the species and concentration of surface adsorbed molecules.[134] These semiconducting oxide nanowires have been successfully incorporated as the most basic circuit component, a field-effect transistor (FET).[91] Thus, they are ideal for the fabrication of electric-signal based nanosensors for chemical and biological applications,[135] which are superior to bio-detection because of their

potential for in-situ and real-time detection as well as implantation in biological systems.

Because of the advanced properties of ZnO and its representatives as a typical semiconducting oxide, we will mostly focused on the applications and research advance on ZnO nanowires/nanobelts to elucidate the supreme application potentials of semiconducting nanowires in transistors, optoelectronics, sensors and piezotronics.

As a typical semiconducting oxide material, ZnO has a large direct band gap of 3.37 eV, which could lead to lasing action based on exciton recombination even above room temperature. This makes ZnO a very promising candidate for applications in optoelectronics. Except for the above advantages, there are also other special properties making ZnO more preferable than other material in the application of the one dimension nanostructures such as its large piezoelectricity effects, ± (0001) polar-surfaces and pyroelectricity. Recently, great research efforts on device applications of ZnO nanowires have been carried out. The research is mostly focused on and normal transport properties, optical and, piezotronic of ZnO nanowires.

1.3.1 Transport Properties of ZnO Nanowires/Nanobelts

To fully employ the semiconducting oxide nanowires and explore the potential to use these 1D nanowires to replace current electronic circuit device

components would be a great interest of current nanotechnology research. The most basic and essential aspect in realizing this objective is to test the transport properties of semiconducting oxide nanowires and compare its performance with the bulk materials.[102, 104, 136-138]

A typical nanowire based device was fabricated based on a lithography process. First, the as-synthesized ZnO nanowire/nanobelt samples were placed in ethanol and ultrasonicated for 15 minutes to disperse the bundles into individual nanobelts. These nanowire suspensions are then dispersed onto a Si substrate coating with a SiO_2 insulating layer. A typical annealing treatment is normally conducted to secure the bonding between the dispersed ZnO nanowire/nanobelt and the substrates. Then, the SiO_2/Si substrates are spincoated with a layer of polymer, PMMA. These as prepared substrate can be patterned with E-beam lithography in a SEM to draw an electrode pattern right on the previous deposited ZnO nanowire/nanobelt. After development, a thin layer of titanium and a layer of gold are deposited consecutively onto the patterned electrodes and formed the source and drain patterns. The remaining PMMA are lifted off with defined electrode patterns fabricated on the substrate.

From the work of Heo et al.,[138] the basic transport properties of ZnO nanorods were investigated with a similar process as introduced previously. Here, three layers of metals Al/Pt/Au are deposited as the metal electrode. This is to build an Ohmic contact between the metal and ZnO nanorods

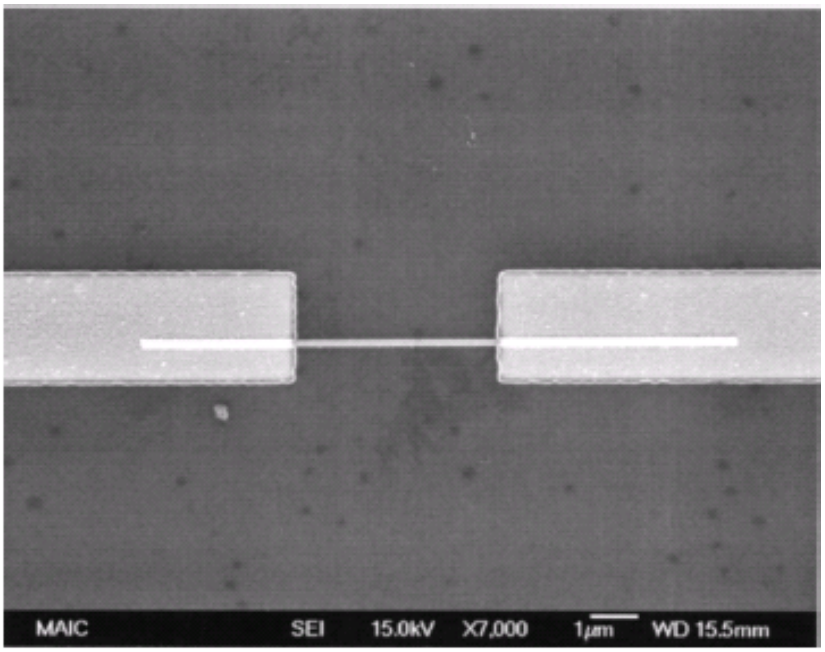

Fig. 1.17 SEM micrograph of single ZnO nanorod bridging two Al/Pt/Au Ohmic contact pads

because of the similar work function of Al and ZnO. Figure 1.17 is a SEM image of the as fabricated ZnO nanorod based devices. Figure 1.18 shows the I-V characteristics of ZnO nanorod as a function of temperature. With increasing of temperature, the current flowing through the device also increased. According to the measured data, the resistivity of a ZnO nanorod is calculated to be 4 Ω-cm. The current is increased due to thermal activation obey the form $I=I_0\exp(-E_a/kT_d)$. Here E_a is the activation energy, k is boltzmann's constant, and T is the absolute measurement temperature. The activation energy derived from the data is 0.089eV.

In the attempts to investigate the transport properties of ZnO nanowires, Li et al.[104] demonstrated that surface oxygen species played a significant role in determination of conductance and transport process through individual ZnO nanowires. The sample was loaded into a chamber. High purity

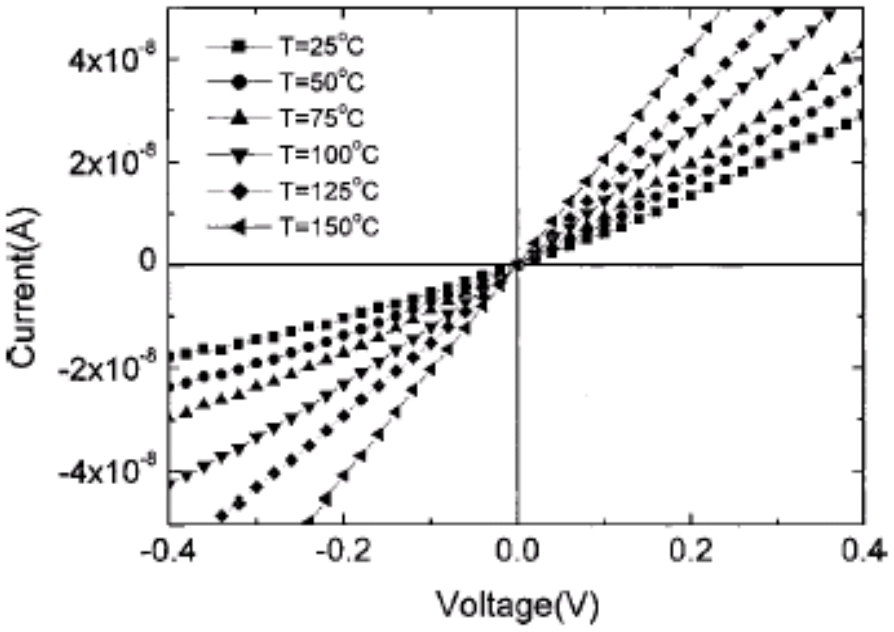

Fig. 1.18 *I–V* characteristics of single nanorod measured at different substrate temperatures.

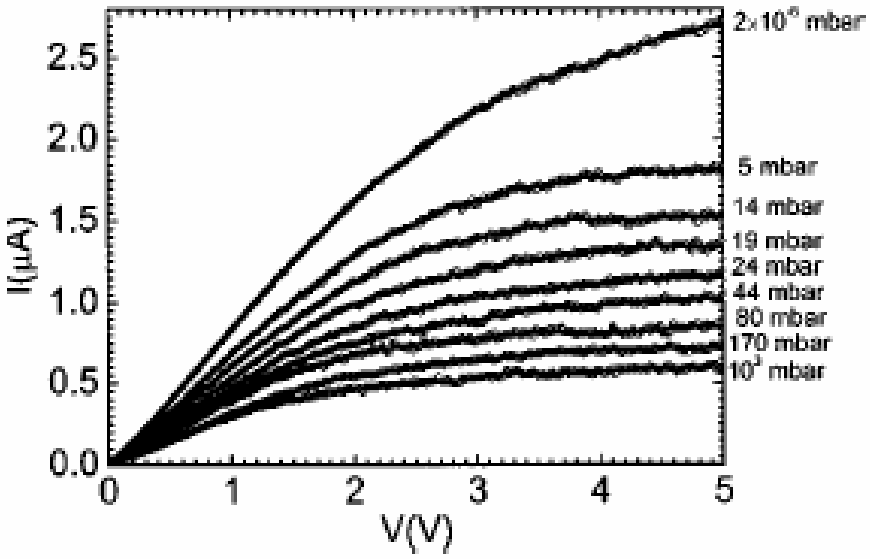

Fig. 1.19 *I-V* curves at different oxygen pressure. $2x10^{-6}$, 5, 14, 19, 24, 44, 80, 170 and 10^3 mbar, respectively.

~99.99% oxygen gas is added into chamber to adjust the oxygen pressure. I-V measurement showed that the conductance decreased with increasing the

oxygen pressure, as shown in Figure 1.19. The pressure was $2x10^{-6}$, 5, 14, 19, 24, 44, 80, 170, and 10^3 mbar respectively. The current decreased from 2.7 to 0.6 A as the oxygen pressure increased from $2x10^{-6}$ to 10^3 mbar. The current decrease of ZnO nanowire is mainly a result of further electron depletion due to the enhanced oxygen adsorption as the concentration of the oxygen increases. This result shows that the surface states of ZnO nanowire play a

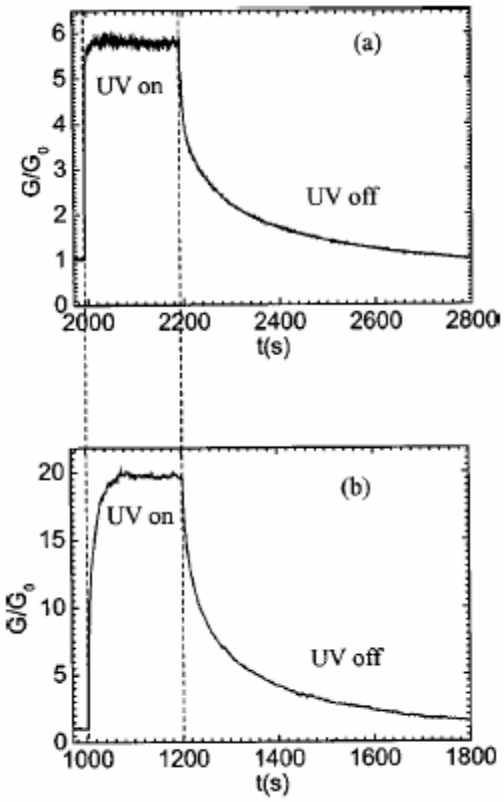

Fig. 1.20 The relative conductance (G/G_0) as a function of time as the UV light is switched on and off (a) under vacuum and (b) in air.

significant role in electric transport. Figure 1.20 shows the UV response of a ZnO nanowire in Li et al.'s work. In the demonstrated data, the ratio of G/G_0 is used to present the conductance change, G_0 is the initial value. The conductance increases by 5.8 times with a 254nm UV source illumination in

vacuum and 20 times in air ambient. The increase of conductance upon UV illumination is attributed the enhanced carrier density with the excitation of the UV source and the reduced depletion region by desorption of the surface oxygen species on the ZnO nanowire. Detail analysis of the optical response of ZnO nanowire will be discussed in another section of this chapter.

1.3.2 ZnO Nanowire Based Field Effect Transistors (FET)

Nowadays, the development of microcircuit system has come to a bottle neck as predicted by Moore's law. With the traditional thin-film/lithography fabrication method, it's getting harder and harder to achieve the increase transistors' density and processing speed at the rate predicted by Moore's law. As a result, new types of transistors, such as novel nanostructures based FETs, are attracting great research interests. So, except for previous basic carrier transport properties study, it is also important in to study the performance of ZnO nanowires in the circuit components. Field Effect Transistor is one of the most important building blocks for modern microelectronic devices. It is ideal to investigate the basic transport properties of ZnO nanowires.[40] Traditional FET operates by using a gate voltage to control the source-drain current to an on and off state. A typical nanowire based FET, as shown in Figure 1.21, is composed of two metal electrodes, a single nanowire lying across the electrodes. The two metal contacts are connected to outer measurement equipments to study the transport performance of the

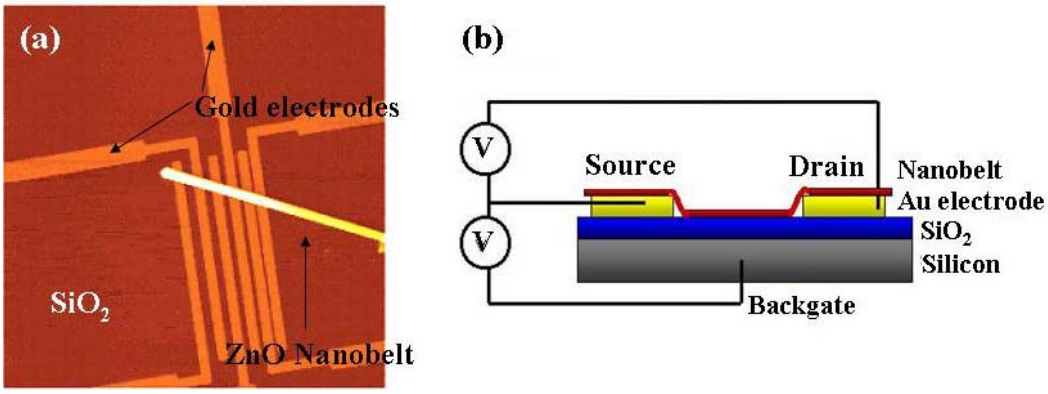

Fig. 1.21 (a) AFM image of a FET based on ZnO NB. (b)Schematically illustration of the FET

incorporated ZnO nanowire. The whole device is fabricated on a highly doped Si substrate, which is also used as the back gate for the FET. There is a non-conducting oxide layer coated on the substrate to isolate the back gate with the testing nanowires.

In the research work of Arnold et al.,[40] a typical FET based on ZnO nanowire/nanobelt are fabricated and characterized. This FET was fabricated based on a typical lithography process as introduced before. FET based on ZnO nanobelts of thickness between 10 and 30nm. ZnO nanobelts were deposited on the predefined gold electrode arrays. The thickness of the SiO_2 oxide gate dielectric layer was 120nm and the back gate electrode was composed of a layer of gold on the Si (p+) side of the substrate. A typical ZnO field effect transistor (Figure 1.22) showed a gate threshold voltage of -15V with switching ratio of around 100. The peak conductivity of ZnO nanobelt was measured to be 1.25×10^{-3} $(\Omega cm)^{-1}$. Here, V_g increases positively (negatively), I_{sd} increases (decreases). This indicates that ZnO nanorods are typical n-type semiconductors. I_{sd}–V_g curves of ZnO nanorod FETs also show

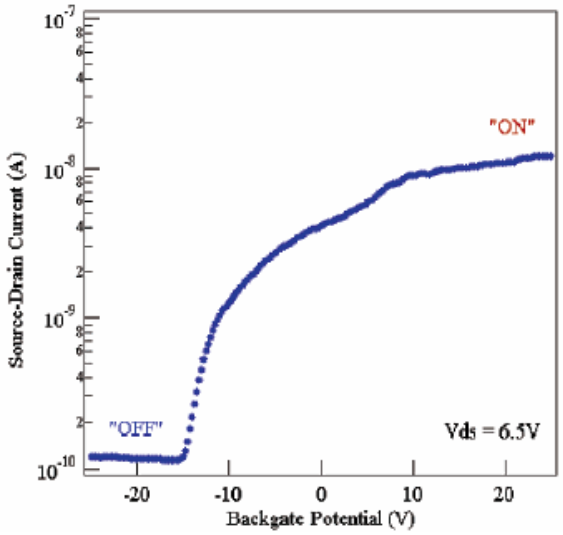

Fig. 1.22 *I-V* characteristics of a typical ZnO NB based FET showing a gate threshold voltage of -15V with switching ratio of around 100.

that the devices operate in a depletion (normally ON) mode. This field effect transistor based on ZnO nanobelt can also be used as a UV detector showing on/off response to the UV light.

However, the properties of this ZnO nanobelt FET fabricated in a traditional way without any further treatment is not very promising comparing with current thin-film based FET. High concentration of impurities in ZnO nanobelts, large contact resistance, and surface-mediated effects including chemisorptions, carrier scattering and trap processes by surface states, these are the possible reasons the lower the performance of ZnO nanobelt based FET. To enhance its performance to make it more applicable for future application, its basic characteristics as a circuit component must be improve, such as the switching on/off ratio, transconductance, and mobility of the carriers. In the work of Park et al., the performance of a ZnO nanowire FET was greatly improved with coating of a

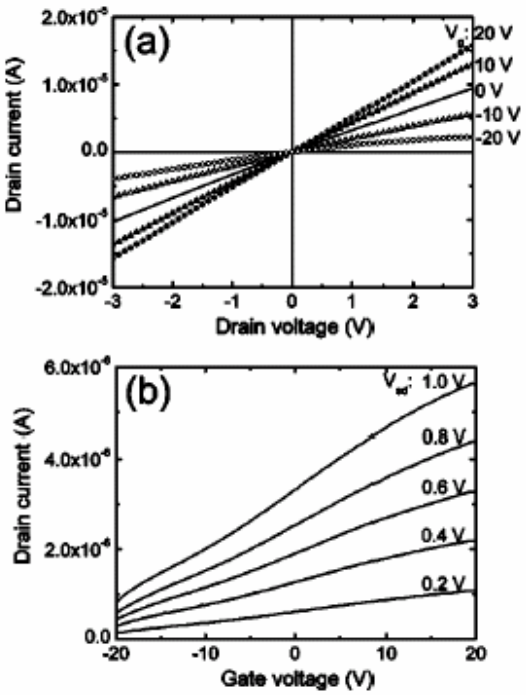

Fig. 1.23 (a) Typical I_{sd}–V_{sd} characteristic curves as a function of V_g for ZnO nanorod FETs prepared without any intentional surface treatment. The linear and symmetric I_{sd}–V_{sd} curves were obtained under different V_g, indicating the low resistant ohmic contact formation between ZnO and Ti metal layers. (b) I_{sd}–V_g curves of ZnO nanorod FETs show that the devices operate in an *n*-channel

polyimide polymer layer on the surface of ZnO nanowire.[139] Figure 1.23 is a typical I_{sd}-V_{sd} characteristics measurement as a function of gate voltage (V_g) for FET based on ZnO nanorod. At V_{sd}=1.0 V, transconductance gm is 140 nS. Assuming that an effective channel width (W) equals a nanorod diameter of 100 nm, normalized transconductance g_m/Wd is estimated to be around 1.4 mS/ mm. To enhance the performance of this ZnO nanowire FET and explore the surface passivation effect on the electrical properties, A 2 μm thick polyimide layer was spin coated on the surface of ZnO nanowire. Polyimide is frequently used in a bipolar technology to reduce surface effects. This as-treated device was the ncured at 120°C for 5h. I-V characteristics of this

polymer coated nanowire based FET is shown in Figure 1.24. The electrical characteristics of ZnO nanorod FETs were greatly improved with this coating layer of polyimide. As show in Figure 1.24, the transfer I_{sd}-V_g curves exhibit excellent conductance response to gate voltage. In regardless of the source and drain voltage bias, the FET was fully turned off at a small value of negative bias V_g=-5V. At V_{sd}=1.0V, the transconductance exhibited its maximum value of 1.9mS at V_g=2.3V which is thirteen times higher than that of the untreated ZnO nanorod. In addition, the drain current decreased drastically below threshold voltage V_{th}, so the I_{sd} -V_g curve shows a large on/off ratio of 10^4 -10^5. Mobility of this polymer coated ZnO nanorod based

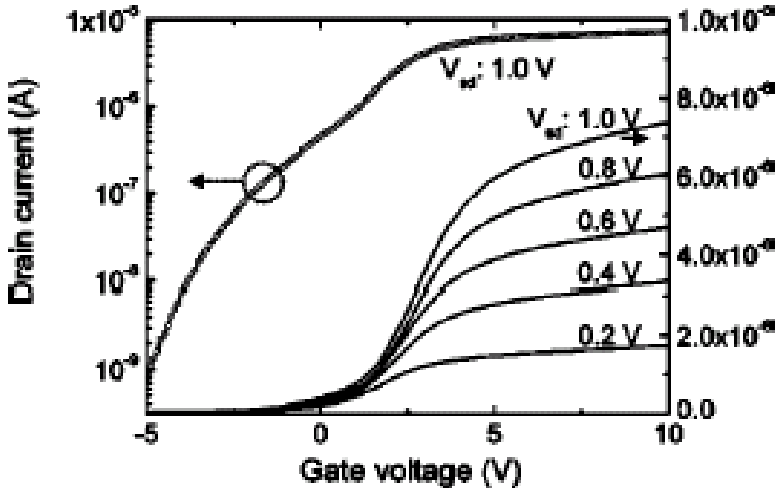

Fig. 1.24 *I-V* characteristics of polymer coated NW based FET.

FET was analyzed. The electron mobility in ZnO nanorod FETs is decided by g_m, which can be calculated by $\mu=g_mL^2/(CV_{sd})$. The maximum electron mobility value of untreated ZnO nanorod FET is 75cm^2/Vs. However, the electron mobility of polyimide coated ZnO nanorod FET is enhanced to a

much higher value, with a value of 1000cm^2/Vs. This achieved high mobility of oxide nanowire FETs is a great progress in enhancing the performance of nanowire based FETs. As one of the suggested reasoning of the polymer coating effect on enhancing FET characteristics, the coated polyimide layer might block the interaction of ZnO nanorod surfaces and ambient impurities. This help to increase the conductance response to the applied gate voltage.

Other than coating a polymer layer on the surface of ZnO nanorod, scientists explore different possibilities and methodologies to enhance the performance of FET based on oxide nanowires to further improve the properties of these devices. In the work of Cha et al, another sort of high performance ZnO nanowire FETs is realized with self-aligned nanogap gate electrode.[140] With extremely precise control in lithography process, a FET with nanogap gate electrode was fabricated. As shown in figure 1.25, a ZnO

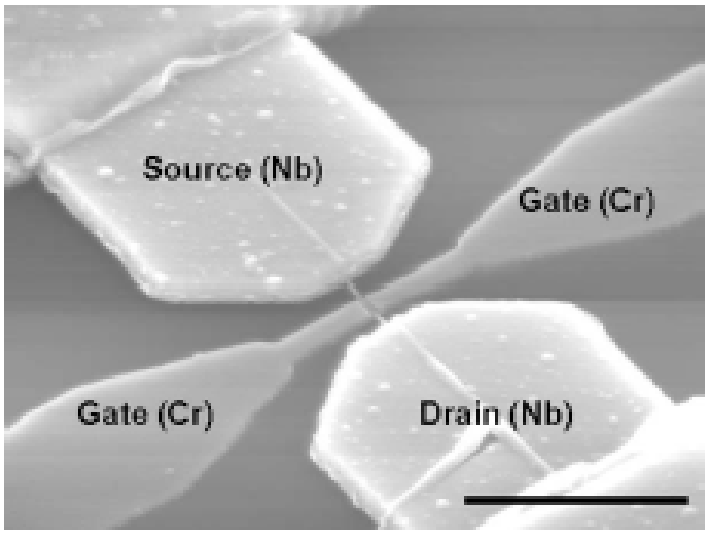

Fig. 1.25 45° tilted SEM image of fabricated ZnO nanowire FET with selfaligned gate electrodes and nanosize air gaps. Scale bar is 2.5 μm.

nanowire lies across two Nb source and drain electrodes. Two Cr metal

electrodes are used as side gate for this FET. ZnO nanowire is suspended between the electrodes. Channel length for this FET is 968 nm, channel width is 60nm, gate width is 360nm, and thickness of gate insulator (air gap around the suspended nanowire) is 26nm. Due to the close distance of the air gap,

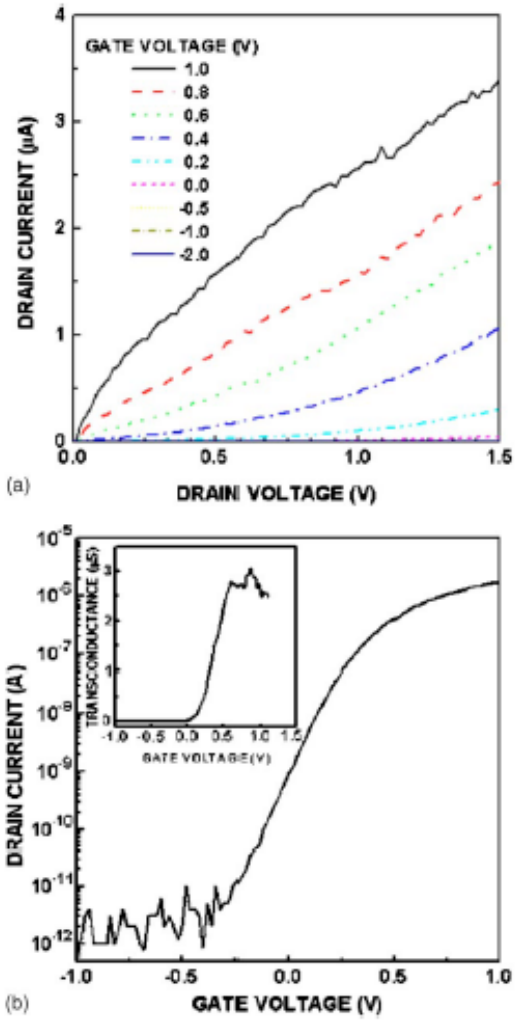

Fig. 1.26 (a)Output characteristics of ZnO nanowire FET. The gate voltage range is from −2 to 1.0 V. (b) Transfer characteristic of the device with 0.8 V of source-drain voltage. Insert is transconductance curve of the device. The saturation

simulation result shows that the electric field distributed outside the physical gate must be taken into account because of its comparable magnitudes to that within the physical gate. This small gate insulator thickness makes a significant effect on enhancing the performance of ZnO nanowire FETs.

Figure 1.26 shows the IV characteristics of these FETs. The FET exhibits excellent performance with a transconductance of 3.06 S, a field effect mobility of 928cm^2/Vs, an on/off ratio of 10^{-6}. The electrical characteristics are the best reported data for ZnO transistor and closed to previously reported p-type carbon nanotube FETs. By reducing the physical gate insulator only, without the complexity and uncertainty of the chemical functionalized layers, this raised the possiblitiy of using ZnO FET in a nanoscale logic circuit.

1.3.3 Optoelectronics Based on ZnO Nanowires

ZnO is a wide band gap semiconducting material. It has a wide band gap of 3.4eV with an exiton binding energy of 60meV, which makes ZnO 1D nanostructures ideal for optical device applications. Due to its promising properties on optoelectronics, great amount of research efforts have been performed on its application in different optoelectronics for 1D nanowires, such as the UV sensors, optically pumped nanolaer, photodiode, phonto conductor, and etc.

1.3.3.1. UV Detector

Due to the significant intrinsic optical properties of ZnO, ZnO nanowire is adapted to be used as a UV detector.[125, 141-143] This is the most common and straight forward application of ZnO nanowires. The UV absorption spectrum of ZnO has a peak at the wavelength of around 380nm, as shown in

Figure 1.27. This means that incidence of UV light will generate

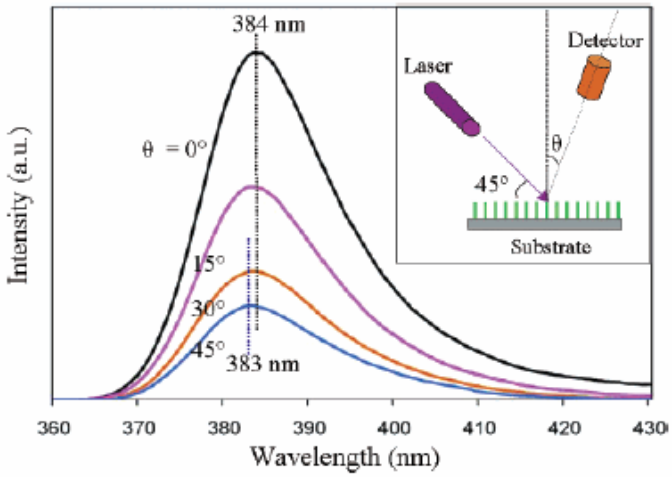

Fig. 1.27 Photoluminescence (PL) spectra acquired from an aligned ZnO nanorod array as a function of the angle between the detector and a direction normal to the substrate. The inset shows the experimental set up.

electron-hole pairs inside ZnO nanowire. By incorporating ZnO nanowire into a general nanodevice, ZnO nanowire exhibit significant conductance change upon UV illumination. Figure 1.28 is typical IV characteristics of a ZnO nanowire based transistor when it is illuminate by a UV lamp. The wavelength of this UV light is 254nm. The photon energy is 4.9eV and above the band gap of ZnO. So, electron hole pairs can be generated by illumination. Different configurations of UV detectors were fabricated to test the ZnO nanowire performance, such as UV detectors based on a single ZnO nanowire or a large scale of ZnO nanowire arrays.[101, 140] Most recently, a high internal gain UV photodetector was realized by Soci et al. [144]

In Soci's work, upon UV illumination at relatively low light intensity (I= 10 W/cm^2), the current increases by several orders of magnitude. With theoretical calculation, this current response is equivalent to a

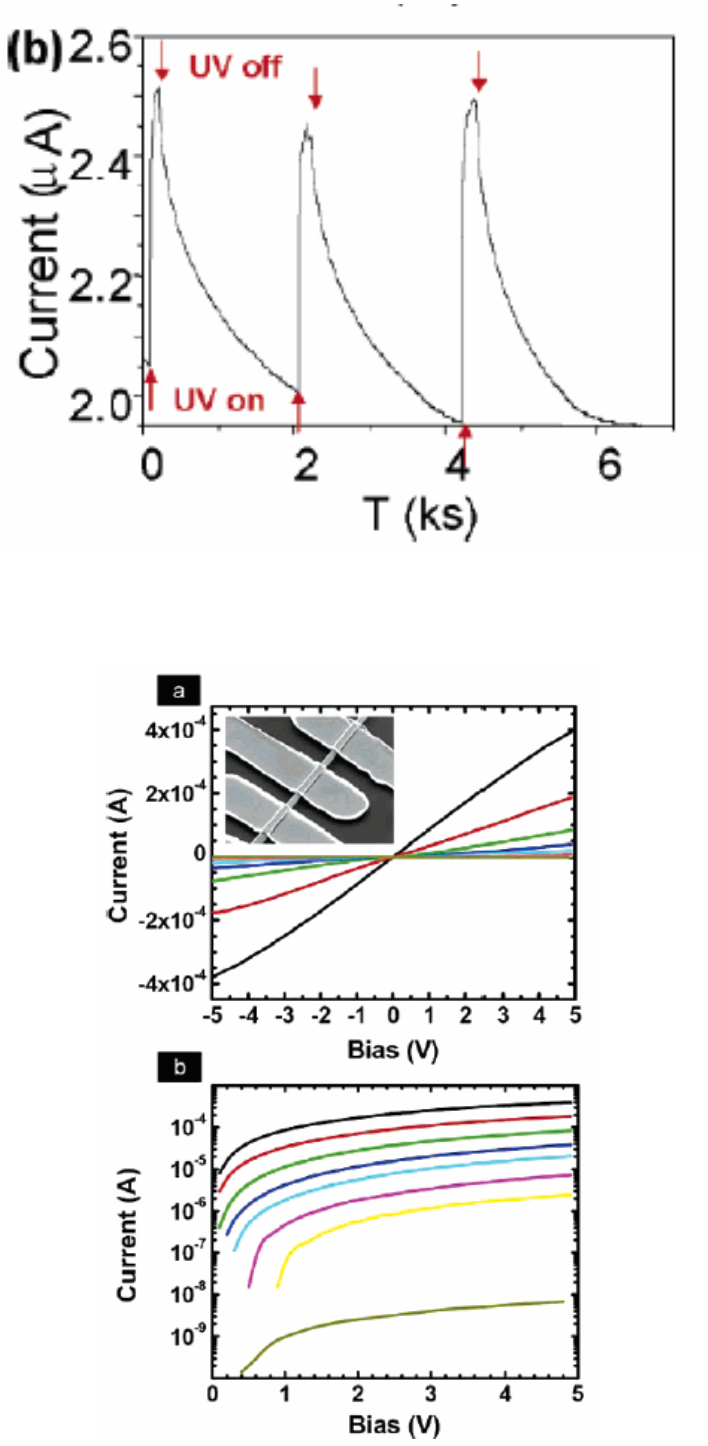

Fig. 1.29 (a) I-V characteristics of a single-NW photodetector as a function of light intensity; from top to bottom, the curves were measured at the following intensities: $4x10^{-2}$ W/cm^2 (black), $4x10^{-3}$W/cm^2 (red), $4x10^{-4}$W/cm^2 (green), $1.3x10^{-4}$W/cm^2 (blue), $4x10^{-5}$W/cm^2 (cyan), $1.3x10^{-5}$W/cm^2 (magenta), $6.3x10^{-6}$W/cm^2 (yellow), and in dark (brown). Inset is the SEM image of a typical ZnO NW device (obtained at 450 tilt angle); the spacing between the interdigitated electrodes is 2mm. (b) The I-V curves presented in Figure 1a are replotted on a natural logarithmic scale.

photoconductive gain of $G>10^8$. Figure 1.28 is the typical I-V characteristics of the ZnO nanowires in dark and under UV illuminations (390nm) at different light intensities. As can be seen from the data, the current increases significantly under illumination. When the light intensity is only 6.3 $\mu W/cm^2$, it can trigger 2 orders of current magnitude increase. With light intensity increase, the photocurrent also increases. The highest magnified ratios are obtained as high as 5 orders of magnitude in this experiment at light intensity of $40mW/cm^2$. Figure 1.29 is the IV curves drawn on a natural logarithmic scale to better demonstrate the increase of current intensities.

Generally, the photoconduction mechanism of nanowire involves fast carrier thermal excitation and trapping at the nanowire surface and electron-hole recombination at extended and localized states. Figure 1.30 is the schematic illustration of ZnO nanowire photoconduction mechanism. Because of the high surface-to-volume ratio of a nanowire, ZnO nanowires have a high density of defects at its surface which can trap holes and increase the photocurrent response. Upon UV illumination of photon energy larger than the semiconductor band gap, electron-hole pairs are generated. With exiting of high density surface trapping states, the photogenerated holes are easily trapped at the surface. The photogenerated electrons are left unpaired and contribute to the drastically increase of photocurrent. Schematics of the nanowire energy band diagrams and the photogeneration and recombination process under illumination are displayed respectively in Figure 1.30. For

ZnO nanowire, oxygen adsorption and desorption are the governing surface trapping mechanism for the photoconduction. First, in air ambient without UV illumination, oxygen molecules are adsorbed on the surface and capture free electrons presented in the n-type oxide semiconductor [O_2 (g) + e- =O_2^- (ad)]. This forms a low-conductivity depletion region at the surface of ZnO

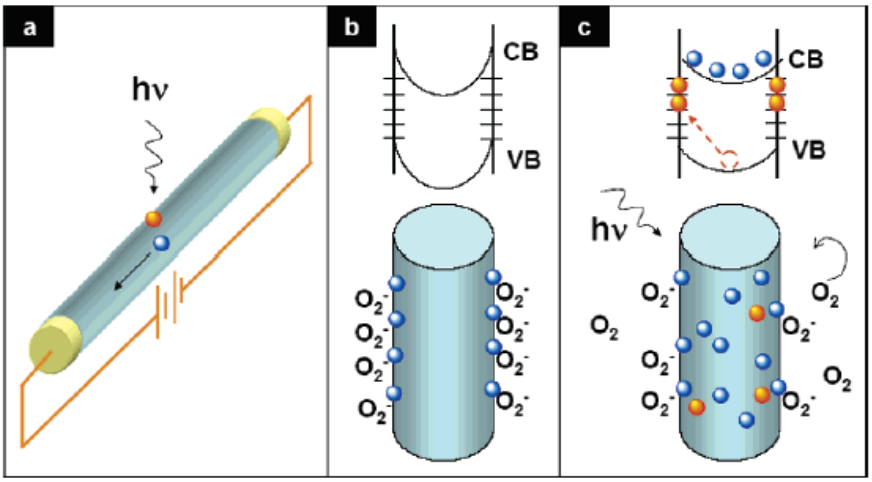

Fig. 1.30 (a)Photoconduction in NW photodetectors. (a) Schematic of a NW photoconductor. Upon illumination with photon energy above E_g, electron-hole pairs are generated and holes are readily trapped at the surface. Under an applied electric field, the unpaired electrons are collected at the anode, which leads to the increase in conductivity. (b and c) Trapping and photoconduction mechanism in ZnO NWs: the top drawing in (b) shows the schematic of the energy band diagrams of a NW in dark, indicating band-bending and surface trap states. VB and CB are the valence and conduction band, respectively. The bottom drawing shows oxygen molecules adsorbed at the NW surface that capture the free electron present in the n-type semiconductor forming a low-conductivity depletion layer near the surface. (c) Under UV illumination, photogenerated holes migrate to the surface and are trapped, leaving behind unpaired electrons in the NW that contribute to the photocurrent. In ZnO NWs, the lifetime of the unpaired electrons is further increased by oxygen molecules desorption from the surface when holes neutralize the oxygen ions.

nanowire. Upon UV illumination, photogenerated holes migrate to the surface along the potential slope produced by band bending and combine with the negative charge adsorbed by oxygen. Consequently, oxygen is

released and desorbed from the surface. [$h^+ + O_2^-$ (ad) = O_2]. With hole trapped at the surface, the electrons-hole recombination is greatly suppressed. This results in the carrier life time increase. Also, the hole-trapping effect will reduce the surface depletion region and help with the increase of photo gain. As a result, this surface hole trapping by the oxygen absorption and desorption is proposed to account for the high photoresponse of ZnO nanowire.

Basically, UV illumination response of ZnO nanowire can be achieved in a significant extent. With a giant photo gain as a result of the surface trapping effect, ZnO nanowires are of critical in the application of photo sensing and the design of novel photo detector architectures.

1.3.3.2 Nanolasers

For usual semiconducting material, an electron-hole plasma (EHP) process is required for lasing action. This EHP process is common for conventional laser diode operation and normally require high lasing threshold. However, for ZnO, due to the existing of exiton states and the relatively large exiton binding energy, 60meV. This value is substantially larger than that of ZnSe (22meV) and GaN (25meV), which greatly increase the efficiency of exiton binding. Therefore, ZnO is an ideal candidate for low-threshold stimulated emission. Considering the the large amount of surface states of 1D ZnO nanowire, which enhance the radiative

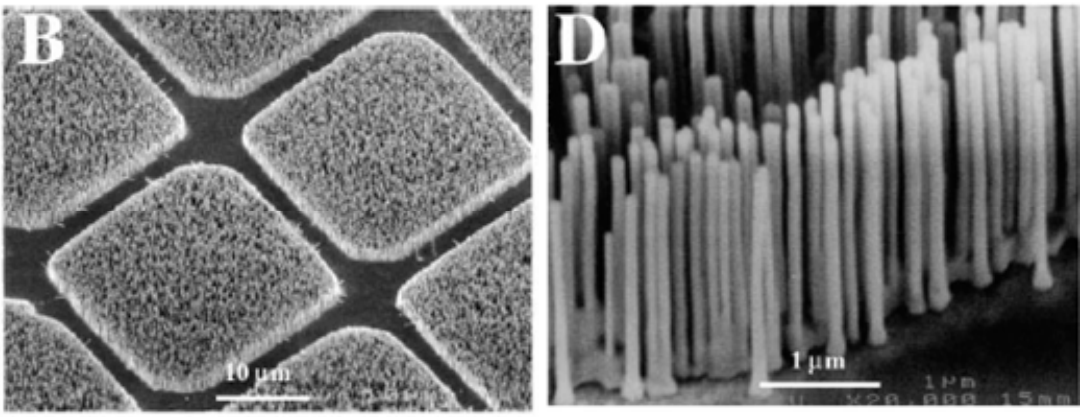

Fig. 1.31 SEM images of ZnO nanowire arrays grown on sapphire substrates.

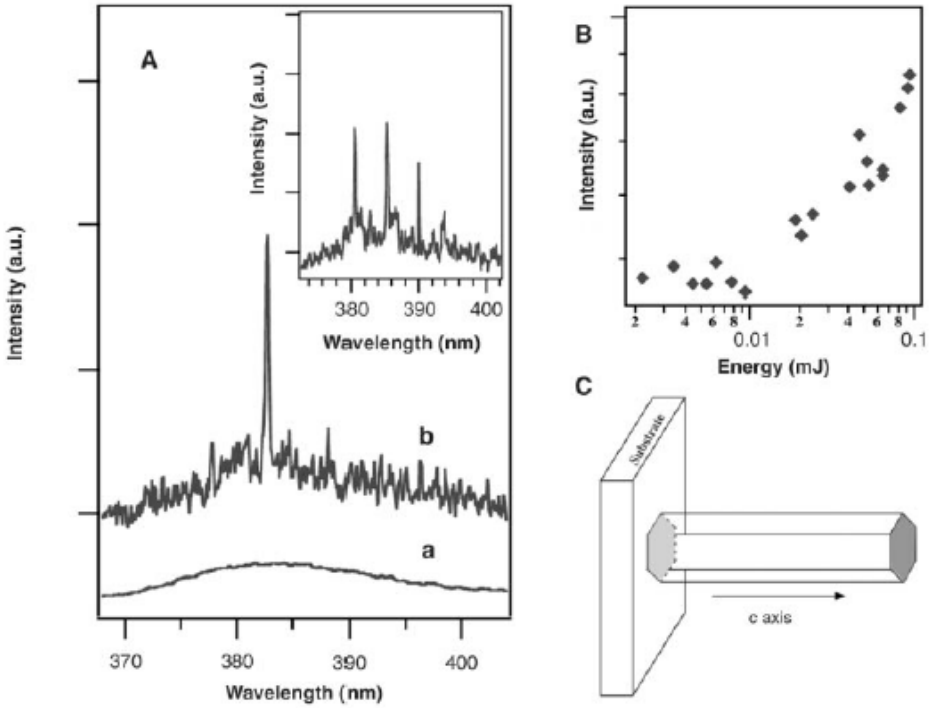

Fig. 1.32 (A) Emission spectra from nanowire arrays below (line a) and above (line b and inset) the lasing threshold. The pump power for these spectra are 20, 100, and 150 kW/cm^2, respectively. The spectra are offset for easy comparison. (B) Integrated emission intensity from nanowires as a function of optical pumping energy intensity. (C) Schematic illustration of a nanowire as a resonance cavity with two naturally faceted hexagonal end faces acting as reflecting mirrors. Stimulated emission from the nanowires was collected in the direction along the nanowires end-plane normal (the symmetric axis) with a monochromator (ISA, Edison, New Jersey) combined with a Peltier-cooled charge-coupled device (EG&G, Gaithersburg, Maryland). The 266-nm pump beam was focused to the nanowire array at an angle 10^0 to the end-plane normal. All experiments were carried out at room temperature.

recombination due to carrier confinement in quantum size, it represents an optimistic future for potential application in lasing application.

In the work of Huang et al,[145] room temperature UV lasing in semiconductor nanowire arrays has also been demonstrated. The experimental SEM images of nanowires are shown in Figure 1.31. In the experiments, the samples were optically pumped by the Nd: yttrium-aluminum-garnet laser (266nm, 3-ns pulse width). The pump beam was focused on nanowires with an incident angle of 10^{o} to the normal axis. Light emission was collected along the growth direction of the nanowire. At low excitation intensity, the spectrum consists of a single broad spontaneous emission peak as shown in Figure 1.32. As the incident light power increases, the emission peak narrows. Ultimately, when the excitation intensity exceeds a threshold, sharp peaks are observed in the spectrum. Above the threshold, the intensity of the mission increased rapidly with the excitation power. Linewidth of these peaks are 0.3nm and 50 times smaller than that of the spontaneous emission peak below the threshold. These sharp peaks represent different lasing modes at wavelength between 370nm and 400nm. Here, the lasing threshold obtained for these nanowire array lasing is only 40kW/cm^2, which is very low comparing with random lasing's value (300kW/cm^2).

Lasing generation mechanism of these nanowire lasers is proposed. As shown in Figure 1.32, the nanowire surfaces serve as good laser cavity mirrors.

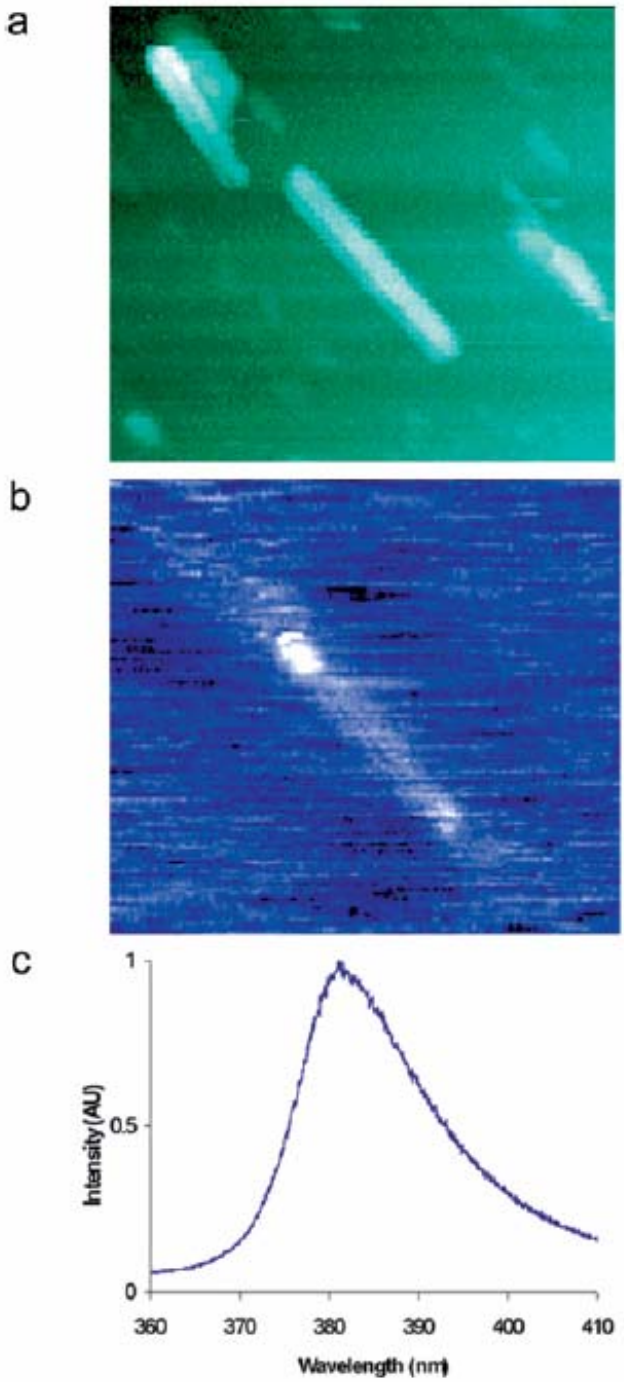

Fig 1.33. Near-field images of a single ZnO nanowire waveguide. (a) Topographical and (b) PL NSOM image size is $(10\ \mu m)^2$ with maximum topographical height of 140 nm. The sample was excited with approximately 100 nJ pulses at 285 nm, resulting in an excitation intensity of about 200 kW/cm^2. (c) The PL spectrum from the wire (fwhm ~ 20 nm), which did not show

Due to the refractive indexes of air and ZnO, the nanowire forms a natural cavity. This help to generate the lasing from the excitation. With the

chemical flexibility and one-dimensionality, the ZnO nanowire could be an ideal miniaturized laser light sources.

In the same research group, Johnson et al.[146] further develop this nanowire lasing technique and realize UV lasing from a single ZnO nanowire. It is shown in Figure 1.33. Near-field optical microscopy images is used to identify and quantify the laser beam. As the same, the linewidth, wavelengths, and power dependence of the nanowire emission characterize the nanowire as an active optical cavity.

1.3.3.3 Nanowire Array LED

Because of the difficulty in fabrication of p type ZnO nanowire, there is still no report on the fabrication of p-n junction of ZnO nanodevices. Park et al. seek an alternative approach to use n-ZnO/p-GaN heterojunction to replace the ZnO p-n homojunction.[147] Generally, the heterojunction shows a lower efficiency than the homojunction. That is because the energy barrier at the interface impedes the carrier injection from one side to the other side.

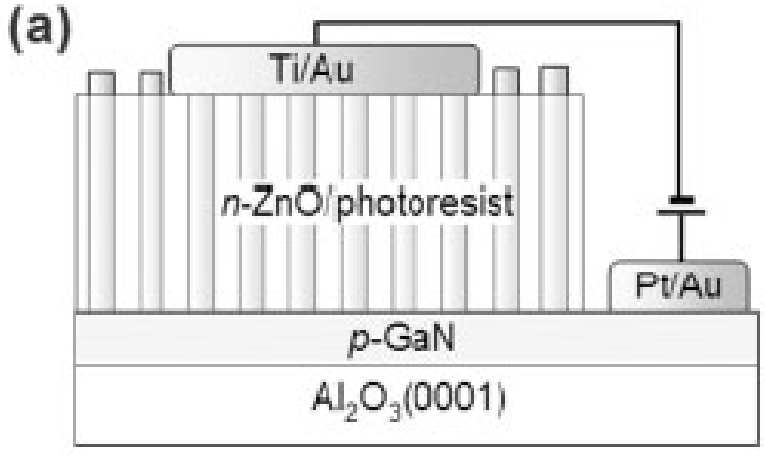

Fig. 1.34 Schematic illustration of a p-GaN/n-ZnO nanorod hetero-structure

This problem is solved by growing n-type ZnO nanowire arrays out of p type GaN substrate. This forms a nano-junction in between the n-type ZnO nanowires and p-type GaN substrate and significantly increases the carrier injection efficiency. Schematics of a such fabricated devices is shown in figure 1.34. A top electrode is deposited onto the tip of the nanowire arrays with assistant of a layer of polymer stuffing layer. By applying voltage signal across the top and bottom electrode, a n-ZnO/p-GaN heterojunction is realized.

Electroluminescent (EL) spectrum of such a n-ZnO/p-GaN EL device is measured at different bias voltage, as shown in Figure 1.35. For the EL device, no light emission was observed at forward bias. Under reverse bias, the nanorod device showed different EL spectrum at different bias level. As shown in Figure 1.35, by increasing the reverse bias from 3V to 7V, emission peak at 560nm (2.2eV) was generated and increased from low excitation intensity to a pretty high level. For reverse bias above 4V, the EL spectrum exhibit a blue emission peak 2.8 EV and a UV peak after 5V at 3.5eV. As investigated by front and back and back side PL spectrum of the n-ZnO/p-GaN devices, the PL data suggested that the EL emission peaks originated from the deep level in ZnO and the Mg acceptor in GaN.

This p-n hetero junction nanowire EL device exhibit high current density and strong electroluminescent peak at very low reverse bias, which suggests

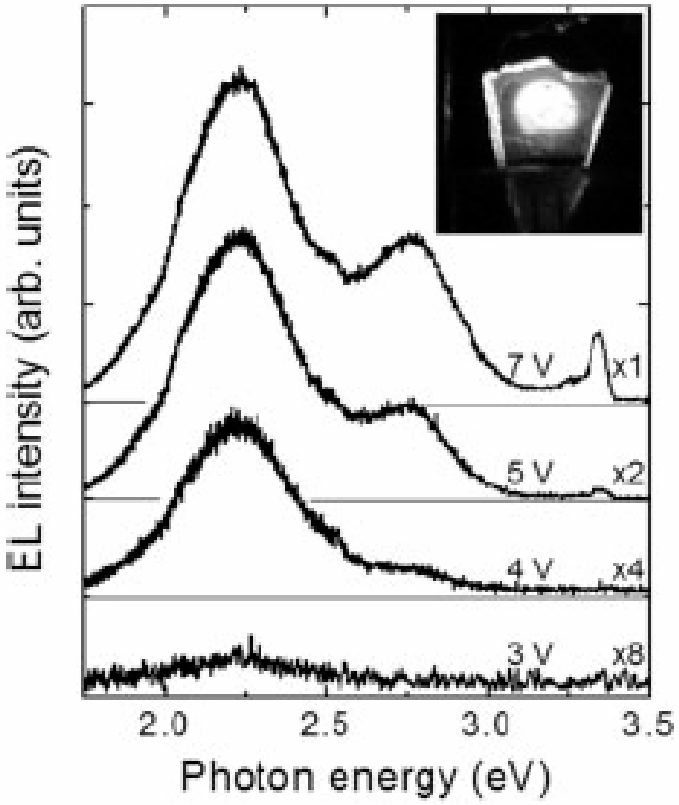

Fig. 1.35 Room temperature EL spectra of a p-GaN/n-ZnO heterojunction device. For reverse-bias voltages larger than 3V, the EL spectra exhibited a yellow emission band centered at 560nm (2.2eV). A weak blue emission band centered at 450nm (2.8eV) appeared for reverse-bias voltages larger than 4V. By further increasing the reverse-bias voltage to 5V, the blue emission peak intensity increased and an additional ultraviolet emission peak was observed at 3.35 eV. The inset is a photograph of light emission from the EL device at a bias voltage of 5V. The electroluminescence was strong enough to be observed clearly by the naked eye.

the optimizing potential application opportunity for EL devices based on nanojunctions.

So far, ZnO nanowires have been demonstrated to possess very promising properties in the application of optoelectronics, such as nanolaser, UV detector and EL devices. With the intrinsic wide bandgap of ZnO nanowires and quantum effect enhanced photo properties, the application of ZnO

nanowire in actual optoelectronics is believed to be an exciting opportunities in nanotechnology.

1.3.4 Chemical and Biological Sensors Based on ZnO Nanowires

As ideal building blocks for constructing nanosized devices, scientists have been exploring different ways to utilize ZnO nanowire in different aspects. Recent research interest in nanoscience due to the special properties associated with ultra-small (nanometer) size materials turns out to be a productive research area. Because of the quantum effect in the nanometer regime, nanostructures display superior properties in many physical and chemical areas such as electric transport, optical response and mechanical resonance.

Due to the high surface to volume ratio and their special physical and chemical properties resulting from the reduced sizes, ZnO nanowire has been explored the potential application as chemical and biological sensors. Generally, ZnO nanowires display high sensitivity to environment condition changes, where significant electric signal transition can be observed as the environment changes. The electrical conductivity of ZnO nanowires depends strongly on the species and concentration of surface adsorbed molecules. Thus, they are ideal for the fabrication of electric-signal based nanosensors for chemical and biological applications, which are superior to bio-detection because of their potential for in-situ and real-time detection as

well as implantation in biological systems. In the research work carried out on ZnO nanowires up to day, it has been approved to be a promising candidate as sensors different gases and environments, such as oxygen, hydrogen, PH value, and ethanol.[40, 103, 134, 148-151]

As demonstrated in these papers, ZnO nanowire exhibit significant conductance change upon different gas exposure. This conductance change is closed related to the surface oxygen species or other chemical species adsorption and desorption effect. In the work of Li et al.,[149] the conductance of ZnO nanowire was demonstrated to be sensitive to oxygen concentration. Also, the threshold voltages of the FET based on ZnO shifted with change of oxygen concentration. The measured data are shown in Figure 1.36. The

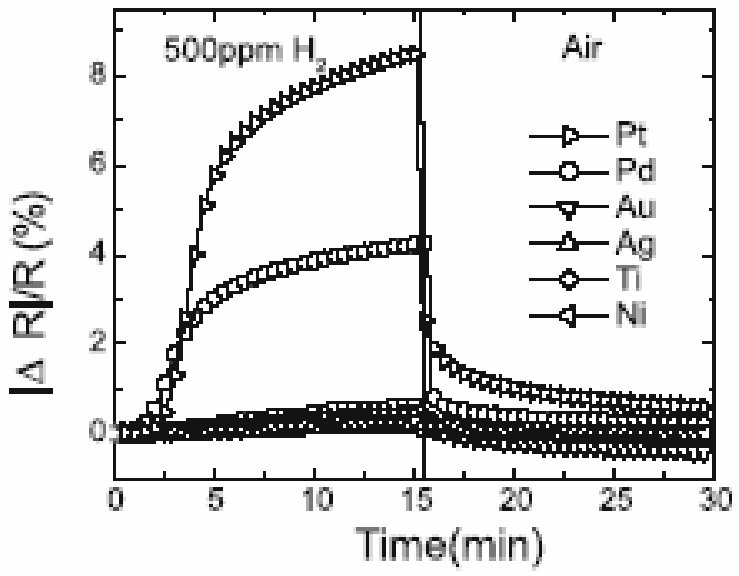

Fig. 1.36 Time dependence of relative resistance response of metal coated multiple ZnO nanorods as the gas ambient is switched from N_2 to 500ppm of H_2 in air as time proceeds. There was no response to O_2.

measurement was first carried out in a chamber with vacuum of 10^{-4} Pa, and the oxygen gas was gradually added in. The transfer characteristics are

measured from -40V to 10V. With the increase of oxygen pressure, the current decreased and V_{th} was positively shifted. This I-V characteristic change is a result of surface oxygen adsorption. With increase of oxygen pressure, more oxygen molecules were adsorbed onto the surface of ZnO nanowire and combined with free electrons forming oxygen ions at the surface of ZnO nanowire. This results in a surface depletion region and decreases the nanowire conductance. Similar mechanism dominates in the sensing application of ZnO nanowire in other chemical or gas species.

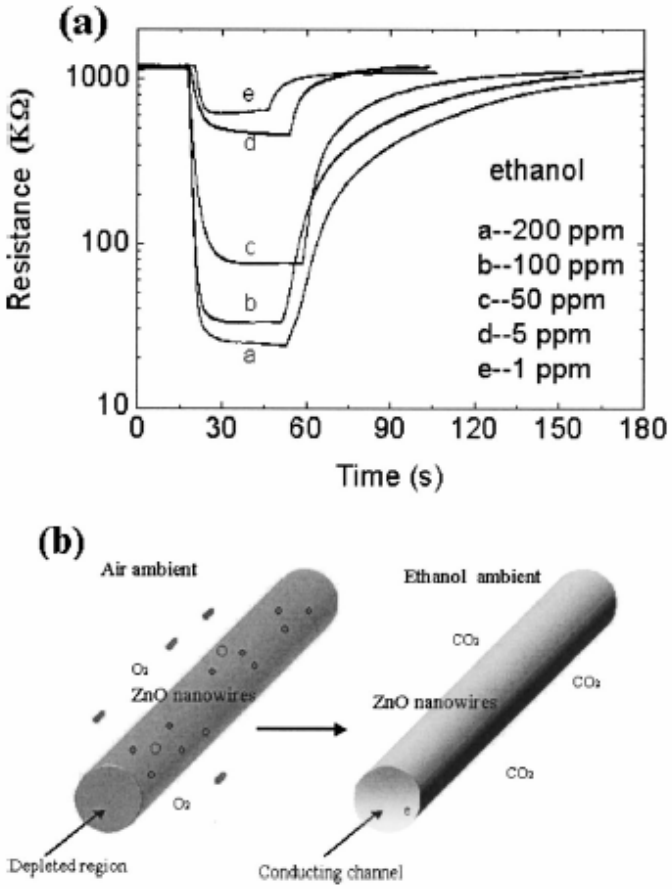

FIG. 1.37 (a) Response and recovery characteristics of ZnO nanowires upon exposure to ethanol with a concentration of 1–200 ppm at 300 °C, and (b) the sensing mechanism of ZnO nanowires to ethanol.

In the application of ZnO nanowires as ethanol sensor, resistivity of ZnO nanowire decreases upon exposure of ethanol vapors, i.e. conductance increases. The measured data and sensing mechanism is shown in Figure 1.37. Due to the oxygen adsorption in air ambient, ZnO nanowire normally is high resistivity. When the ZnO nanowire sensor is exposed to reductive gas at moderate temperature, the gas reacts with the surface oxygen species and releases the immobilized electrons. Consequently, the conductance of ZnO nanowire is increased. This is the mechanism illustrated in Figure 1.37 (b).

Similar effects were observed in PH value and hydrogen sensing application. Sensors based on ZnO nanowire can reach a rather high accuracy and high sensitivity due to the large surface to volume ratio and high density of surface defects. Devices based on ZnO nanowires can detect the existence of different molecule species as low as 10ppm.

With low power consumption and high sensitivity, ZnO nanowire based would be an ideal candidate for future applications in gas sensing.

1.3.5 Doping , Field Emission and Mechanical Properties

1.3.5.1 Doping

The electrical transport properties of ZnO nanowires can be tuned by doping with different elements. Purposed of doping in ZnO nanowire is to

incorporate the special properties of the doped elements into ZnO nanowire and utilizing the coupling effect produced on these fabricated products.

In the work of Ronning et al.,[111] Maganese-doped ZnO nanobelts were realized. The doping is achieved by an ion implantation of Mn ions into ZnO nanobelts with an ion energy of 30keV. These implanted samples were than annealed for 15min at 800 °C under high vacuum condition to remove the implantation defects and activate the implanted species. EDS and PL spectrum measurement were carried out the verify the successful doping of Mn ions. EDS data is shown in Figure 1.38, a small peak of Mn was

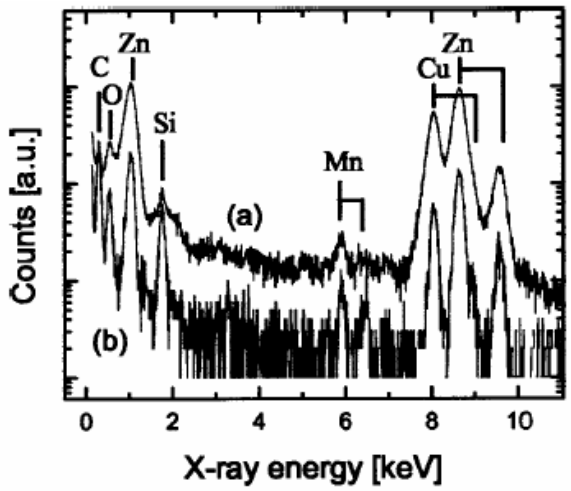

FIG. 1.38 Energy dispersive spectrometry (EDS) spectra of Mn-implanted ZnO-nanobelts (a) directly after ion implantation and (b) after subsequent annealing to 800 °C

observed in the spectrum. The intensity is consistent with the desired doping concentration of about 1 at. %. The PL spectrum also proved the doping of Mn ions showing that after annealing process, PL spectrum peak can be recovered. The reason why Mn doped ZnO nanowire is studied lies in that previous progress achieved in the ZnO:Mn materials and it is promising

application in Diluted magnetic semiconductors (DMS). It is a proposed technology to use electron spin for data storage. ZnO:Mn doped nanowires could offer a very optimizing chance to incorporate these small dimension structures to today's microelectronic system and enhance the devices performance.

1.3.5.2 Field Emission

Due to the stability and controllable electronic property at high temperature, ZnO nanowire is considered as a very important candidate as a field emission (FE) source. Its large exciton binding energy and high melting temperature also prove its advanced performance in FE. Another advantage to utilize ZnO nanowire as FE source is the available high density nanowire arrays for ZnO. The controllable high density arrays provide the flexibility to adjust the FE properties of the samples and achieved the best result by optimizing different parameters.

In the work of Wang et al.,[152] FE property was measured for aligned ZnO nanowires with different densities. Typical top-view SEM images of the samples are shown in Figure 1.39 (a). The FE I-V characteristics of these different density samples are shown in Figure 1.39 (b). Due to the screening effect of the small space between high density nanowire arrays, the highest density nanowire arrays cannot generate the most effective emission. As can be seen from the data, nanowire arrays with a density of around 60-80 μm^{-2}

gave the highest emitting current, 20μA at an electric field of 10Vμm^{-1}. For general ZnO nanowire arrays, the emission was turned on by electric files around 20 μm^{-1} and the current ramp up to the highest value of 20μA at the most appropriate density.

With further optimization of the FE devices based on these ZnO nanowire arrays, such as to obtain more uniform distribution of nanowires, clean and defect free substrates, and better contacts of the nanowire and substrates, this

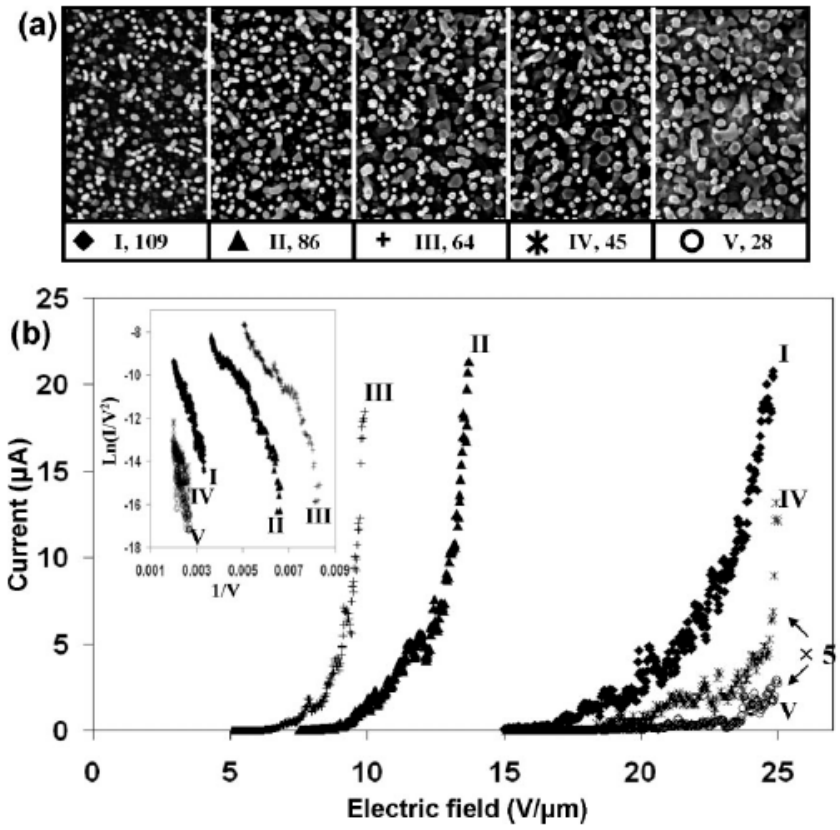

Figure 1.39 a) Top-view SEM images of the aligned ZnO nanowire arrays with five different densities (NWs/μm^{-2}). Curves IV and V are magnified five times for better illustration. b) Corresponding FE *I–V* characteristics and the converted F–N curves.

FE based on nanowire arrays could have better emission efficiency and have better performance as an electron-emitting source.

1.3.5.3 Nanobalances

Mechanical resonance behavior of ZnO nanowire cantilever at ambient condition was studied in the work of Zhou et al.[153] The device is fabricated by suspend a ZnO nanowire on the edge of a substrate. Then an external electric field is used to generate the resonation of the cantilever. Typical experiment setup is shown in Figure 1.40. In the experiment, a constant

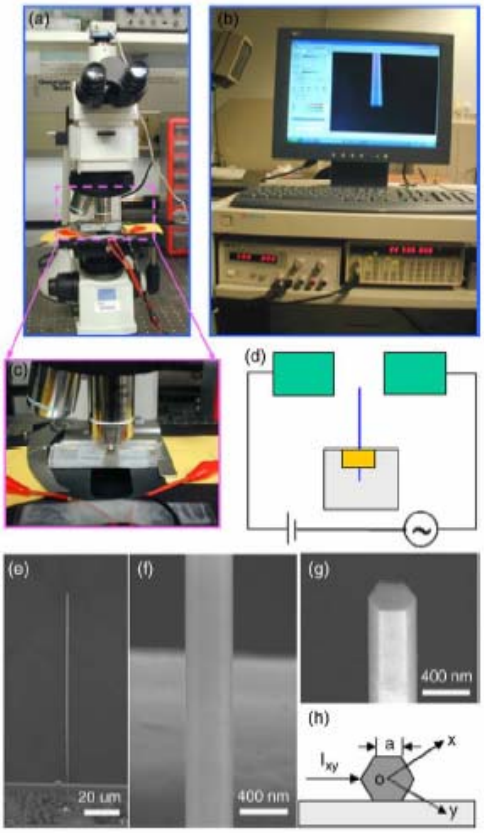

Fig. 1.40 (a) The optical microscope with the resonator at the focal plate for the resonance measurement of ZnO nanowire. (b) The electronic control and imaging system, where a vibrating nanowire is shown. (c) Enlarged image of the square-enclosed area in (a), for illustrating the simplicity of the experiments. (d) Circuit diagram of the experimental setup for the ZnO nanowire based pictogram balance. (b) Low magnification and (c) high magnification SEM images of the ZnO nanowire cantilever; (d) Tilted cross-sectional SEM image of the cantilever; (e) Geometrical model for the calculation of the moment of

voltage V_{dc} and an oscillating V_{ac} with tunable frequency were used to

stimulate the vibration of the cantilever. By generate the mechanical resonance movement of the ZnO nanowire, the in-situ measurement is observed in an optical microscope and recorded with a CCD camera. The amplitude-frequency response of the cantilever was obtained by measuring the resonance amplitude of the cantilever corresponds to different driving frequency.

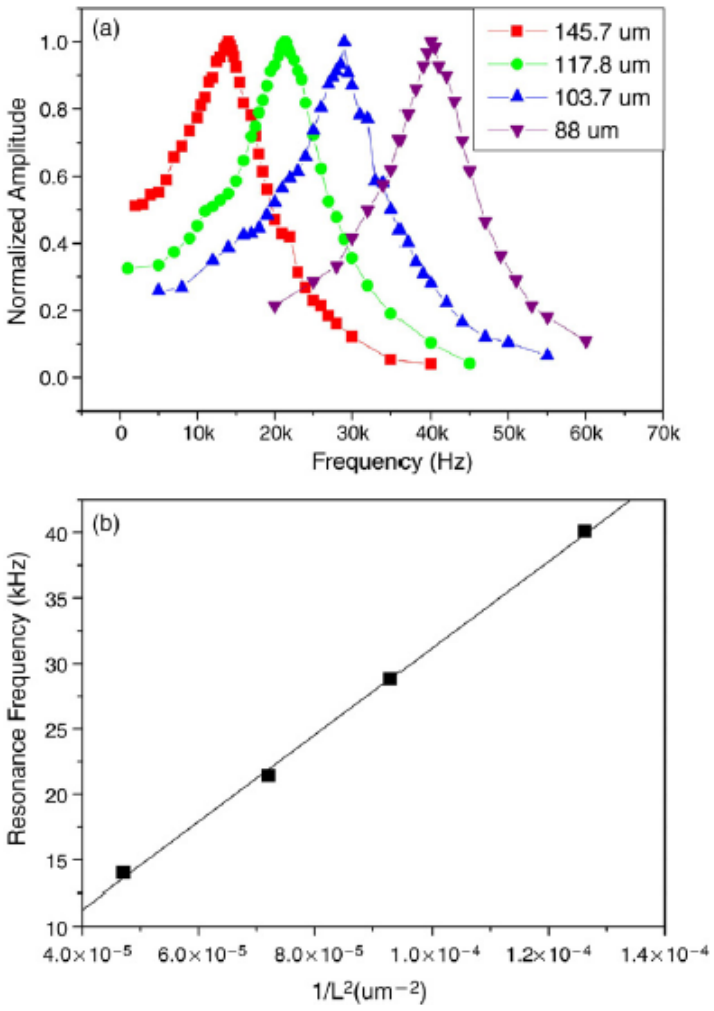

Fig. 1.41 (a) Series frequency response curves of the same ZnO cantilever after sequentially cutting its length by a focused ion beam microscopy. (b) Resonance frequency f vs L^{-2} plot, showing a linear relationship as expected theoretically.

Typical ZnO nanowires with length at the range of ~100μm possess a resonance frequency of around several tens kHz. The length of the cantilever can be changed by Focus Ion Beam(FIB) milling process. The cantilever cut at different length shows a resonance frequency shift. As shown in Figure 1.41, when the length of the cantilever was 145.7 μm, the resonance frequency was 14kHz. When the length is cut to 88μm, resonance frequency was increased to 40.2kHz. The resonance frequency fits into the linear relationship with L^{-2}, as shown in the figure. This is coincident with the resonance result from the classical equation of one-end affixed cantilever.

This nanoresonator is proved to be functionalize as a nanobalance. By depositing a tiny mass on the tip of ZnO nanowire cantilever, the frequency of the cantilever will be changed according to the calculation model. In our experiment, the nanowire is 103 μm in length and 385 nm in width. The resonance frequency is 46.3 kHz without anything on the cantilever. With FIB Pt deposition, a small Pt particle is deposited on the surface of ZnO nanowire. Consequently, the resonace peak is shifted to 38.25 kHz. The mass of the Pt particle is calculated to be M_P ~2.6×10^{11}g, which is about the same value as deducted from the volume of this particle.

With the study of resonance behavior of a ZnO cantilever based on ZnO nanowire, a pico-gram balance is realized. This technique offers the possibility of measuring the mass of tiny objects in different environments.

1.4 Piezoelectronics Based on ZnO Nanowires/Nanobelts

Most recently, a new research direction termed of nanopiezotronics has been coined based on the piezoelectric-coupled properties of ZnO NWs and NBs for fabricating novel and unique electronic components. The first application of nanopiezotronics is the piezoelectric nanogenerator based on ZnO NWs, which demonstrates a unique approach of converting nano-scale mechanical energy into electric energy and an exciting technology for harvesting energy from the environment for self-powered nanosystems.[135, 154, 155] Based on the special coupling effect piezoelectricity and semiconducting properties of ZnO, a new group of piezoelectrinics devices are reported, including piezoelectric field-effect transistors (PE-FET), diodes, and PE-FET based chemical sensors.[135, 156-160]

1.4.1 Piezoelectricity and Structure of ZnO

ZnO is one of II-VI compounds with wurtzite crystal structure. As discussed in previous section, wurtzite structure is a tetrahedral lattice site in a compound AB each A atom is surrounded symmetrically by four nearest neighboring B. Due to the intrinsic nature of wurtzite structure, all of these materials exhibit a piezoelectric phenomenon.

Piezoelectricity is the effect of converting electric energy to mechanical energy and vice versa. This is a result of atomic-scale polarization from the

crystal structures. ZnO wurtzite structure is shown in Figure 1.42. For our discussion, the ion in the center is assumed to be the cation. Four anions surround the cation at 4 symmetric lattice points. With this ion arrangement, the center gravity of the negative charges is coincident with the position of the positive charge cation. When this tetrahedron lattice is exerted by an external force, the crystal lattice will be distorted. The center gravity of the negative charges will be moved away from where the cation locates. This

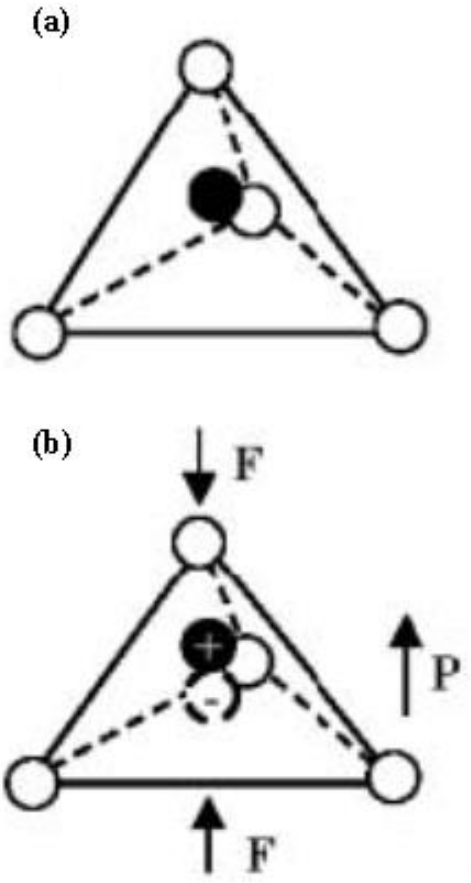

Figure 1.42 Schematic of (a) tertahedral configuration of a II-VI compound and (b) force being applied along the corner direction of the tetrahedron.

gnerates a dipole moment along the direction of the applied force. In a large scope of view, each tetrahedron lattice will generate a small dipole with this

effect. By adding this polarity effect on every single lattice, a macroscale dipole will be generated in the materials.

Crystals can only be piezoelectric if they are non-centrosymmetric to ensure the non-compensation among the dipoles created by the tetrahedral. The piezoelectric effect can convert a mechanical stress into an electrical response or vice versa.

1.4.2 Piezoelectric Nanogenerators

Piezoelectric nanogenerator is the first device demonstrated that utilizes the coupling effect of piezoelectricity and semiconducting properties of ZnO nanowires. The basic function of piezoelectric nanogenerator is to convert mechanical energy into electric power using aligned ZnO nanowires (NWs). [159] The work is based on aligned ZnO NW arrays. These align ZnO NW arrays were synthesized with a Vapor-solid deposition process on a c-plane oriented α-Al_2O_3 substrate covered by a thin layer of ZnO (Figure 1.43). Because of the special coupling effect of the piezoelectricity and semiconducting properties of ZnO nanowires, Atomic force microscopy (AFM) was used in the experiment as the characterization equipment to extract the force and electronic signal simultaneously. By loading the aligned NW arrays into AFM, an AFM tip will scan through the NW arrays with a constant force, 5nN in the normal direction. As shown in Figure 1.43, the AFM tip scanned over the top of ZnO NWs with contact mode. Silver paste

was applied to build an electric contact with the bottom of the nanowire arrays. By connecting the bottom contact to the measurement system in AFM, this formed a measurement circuit. With exerting of constant normal force from the AFM tip, the ZnO NW was bent and generated an output voltage which is monitored continuously with the measurement circuit. In the experiment, no external voltage was applied. The measured voltage signals came solely from the piezoelectricity of the bending ZnO NW.

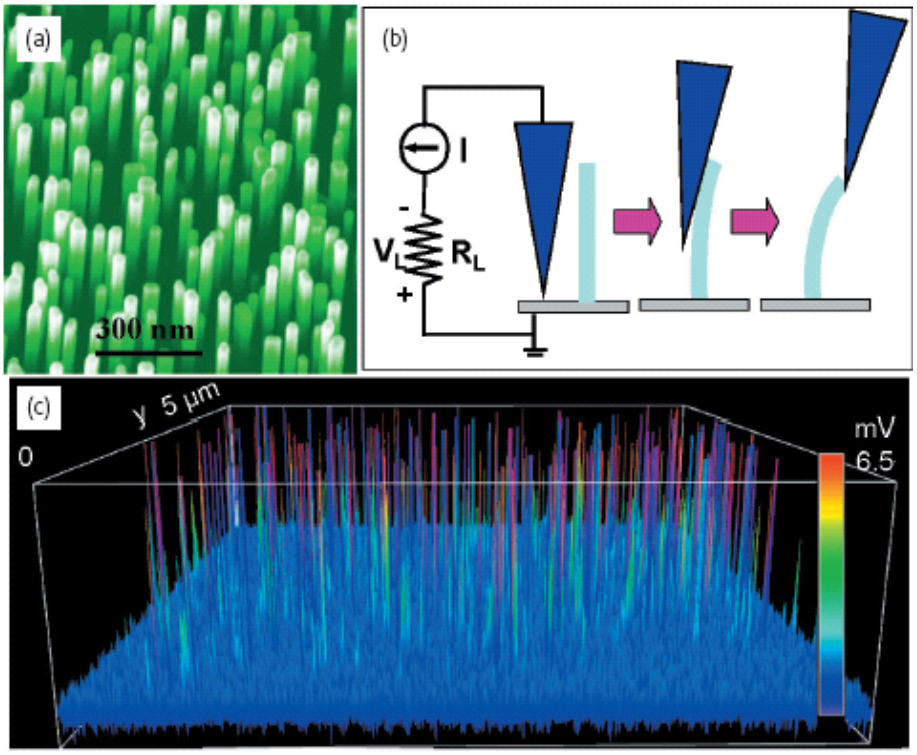

Fig. 1.43 (a) Scanning electron microscopy (SEM) images of aligned ZnO NWs grown on an α-Al2O3 substrate. (b) Experimental setup for generating electricity through the deformation of a semiconducting and piezoelectric NW using a conductive AFM tip. The root of the NW is arounded and an external load of RL = 500 MΩ is applied, which is much larger than the inner resistance RI of the NW. The AFM tip is scanned across the NW array in contact mode. (c) output voltage image obtained when the AFM tip scans across the NW array. The discharging process is so quick that each discharge event is characterized by only a couple of

Images of the topography (feedback signal from the scanner) and the corresponding output voltage (VL) across the load were recorded. Figure 1.43 (c) is the voltage output image. The sharp voltage output peaks are typically about 4-50 times higher than the noise level. Most of the peaks are ~6 to 9mV in height. These voltage peaks locations are coincident with the sites of ZnO NWs, which means that these measured peaks are from the piezoelectric signals from the bending ZnO NWs. To be more specific, V_L was released only at the maximum deflection point of the NW, which is critical in this experiment.

Detail analysis of the origin of these voltage output from deflection of ZnO NW was proposed. It is shown in Figure 1.44. It is a result of the piezoelectricity and semiconducting coupling effect. When a nanowire was deflected, the outer surface was stretched and the inner surface was compress. According to the piezoelectric effect, an electric field E_z was generated along the Z axis of the nanowire. This induced a voltage drop Vs^- to Vs^+ across the top end of the nanowire with first order approximation. This potential drop was created by the relative displacement of Zn^{2+} cations and O^{2-} anions, so it cannot be freely moved or neutralized without any injected carriers. Thus this potential is persisted in the deflection process of the nanowires. The AFM tip is a Si tip coating with Pt layer. Due to the large work function difference of Pt and ZnO, they form a Schottky contact in between the tip and the nanowire. When the AFM tip was in contact with the front end (stretched side)

of the nanowire, there is a positive bias. The metal and semiconductor contact is negative biased. The current flow was prohibited by the Schottky contact. When the tip moved the compressed side of this nanowire, the metal and semiconductor contact is positive biased. This produced a sudden increase in the conducting current. This current is formed by the voltage

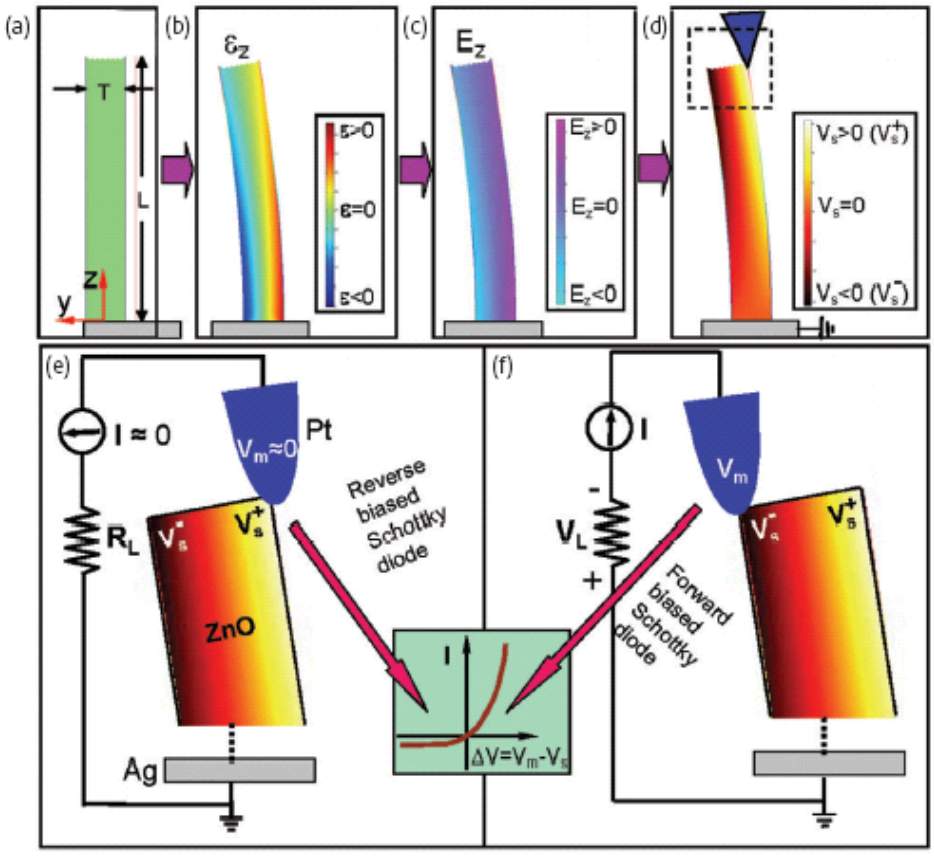

Fig. 1.44 Principle of power generation in a ZnO NW. (a) Schematic of the NW and coordinate system. (b) Longitudinal strain εz distribution in the NW after deflection by an AFM tip from the side. Image shows a FEMLAB simulation for a ZnO NW of length 1 μm and aspect ratio of 10. (c) Corresponding longitudinal electric field Ez distribution in the NW induced by the piezoelectric effect. (d) Potential distribution in the NW. The dashed box indicates the area shown in parts (e) and (f). (e),(f) Interface between the metal AFM tip and semiconducting ZnO NW under local positive and negative contact potentials, showing reverse- and forward-biased Schottky rectifying behavior, respectively. This oppositely biased Schottky barrier across the NW makes it possible to preserve the piezoelectric charges and produce a voltage discharge output. Inset: typical I-V characteristic of a metal-semiconductor (n-type) Schottky barrier. The process in

drop across the contacts. The free electrons flow from the loop into the nanowire and neutralized ionic charges formed by the piezoelectric effect. Thus the V_L starts to drop to zero. This is proposed to be the basic working principle of nanogenerator and nanopiezoelectronics.

1.4.3 DC nanogenerator

With the understanding of the working principle of nanogenerators based on aligned ZnO NWs, it is straightforward to explore methods to utilize this power generation mechanism in nanoscale. One of the requirements is to find other methods to replace the AFM tips in a delicate, redundant and expensive system. Most recently, in our group a DC nanogenerator based on aligned ZnO NWs is realized driven by ultrasonic waves.

The basic idea of this DC nanogenerator is to use ultrasonic wave to generator the vibration of the aligned ZnO nanowire arrays.[155] Piezoelectric potential will be generated with the bending of nanowires. This energy is collected by a special designed circuit. Figure 1.44 is a schematically illustration of the working principle of a whole devices. The most important feature in this device is the top electrode which is a zigzag Si substrate coated with a layer of Pt. The zigzag feature of this electrode is to provide vibrating space for the nanowires under ultrasonic wave vibration. The coating of the Pt layer is the build a Schottky contact between the semiconducting

nanowires and the top electrode which ensures that the current flowing in only one direction and help to form the AC current.

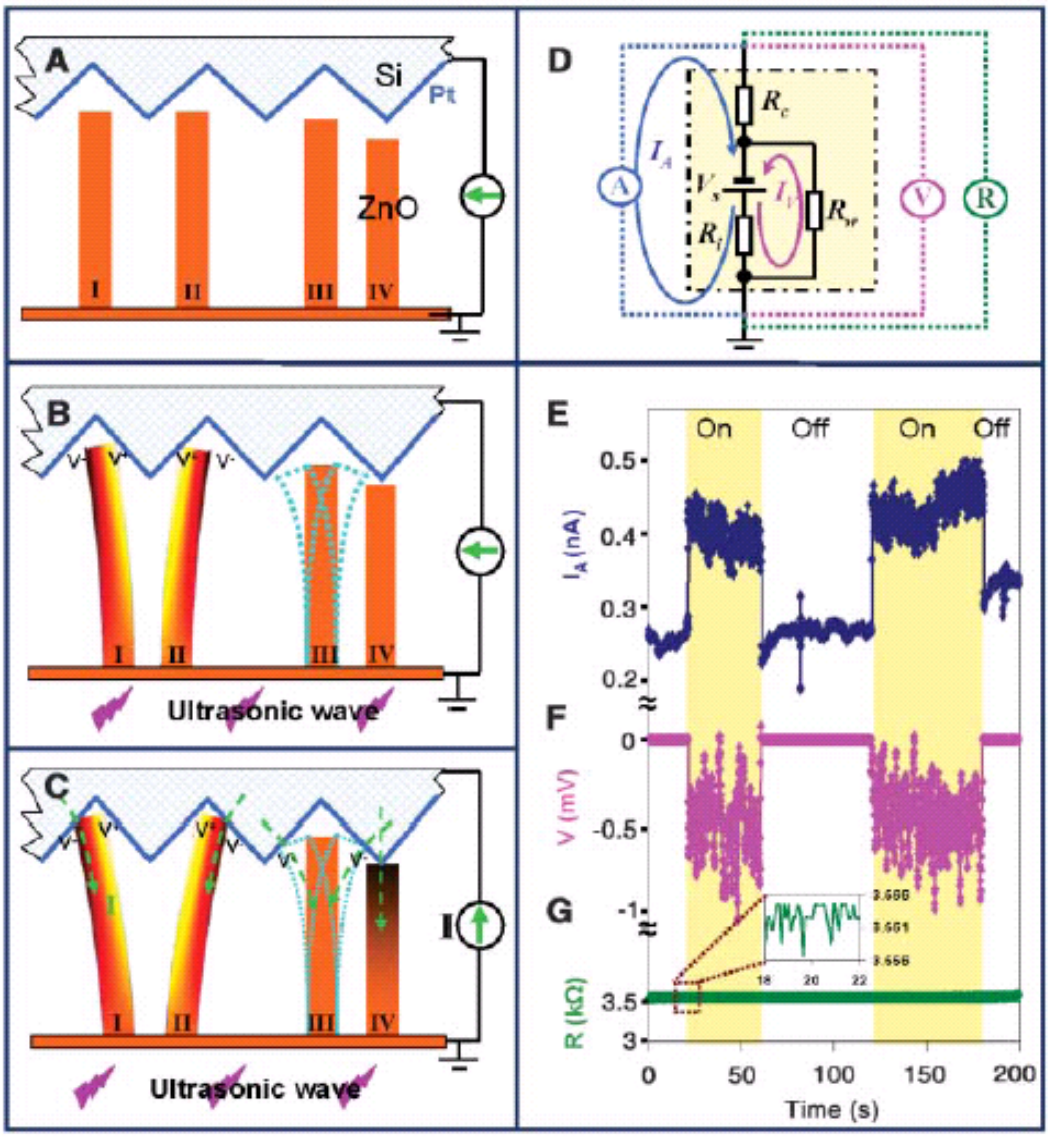

Fig. 1.45 Working mechanism of a aligned ZnO nanowire based DC

As shown in figure 1.45, 2a to 2c are four possible contact modes between the nanowire and the top electrode. With similar mechanism in nanogenerator in AFM, NW II has no effect on the current output. NW I will produce the same charge output effects. NW III is a free standing NW and

will vibrate on the resonance induced by ultrasonic wave. This will generate a discharging effect when the compressed side of the nanowire gets in touch with the electrode. NW IV is forced by the top electrode into compressed status. In this case, the top surface of ZnO NW is negative and electrons can flow across the interface and contribute to the total current. Figure 1.45 is the equivalent circuit for this DC nanogenerator. With this circuit configuration, when the ultrasonic wave is turned on, the DC nanogenerator will start to produce current and voltage output.

The significance of this DC nanogenerator is that it realizes the conversion of ultrasonic wave energy with electrical energy in a nanoscale miniature circuit, which provides an option for energy harvesting and potential nanocircuit power source.

1.4.4 Nanogenerator in Biofluid

There has been extensive study in the application of different nanoscale devices.[161] These nanodevices are demonstrated to have promising properties for future applications. However, there is little research carried out on self-power systems for these devices. For the application of nanodevices in biosensing and electromechanical systems, self-powered source in nanoscale is of great importance. ZnO NW arrays based nanogenerator would be an ideal source for this miniature generation system

purpose. Also, as a biocompatible and non-toxic material, ZnO nanowire is suitable material to be utilized as the power source for other biosensors.

In the research work of Wang et al., an aligned ZnO NW based generator is realized in biofluid. Also, the performance of this nanogenerator was greatly enhanced with 30 times increase in output current. To further test the characteristics of these nanogenerators, they were integrated to a complicated circuit which has a significant result on the output voltage and current signals. The nanogenerator was modified from the previous model. A polymer layer was used to pack the whole nanogenerator core to prevent biofluid from infiltration. Also, because of the flexibility of polymer, ZnO NWs are still free to make small vibrations with respect to the top electrodes. In the experiment, the nanogenerator was placed into 0.9% NaCl biocompatible solution. The applied signal was a 41kHz ultrasonic wave. When the ultrasonic wave was trigger on, it transported through the fluid and caused the electrode and NWs to vibrate and generate electricity. The output signals of the nanogenerators are in the nanoampere and millivolt range. Figure 1.46 is the biofluid measurement system setup and the current and voltage measurement results. The positive and negative signals were a result of exchanging the connection of the nanogenerator positive and negative electrodes with the outer measurement system. This is to confirm the signal came solely from the nanogenerator without any noise interference and artifact. By parallel or series connecting these nanogenerators together,

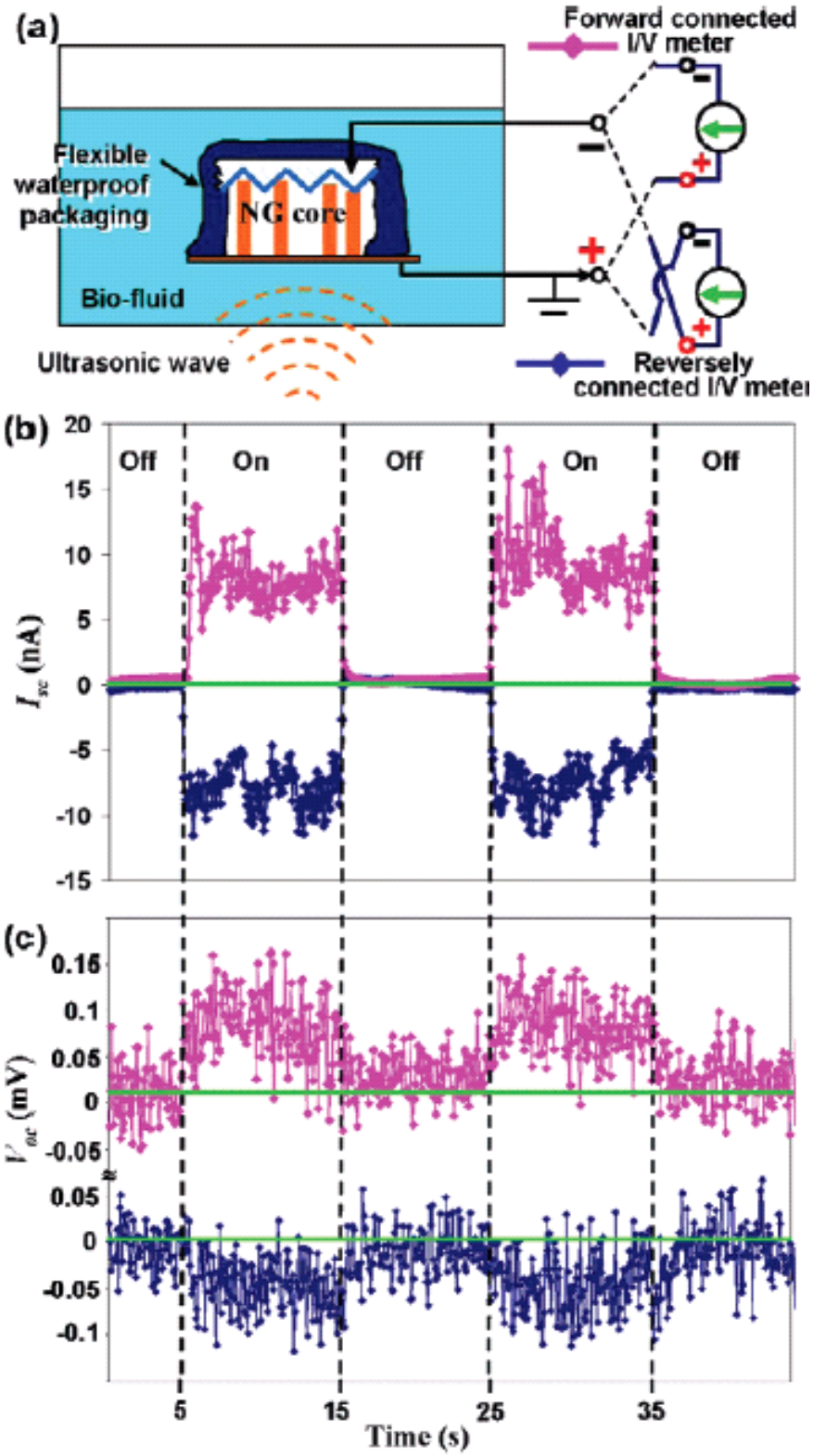

Fig. 1.46 Experiement setup and measurement result of nanogenerator in biofluid.

an integrated nanogenerator system was realized. As shown in Figure 1.47

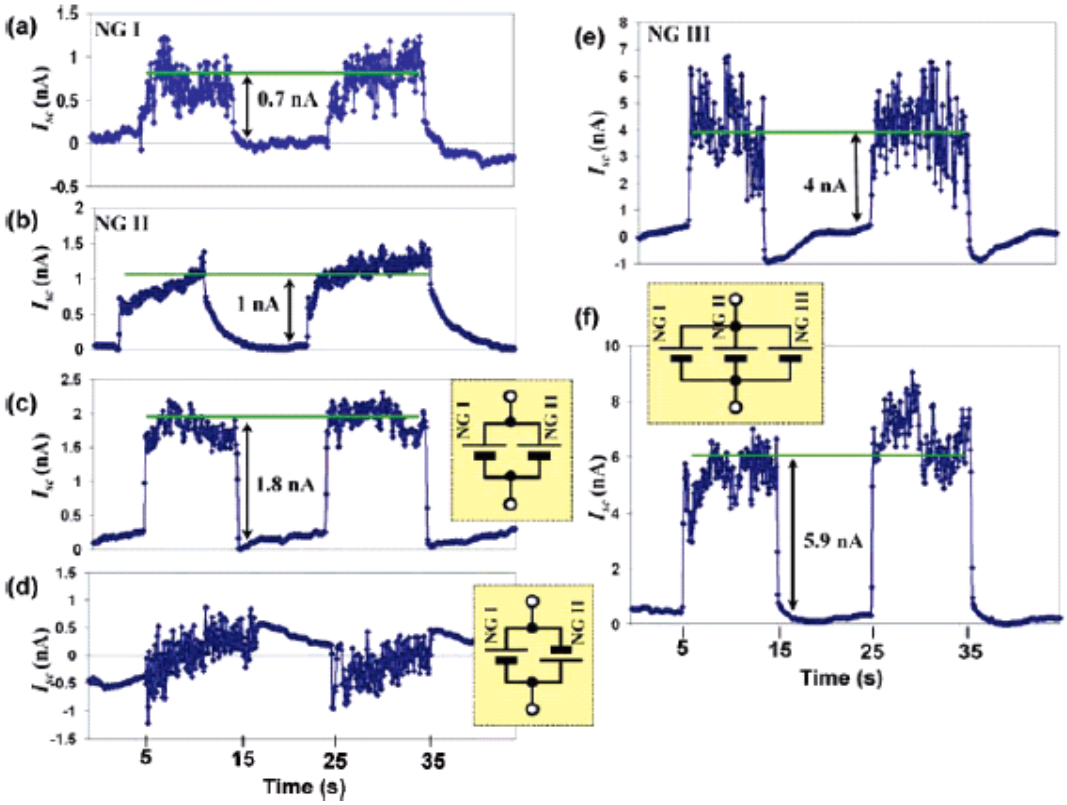

Fig. 1.47 Current out put of serial and parallel nanogenerators.

and Figure 1.48, serial nanogenerators increased the output voltage. The

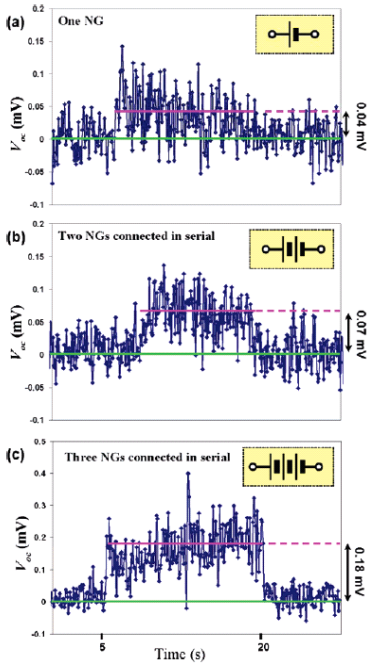

Fig. 1.48 Voltage out put of serial and parallel nanogenerators.

voltage increase was roughly proportional to the number of nanogenerators connected. Not surprisingly, serial nanogenerator has no effect on the magnitude of output current. Similarly, the parallel nanogenerators increased the output current with proportion to the number of nanogenerators and have no effect on output voltage strength.

The ability of generating electricity inside biofluid opens up the potential application of nanogenerators in different environmental conditions. By integrating the nanogenerators in to a serial or parallel system, it is possible to enhance the output signal strength and increase the flexibility of applications of these systems.

1.4.5 Nanopiezotronic Devices

Besides the exhibited energy converting effect of the nanogenerators by utilizing the piezoelectric effect of ZnO, novel devices based on the coupling effect of piezoelectricity and semiconducting effect ZnO were also demonstrated. Electronic devices fabricated based on this coupling effects converts mechanical energy into electric signal response. This provides an attractive and effective way to recycle energy from the environment and generate self-powered nanosystems. Some preliminary results and applications of nanopiezotronics have been reported recently, such as piezoelectric field-effect transistors (PE-FET), diodes, and PE-FET based chemical sensors. These newly reported devices are normally based on ZnO

nanowires and nanobelts due to the special coupling effect piezoelectricity and semiconducting properties of ZnO.

1.4.5.1 Piezoelectric Field-Effect Transistor

Piezoelectric field-effect transistor (PE-FET) is a FET based on nanowires using mechanical force to generate an effective depletion effect other than applying an electronic gate.[156]

In the experiment, the PE-FET was fabricated as such that one end of the electrode could be freely and precisely move. A ZnO nanowire was connected between two electrodes. By approaching the free standing electrode towards the fixed electrode or retracting it, mechanical force can be applied onto and released from the nanowire. As a result of the piezoelectricity effect of ZnO NW, an electric field was generated across ZnO nanowire by this applied mechanical force. This electric field served as gate to control the carrier density and tunneling channel inside the ZnO nanowire. This is analogous to the role of a gate voltage signal in a traditional field-effect transistor. This is why this device is named as PE-FET.

The experimental design is shown in Figure 1.49. The measurement system including the movable electrode was located in a scanning electron microscope (SEM) to monitor the fine movement of the electrode. The movable stage is composed of an x-y mechanical stage with a fine moving step of ~20 nm. This mechanical stage can be controlled independently

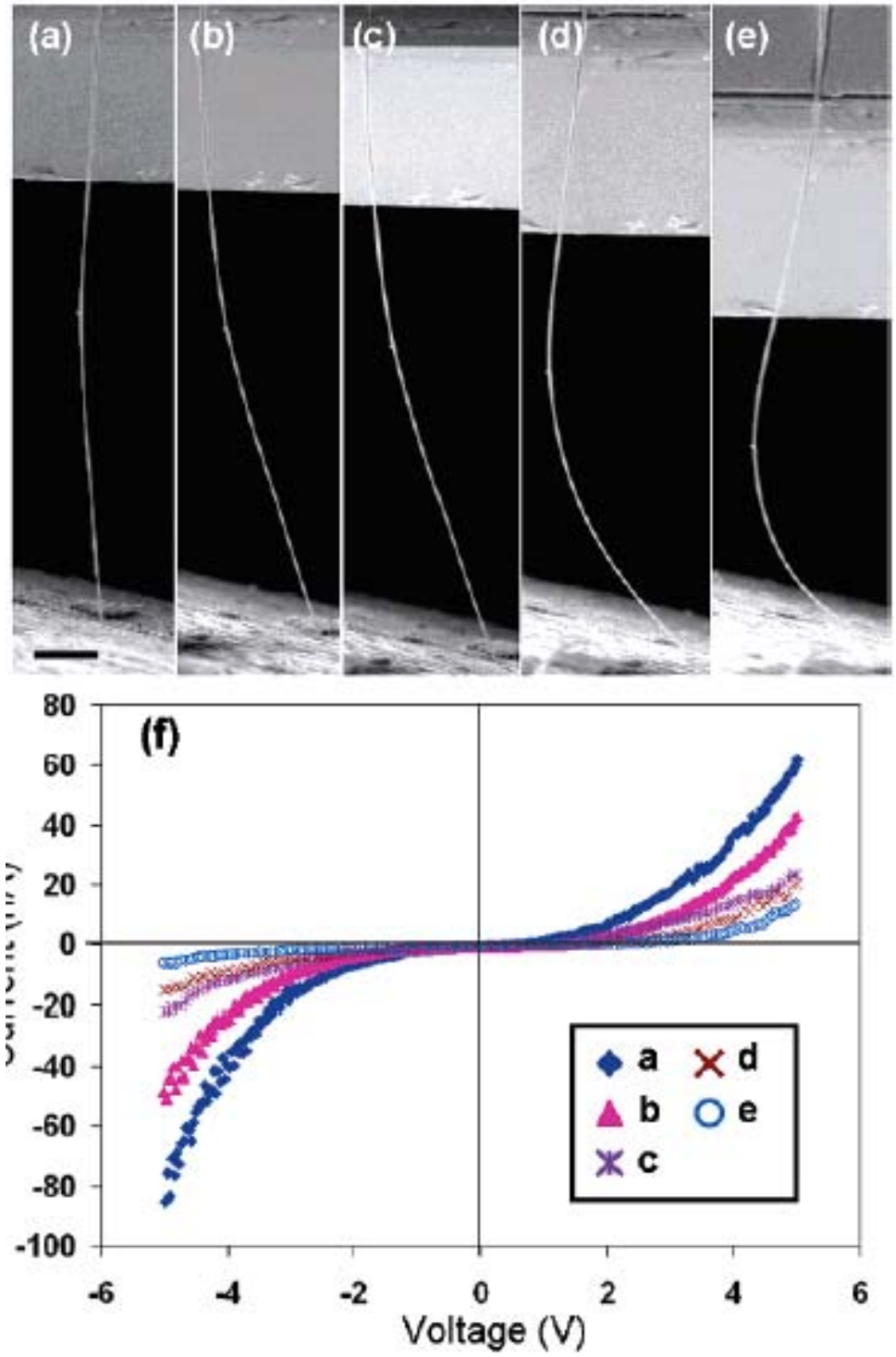

Fig. 1.49 Experimental design and IV measurement of PE-FET

from the outside of SEM. A tungsten needle is used as the positive electrode. A ZnO wire with length of ~100μm was manipulated with a prostration to

suspend it on a silicon substrate. By fixing this substrate on the movable stage and pointing the nanowire towards the tungsten needle, we can then get precise control of the nanowire position. When the required vacuum was achieved in the SEM chamber, the tungsten needle tip was first moved to the center of the image screen. The ZnO NW was then controlled to approach the needle tip by controlling the SEM stage. Focusing the NW and the needle tip at the same time guaranteed that they were aligned at the same height level. When ZnO nanowire get in touch with the tungsten tip, a contact is established, we can then measure the IV characteristics of the ZnO nanowire under different bending force.

During the measurement process, the ZnO nanowire was bent at different level by applying different forces. When the measure system is collecting the I-V characteristic data, the electron beam of the SEM was turned off to avoid interference effect on the measurement. Following such a procedure, a sequential IV data on different bending degree were collected and demonstrated in figure 1.49. We chose five typical bending curvatures of the ZnO nanowire. Their corresponding IV curve are measured and shown in figure 1.49(b). As indicates in the figure, the current dropped significantly with increase of the bending level, indicating the decreased conductance with increase in strain.

It is demonstrated in previous section that a bent ZnO nanowire can produce a positively charged and negatively charge surface at the outer and

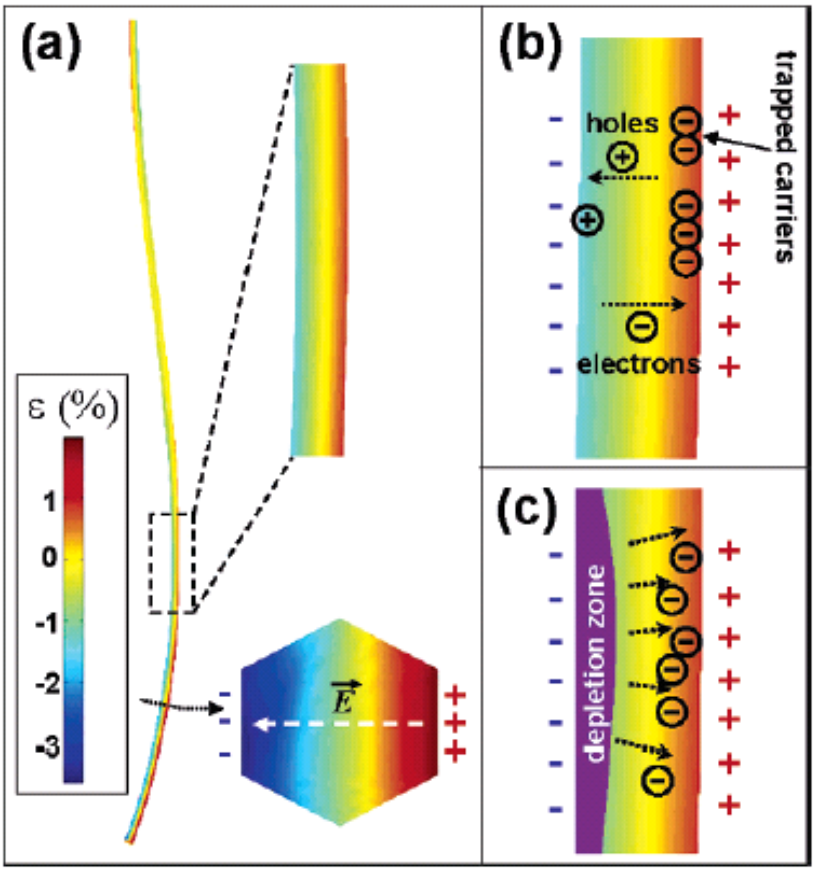

Fig. 1.50 Mechanism of a ZnO nanobelt based PE-FET.

inner bending side of nanowire as a result of the stretching and compression respectively. These charges are induced by a piezoelectric effect and non-mobile on the surface. A local electric field will then be generated across the width of ZnO nanowire, as shown in Figure 1.50. With the generation of this electric field, there are two possible mechanism account for the change of nanowire conductance to the bending force: carrier trapping effect and the creation of charge depletion region. As indicated in the figure 1.49, when the non-mobile surface charges are induced by the external force, it can trap the free carriers in the ZnO nanowire, free electrons trapped at the positive charged surface at this case. Meanwhile, the unchanged negative

charges on the other surface will repulse free electrons inside the nanowire away from this side of surface which will generate a charge depletion region in ZnO nanowire. This is similar to the case of applying a gate voltage across the width of ZnO nanowire as for a usual FET. As a consequence, the repulsing effect decreases the conducting channel width and change the conductance of the nanowire. So with changing of applying force, the conductance of ZnO nanowire can be tuned according to the effect of the piezoelectric field. This working principle of such a PE-FET is shown in figure 1.50. Therefore, the single ZnO across two Ohmic contacts is a piezoelectric field effect transistor (PE-FET), which is a unique coupling result of the semiconducting and piezoelectric properties of ZnO.

1.4.5.2 Piezoelectric-Gated Diode

As discussed previously, when ZnO nanowire is bent, the surface charges accumulated eventually. Consequently, the surface energy state is adjusted by this piezoelectric field. This effect also induced the discovery of a new type of piezoelectric devices: piezoelectric-gated diodes.[157]

The experimental setup is shown in Figure 1.51. ZnO nanowire was first dispersed onto a Si/SiO_2 substrate. Then two nanomanipulator s were used to make the two terminal contacts with a single ZnO nanowire. The tips of nanomanipulators were coated with a layer of Ti to help to build up Ohmic contacts with ZnO nanowire. In the experiment, one probe is used to hold

an end of nanowire stationary, while the other one bends the ZnO nanowire at different extent. From Figure 1.51, the linear and symmetric I-V characteristics of the set up shows that the contacts are Ohmic. However, with bending of the nanowire, the current drops significantly for negative bias. With proceeding of the bending process, the asymmetric I-V behavior

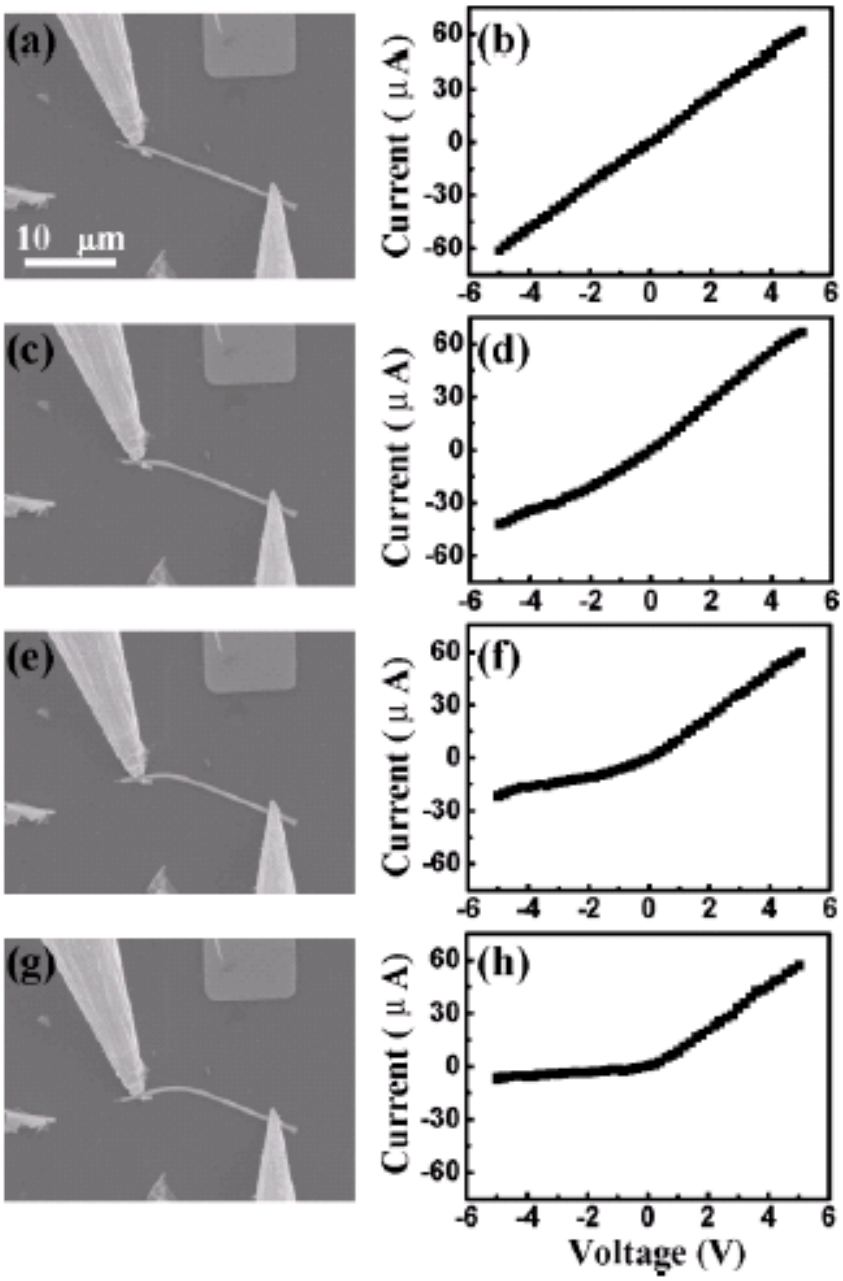

Fig. 1.51 Measurement of ZnO nanopiezoelectric based diode.

was enhanced. In the experiment, the probes are firmly attached to the

nanowire which indicates a good contact during the experiment. This rectifying behavior of the bent nanowire is reversible due to the elasticity of the nanowire.

Suggested mechanism to explain this rectifying behavior on an Ohmic contact device is proposed. As shown in Figure 1.51, an equivalent Fermi energy lever is assumed for the contacts of Ti coated probe and ZnO nanowire. When the nanowire is bent by the probe, a positive potential is produced at

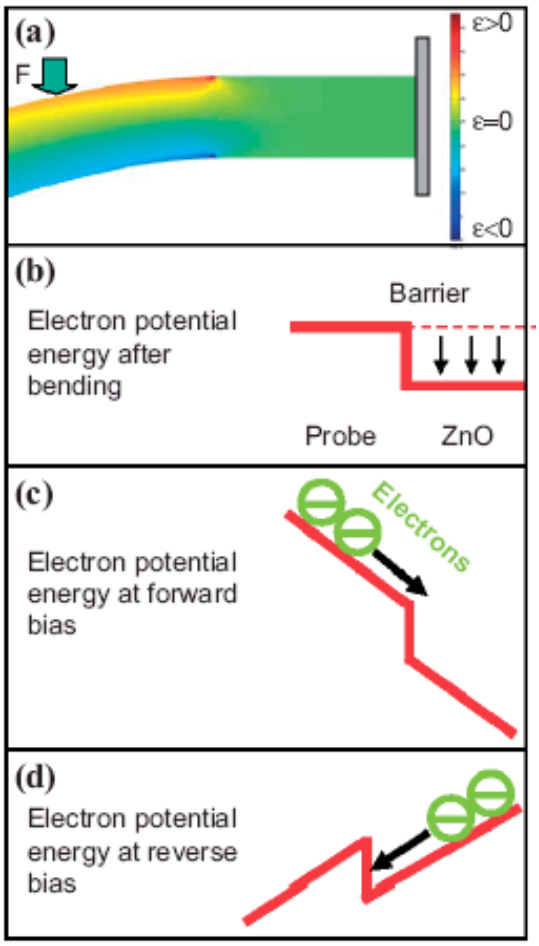

Fig. 1.52 Mechanism analysis of the piezoelectric diode.

the stretched side of the nanowire (the side contacts with the probe). As a result, an energy barrier is produced at the interface. This energy barrier is

illustrated in Figure 1.52. For the bent ZnO nanowire under forward bias, the electrons are not blocked by this energy barrier, the current is still linear with voltage bias. On the other hand, under reverse bias, electrons are blocked by the barrier as shown in Figure 1.52. The energy barrier effectively serves as a p-n junction at the interface of tip and nanowire. The magnitude of the energy barrier increases with the degree of bending, resulting in a more significant rectifying effect. Due to the piezoelectricity induced mechanism, this device is named as a piezoelectric-gated diode.

In summary, ZnO nanowires have been processed a lot of promising properties in the application of nano-optoelectronics, sensors, transistors, and nanopiezotronics. Due to the unique piezoelectric and semiconducting dual properties, ZnO nanowires and nanobelts are the fundamental material for nanogenerators. With a bandgap of ~3.4 eV and an exciton binding energy of 60 meV, ZnO nanowires are also demonstrated to pocess outstanding performance in optical device applications and a lot of other device applications.

CHAPTER 2

CONTROL MORPHOLOGY SYNTHESIS OF 1D ZNO NANOSTRUCTURES

Controlled morphology synthesis of different ZnO 1D structures is of great importance for exploring its application in different nanodevices. For instance, the large scale synthesis of nanobelts with ideal rectangular geometry brings consistent performance in transistor. The well-controlled synthesis of nanostructures will benefit the devices fabrication and application. With the high yield of ZnO nanobelts, the device characteristics will be more reasonable controlled without any significant deviation from the intrinsic response of an ideal ZnO nanobelt. Besides, the specially synthesized nanostructures will have their own advantage in the device, like a nanocomb, which can bridge a series of electrodes to form a parallel testing system.

Due to the special wurtzite crystal structure of ZnO, the morphology control in the synthesis of ZnO nanocrystals has been demonstrated to be effective method. ZnO has three types of fast growth directions: <0001>, <01 $\bar{1}$ 0> and <2 $\bar{1}$ $\bar{1}$ 0>, together with the $\pm$(0001) polar-surfaces, various unusual structural configurations have been reported for the fabrication of ZnO, such as nanobelts[82], nanosprings [87], nanorings[84] and nanocombs[162]. By studying the intrinsic growth mechanism of different sorts of ZnO nanostructures, insights of nanocrystal growth can be fully investigated and

developed. In this section, we will mainly focus on the synthesis methods and growth mechanisms of different ZnO nanostructures to elaborate the basic physics in the nanostructure synthesis and most recent development in this area.

2.1 Fabrication Methodology

General nanocrystal synthesis method includes thermal evaporation, laser ablation, template-assisted growth, arc discharge, lithography and the sol-gel method. Of these, thermal evaporation represents the most widely studied method for nanocrystal synthesis due to its simplicity in operation and variety in the as fabricated nanostructures. In this chapter, we will mostly focused on nanowires synthesis through vapor phase evaporation, more specifically, physical vapor deposition (PVD). Briefly reviewed, PVD describes the solidification of a vapor directly onto a surface. Direct deposition implies that no chemical reactions are permitted to occur in the vapor, with the vapor, and/or with the surface to be deposited. If a chemical reaction does occur, then the process is not PVD, but rather chemical vapor deposition (CVD).

Morphology control synthesis of ZnO nanomaterials reported in this work are mostly carried out via this PVD method because of its simplicity in operation and efficiency conducting desire experiments. The thermal

evaporation process is based on a single-zone tube furnace. It has been extensively employed for synthesizing all of the 1D nanostructure, which serves as the basis of electric transport properties study of different oxide materials. The experimental apparatus for the thermal evaporation process includes a horizontal tube furnace. This furnace system used throughout the entirety of the fabrication was comprised of two basic components: a furnace and vacuum system. There are a variety of parameters that control the synthesis of nanostructures in the thermal evaporation process, such as the temperature, pressure, gas flow rate, and duration time. The substrate and chemical composition can also play a significant factor in morphology control of different nanostructures. During the syntheses, controlling the parameters in the chamber such as pressure, temperature gradient and gas flow rate, especially the source materials composition, is a key to design and synthesize desired nanostructures. Variety nanostructures with different composition and different morphologies have been successfully synthesized via this methodology.

2.1.1 Furnace System

The furnace system employed in the high-temperature solid-vapor deposition process is shown in Figure 2.1. This experimental apparatus are comprised of two basic components: a furnace and pressure system. The furnace includes included a horizontal high temperature tube furnace, an

enclosed alumina tube, a rotary pump, and a gas controlling system as shown in Figure 2.1.

A Thermolyne 79300 single zone split tube furnace was used to carry out all of the synthesis. An alumina (Al_2O_3) tube measuring 30″ in length and having a 1.75″ outer diameter and 1.50″ inner diameter was used as the reaction chamber for nanomaterials synthesis. With the furnace measuring

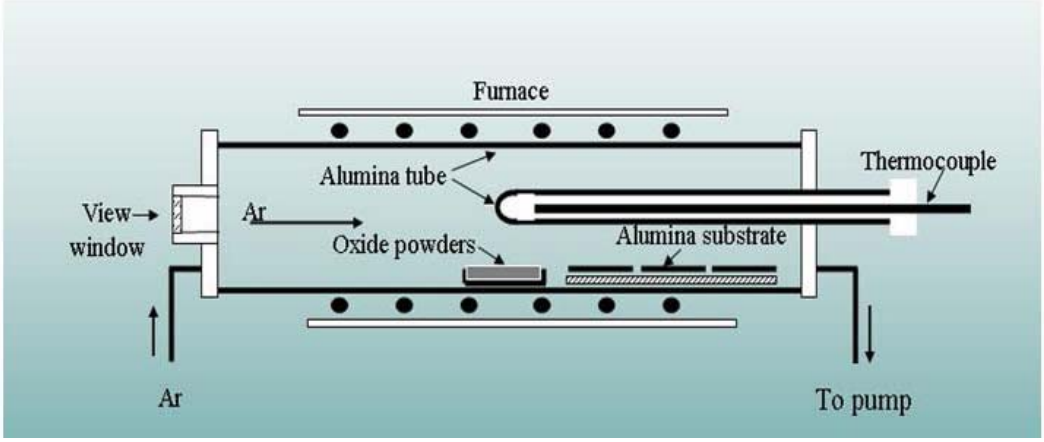

Fig. 2.1 Schematic of furnace setup.

only 24″ in length, the Al_2O_3 tube protruded from the furnace six inches on either side (Figure 2.1). Three-inch tube collars lay at the open end of the tube furnace and the alumina tube was placed across the furnace, supported by the collars. Cooling system is embedded in this tube collars. By flowing cool water through this hollow metal tube collar, temperature at the end of the alumina tube is kept at a desired low level. This helps to form a temperature gradient inside the tube during the synthesis, which is critical for different nanostructure formation. Heating of the furnace system is of great importance in the nanostructure synthesis. The heating rate of the furnace

was controlled by a C1 programmable controller. The C1 is a digital program controller with one stored program of eight segments. Each segments of the program consisted of three parts: a ramp rate (ranging from 1 ˚C/min to 60 ˚C/min), a temperature set point (ranging from 100˚C to 1500˚C), and a dwell time (ranging from 0.1 min to 999.9 min). One end cap was fitted with a gas inlet connection for introducing the inert carrier gas into the system. It works as carrying gas to transport the source materials from the high temperature region to low temperature and play a significant role in the thermal evaporation synthesis process.

2.1.2 Vacuum System

Schematic illustration of the vacuum system used in thermal evaporation synthesis is shown in figure 2.2. The vacuum system is composed of 3 components: a rotary vacuum pump, pressure monitoring system (vacuum gauge), and the gas flowing control system. Its functions include evacuating the chamber for synthesis, introducing a carrier gas into the system, monitoring and controlling the pressure in the synthesis chamber.

The vacuum pump used in the system is a BOC Edwards RV8 Hydrocarbon rotary vacuum pump. The purpose is to purge the system of oxygen and require a high vacuum status which is required for the nanostructure synthesis. The mechanical pump can reach a gas pumping rate of 8.0 m^3/h with an ultimate vacuum of $2x10^{-3}$ mbar. Despite excess oxygen

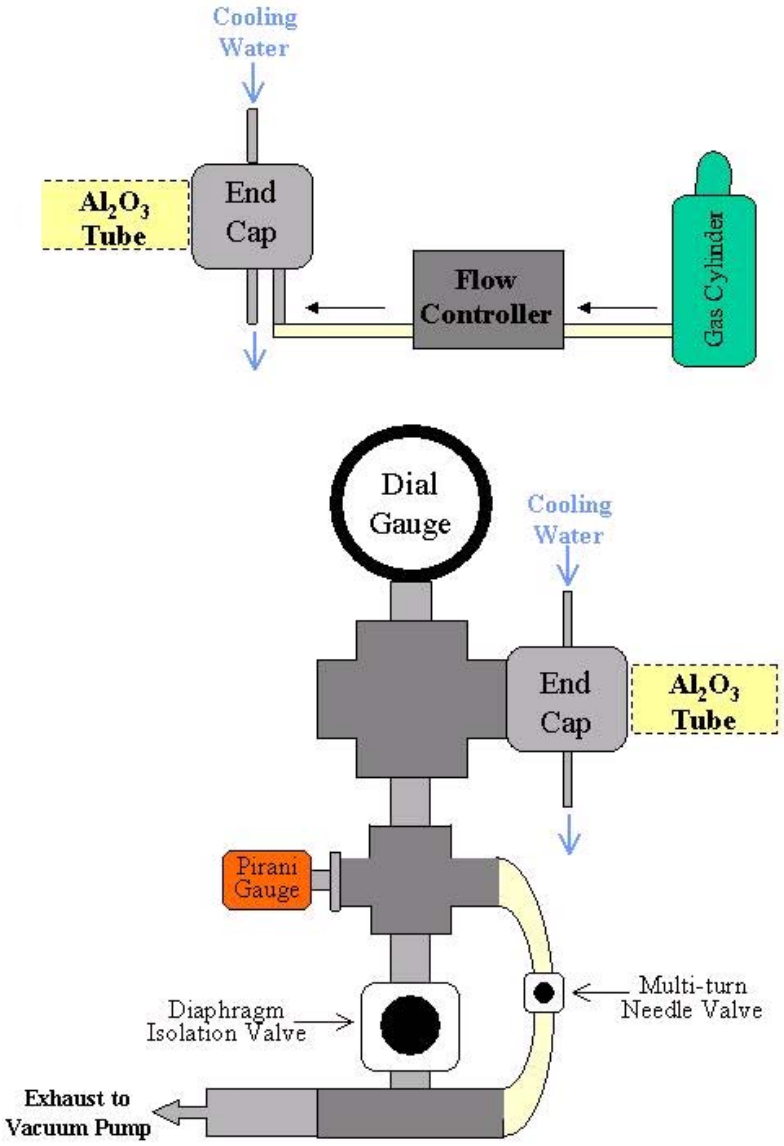

Figure 2. 1: Schematic of vacuum system.

content having an adverse effect on deposition, this machinery is sufficient for our needs. The mechanical pump was connected to the synthesis chamber through a series of aluminum tube segments of t-bars, cross bars, and one of the water-cooled end gaps. The pressure monitoring system is achieved through two analog gauges, a BOC Edwards analog Pirani vacuum gauge series 500 and a BOC Edwards analog dial vacuum gauge series CG16K. These two pressure

gauges are responsible for pressure monitoring at different pressure range. The first gauge monitors lower pressures ranging from 100-10^{-3} mbar. Typically this gauge is only used to observe the system pressure during the evacuation process. The second dial gauge measures pressures from 1000 to a 20 mbar in increments of 20mbar. This is the pressure of where bulk synthesis running process occusr. Two valves are incorporated into the vacuum system in order to control the system pressure with coarse and fine adjustments. The coarse valve is a BOC Edwards diaphragm isolation valve. The primary purpose of this valve was to open the system to the mechanical pump and purge the chamber. The fine adjustable valve, a Cole-Palmer multi-turn needle valve, was used during synthesis to make small adjustments to pressure. The last function of the vacuum system was to introduce a carrier gas into the system. An inert nitrogen gas was first sent through an Aalborg N_2 mass flow controller in order to regulate the flow of gas running through the chamber (see Figure 2.1). The flow controller could send N_2 through at a rate ranging from 0-200 standard cubic centimeters (sccm) ±0.1. Once a flow rate was selected and the carrier gas sent through the flow controller, it entered the chamber through one of the end caps via 3/8" plastic tubing connected from the flow controller to the water-cooled end gap.

Figure 2.2 is a schematic of the entire vacuum system. The two end caps, one connected to the pressure system and the other connected to the mass flow controller, were placed at the ends of the alumina tube. Rubber O-rings

coated with vacuum grease positioned between the alumina tube and end caps deform as they are compressed between the tube and the caps, sealing the vacuum and furnace systems together. The pump was then turned on, beginning the evacuation process, and so as the pressure monitoring and gas flow controlling.

2.1.3 General Experimental Process

As shown in Figure 2.3, the desired source materials (in the form of powders generally) were placed in the center of a horizontal tube furnace in the experiment, where the temperatures, gas flow rate, pressure and deposition times were controlled. In this system, the alumina tube acts as the

Figure 2.3 Thermolyne 54500 High Temperature Tube Furnace.

reaction chamber for evaporation and deposition. Generally, high purity

source powders loaded in an alumina boat were located in the middle of the furnace, the highest temperature region. The desired nanostructures were deposited on substrates placed a set distance away from the source in the down-stream direction of the carrier gas. By controlling of the synthesis conditions, such as reaction temperature, pressure, source materials, temperature ramp rate, and catalyst, we can get a variety of as-fabricated ZnO nanostructures. For example, ZnO nanobelts are normally obtained at a higher temperature which is around 1400 ^{o}C. ZnO nanowires are normally synthesized at a lower temperature of around 1100 ^{o}C.

2.2 1D ZnO Nanostructures with Controlled Morphologies

One-dimensional nanostructures, such as nanowires and nanotubes, have attracted great attention because of their peculiar optical, electrical and mechanical properties. The synthesis technologies for the growth of nanowires and nanotubes of many materials have been extensively developed. However, the formation mechanisms are mostly yet to be clarified. The growth of single-crystal semiconductor nanowires mediated by thermal evaporation is one of the most widely used methods and the formation is proposed via bulk diffusion of reactant atoms mediated by nanoparticles. However, there is a wide variety of ZnO nanostructures achieved from the syntheis. In order to investigate the growth processes involving differnt growth mechanisms, the physical vapor deposition, with the growth

environment adjusted to vary dominant growth mechanism, was used to grow ZnO nanostructures. The adjusted parameters included the carrier gas and precursor flow rates, growth temperature and ambient pressure.

Being a functional oxide, Zinc oxide is an important material for applications in optoelectronics and piezoelectric devices. It received much attention recently in nanoscience both in synthesis and device applications. Based on the previous introduced thermal evaporation system, a variety of 1D ZnO nanostructures with controlled morphologies are obtained via the performed synthesis study.

2.2.1 High Yield Synthesis of ZnO Nanobelts

The reaction was performed in the alumina tube with a base pressure less than 2×10^{-6} torr. The ZnO source powder was kept at the center of the alumina tube, and nitrogen gas were used as ZnO precursor and carrier gas, respectively. The nitrogen gas was supplied at a constant flow rate of 50 sccm with a mass flow control meter. Several pieces of Alumina substrates were loaded at the down stream region at a certain temperature range to collect the as-synthesized producets. The growth temperature and pressure were set to be 1350 ^{o}C to 1475 ^{o}C and 100mbar to 300mbar, respectively. At the beginning of the growth process, pure N_2 was passed into the system via a mass-flow controller. The process chamber was heated using a heating coil furnace for various periods of time. The parameters varied included (1) carrier gas flow

rate, (2) local distribution of growth products along the furnace, (3) growth temperature and (4) chamber vacuum and pressure. These were tested by changing one parameter while keeping the other parameters constant.

Following the deposition, the morphology of the one-dimensional nanostructures was examined with a field-emission scanning electron microscope. The nanostructures were dispersed on carbon coated TEM grids. Structural characterization of these nanostructures was carried out with a transmission electron microscope through the use of selective area electron diffraction, energy dispersive spectroscopy.

With a process temperature of 1475 ^{0}C, a ramping rate of 20^{o}C per minute, N_2 carrier gas flowing rate of 50 sccm and environment pressure of ~150 mbar, a more consistent and reliable synthesis condition was achieved for high yield synthesis of ZnO nanobelts. SEM and TEM images of the as-synthesis product are shown in figure 2.4. Figure 2.4 a) is a typical SEM image showing the morphology and high yield synthesis of these ZnO nanobelts. The ZnO nanobelt products are uniform in width, thickness and cover the whole substrate. TEM image of a typical ZnO nanobelt is shown in figure2.4 b). Typically, width of the as-synthesized ZnO nanobelts is around 50 to 200 nm. Thickness is of around 5 to 20 nm. Depending on the growth period, length of a nanobelt can range from several micrometers to several millimeters. Diffraction pattern if figure 2.4 c) reveal the growth direction of

the ZnO nanobelt is along [0001], which is the same as previous reported result.

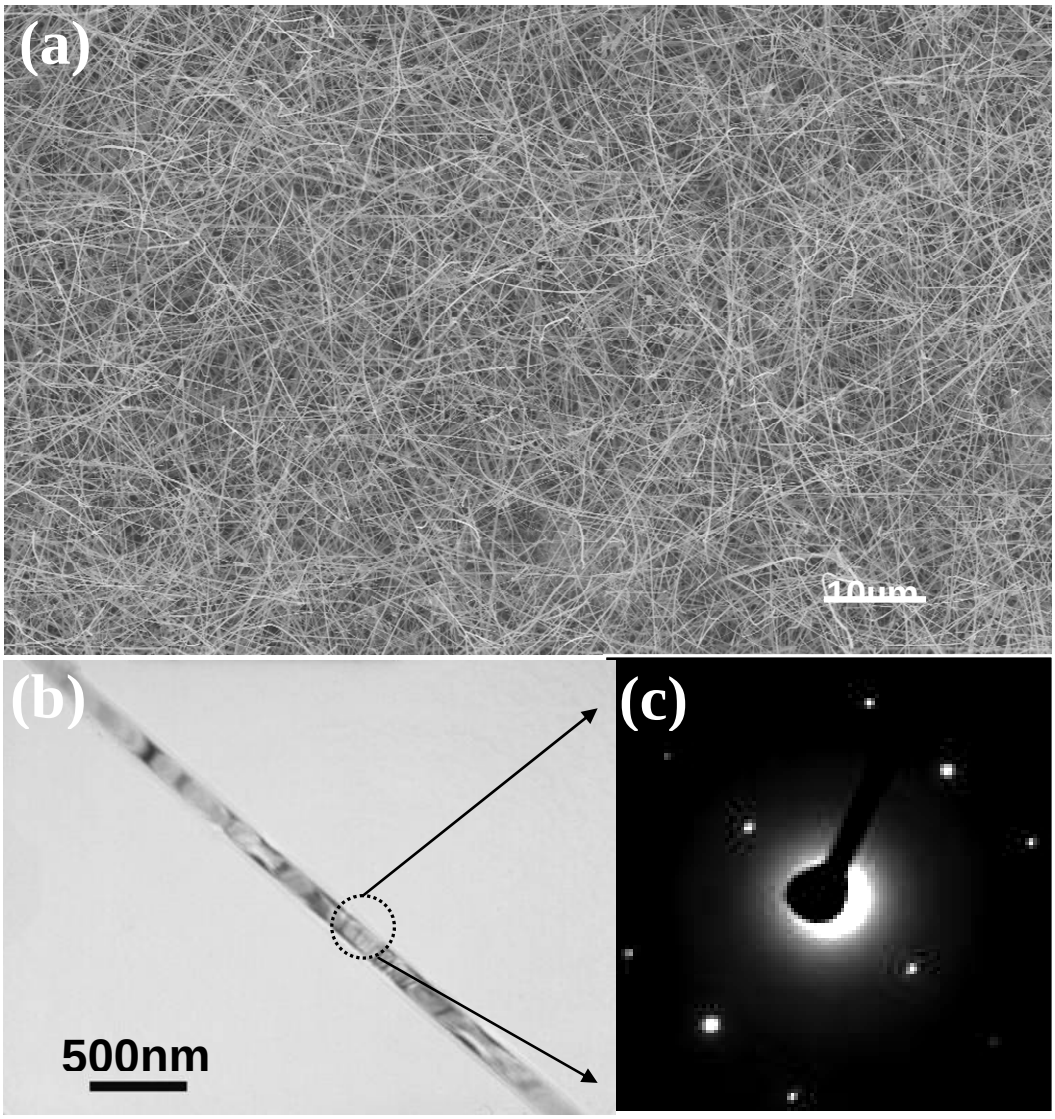

Fig2.4 (a) Low magnified SEM of ZnO nanobelts. (b) TEM image of a

In conclusion, ZnO nanobelts were synthesized by thermal vapor deposition at 1475°C as shown in Figure. 2.4. A high density of ZnO nanobelts was present on the surface collecting substrates. The as-growth nanobelts are dominated by [0001] growth direction. On the other hand, the radial growth is controlled by the surface diffusion. The shape and size of nanowires are

related to the surface diffusion length which depends on the growth temperatures. The as-synthesis nanobelts are normally 50-200nm in width, 10 to one in aspect ratio and possess smooth, defect free surfaces, which is ideal for the devices fabrication.

2.2.2 ZnO Double-Sided Nanocombs

In this section, polar surface induced self-catalyst growth of double-sided and single-sided teeth ZnO nanocombs through a high temperature solid-vapor deposition process was realized.[163]

The primary ribbons of the combs grow along $[2\bar{1}\bar{1}0]$. For the nanoteeth of the both sides of the double-sided combs and that of the single sided combs, the growth directions of them are all [0001], which are out of the Zn-terminated (0001) plane of the ribbon because of its relatively higher chemical activity compared to that of the O-terminated – (0001) pane. The symmetric growth of the nanoteeth in the double sided combs is caused by an anti-phase domain boundary in the ribbon, which creates two chemically active Zn-terminated facets, thus promoted the symmetric growth. Other structures, such as tetra-leg ended combs and feather-like double-sided combs were also found. These structures are induced by the alternative ± (0001) planes on an octahedral multiple twin nucleus, which is formed by eight tetrahedral crystals with one c basal plane and 3 $\{11\bar{2}2\}$ pyramid planes.

2.2.2.1 Experimental Procedure

The synthesis of the "comb-like" structures is based on a high-temperature solid-vapor deposition process. The experimental apparatus included the thermal evaporation system described previously. In the experiments, 2 grams of commercial (Alfa Aesa) ZnO powder was loaded on an alumina holder and placed in the center of the tube as the source material. Several pieces of polycrystalline Al_2O_3 substrates were positioned downstream to gather the products. The whole furnace was then heated up to 1400°C ~ 1450°C at the ramp rate of 20°C per minute with a flow rate of 50 sccm (standard cubic centimeters per minute) Ar and a pressure of 200mbar~250mbar. With a consistent pressure and gas flow rate, the evaporation process was kept running for 100-150 min. Then the growth of the double-sided, single-side, tetra-leg and feather-like comb structures were observed on the Al_2O_3 substrates at a temperature zone of 600°C-800°C.

2.2.2.2 Experimental Results

A typical low magnification scanning electron microscopy (SEM) image of the as-grown ZnO nanocombs is shown in Figure 2.5 (a) with an over 90% yield of these comb-like structures. In the magnified upper inset, a typical nanocomb is displayed, with many thin nanoteeth at similar length and diameters growing out of a straight primary ribbon. These thin wires have spacing around 200nm, diameter ~50nm and length ~2 μm. Fig. 2.5 (b) is another configuration for the single-sided combs, in which a row of hexagonal

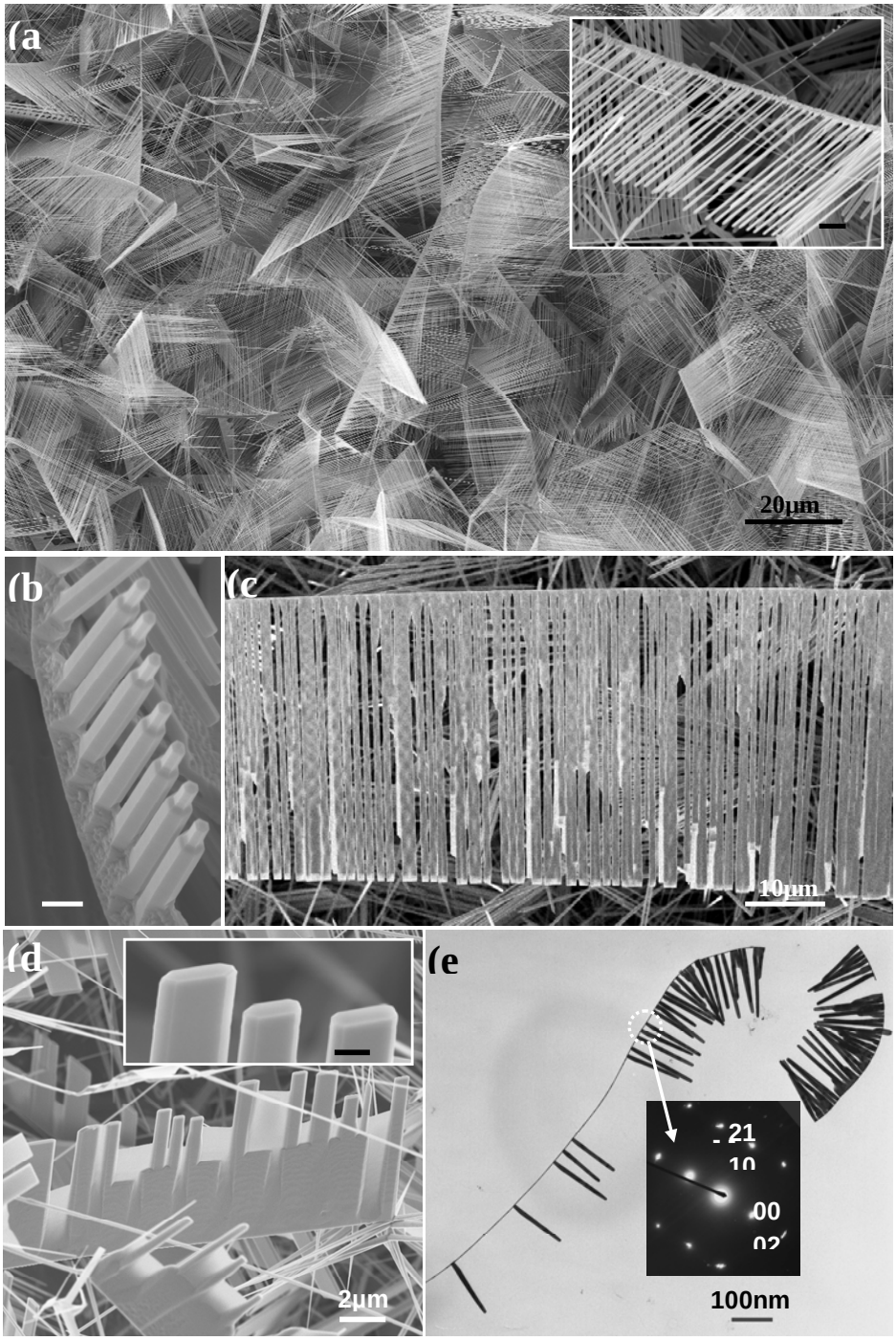

Fig 2.5 (a) As-grown single-sided ZnO comb structures. Inset is the magnified image of a single-sided comb, scale bar, 1μm. (b), (c) and (d) are SEM images of single-sided combs with different morphologies. Scale bar of (b) 200nm; Scale bar in inset of (d), 300nm. (e) A typical TEM image of the single-sided nanocomb. Inset diffraction pattern from the circled area shows that the growth direction of the nanoteeth is along [0001].

nanowires with two layer of rods at different thickness grow on the ribbon.

From the hexagonal geometry of the nanowires' side facets, the growth

direction of the hexagonal wires can be determined as [0001], epitaxially from the (0001) surface of the primary ribbon. Fig. 2.5 (c) shows a comb structure with a series of long thin belts (40-50μm in length, 0.5-4μm in width and a wide range pitch distance from tens of nanometers to several micrometers), growing parallel from the ribbon and forming a waterfall-like look. In fig. 2.5 (d), the nanocombs have a set of much wider teeth, with a wide range of spacing, a length normally from 1 to 5 μm and a width of 200 to 500 nm. The upper inset image reveals the quasi belt shape of the cross section of the teeth. Fig. 2.5(e) is a TEM image of a typical single-sided comb structure and the corresponding electron diffraction pattern. The diffraction pattern shows that the growth direction of the teeth is [0001] for the teeth and $[2\bar{1}\bar{1}0]$ for the primary wire. These observed result is consistent with our previous study on other comb structures, where combs have teeth along [0001], side surface ± $(2\bar{1}\bar{1}0)$ and top/bottom surface ± $(01\bar{1}0)$. The polar surfaces play an important role here in the formation of these single-sided comb structures. With the chemically active surface ending with the positively charged Zn-(0001) plane and the relatively inert surface with the negatively charged O-$(000\bar{1})$ plane, the growth of the teeth are dominantly along the [0001] on the Zn plane, then the single-sided ZnO nanocombs are formed.

Fig. 2.6 is another type of comb structures with the nanoteeth growing from both sides of the primary ribbons. In fig. 2.6 (a), a low magnification SEM image shows a high yield of the double-sided teeth comb structures. Fig.

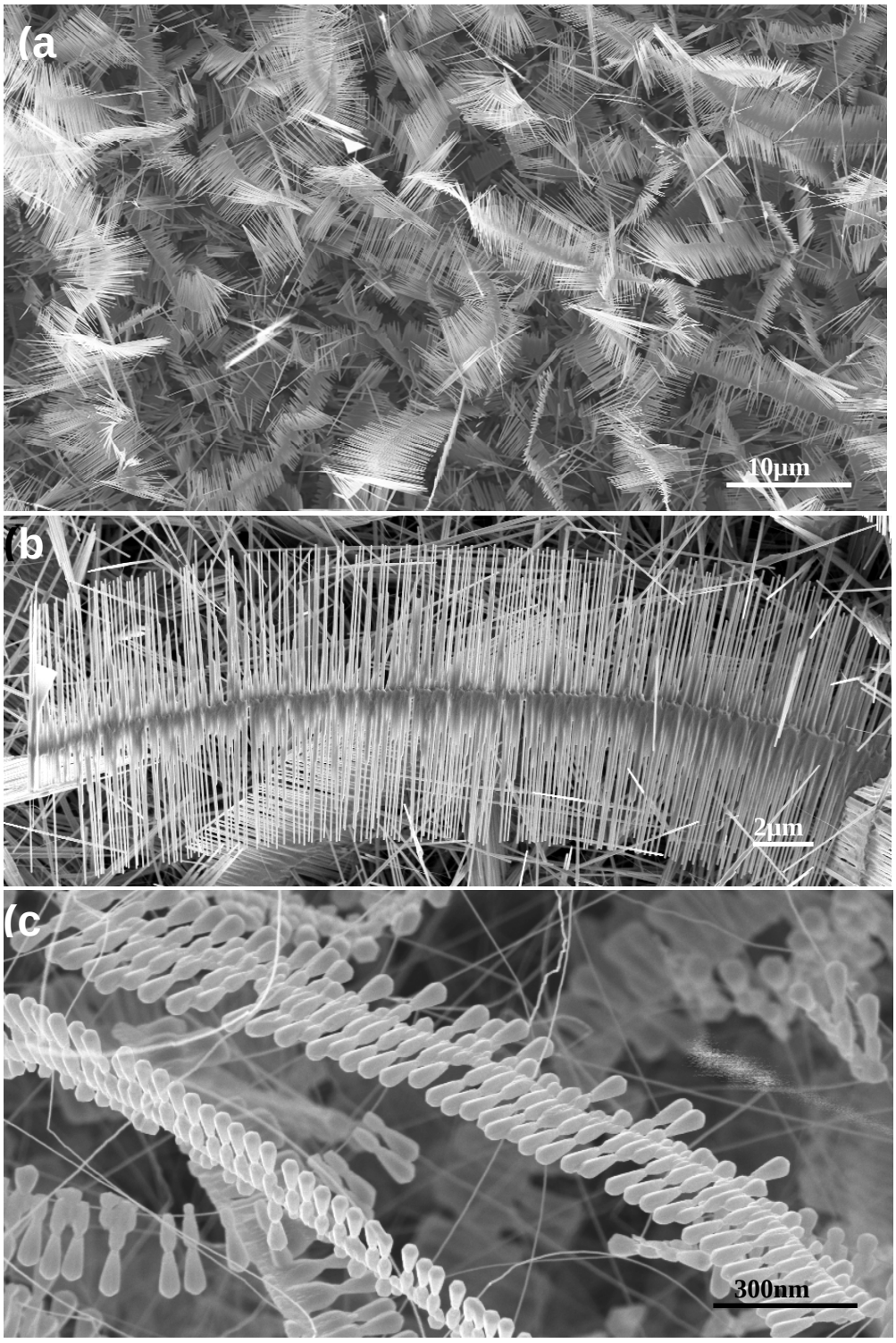

Fig 2.6 SEM images of the double-sided ZnO comb structures (a) A low magnification SEM image showing the high yield of double-sided combs. (b) and (c) double-sided ZnO nanocombs with different morphologies.

2.6 (b) is a magnified image of a double-sided comb, which clearly displays that the comb teeth symmetrically grow out from both sides of the ribbon

with a length of around 5μm and a pitch distance at 100nm range. The teeth are all hexagonal wires, revealing the [0001] growth direction of the teeth. Fig. 2.6 (c) is another type of double sided combs with two rows of hexagonal spindle shape teeth. Usually, the teeth are composed of two spindles connected head by head with the outer diameter of the spindles bigger compared to the inner part.

The structures of the double-sided combs were analyzed by TEM. Fig. 2.7 (a) is a low magnification TEM image, displaying the quasi symmetry growth of the teeth from two opposite surfaces of the primary ribbon. The teeth on both sides are all growing along [0001], as indicated by the arrows along them. Electron diffraction pattern recorded from the big circled area is displayed in fig. 2.7 (b), showing that the comb ribbon grows along $[2\bar{1}\bar{1}0]$ (a axis) with ± $(01\bar{1}0)$ top/bottom surfaces. The elongation, which is stressed out by the dash lines, of the diffraction spots is caused by the bending of the comb. Fig. 2.7 (c) and (d) are the convergent beam electron diffraction (CBED) patterns from the small circled areas in fig. 2.7 (a), which were precisely selected from two symmetric spots from the ribbon. As indicated by the arrows, the #1 disk in fig. 2.7 (c) is the mirror image of the #1 disk in fig. 2.7 (d). The same symmetry can be seen for #2 and #3 disks, thus these tow images form mirror symmetry of each other. From our previous modeling, the #2 disks are the (0001) diffraction disks, thus revealing the growth directions of the teeth on both sides are [0001]. An anti phase domain boundary (APDB) observed in fig. 2.7

(e) explains this growth phenomenon. With is the formation of the APDB, two chemically active Zn-terminated planes were formed on the opposite facets of

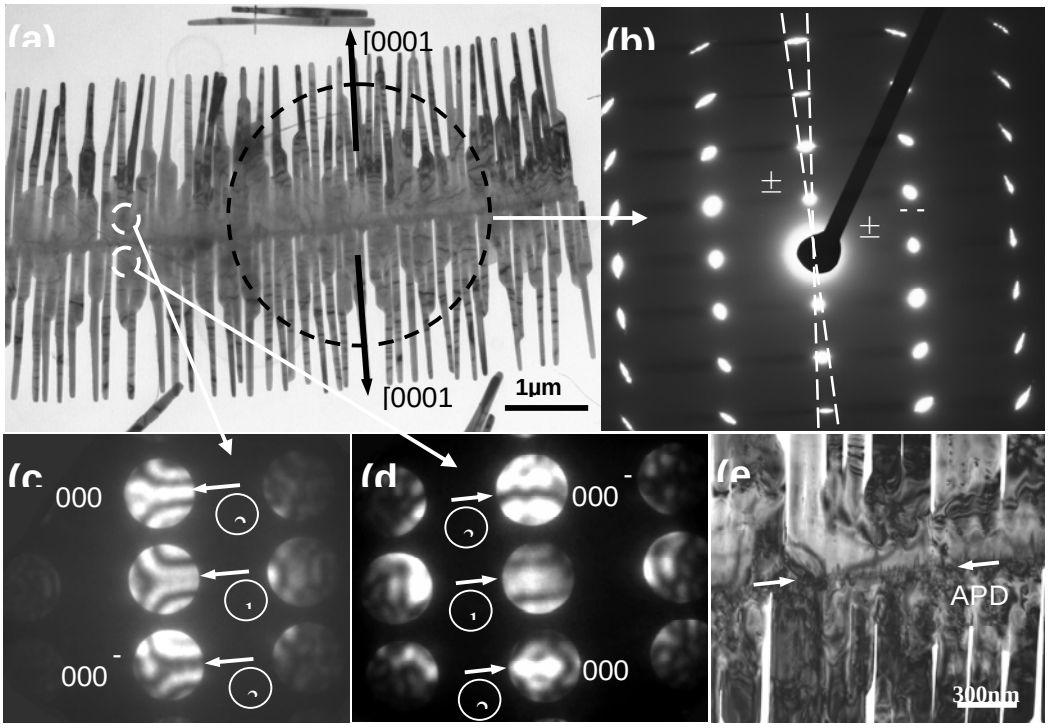

Fig 2.7 (a) TEM image of a double-sided ZnO nanocomb. (b) Diffraction pattern from the big circled area showing the growth direction of the teeth is [0001]. The "±" symbols come from the same [0001] growth direction of both sides of teeth. The stretched diffraction spots are created by the bending of the nanocomb. (c) and (d) are convergent beam diffraction patterns from the upper teeth and lower teeth of the nanocomb, which are mirror-symmetric with each other, revealing the [0001] growth direction for both sides of the teeth. (e) A magnified TEM image showing the existence of the anti-phase domain boundary in the ribbon that

the primary ribbon. The nanoteeth were then able to grow on different facets with the same [0001] direction.

In the synthesis of the nanocomb structures, the teeth length of both single-sided and double-sided combs can be obtained from several hundred nanometers to tens of micrometers, depending on the specific temperature and pressure conditions for different experiments and also the temperature

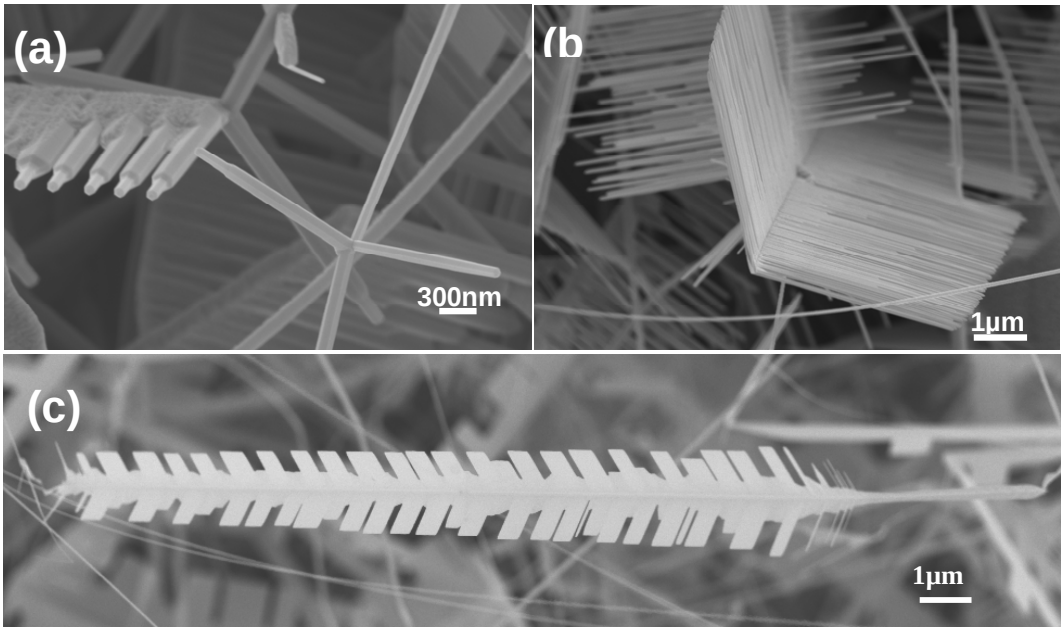

Fig 2.8 (a) A singled sided nanocomb ending with a tetra-leg structure. (b) and (c) feather-like double-sided nanocombs.

zone the substrates were placed in the furnace. Longer teeth nanocombs are more preferential to be found in the higher temperature region, where more source materials are available. Comparing the experiment conditions of the formation of the single-sided and double-side comb structures, that of the double-sided combs requires higher temperature, probably due to the higher formation probability of the anti phase domain boundary at the higher temperature.

Except for the previous discussed two kinds of comb structures, other interesting structures were also discovered, as shown in fig. 2.8. The structure in fig. 2.8 (a) is a normal single-sided comb, mostly like that in fig. 2.8 (b), except that a tetraleg ZnO structure forms at the end of the comb. In fig. 2.8 (b) and (c), feather-like comb structures are shown. In fig. 2.8 (b) it is a double sided comb structure with the two rows of teeth forming an angle with each

other at around 110° and the two rows of teeth are closely aligned on the ribbon. In Fig. 2.8 (c), the feature-like comb structure has two rows of wider and well separated teeth growing from the central ribbon.

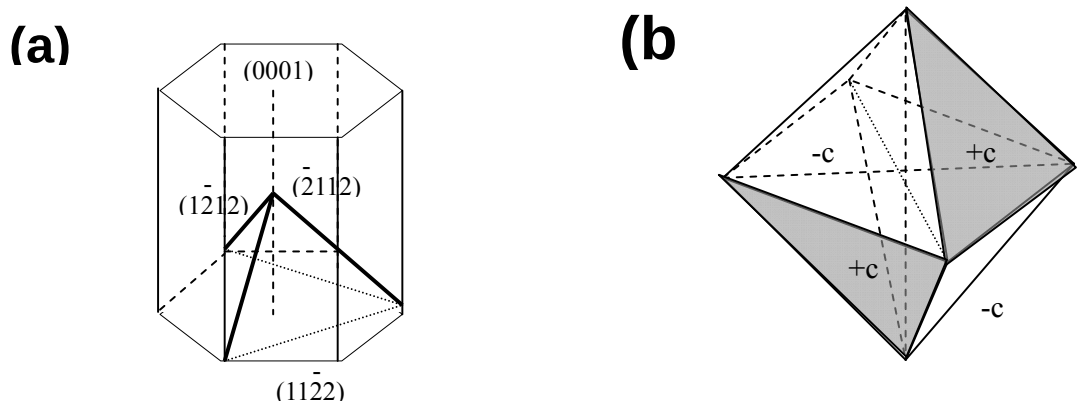

Fig 2.9 The structure model of the formation of the tetra-leg structures and the feather-like double-sided nanocombs. (a) A pyramid crystals formed by three $\{11\bar{2}2\}$ and one (0001) facets. (b) A nucleus composed of eight of pyramid crystals with the $\{11\bar{2}2\}$ faces contacting with each other, the ± (0001) planes facing the outer space in an alternative sequence.

The growth mechanism of these comb structures can be contributed to the formation of an octahedral multiple twin nucleus, which has 4 Zn-terminated surfaces.[164] Fig. 2.9 is an illustration of this model. The central octahedral nuclei are composed of eight tetrahedrons, which are shown in the hexahedron in fig. 2.9 (a). This tetrahedron has one (0001) facet and three $\{11\bar{2}2\}$ pyramidal facets. Eight of them are combined together to form the nucleus, with the pyramidal faces contacting with each other, the ± (0001) planes facing the outer space in an alternative sequence, as shown in fig. 2.9 (b). Because the +c plane terminated with Zn are more active, the growth of the nano structures is more preferential on these planes, thus forming the tetraleg structures in fig. 2.9 (a). If the nuclei contain only 4 tetrahedral

crystals, that is, 2 Zn-terminated planes, the feather-like structures in fig. 2.9 (b) and fig.2.9 (c) are obtained.

In summary, by controlling the growth kinetics through adjusting the temperature and pressure of the system, double-sided and single-sided comb structures were synthesized. The (0001) polar surface defines the growth direction of the teeth out of the ribbon. For the double-sided combs, an anti-phase domain boundary is formed in the central of the ribbon, so two rows of teeth are both in [0001] direction. And also, an octahedral multiple twin nucleus induced growth of the tetra-leg and the further-like ZnO comb structures was also reported. The result here further confirms the important role the Zn-terminated (0001) plane in synthesis of ZnO nanostructures. The uniform structures and the well aligned nanoteeth of the combs make themselves a good candidate for the application in nanosensors and nanomechanical devices.

2.2.3 ZnO Nanowire Networks

In this section, three-dimensional (3D) interconnected networks of ZnO nanowires and nanorods are synthesized by a high temperature solid – vapor deposition process.[165] The nanorods and nanowires have diameters of 20 – 100 nm and they grow along the c-axis. Due to the diverse orientation of the nanowires grown from a polycrystalline substrate, the networks are formed by a

sintering process of the crossed nanowires during growth. The thickness of the multilayer nano-network could be as thick as 30 μm. The sharp nanowire tips, the high degree of networking, and high surface area of these unique nanonetworks make them a potential candidate for field emission, ultra-sensitive gas sensing, catalysts and filtering

2.2.3.1 Experiment Procedure

Synthesis setup for the interconnected networks of ZnO nanowires was similar with the set-up for process in previous section. The difference comes from the experimental parameters. Here, in the synthesis of 3-D ZnO nanowire networks, the evaporation was conducted at 1400^{o}C for 30-120 min under a constant pressure of 300 mbar throughout the heating, high-temperature synthesis and cooling processes. The Ar carrier gas flow rate was controlled at 50-100 sccm after the temperature had reached 800 ^{o}C. The 3D networks of ZnO nanowires were grown on either a polycrystalline Al_2O_3 substrate or on a (110) Si wafer in a temperature zone of 700–800 ^{o}C.

Scanning electron microscopy (FE-SEM) (field emission LEO 1530 FEG) and transmission electron microscopy (TEM) (field emission TEM Hitachi HF-2000), and energy-dispersive X-ray spectroscopy (EDS) attached to the SEM and TEM, respectively were used to investigate the morphology, crystal structure and composition of the as-grown nanostructures.

2.2.3.2 Experimental Results

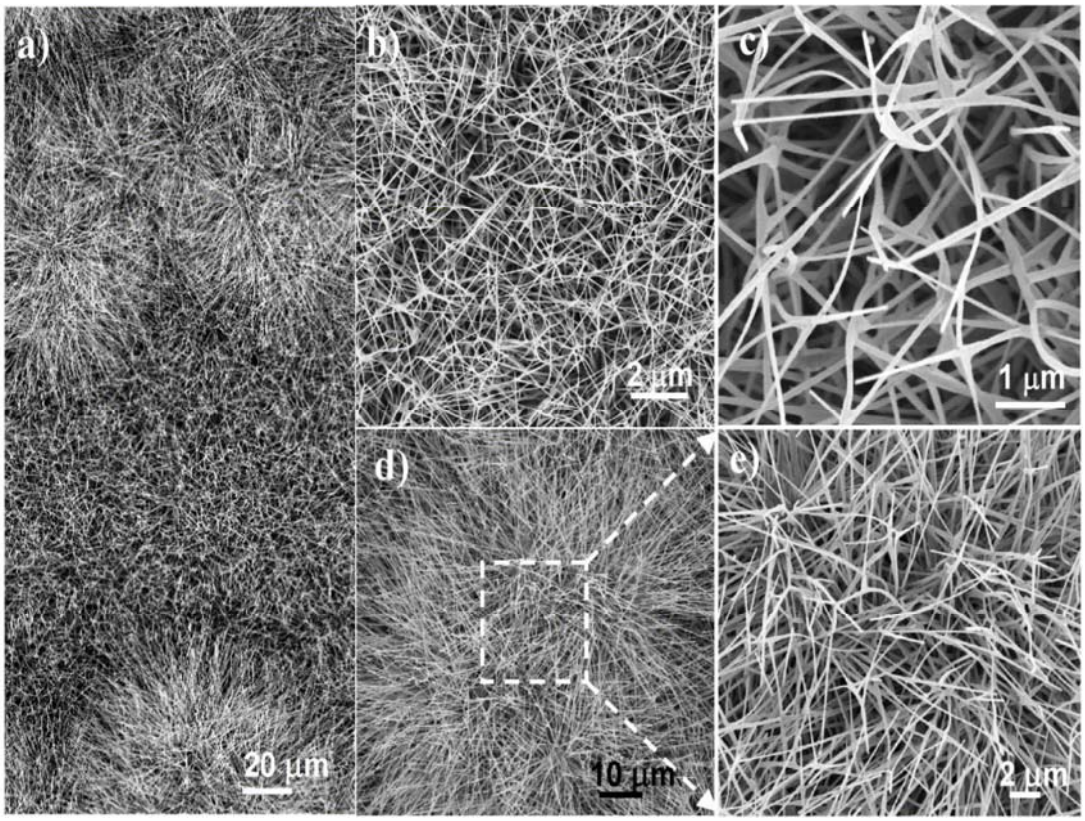

Fig. 2.10 (a) A typical low magnification SEM image of the as-grown networks of ZnO nanowires and nanorods consisting two types of morphologies, as indicated by area B (figs. 2.10 b and c) and C (figs. 2.10 d and e); (b) & (c) Enlarged SEM images of uniform fish-networks of ZnO nanowires and nanorods. (d) & (e) Enlarged SEM images of clumps of nanowires showing the interconnected

Figure 2.10 a is a typical low magnification SEM picture of the as-grown networks of ZnO nanowires and nanorods. Two typical morphologies were found: one shown in the top is the area with distinct clumps of nanowires; the other in the middle area is a uniform layer of nanowires networks. The respectively enlarged SEM pictures of the two areas are described in Figs. 2.10b &c, and Figs. 2.10d & e. From Fig. 2.10b, the network feature is clearly a fish-network like morphology, for which the mesh element is nanowires with a diameter around 100 nanometer. The further magnified picture in Fig. 2.10c

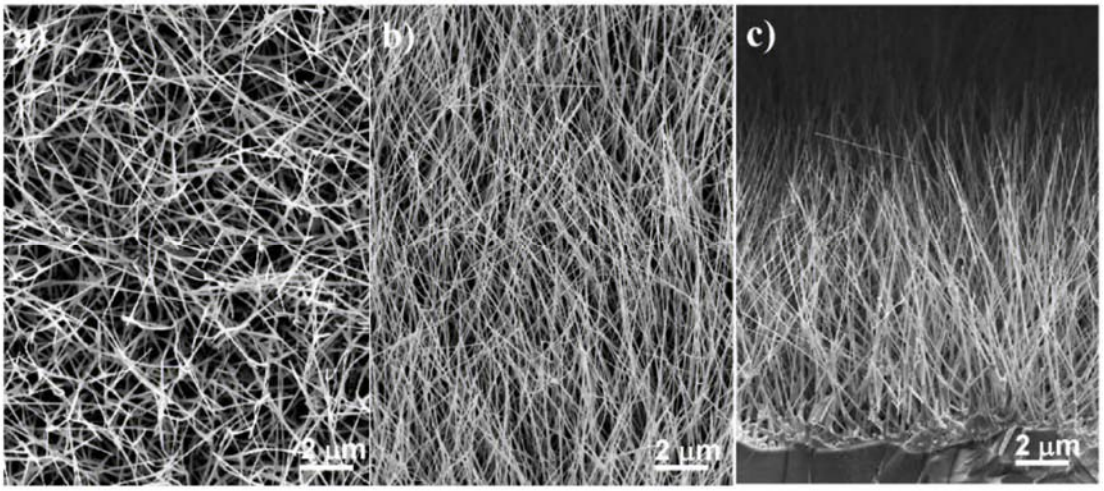

Fig 2.11 Three typical SEM images of the uniform fish-networks of ZnO nanowires: (a) viewed from top; (b) viewed at 45 degree tilt; and (c) cross section view.

describes the three dimensional structure of the fish-networks with certain 3D void spaces confined by adjacent nanowires and nanorods. Figures 2.10d and e depicted four clumps of radially grown nanowires joining with each other, forming interconnected networks.

Figure 2.11 shows three typical SEM images of the uniform fish-networks of ZnO nanowires respectively from top view (fig. 2.11a), 45 degree tilted view (fig. 2.11b), and cross section view (fig. 2.11c). The top view image indicates the interconnected and periodically spaced features of the network; the tilted view picture in fig. 2.11b gives a description that these interconnected nanowires and nanorods have a tendency to align along a specific direction; the cross sectional image in figure 2.11c clearly proves that these network nanowires and nanorods are quasi-aligned normal to the polycrystalline Al_2O_3 substrate with a uniform height of around 15~20 μm. In

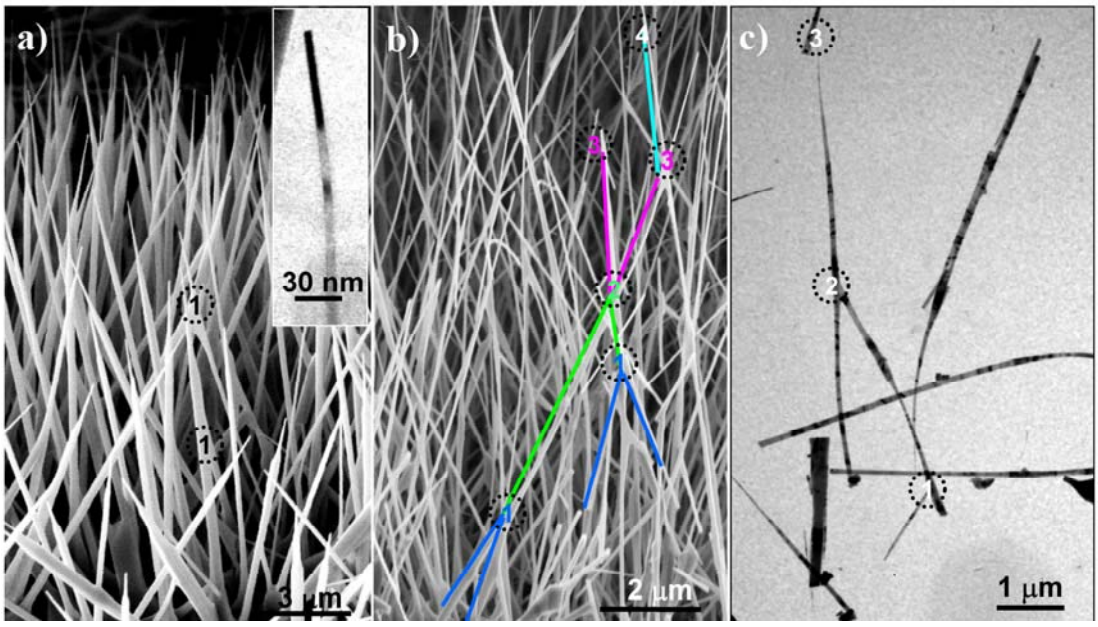

Fig. 2.12 A series of cross sectional SEM and TEM images of the 3D network structures of ZnO. (a) A cross-sectional SEM image showing the beginning layer of the network; (b) A comparatively dense fish-network cross sectional SEM image; (c) A TEM image for a broken network, three dotted circles depicted at-least three-layer interconnected network of ZnO nanowires.

addition, the image indicates several periodic layers of interconnected features along the height direction.

To further investigate the extent of network structure, higher magnified cross-sectional SEM and TEM images are comparatively studied. Fig. 2.12a is a SEM image showing the cross section at the beginning of a networking. As indicated by circles, the first interconnection between the nanowires and nanorods occurs at around 5~10 μm long; a common sharp tips as thin as 10 nm is formed after the first merging at around 5 μm. The cross section view of a comparatively dense fish-network is described in fig. 2.12b. Along the two nanowires of about 15 μm in length, four orders of joining nodes were clearly

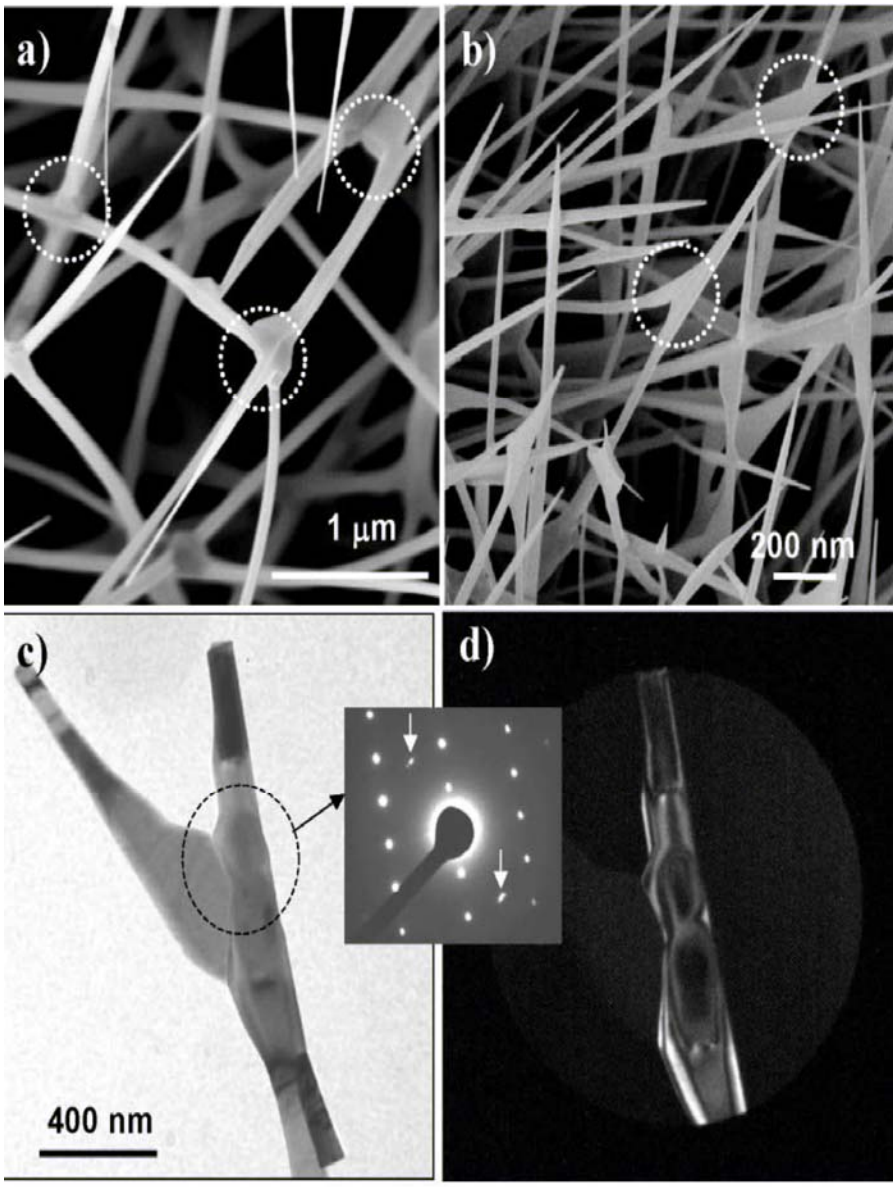

Fig. 2.13 (a, b) Interconnection modes of ZnO nanowires in the fish-network. (c, d) Bright-field and dark-field TEM images of two nanowires interconnected with each other, indicating that the two nanowires are single crystals but they have no orientation relationship. The circle area is used for recording the selected area electron diffraction pattern (inset).

identified, as indicated by dotted circles 1, 2, 3 and 4. The circle 4 represents the beginning of the fourth layer of interconnecting fish-network of ZnO nanowires.

Then the question is how could these nanowires meet and interconnect with each other to form a network? Under SEM, it is found that two nanowires would joint if their tips are close enough. As shown in Figs. 2.13a and b, a joint node is formed if the two nanowires come to a cross or one terminates at the joint point. The images appear to suggest that the joint is a "welding" rather than a simple physical contact. This result has been confirmed by TEM analysis. Figure 2.13c shows a bright field TEM image at the joint point of two nanowires. Electron diffraction pattern recorded from the nanowires shows that the right-hand side nanowire is single crystal and oriented along [01-10] with a growth direction of [0001], while the nanowire on the left-hand side is at an arbitrary orientation whose diffraction spots are indicated by two arrowheads in the pattern. Dark-field TEM image (Fig. 2.13d) using one of the diffraction spot from the [01-10] oriented nanowire indicates that it has no orientation relationship with the nanowire on the left-hand side, but two of them join together with a clear grain boundary.

To track the formation process of the nanowire network, several samples grown for different lengths of times have been prepared. Figure 2.14a is the initial stage of the nanowire growth, which suggests that large crystals are formed first, from which the nanowires are nucleated but with a diverse of orientations. As the growth continues, the lengths of the nanowires increase, and they start to get in touch (Fig. 2.14b). Under the growth temperature of 700~800 ^{o}C, sintering of nanowires is possible, forming the "welded" joints

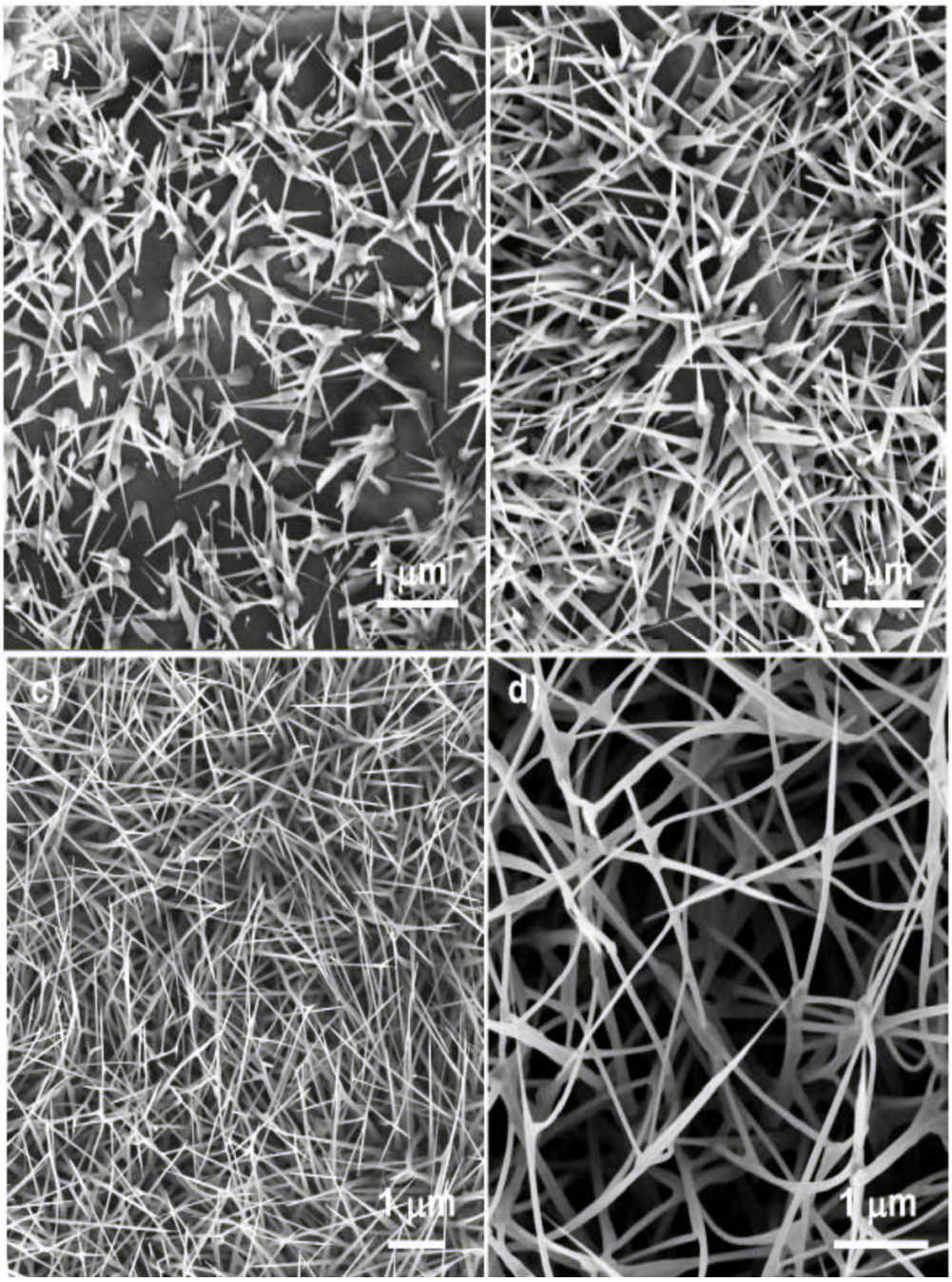

Fig. 2.14 Formation process of the 3D network. (a) The initial stage of interconnected nanorods growth; (b) The first layer of networking between short nanowires and nanorods; (c) The beginning of the second layer of networking; (d) Highly magnified SEM image giving a clear description about the 3D ZnO networks with mesh space around 2 by 2 by 2 (μm).

among the nanowires (Fig. 2.14c). This is likely to be the first level of networking. The crossed nanowires continue to grow and then they meet the

branches of other nanowires, another welded sintering forms the second nodes of the network. Such a process continues and finally forms a 3D network of nanowires (Fig. 2.14d). The density of the nanowires should be high enough to increase the chances of nanowire meeting in order to make the sintering possible. The high local growth temperature of 700-800 ^{o}C at the substrate makes sintering possible for nanowires.

In summary, three-dimensional (3D) structures of interconnected ZnO nanowires and nanorods, so called "fish-networks", were synthesized by a high temperature solid-vapor deposition process. The nanorods and nanowires have diameters of 20-100 nm. With increasing the duration of deposition time at high temperature, the thickness of 3D networks increase, as well as the increased degree of networking. The thickness of the multilayer fish-network could be as thick as ~30 micron. The nanowires and nanorods are along the *c*-axis of ZnO; and the networks are formed by sintering of crossed nanowires. It is suggested that by controlling the growth parameters such as pressure, temperature and duration time, different 3D-mesh size of fish-networks could be fabricated. The quasi-aligned sharp nanowire tips, interconnecting structure characteristics, high degree of networking and high surface area of these unique nano-networks make them a potential candidate for field emission, ultra-sensitive gas sensing, catalysts and filtering.

2.2.4 ZnO Core-Shell Nanodiskettes

As the partner of ZnO, metal Zn also has the hexagonal structure. An important fact is that ZnO tends to grow epitaxially on the surface of Zn via an oxidation process, forming Zn-ZnO metal-semiconductor core-shell structures. In this work, by using a solid-vapor synthesis approach and taking the advantage of selective oxidation on the surfaces of the as-formed Zn nanostructures, we present the synthesis, structure and growth process of Zn-ZnO core-shell nanostructures, such as single crystal nanodisks, polycrystalline nanodisks, mesoporous nanodisks. The results suggest that, by controlling the oxidation process, different morphological configurations of metal-semiconductor core-shell nanostructures can be received. The newly synthesized nanostructures made of textured and aligned nanocrystallites of ZnO could be the fundamental building blocks for fabricating piezoelectric resonator and sensors.[166]

2.2.4.1 Experimental Procedures

Our synthesis is based on a similar solid-vapor phase process. Different synthesis conditions were chosen for receiving different morphological structures. By tuning the synthesis parameters such as pressure in this study, various configurations of diskette-like ZnO nanostructures were achieved. The vapor phase transport synthesis parameters are: source materials: ZnO powders + graphite (C); evaporation temperature: 1100-1150 ^{o}C, evaporization time at the peak temperature: 30-60 minutes; short time pause for 10 min at 1000 ^{o}C during the cooling process; and pressure: 20-400 mbar. In the

temperature zone that we are interested in, diskette-like nanostructures were observed to be in the form of clumps. The observed ZnO nanodiskettes can be classified into three types of morphologies with slightly different composition: textured core-shell Zn-ZnO nanodiskettes, "single-crystal-like" textured ZnO nanodiskettes, nanostructured polycrystalline ZnO diskettes and mesoporous ZnO diskettes. The as-deposited samples were collected at a temperature range of 400 to 600 ^{o}C.

2.2.4.2 Textured Zn-ZnO core-shell nanodiskettes

For a typical synthesis by evaporating a mixture of ZnO and graphite at 1100 ^{o}C for 30 minutes (pressure was controlled around 20 mbar), textured diskette like ZnO and core-shell Zn-ZnO nanoparticles are received (Figs. 2.15-2.18). It is worth noting that this process is of high reproducibility and high-yield.

Figures 2.15a-d are a series of SEM images displaying the diskette-like ZnO nanostructure. A low magnification SEM image of the densely grown diskettes with uniform size of 1-2 μm was illustrated in Figure 2.15a. These diskettes are always in connection with zig-zag shaped nanowires. A side-view magnified image of a ZnO nanodiskette in Figure 2.15b presents a clear description that each diskette has a regular hexagonal faceted shape. The thickness of the disk is 100-200 nm. It is indicated by a white arrowhead in Figure 2.15b that an extended nanowire with a similar hexagonal

cross-section grew normal to the hexagonal nanodiskette in the center area. It

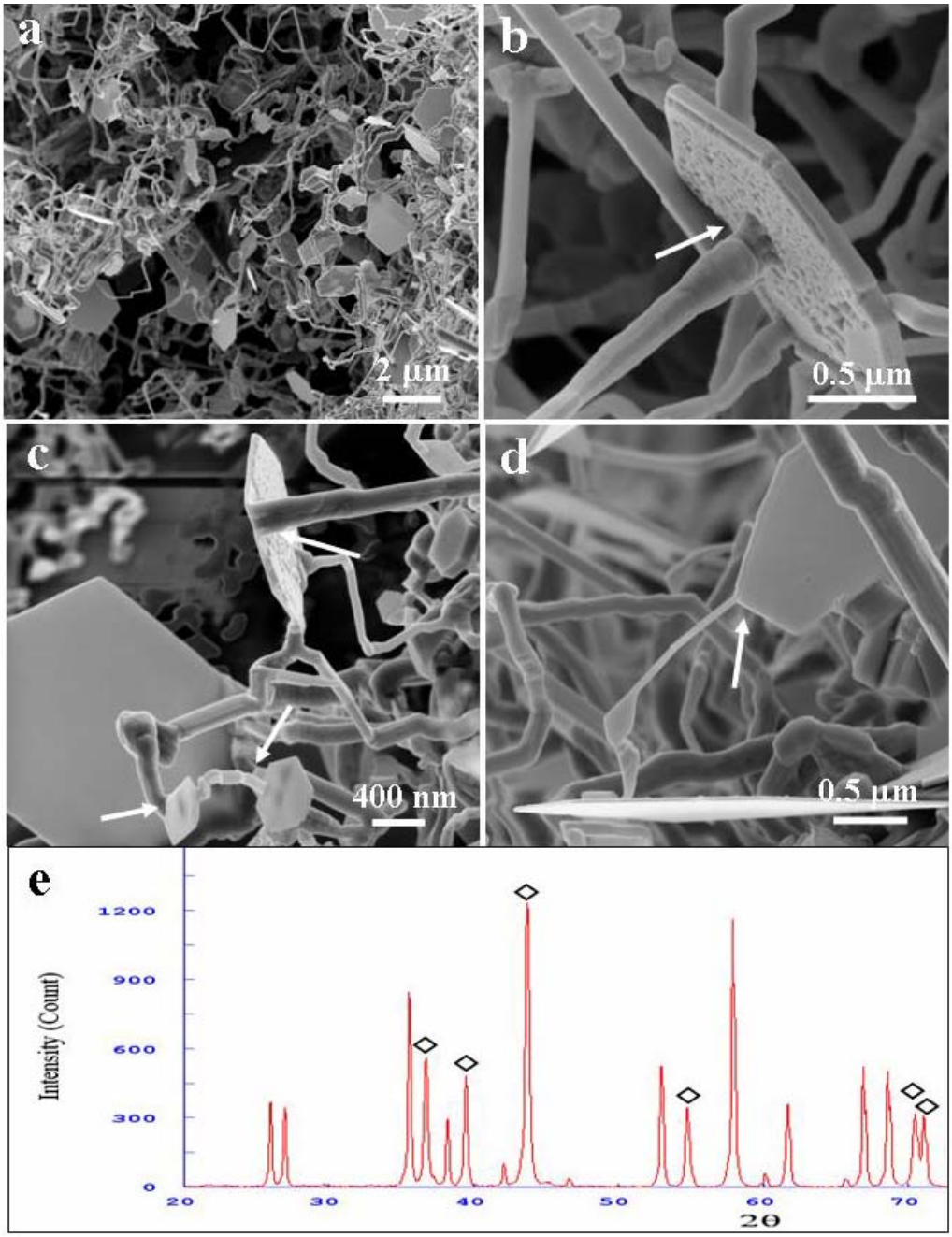

Fig. 2.15. (a) A typical SEM image showing the densely distributed nanodiskettes of ZnO on alumina substrate. (b) A bottom side view of a nanodiskette, revealing a normally extruded nanowire from the center of the rough large surface of the nanodiskette. (c) Three irregular shaped nanowires grew from the side surfaces of nanodiskettes or their edges (as indicated by arrowheads). (d) A nanoribbon grown in the plane of the large surface of a nanodiskette. (e) A typical X-ray diffraction spectrum indicating majority peaks from ZnO (as indicated with diamond symbols), the extra peaks come from the alumina substrate.

is also found that the normally emerging nanowire in fact could also extend from the side edge of the hexagonal nanodiskette (as displayed in Figure 2.15c). In general, one large surface of the nanodiskette is rather smooth while the other side is rough. The diameter of nanodiskette could be as small as 300 nm, and its thickness could be as thin as 50 nm. The cross-section of the extended nanowire could also be irregular. Figure 2.15d shows a nanowire that directly grew from the edge in the plane of the hexagonal diskette (as pointed at by an arrowhead). X-ray diffraction spectrum of the as-prepared sample is shown in Figure 2.15e, which proves that the majority of the peaks come from ZnO, whose diffraction peaks are marked by "◊". The extra peaks were contributed by the alumina substrate used for collecting sample. To find out the crystal structure of an individual nanodiskette, a systematic TEM imaging and diffraction analysis was conducted. Figure 2.16a is a TEM image of two hexagonal nanodiskettes of ~3 μm in width. The corresponding electron diffraction pattern in Figure 2.16b is a single crystal [0001] pattern of ZnO, which reveals that the top and bottom large surfaces of the nanodiskette are a pair of (0001) and $(000\bar{1})$ c-planes, while the six side facets are $\{01\bar{1}0\}$. Figure 2.16c is a TEM image showing a ZnO nanodiskette with three normally extended nanowires from the edge of the side surface (A), the center of the bottom rough surface (B), and the edge of the side surface (C). The size of the nanodiskette is about 600 nm. The recorded top view of a 2 μm nanodiskette

in Figure 2.16d displayed two extended nanowires from the edge of the nanodiskette.

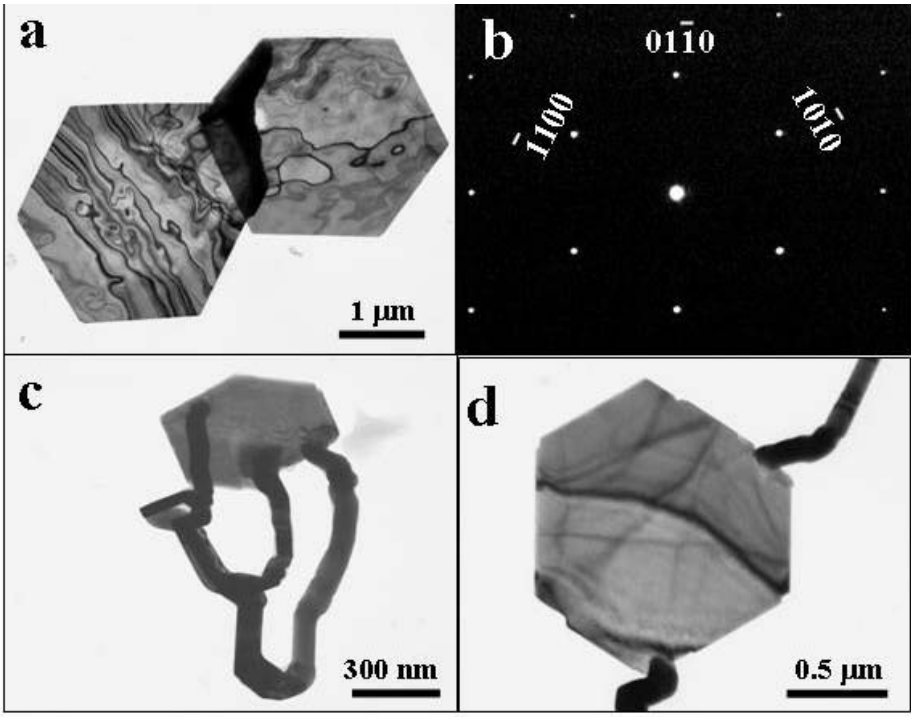

Fig. 2.16. (a) and (b) are respectively a TEM image of two overlapped hexagonal nanodiskettes and the corresponding single crystal [0001] diffraction pattern from a diskette. (c, d) Nanowires grown out of the top and side surfaces of a ZnO diskette.

Further TEM analysis was conducted to investigate the fine structure in the nanodiskette. Figure 2.17a is a bright field TEM image of a nanodiskette, which shows that the dominant surface of the diskette is rough. The corresponding dark field TEM image in Figure 2.17b clearly demonstrates the surface roughness, where nanosized nanocrystals were exposed. The corresponding diffraction pattern is composed of two sets of [0001] diffraction patterns corresponding to elemental Zn and ZnO, between which an epitaxial orientation relationship was preserved. Figure 2.16d is an HRTEM image recorded from the middle part of the nanodiskette in Fig. 2.17a. The image depicts a two-dimensional Moire′ pattern with electron beam parallel to the

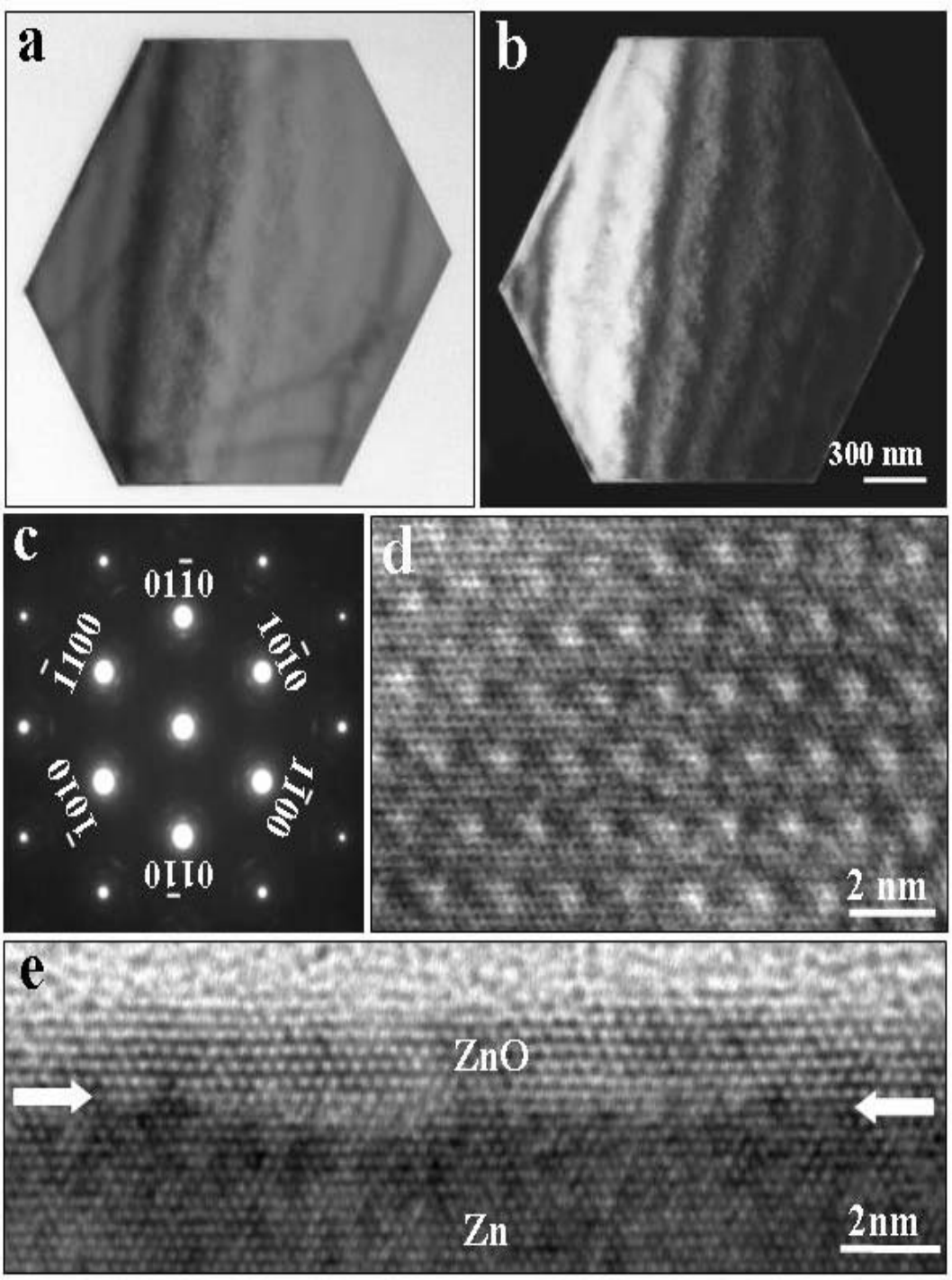

Fig. 2.17. (a, b) Bright field (BF) and the corresponding dark field (DF) TEM images of a Zn-ZnO core-shell nanodiskette composed of ZnO nanocrystals. (c) The corresponding diffraction pattern of the nanodiskette that is composed of two sets of [0001] diffraction spots from Zn and ZnO, respectively, showing their epitaxial orientation relationship. (d) High resolution TEM image from the diskette showing a two-dimensional Moire' frings. (e) HRTEM lattice image displaying the side wall of the ZnO and the middle Zn core, where two arrowheads point out the interface

c-axis of the two overlapping Zn and ZnO lattices. Considering that a Moire′

fringe pattern is produced by two sets of parallel overlapped lattice planes of Zn and ZnO, respectively, there are three sets of intersecting Moire′ fringes; every individual pattern is rotated with respect to the other by 60°, forming a Moire′ pattern as shown in Fig. 2.17d. This is due to the epitaxial orientation relationship between Zn and ZnO as well as the perfect alignment in c-axes. Considering the lattice mismatch between Zn and ZnO, the *D* spacing of the $\{01\bar{1}0\}$ Moire′ fringes is about 1.30 nm, which corresponds to one Moire′ fringe every 4.6 atomic planes of ZnO or 5.6 atomic planes of Zn. An HRTEM image from the edge part of the hexagonal nanodiskette is shown in Figure 2.17e. The lattice image displays the interface between Zn core and ZnO shell as indicated by two arrowheads. The upper part of the image reveals the lattice image of the ZnO shell, while the bottom part corresponds to the elemental core Zn. The thickness of the ZnO shell is 1.5-2 nm.

To further investigate the lattice structure at the Zn-ZnO interface, the HRTEM image has been digitally processed. By taking a Fourier transform of the raw image displayed in Fig. 2.18a, selecting only the reflections from Zn and ZnO, respectively, two sets of images corresponding to Zn and ZnO are presented in Figs. 2.18b and c. The Zn lattice is rather perfect without much distortion due to the fact that Zn was the “mother”crystal formed first at the core. The ZnO is formed via oxidation so that the lattice exhibits imperfection due to the multiple nuclei’s of the oxide grains on the surface. Mismatch

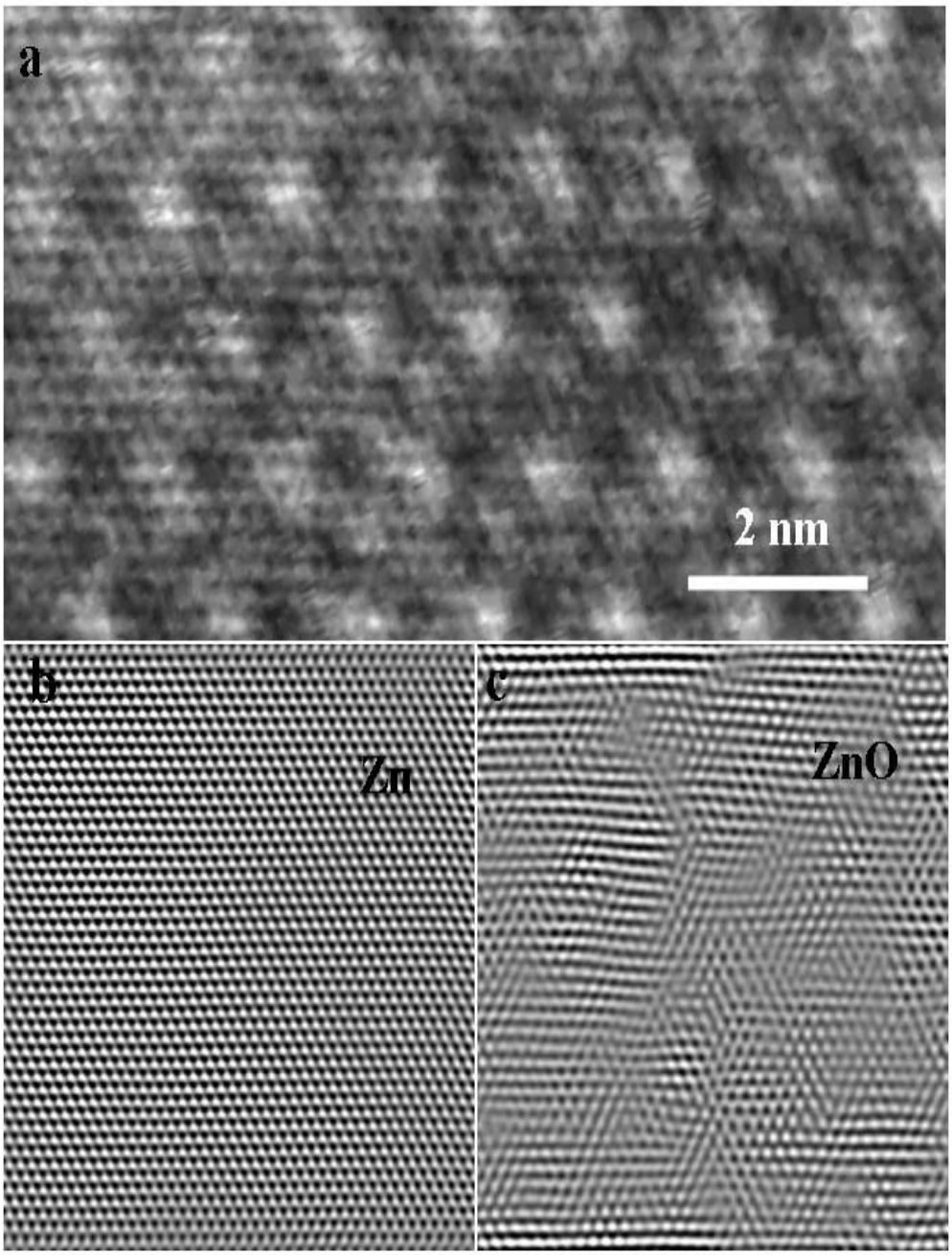

Fig. 2.18. (a). HRTEM image recorded from a Zn-ZnO diskette. (b, c) Fourier filtered images of (a) showing the lattices from Zn core and ZnO shell, respectively.

dislocations and strains are apparent in the lattice image from the thin ZnO shell (see Fig. 2.18c).

2.2.4.3 Nanostructured polycrystalline ZnO diskettes and mesoporous diskettes

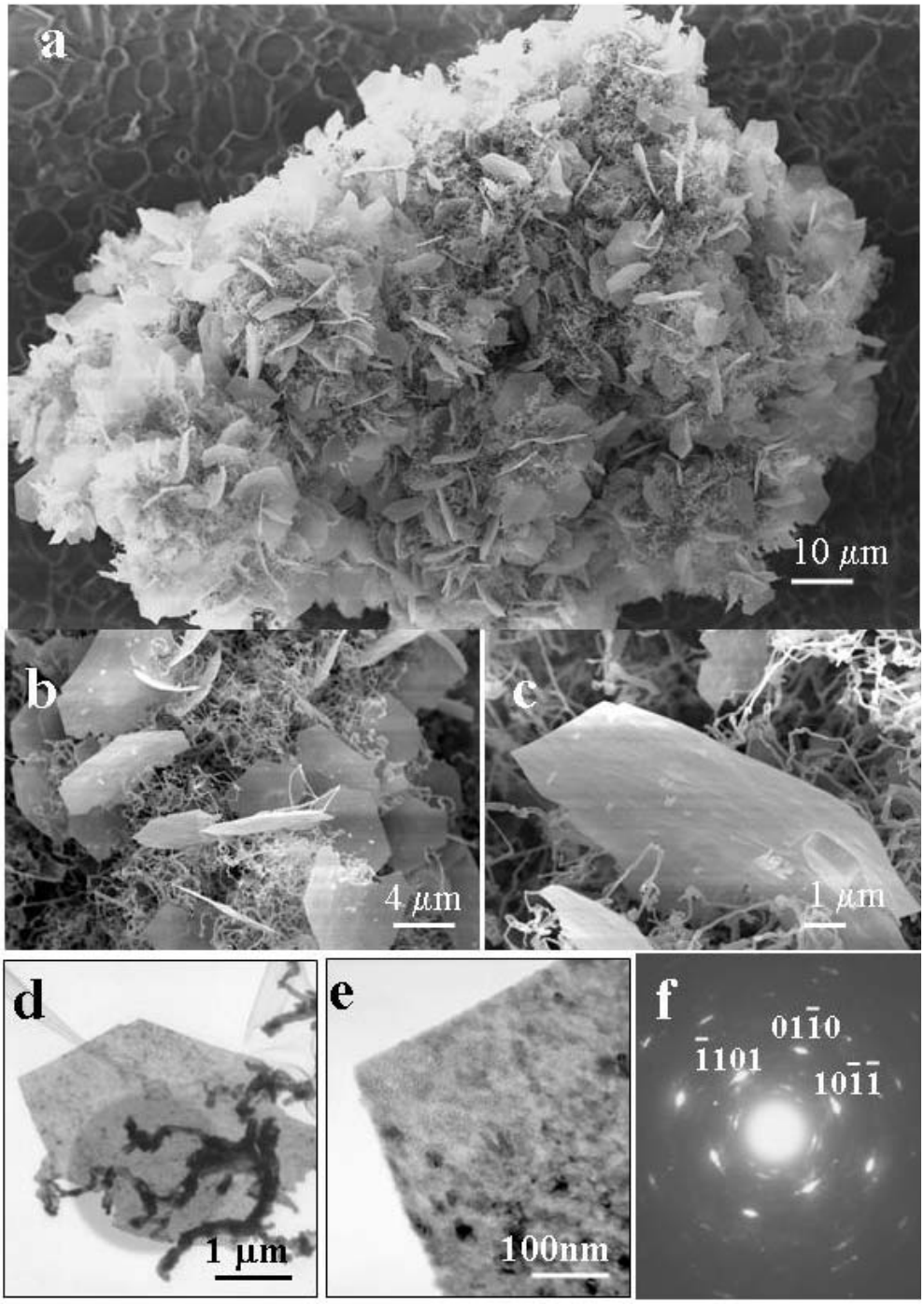

Fig. 2.19. (a) A clump of ZnO nanodiskettes intermediated with lots of tiny nanowires. (b) A magnified SEM image showing the small thickness of the ZnO nanodiskettes and the intermediated tiny ZnO nanowires. (c) An enlarged side-view SEM image of a ZnO nanodiskket, revealing the secondary growth of ZnO nanorods on the large surface. (d, e & f) are respectively a low-mag TEM image of a ZnO nanodiskette, an enlarged TEM image corresponding to the corner of the ZnO nanodiskette, and its corresponding electron diffraction pattern, showing textured grains of the ZnO nanocrystals composing of the nanodiskette.

To investigate the effect of pressure variation on the formation of ZnO nanodiskettes, we tuned the pressure from original 20 mbar to 200 mbar, and kept the other parameters the same as the one described in previous section. It is interesting to find out that similar hexagonal diskette-like nanostructures of ZnO were grown in the form of clumps in a temperature range of 400-600 ^{o}C. Typically, three types of nanodiskette have been observed under SEM, which are respectively single crystal ZnO nanodiskettes, polycrystalline nanodiskettes and mesoporous nanodiskettes as the substrate temperature increasing from 400 ^{o}C to 600 ^{o}C.

Figure 2.19a is a clump of densely packed ZnO nanodiskettes found in low 400 ^{o}C area, which have a uniform size of around 5 μm. Between the nanodiskettes, lots of tiny nanowires were grown. The magnified SEM image in Figure 2.19b clearly displayed that the thickness of each nanodiskettes is about 10 nm. Figure 2.19c describes that on one large surface of a nanodiskette, secondary growth of nanowires are clearly visible (as indicated by arrowheads). A typical low magnification TEM image in figure 2.19d is a front projection view of a ~5 μm wide nanodiskette.

The corresponding enlarged image on the left corner of the nanodiskette in figure 2.19e reveals its grainy and patch dominant surface, an indication of a possible polycrystalline structure. While in figure 2.19f the corresponding electron diffraction pattern proved it to be textured and self-assembled by ZnO nanocrystals with orientation along c-axis.

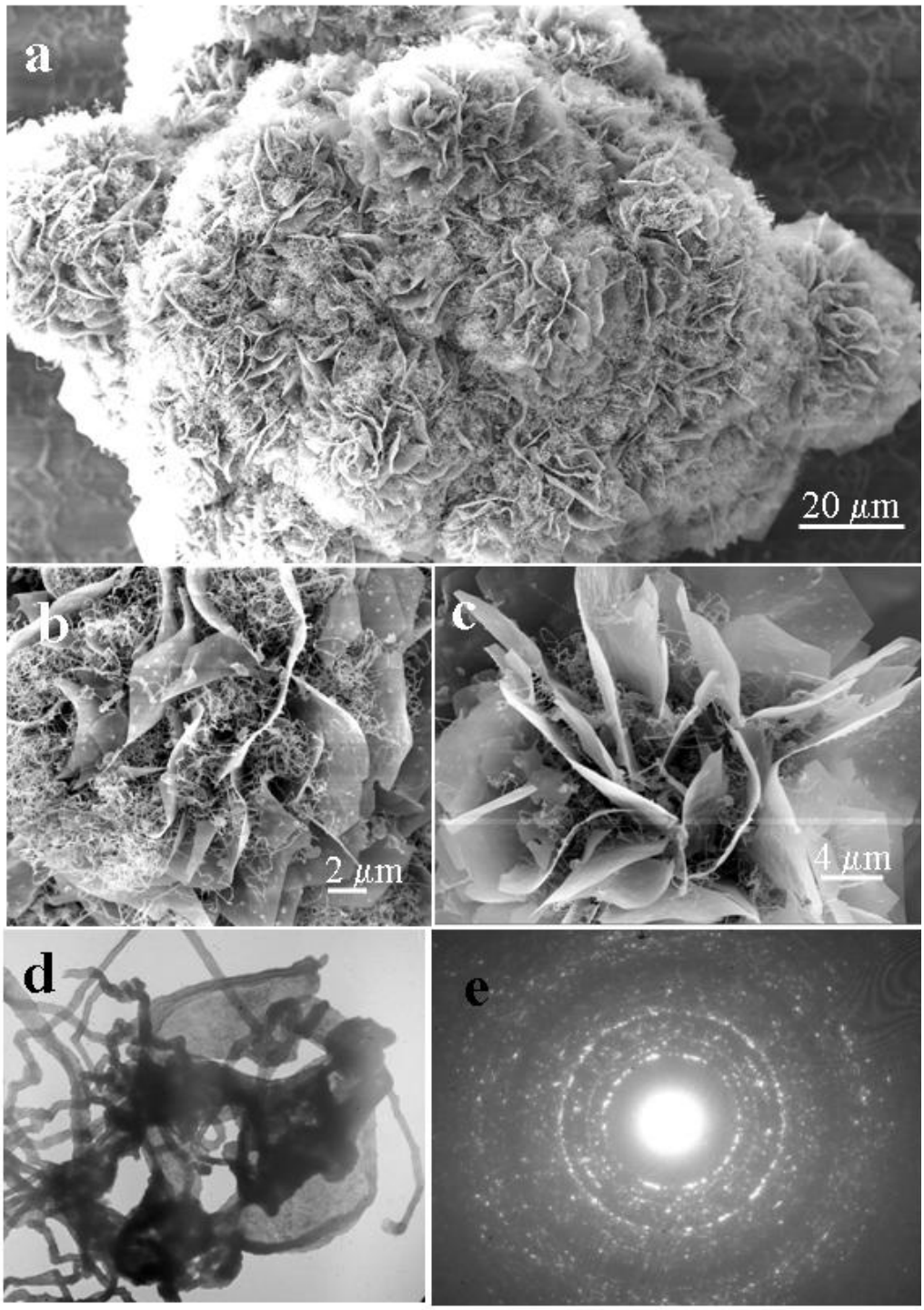

Fig. 2.20. (a) A flower-like clump of packed ZnO nanodiskettes intermediated by nanowires. (b) A magnified SEM image showing a flower-like nanodiskettes with curved large surfaces. (c) Curved flakes of nanodiskettes with a uniform thickness as thin as ~30 nm. (d) a typical TEM image of two curved nanodiskettes with nanowires surrounding them. (e) The corresponding electron diffraction pattern revealing the polycrystalline structure of the curved nanodiskette.

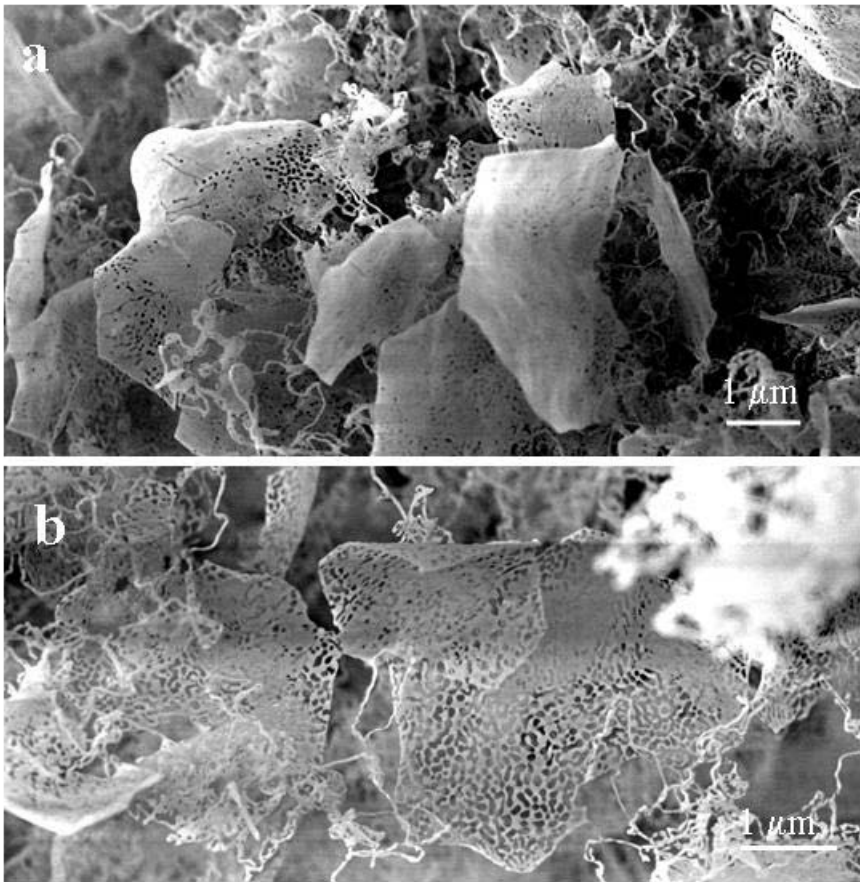

Fig. 2.21. (a, b) Mesoporous nanodiskettes with a uniform hexagonal shape, small thickness (tens of nanometers) and pore structure. (c) and (d) are respectively a TEM image of a mesoporous nanodiskette and its corresponding electron diffraction pattern.

As the local growth temperature increases to ~500 °C, the morphology and structure of the diskettes were changed. In Figure 2.20a, it is shown that more densely packed ZnO nanodiskettes/nanosheets form a big clump of flower-like morphology. The nanodiskettes tend to be wavy (Figures 2.20b and c) instead of flat like the nanodiskettes collected in low 400 °C temperature region (Figures 2.20b and 2.20c). To determine if the nanodiskettes still kept the single-crystal-like textured structure, TEM results are displayed in Figures 6d and 6e. Figure 2.20d is a TEM image showing two curved nanodiskettes with a diameter around 10 μm, between them quite a

few Zn nanowires are around. The imaging difference between Zn nanowires and ZnO nanowires is that the former is curly and the latter is straight. The selected area electron diffraction pattern shown in Figure 2.20e is from a local small part of a curly nanodiskette. The ring pattern clearly shows that the nanodiskette is made of nanocrystallites that are randomly oriented. This is very different from the single-crystal-like textured structure of the nanodiskettes collected at a lower temperature zone

As the local temperature goes high to ~600 ^{o}C, it is found that mesoporus nanodiskettes are the dominant morphological configurations. Figures 2.21a and b show two low magnification SEM images of the mesoporous nanodiskettes that still kept a uniform hexagonal shape. The thickness of the diskettes is as thin as tens of nanometers and the pore size is ~50 nm. Its corresponding electron diffraction pattern shows a mesoporous nanodiskette. The mesoporus feature is apparent, where the nanosized grains are uniformly distributed on the diskette surfaces. The electron diffraction pattern proves the random orientation of the nanocrystallites that compose the mesoporous diskette.

2.2.4.4 Growth mechanism of ZnO nanodiskettes

In previous work on the textured polyhedral ZnO shell and cage structures, the formation process has been proposed to be a process comprised of solidification of liquid droplets, surface oxidation and sublimation. In our current work, similarly, the epitaxial oxidation on Zn

surfaces is the fundamental process of forming the core-shell structure. The introduction of graphite in the raw materials is to reduce the oxides into metals as given by:

$$2ZnO\ (s) + C\ (s) \rightarrow 2Zn\ (g) + CO_2\ (g) \qquad (2.1)$$

The sublimated Zn atoms are carried down stream by the Ar carrier gas. In the lower temperature region, Zn atoms condense and form liquid clusters (as schematically shown in Fig. 2.22a), which tend to deposit fairly uniformly onto the alumina substrate. The liquid droplets quickly solidify on the substrate in the deposition temperature zone of 400-600 ^{o}C. From the surface energy point of view, the lowest energy facets for Zn are {0001}, and then $\{10\bar{1}0\}$ and $\{2\bar{1}\bar{1}0\}$. Thus, the faceted single crystalline Zn hexagonal diskettes tend to form, which are enclosed by {0001} top and bottom surfaces and $\{10\bar{1}0\}/\{2\bar{1}\bar{1}0\}$ side surfaces, as shown in Fig. 2.22b. With consideration of the lower local growth temperature, the residual oxygen in the growth chamber is likely to oxidize the surface of the Zn nanodiskettes, but the degree to which the diskettes to be oxidized depends on the local temperature. As shown in previous figures, with the local growth temperature increased from ~400 °C to ~500 °C and until ~600 °C, the hexagonal nanodiskettes evoluted from core-shell textured Zn-ZnO nanodiskettes and textured ZnO nanodiskettes (III) to nanostructured and polycrystalline nanodiskettes (II) and to mesoporous nanodiskettes (I), respectively, as sketched in Figure 2.22c. A slight difference between the work reported here from the cages and shells

reported previously is that Sn catalyst is absent in the current study, thus, the formation of ZnO nanocrystal is contributed from the surface oxidation of Zn and the deposition of ZnO vapor directly vaporized from the source material:

$$ZnO\ (s) \rightarrow ZnO\ (g) \qquad (2.2)$$

At the lower temperature region of ~400 ^{o}C, epitaxial surface oxidation is the major contribution to the growth of textured Zn-ZnO diskettes and ZnO diskettes. The difference between textured Zn-ZnO diskettes and ZnO diskettes is the degree of oxidation being incomplete or complete.

With the increased local growth temperature to ~500 ^{o}C, the oxidation rates are likely to be higher, resulting in the quick formation of larger size ZnO nanocrystallites and non-uniform thickness of the ZnO nanodiskettes (Fig. 2.22c II). In this case, the deposition of the coming ZnO vapor may become significant, which may directly deposit on the surfaces of the ZnO nanocrystals or form new nanocrystals on the nanodiskettes, thus, the epitaxial growth of ZnO nanocrystals is terminated partly because of the quick surface oxidation and the redeposition of ZnO vapor at a faster rate, forming nanostructured polycrystalline objects.

When the local temperature is as high as ~600 ^{o}C, a re-sublimation of Zn is possible; the sublimation rate of Zn nanodiskettes may be so fast that the deposition of polycrystalline and nanostructured ZnO is not enough to cover the entire surface of the nanodiskette. The areas covered or oxidized into ZnO

are preserved, while the uncovered areas are resublimated, leaving behind a

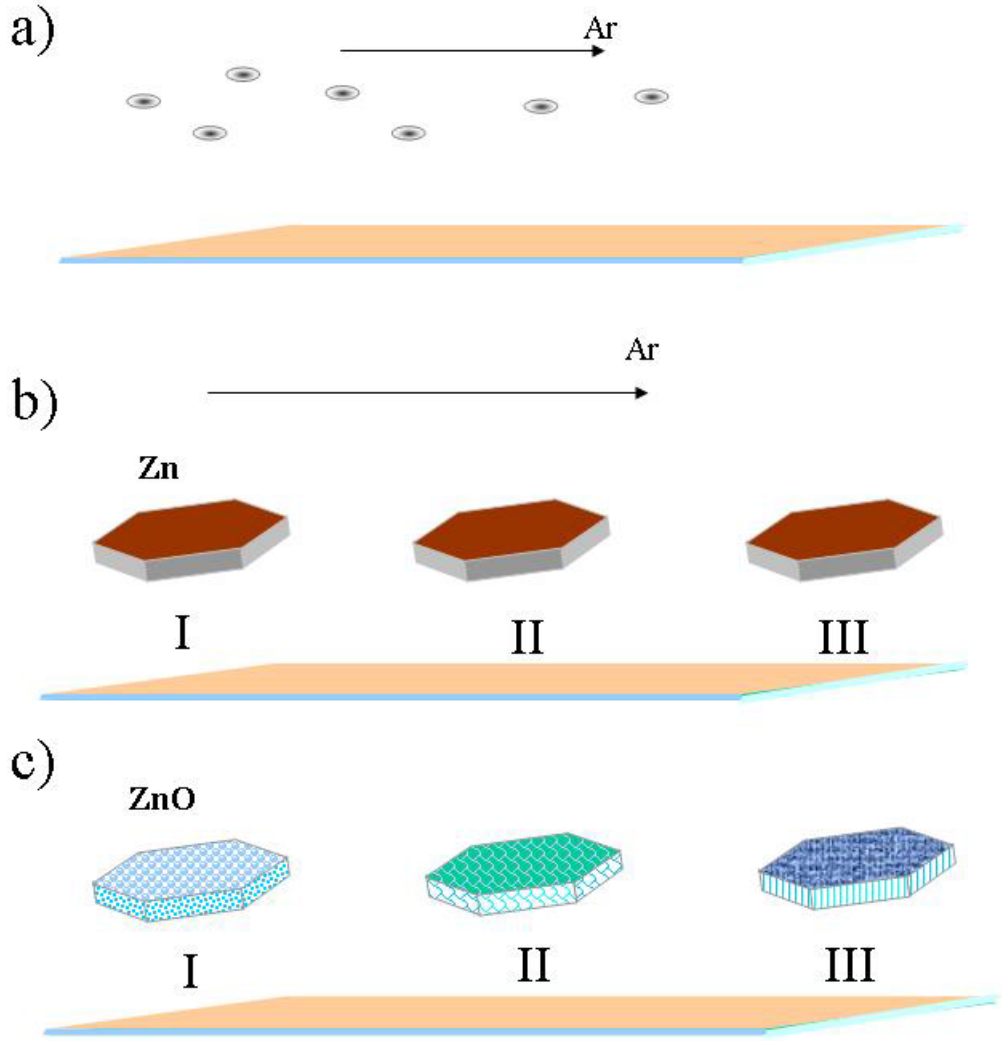

Fig. 2.22 A proposed growth model of the ZnO nanodiskette (for detail see text).

ZnO "skeleton" and the formation of holes or pores in the body of the nanodiskettes (Figure 2.22c I). In this case, the mesoporous structured ZnO is formed.

In this section, by using a solid-vapor synthesis approach, as well as taking advantage of selective surface oxidation on the as-formed Zn nano-object, textured ZnO nanostructures are synthesized. It is mainly about the growth

and formation process of single crystal nanodisks, polycrystalline nanodisks, mesoporous, and nanodisks. It is suggested that by controlling the oxidation process of different morphological configurations of Zn, different configurations of single crystalline to polycrystalline ZnO nano/micron objects could be achieved.

2.3 Summary

Semiconducting oxides have been successfully employed as materials for chemical and biological sensing in bulk and thin film materials. This section includes the synthesis of different nanostructures of semiconducting oxides, i.e. ZnO for this section. ZnO nanobelts, nanocombss, nanonetworks, nanodiskettes, have been successfully fabricated. Among these newly reported nanostructures, novel physical and chemical factors play significant role in determination of the formation of these nanostructures, which are discussed in each section. These researches provide useful insights to illuminate the complex growth mechanism and the perfect art of the combination of physical effect, chemical effect and mechanical effect. Also, these semiconducting oxides nanostructures are of great importance in application in electronics, optics, and nanopiezotronics.

CHAPTER 3

TRANSPORT STUDY OF 1D OXIDE NANOWIRES

Being a smart functional material, ZnO has received much attention recently for its possible application as UV light-emitting diodes (LEDs), spin functional devices, gas transparent electronics, and surface acoustic wave devices. It has shown promising properties in the research of these basic electric and optic devices. Fully employing the semiconducting oxide nanowires and exploring the potential to use these 1D nanowires to replace current electronic circuit device components would be a great interest of current nanotechnology research. To fulfill this objective, the most basic and essential requirement is to test the transport properties of semiconducting oxide nanowires and compare its performance with the bulk materials. With further understanding and developing of current basic electric components based on nanowires, we can then further develop and advance our current nanotechnology. In nanoscale, dimensional confinement and the surface effect is substantially greater than in the bulk, which will result in a lower threshold for laser excitation, better gas sensitivity, and other enhanced properties. This further increase the emergence for developing in nanoscale device investigation.

A key requirement for advancing the technological uses of nanowires is to improve the control of device stability, simplify the fabrication process and detailed knowledge of the intrinsic transport properties of the devices.

3.1 Device Fabrication

Optical lithography has been playing a key role in the success of CMOS technology in microelectronics. By using smaller and smaller wavelengths year upon year, the required performance on critical feature sizes has been achieved. However, with scale-down of the critical size for the circuits, more complex processes and expensive price for the fabrication process increase giantly. When coming in to the problem of nanowire based devices, we normally used other lithography options to improve the feasibility for devices fabrications. This is the so-called "Next Generation Lithography'' (NGL) options proposed several years ago such as X-ray, In this section, brief overview of the the e-beam lithography, focused ion beam, and photolithography which are used in the fabrication of nanodevices will be discussed.

3.1.1 E-beam Lithography

Electron beam lithography (EBL) makes use of the fact that electrons can be deflected and modulated by electrostatic or magnetic fields to produce a pattern on the substrate, which is a specialized technique for creating small patterns.[167] The fundamental resolution limit is given by the Heisenberg uncertainty ($\Delta x \Delta p \geq h/2\pi$) offering the possibility to achieve patterning below 10 nm. There are two ways to perform E-beam lithography, either by scanning the beam to generate patterns or to perform electron imaging through masks like conventional photolithgraphy. Upon

scanning an electron beam across a surface covered with a resist film sensitive to those electrons, a desired pattern will form in the resist film, which could be later on lifted off or left as the stamp pattern.

Detail process for fabricating a nanowire based devices is shown in figure 3.1. Normally, the nanobelt devices are typically fabricated using polished silicon wafer (100) with a thermally grown oxide or SiN layer made by plasma enhanced CVD. The procedure for the fabrication is: a). Firstly ultrasonically clean the Si wafer in trichloroethylene (TCE) followed by acetone and isopropanol (IPA) for 15 minutes in each solution. b). Then the wafer is blown dry using compressed dry N_2. c). ZnO nanobelt samples are dispersed into ethanol and ultrasonicate for 15 minutes. Then this ZnO nanobelt suspension was dispersed onto the Si wafer. After the ethanol dry out, ZnO nanobelts are left and randomly distributed on the surface of the substrate; d) Electron- sensitive resist PMMA coating; e). Eelectron beam scanning for generating desired pattern on PMMA on desired ZnO nanobelt; f). acetone development of exposed area (dissolution of e-beam exposed area); g). Metal (Ti/Au) deposition; h) Lift off of PMMA area, a pattern transfer process. PMMA resists represent a popular used polymethyl methacrylate with a large molecule weight (950k) resins in 2% chlorobenzene for the top layer. Thermal evaporation technique was used for metal (Au) deposition. The electron-beam lithography equipment that is used is a Scanning Electron Microscope JSM 5910, which is controlled

by Nanometer Pattern Generation System (NPGS) software during the writing of the patterns. Using NPGS, a variety of parameters such as beam current, center to center spacing, line spacing, dosage and magnification can be set to write properly on the samples.

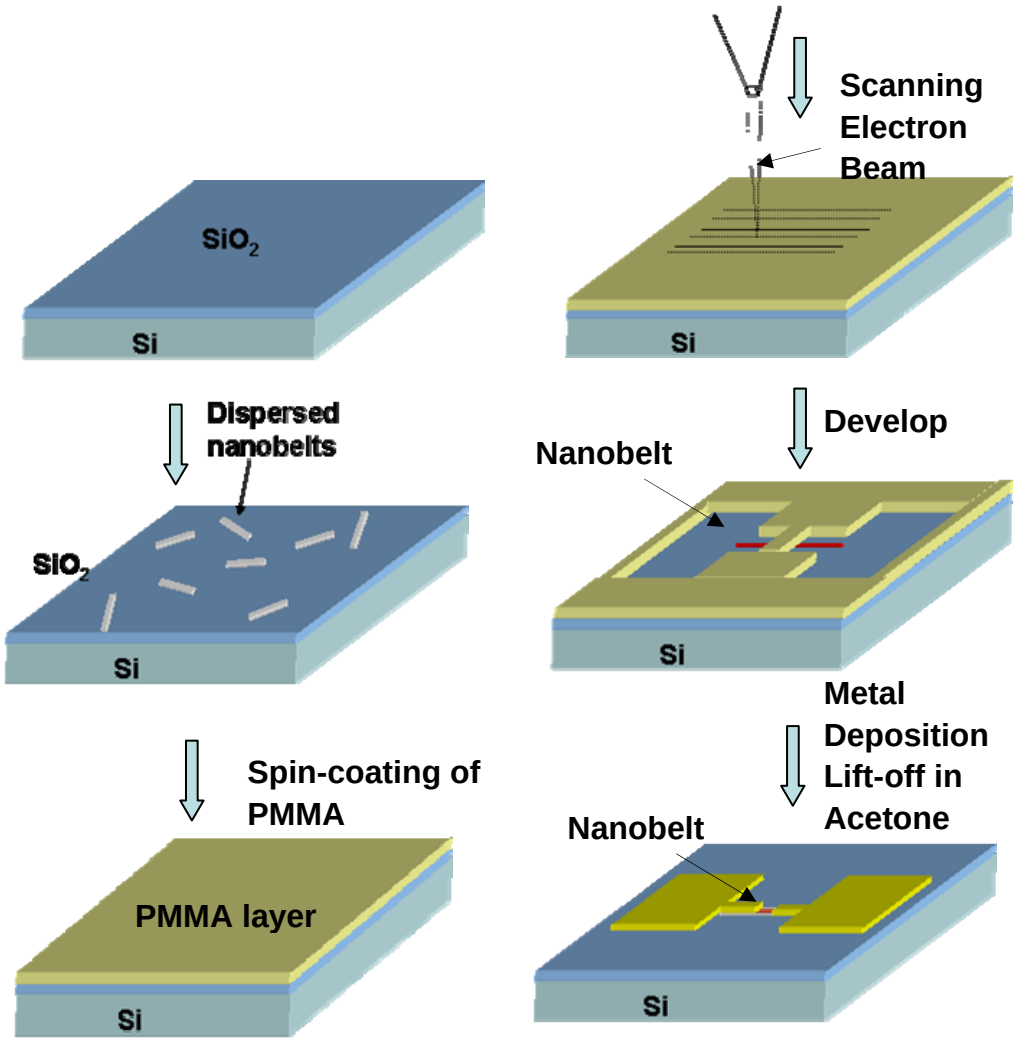

Fig. 3.1 Schematic illustration of E-beam lithography based nano-device fabrication process.

To achieve good enough contact between the electrodes and the nanobelts, double layer deposition was chosen build an Ohmic contact between the metal electrodes and the nanobelts. After above described

processing, a whole Si wafer defined electrodes covered on a single ZnO nanobelt can be achieved as shown in Fig. 3.1.

Electron-beam lithography is the essential basis of nanostructure fabrication at present. Gaussian beam pattern generators or scanning electron microscopes are used with high-energy electrons (100 to 200 keV) and a small electron probe size (1 to 10 nm). Using high resolution and low sensitivity PMMA resist, dimensions down to 30 nm are routinely produced in many research laboratories with high reproducibility. Resolutions down to 4 nm have been demonstrated. The biggest disadvantage of this technology is the large writing time, causing a low throughput that makes electron beam lithography prohibitively expensive for the mass production of integrated circuits.

3.1.2 Focused Ion Beam Lithography

Focused Ion Beam lithography (FIBL) uses a technology called "direct writing" for nanofabrication, which transfers patterns by direct impingement of a small spot of the FIB onto a substrate.[168] Direct writing is comprised of several major approaches, including milling, implantation, ion-induced deposition, and ion-assisted etching, which respectively perform material removal from, property change on, material addition on, and material removal from the substrates with or without chemical assistance. The FIBL could be controlled in a variety of parameters, such

as the beam size, current density, and energy density to remove or add a required amount of material with or without chemical reactions from a predefined location. In this way, high-precision and complex three-dimensional (3D) nanostructures can be created.

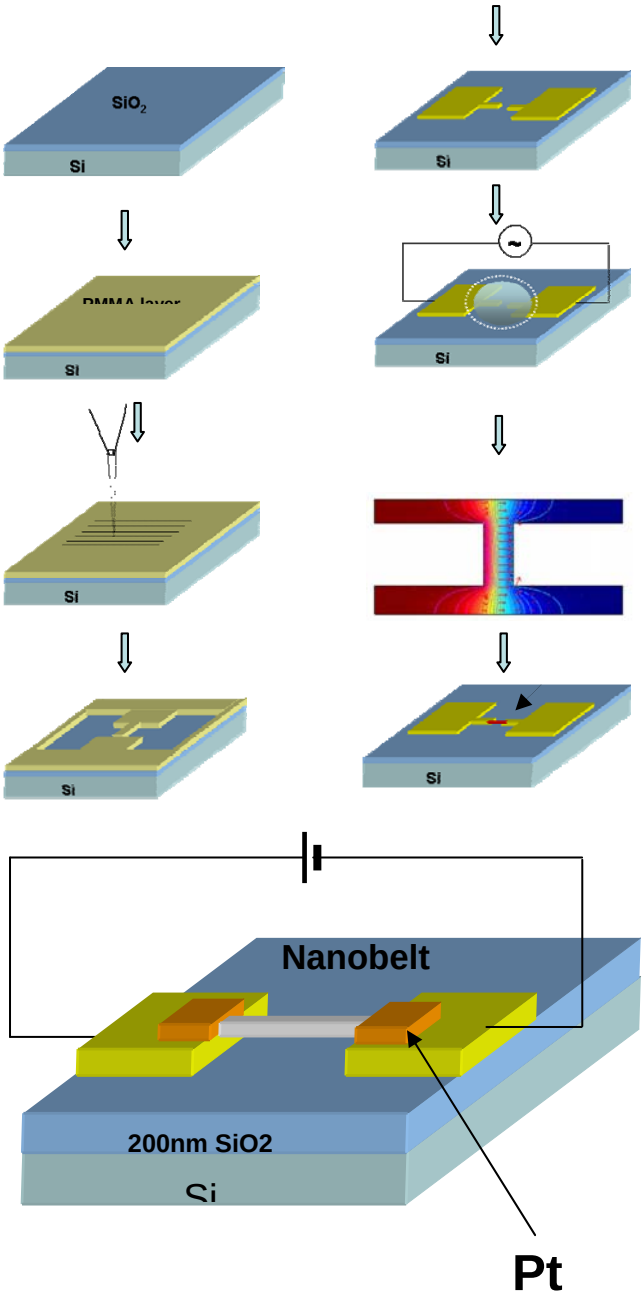

Fig. 3.2 Schematic illustration of Focused Ion beam lithography based nano-device fabrication process.

One of the disadvantages for FIBL is its relatively low processing speed for large scale patterns. However, due to its precise control capability, it is widely adapted to combine with other lithography methods for nanodevices fabrication. Detail process for fabricating a nanowire based devices is shown in figure 3.2. First, an electrode pattern is pre-defined by photo-lithography. This provides a large scale productivity of the required electrodes for fabrication of final nano-devices and largely increases the efficiency of device fabrication process. Then, ZnO nanobelt suspension is prepared with similar method in previous section. This suspension is applied on the pre-defined electrode patterns. In this method, the nanowire aligning across two electrodes are achieved with dielectrophoresis. In the experiment, the electrode pattern is connected to a high frequency power generator (normally, 5V, 1MHz) which will generate an electric field across the electric field. This electric field induces a dipole moment in the ZnO nanobelt in the suspension and force the nanobelt move towards the electrode. This process is illustrated in Fig. 3.2. With precise control of the suspension density, applied signal frequency and amplitude, a single nanobelt based device can be achieved via this dielectrophoresis method. Since the large work function difference of ZnO and Au, the metal used for the electrode patterns, the contact of ZnO nanobelts with Au electrodes are normally very poor. The FIBL is used to deposit a Pt contact pad to enhance the contact of ZnO nanobelts. Although work function difference

of Pt and ZnO is very large, the deposition process of Pt via FIB system induce some impurity to the Pt contact pads which modify the surface states of ZnO nanobelt and make the contact an Ohmic contact. The final devices fabricated via this method is shown in Fig. 3.2.

3.1.3 Summary

Previous introduced lithography methods are two typical ways to fabricate nanowire/nanobelt based devices in our lab. They have both advantages and disadvantages comparing with each other. EBL are more precise and easy control of the process. However the whole process is relatively time consuming. FIBL is a much faster process. But the dielectroporesis process brings some uncertainty with the aligning process. To choose which method depends on the requirement of each experiments.

3.2 Schottky Diodes Based on ZnO Nanobelts

ZnO is an important optical and optoelectronic material. With a large direct band gap of 3.37 eV, together with the piezoelectricity and the pyroelectricity, ZnO is most attractive for applications as field-effect transistor (FET), sensor, and optical electronics. Extensive research on the electronic properties of the nanostructures, especially on ZnO has been performed.[149, 169] To apply ZnO nanostructures on various electronic devices, it is important to understand its transport properties and its interaction with metal contacts.

In this section, we investigated the contact of single ZnO nanobelt with gold electrodes.[170] After investigating the transport properties of over 60 single nanobelt based circuits, a spontaneous formation of Au/ZnO nanobelt Schottky diode has been found in 80% of the samples when nanobelt sizes are well controlled. This effect is likely due to the non-symmetric contacts at the two ends of the nanobelt.

3.2.1 Experiements and Discussions

The ZnO nanobelts to be used for fabricating the FET devices were synthesized through a solid-vapor process in a high-temperature horizontal furnace system.[171] The Au electrode patterns were defined with photolithography on a SiO_2 substrate. The electrodes consisted of two 3 μm wide fingers pointed head to head with a 4 μm distance. These two fingers are connected to two 500×500 μm contacting pads for probe contacts. The as-synthesized nanobelt samples then were placed in ethanol and ultrasonicated for 15 minutes to disperse the bundles into individual nanobelts. A single nanobelt is "placed" across the pre-fabricated electrodes using the dielectrophoresis technique. After applying a droplet of the nanobelt solution onto the electrodes, the electrodes were connected to a 5 V and 1 MHz AC signal, which was chosen for optimizing the alignment of a single nanobelt. This signal generated an alternating electrostatic force on the nanobelts in the solution. Under the electrical polarization force, the nanobelts

were deposited on the electrodes. By precisely controlling the concentration of the nanobelt in the solution, a circuit with only a single nanobelt across the two electrodes has been made (Inset in figure 3.3).

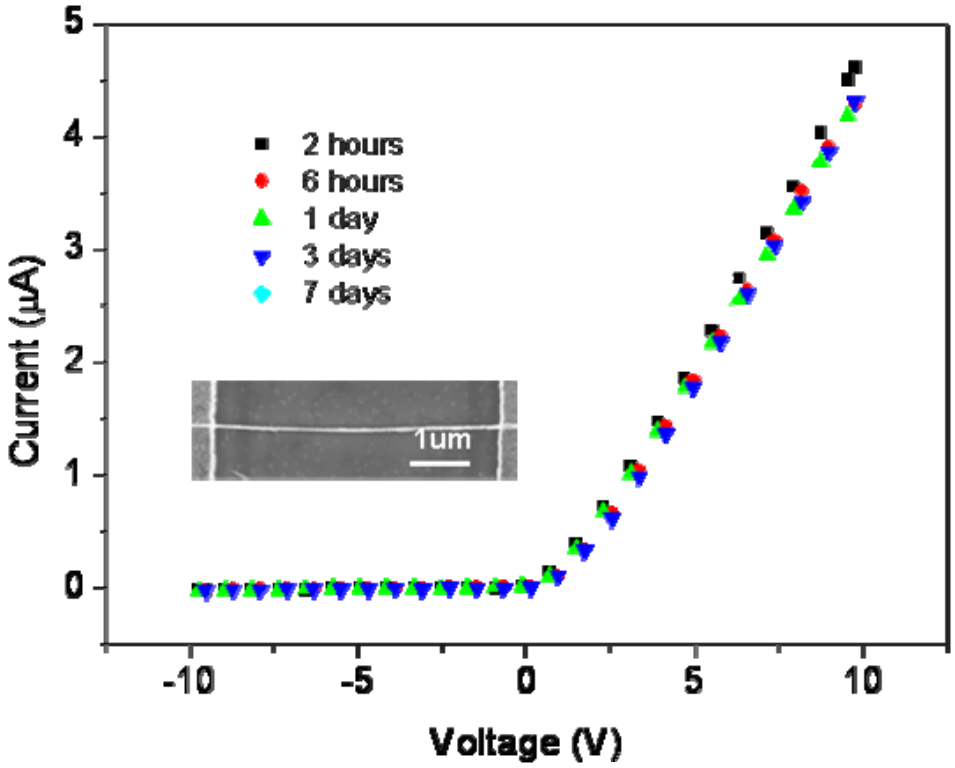

Fig. 3.3 Rectifying IV characteristics of a single ZnO nanobelt lying on Au electrodes at different times after the fabrication, showing the stability of the device. The current ratio at "on" and "off" state is 2000. Measurements were done at room temperature.

The most striking feature is that the IV characteristics of the devices formed by this process displayed a rectifying behavior as shown in figure 3.3. Inset is an SEM image of the electrodes. Data correspond to different measurements of the same devices at different time intervals after the device was made. The last measurement was performed 7 days after the device was exposed to air. It is consistent with the data obtained 2 hours after the sample

was made, showing that the rectifying behavior of the nanodevice is very stable.

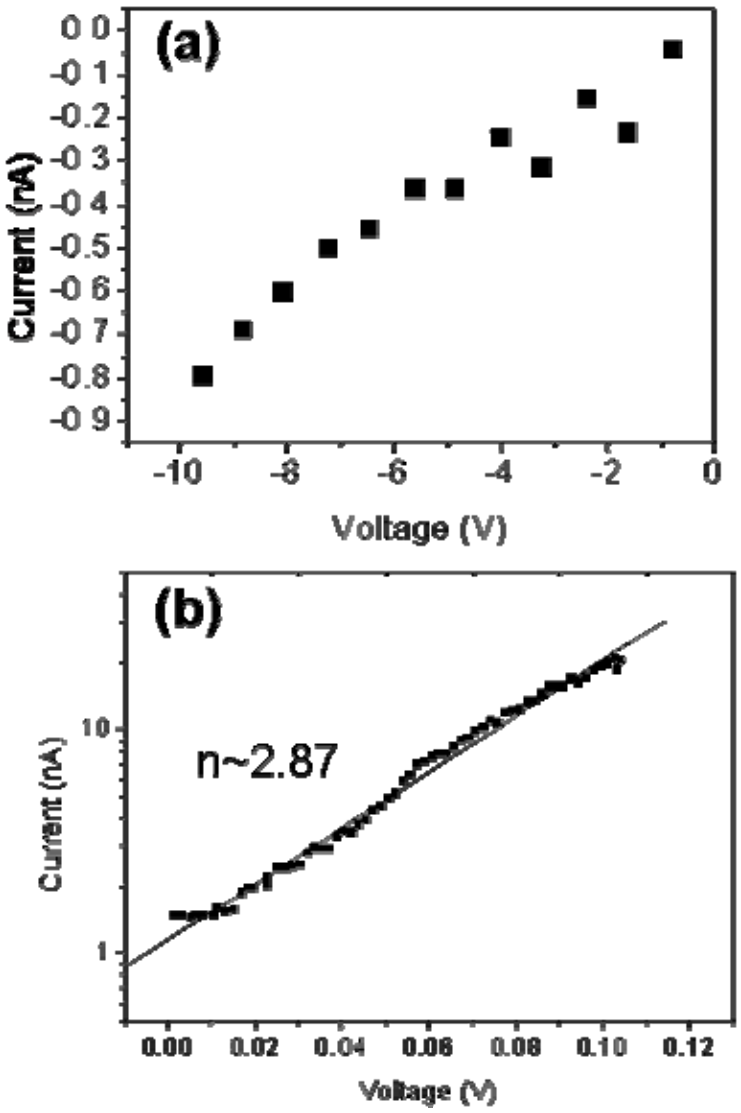

Fig 3.4 (a) Detailed IV characteristic of the Schottky diode under reverse bias. (b) The IV characteristics of the device at forward bias. The line displays the best fit to Eq. 1. Measurements were done at room temperature.

Figure 3.4(a) is the detail inversed current characteristic. At a 10 V reverse bias voltage, the reverse current was only 0.8 nA corresponding to a current density of 10.5 A cm^{-2}. The ideality of the diode can be determined from the forward bias characteristic, as shown in figure 3.4(b). The diode current is

$$I = I_0[\exp[e\frac{V - V_{th}}{nkT}] - 1] \qquad (3.1)$$

where n is the ideality factor that is a quantity for describing the deviation of the diode from an ideal Schottky barrier, for which n = 1; I_0 is the saturation current, V_{th} the threshold voltage, k the Bolzmann's constant, and T the absolute temperature. The ideality factor of the device is determined to be 2.87, larger than one. This higher value of n is probably due to a barrier at the ZnO-Au contact formed during the dielectrophoresis alignment.

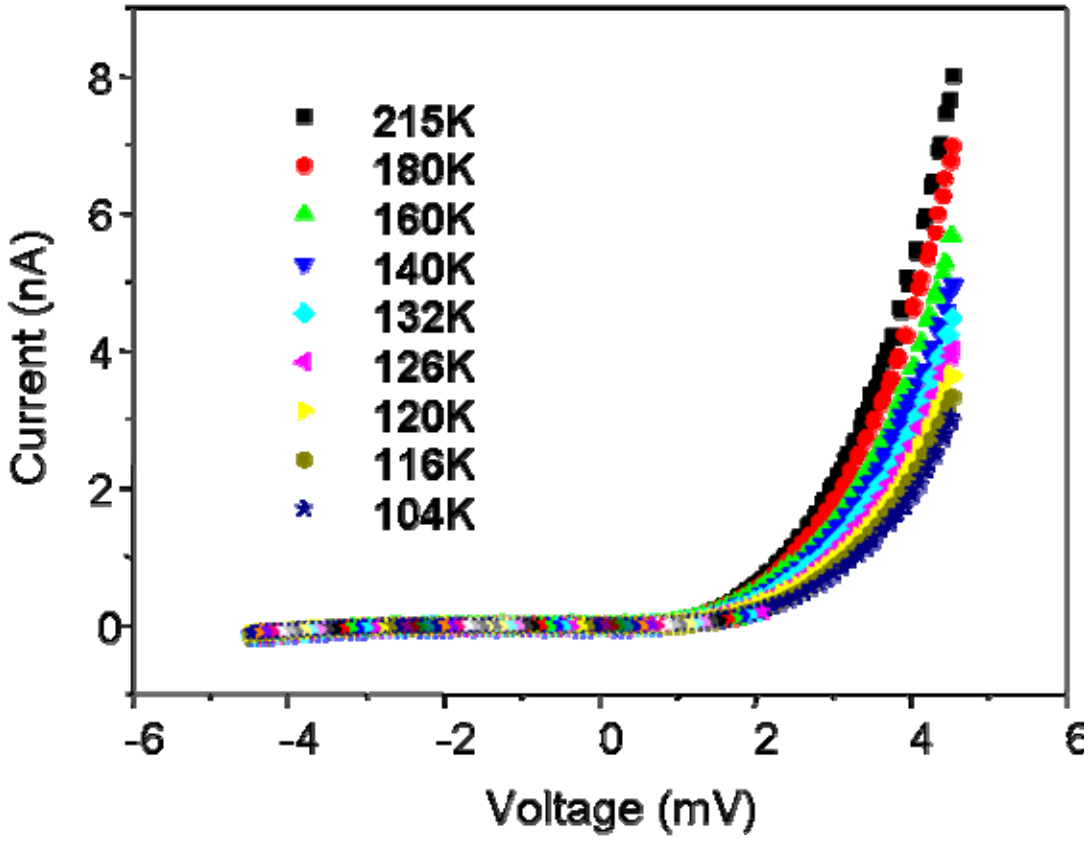

Fig 3.5 IV characteristics of the Schottky diode at different temperatures showing the semiconducting behavior.

The temperature dependence of the diode was measured (figure 3.5). The current under the forward bias decreased with the lowering of the temperature. The resistivity of the nanobelt increased by a factor of two when the temperature decreased from 215K to 104K, showing a typical

semiconductor IV characteristic. When the temperature was below 50 K, the carrier transportation was greatly depressed. The device acted like an open circuit with a resistivity greater than 10^5 Ω-cm.

Table 3.1 IV characteristics of dielectrophoresis aligned nanobelts with different sizes and on different substrates.

Sample	Number of devices with rectifying current	Number of devices with infinity resistance	Number of devices with linear IV
~200 nm wide belts (SiO_2 substrate)	27	7	1
>500 nm wide belts (SiO_2 substrate)	2	17	0
~200 nm wide belts (Si_3N_4 substrate)	7	2	1
Total # of devices	36	26	2

Table 3.1 shows a summary of the IV characteristics of all of the devices we made using ZnO nanobelts. The data show a high reproducibility of the diodes. Devices fabricated on two different substrates, SiO_2 and Si_3N_4 ,were tested. The data showed that there was no obvious difference in the IV characteristics of the devices; so, the influence of the substrate on the rectifying behavior of the devices is eliminated. By carefully controlling of the size of the nanobelts at around 200 nm in width, most of the fabricated devices displayed the rectifying behavior. While for nanobelts with widths greater than 500 nm, the devices showed an infinity resistance under both forward and inverse bias, which is probably due to the bad contacts on both electrodes. Thus, the size of the nanobelts played an important role in determining the contact property of the diodes, the smaller nanobelts have a better contact with the electrodes. . For the nanobelts of ~200 nm in width, the

forward current was as high as 0.5 μA at 1V forward bias, corresponding to a resistivity of 8.74×10^{-2} Ω-cm; the reverse current was around 0.2nA. The on/off current ratio is as high as 2000.

The rectifying behavior of ZnO nanowires was reported previously by Harnack et al.[128] Their studies were for chemically synthesized ZnO nanorods that typically have lower crystallinity and higher density of defects. Their study focused on the electrical behavior of multiple nanowires lying on interdigitated electrodes. By characterizing the IV characteristics of a single ZnO nanobelt/nanowire produced by a solid-vapor process at high temperature, our study has shown the following unique results. The current flowing through the diode is ~0.5 μA at 1 V forward bias, which is about 100 times larger than that reported by Harnack et al. The ideality factor for our devices is ~ 3, which is much smaller than the value, 25, as reported in the ref.[128], indicating a much better performance of our devices.[128]

As proposed Harnack et al., the factor that produces this rectifying behavior could be the alternating zinc and oxygen layers parallel to the basal plane by producing a dipole moment that leads to a potential gradient, and then introduce the asymmetry of current flow along the c-axis. This assumption is given based on the non-central symmetric and layered distribution of cations and anions in the wurtzite structure, and more importantly, the contact is at the top and bottom (0001) surfaces (for nanowires). This is apparently not the case in our experiment because the

contacts are at the same side of the nanowire lying on the gold electrodes (see Fig. 3.6a), and the cation- or anion-terminated surface has no effect unless the contacts are at the top and bottom ends of the nanowire.

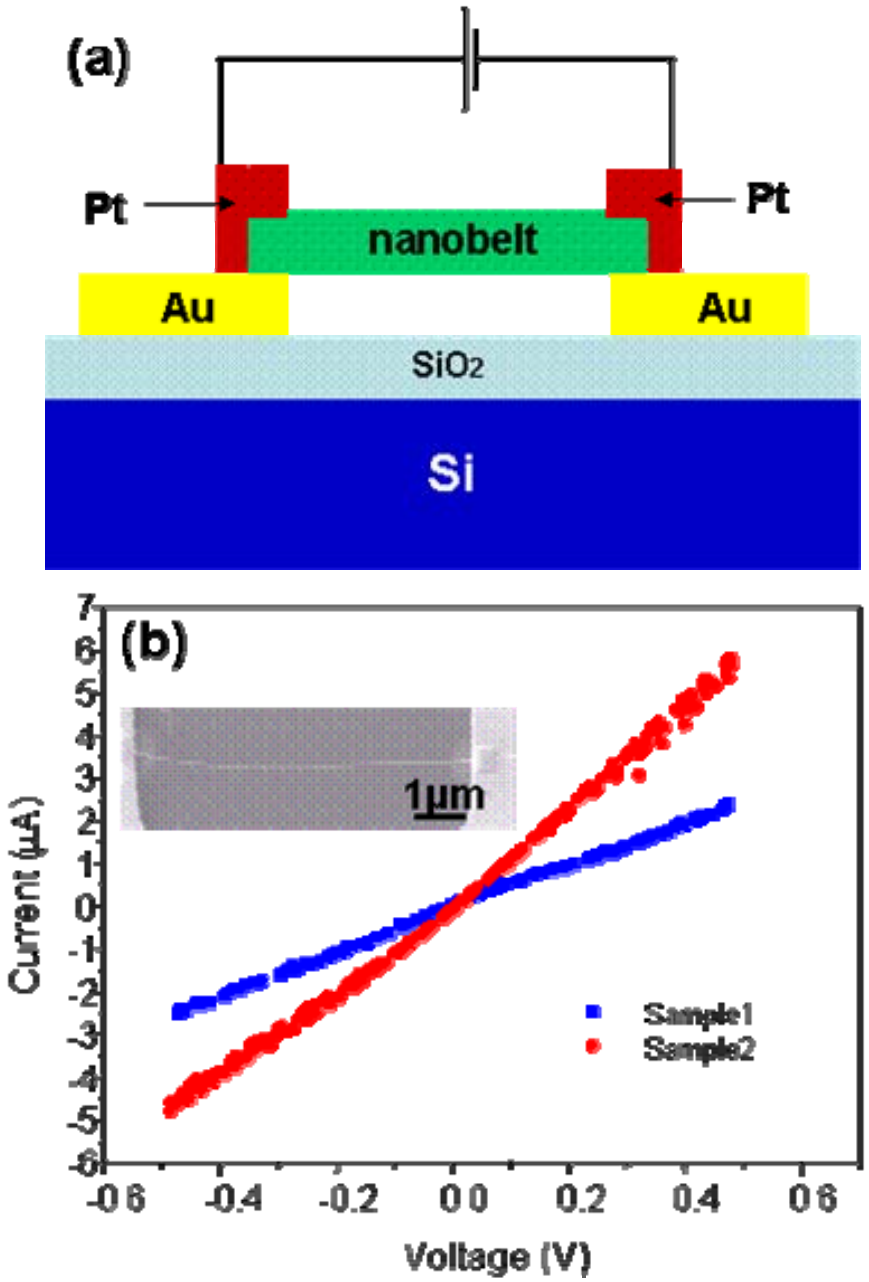

Fig 3.6 (a) Schematic view of the electrode structure after Pt deposition using an FIB. (b) Linear I-V characteristics of the device after Pt deposition. Inset is the SEM image of thedevice after Pt deposition at the two ends.

The diode effect could be a result of the asymmetrical contacts between the ZnO nanobelts and the Au electrodes. To identify the origin of the

rectifying behavior for our case, Pt was deposited using a focused ion beam (FIB) microscope at the contacts between the nanobelt and Au electrodes, as shown schematically in figure 3.6(a). Careful operation was taken to avoid any ion contamination on the nanobelts, so that the change in the IV characteristic is determined solely by the change in contact properties. The devices showed a linear IV curve after the Pt deposition (figure 3.6(b)), indicating the disappearance of the rectifying effect. For a total of over 20 devices deposited with Pt, the current flowing through the nanobelts was greatly increased for 5-20 times. This means that the contact resistance was significantly reduced and the diode effect disappeared after Pt deposition at the contacts. The resistivity of ZnO nanobelt under this condition was measured to be around 6.57×10^{-3} Ω-cm.

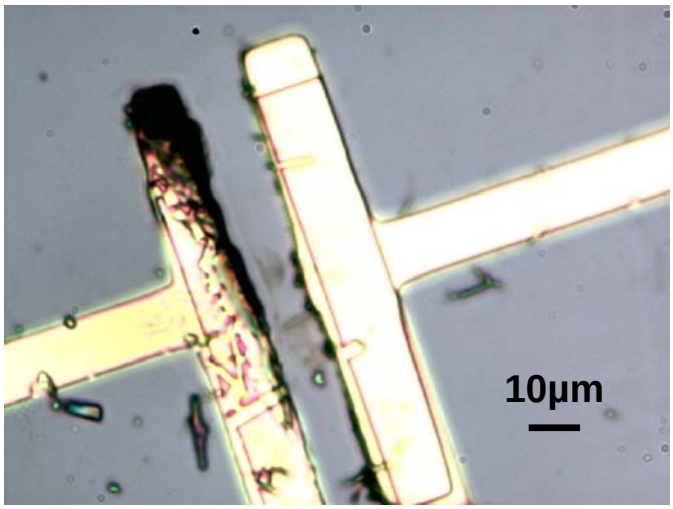

Fig3.7 Optical image of a pair of Au electrodes after dielectrophoresis alignment of the nanobelt at a 5 V 1MHz AC signal.

The linear IV of the nanodevice after Pt deposition proved that the rectifying behavior came from the contact between the ZnO nanobelt and the Au electrode. The ZnO-Au contact is usually the Schottky contact. From this

point of view, an as-fabricated device is composed of two inversely connected Schottky contacts; so, there should be no rectifying behavior if the contacts are symmetric. However, in the dielectrophoresis deposition process, the AC voltage introduces an electrostatic force on the nanobelt; then, the nanobelt moves towards the electrodes until it finally deposits on them. The contacts of both ends of the nanobelt onto the electrodes occur in a consecutive order. We suspect that the side of the nanobelt that touched the electrode first may have firmer contact with the electrode, thus forming a better contact with lower barrier height; while the other end that contacted later had a higher barrier, possibly leading to the formation of the Schottky diode for our devices. In the dielectrophoresis alignment, the heat generated by the AC signal during dielectrophoresis was significant. It produced an asymmetric heating effect in the drain and source areas because of the different barrier height of the two contacts. We have examined this effect, and a typical example is shown in figure 3.7. As shown in the figure, the electrode on the left was molten, while the electrode on the right was left unattained with a 5V and 1MHz AC signal applied. The difference in the heat generated at the two electrodes introduces a different degree of annealing/sintering at the two sides. For the contact on the lower temperature side, the annealing effect was different compared to the other side, indicating a difference in contacts at the two ends. For the side with moderate annealing temperature, a local oxygen vacancy may be created; thus, the local conductivity is enhanced.[172] The contact at

this end with the gold electrode is similar to a metal-metal Ohmic contact. While for the side with higher annealing temperature, the contact was degraded,[127] forming a metal-semiconductor Schottky contact. Then the entire structure is equivalently a Schottky diode.

3.2.2 Summary

In conclusion, rectifying diodes of single nanobelts/nanowires have been fabricated by aligning the as-synthesized ZnO nanobelts/nanowires onto paired Au electrodes using dielectrophoresis alignment. The detail IV characteristics of the Schottky diodes have been investigated. The ideality factor of the diode is ~3. The on- to off-current ratio is as high as 2000. The spontaneous formation of the Au/ZnO nanobelt diodes depends strongly on the sizes of the nanobelts. For the nanobelts with smaller size (~200 nm), the Schottky diodes are preferentially formed. The formation of the Schottky diodes is suggested due to the asymmetric contacts formed in the dielectrophoresis aligning process. Our data show that the single nanobelt/nanowire based diodes can be practically applicable for various applications.

3.3 Ni-doping of ZnO Nanowires

It is highly desired to grow 1D ZnO nanomaterials that have not only controlled shapes and crystal structure but also designed electrical and optical

properties for applications as sensors, field-emitters, p-n diodes, and the diluted magnetic semiconductors (DMS) for spintronics.[173] A key requirement for many of these applications is the doping of ZnO with various elements for enhancing and controlling its electrical and optical performance.

In this section, large-scale Ni-doped ZnO NW arrays are prepared for the first time using a metal vapor vacuum arc (MEVVA) ion source doping technique.[174, 175] By measuring the transport property of a single NW across two electrodes, the electrical conductivity of the doped ZnO NW has been increased for 30 times after doped to a dose of 2×10^{17} cm^{-2}. The photoluminescence (PL) spectrum of the doped ZnO NWs has a red shift, suggesting possible doping induced band edge bending. The doped ZnO NW arrays could be the basis for building integrated nano-scale transistors, sensors, and photodetectors.

3.3.1 Experimental Procedures

In the vapor-liquid-solid (VLS) growth,[176] a nominally 2-nm-thick Au thin film was deposited onto (11-20) Al_2O_3 substrate and served as the catalyst for the VLS growth. The experimental apparatus has been described in a previous study.[177] A mixture of commercial ZnO and graphite powders in a ratio of Zn:C = 4:1 was placed in an alumina boat, which was heated to a peak temperature of 1100℃. The Al_2O_3 substrate was placed at a temperature zone of ~ 800℃ for collecting ZnO nanostructures. After the tube had been

evacuated to a pressure of 1×10^{-3} Torr, the samples were heated to 1100℃ and held at 1100℃ for 60 min with a carrier gas of $Ar+O_2$ flowing through the tube.

Without any treatment, the well-aligned ZnO NWs were directly doped by MEVVA with Ni ion at a dose of 2×10^{17} cm^{-2} and an incident angle of 5° with the vertical NWs (see Fig. 3.8 a), at an extraction voltage of 100 kV and at 200℃. The doped samples were then treated by thermal annealing at 950℃ for 2 hours in O_2 ambient for eliminating the doping-induced defects.

After the annealing process, the substrate-bound NWs were mechanically scrapped off and sonicated in ethanol and deposited on a grid for transmission electron microscope (TEM) characterization. To perform electrical measurements, the NW devices were fabricated by electron beam lithography with lift-off technique. The PL properties of the synthesized NWs were studied at room temperature using a He-Cd laser in the spectral range of 350-800 nm with an excitation wavelength of 325 nm.

3.3.2 Results and Discussion

Figure 3.8b is the well-aligned, Ni-doped ZnO NWs, showing fairly uniform morphology. After the doping process and post- doping annealing, the distribution of Ni dopants and structure of the ZnO NW were studied by TEM in conjunction with energy dispersive x-ray spectroscopy (EDS). Figure 3.8c shows that there are no visible defects, second phase, or precipitation in

the Ni-doped ZnO NWs. It means that, after a proper annealing, the crystal lattice structure of the NW is fully recovered and the dopants are well-integrated into the lattice sites. EDS spectra from a series of locations along one ZnO NW as labeled in Fig. 3.8c are displayed in Figs. 3.8d-g, respectively, and the quantitative elemental distribution in atomic percentage is tabled in Fig. 3.8h. The Zn and O signals of the NWs as well as the Ni signal were observed along the entire length. With consideration the accuracy of the EDS microanalysis, we can conclude that there is ~6 at.% Ni doping in the ZnO NW. The annealing procedure at 950℃ resulted in a fairly uniform distribution of the doped Ni atoms. The corresponding selected area electron diffraction (SAED) pattern from a single doped NW, as shown in Fig. 3.8i, confirms that the NWs has the wurtzite structure and there is no formation of Ni precipitated secondary phase. The crystal lattice structure of the NW has also been examined by high resolution TEM (HRTEM). Both the lattice images recorded from the center (Fig. 3.8j) and the side (Fig. 3.8k) of the NW clearly shows the high crystallinity of the NW with no visible line or planar defects. The diffusion of Ni ion in ZnO and recovery of doped ZnO crystal are most probably due to the high-temperature, long-time annealing as well as ultra large surface area of the NW. Our observed results are consistent with the studies claiming a complete removal of all doping-induced defects in ZnO thin films and the activation of the doped species after annealing.[178]

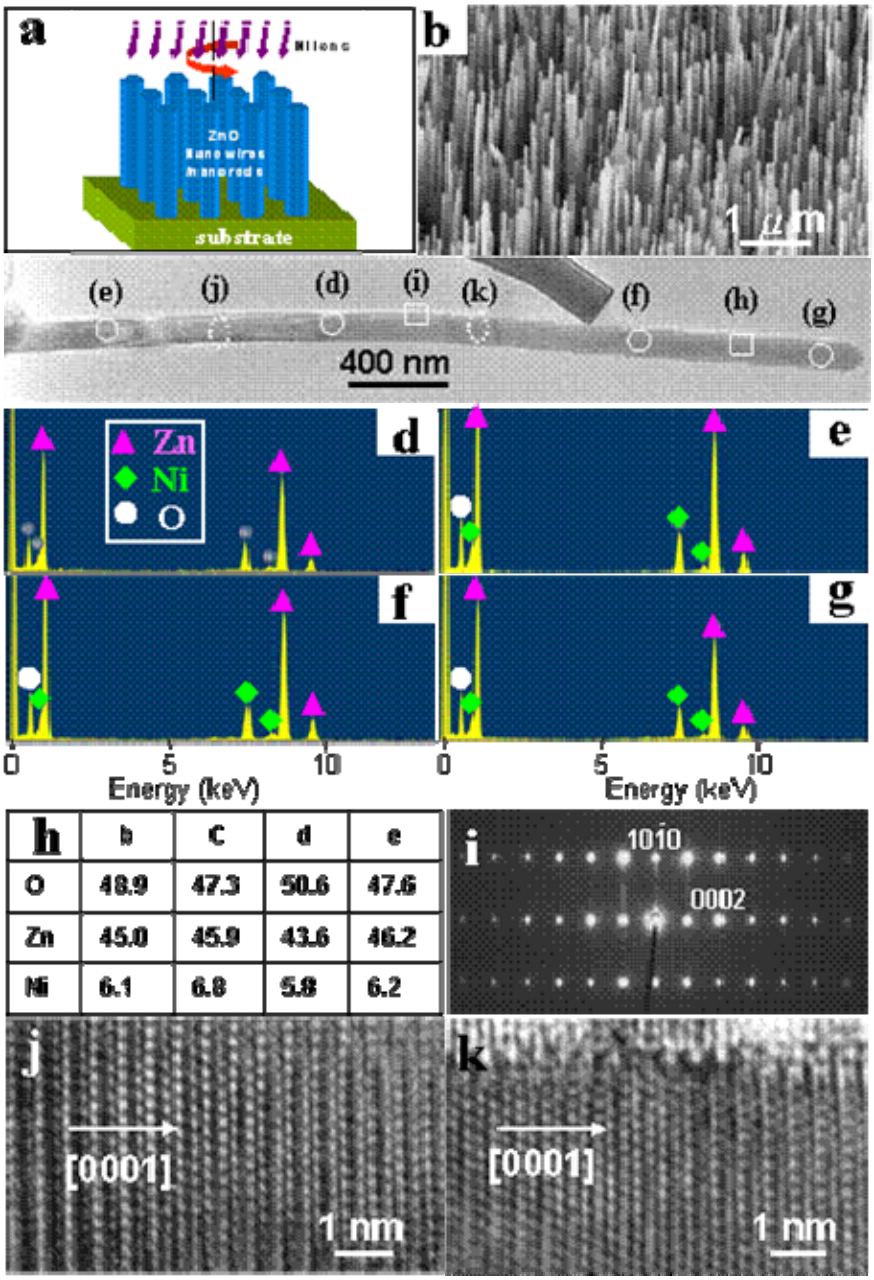

h	b	c	d	e
O	48.9	47.3	50.6	47.6
Zn	45.0	45.9	43.6	46.2
Ni	6.1	6.8	5.8	6.2

Fig 3.8 Electron microscopy characterization of the Ni doped ZnO NW. (a) the schematic setup for ion doping (b) an SEM image of the well-aligned ZnO NWs. (c) TEM image of the ZnO NWs. (d, e, f, g) EDS spectra acquired from the areas labeled with d, e, f and g in (c). (h) The composition (in at.%) distribution along the NW at the labeled positions determined from EDS microanalysis. (i) the corresponding selected area electron diffraction pattern from the NW shown in (a). (j, k) HRTEM images from the outlined areas in (c).

It is known that the as-synthesized and undoped ZnO NWs are the n-type semiconductor due to high density of oxygen vacancies. The typical current–voltage (I–V) curve through a single undoped ZnO NW is given in

Fig. 3.9a. The current changed linearly from about −3 to 3 nA as V was varied from −1 to 1 V with a resistivity ϱ of 390 Ωcm. High electrical resistivity in a single undoped ZnO NW indicates its high quality of crystalline structure with low oxygen deficiencies.[9] This result has been further confirmed by our PL measurement performed on undoped ZnO NWs (Fig. 3.9c). In contrast, the I–V curve for a Ni-doped ZnO NW (Fig. 3.9b) shows a steep increase in conductance, indicating a great enhancement in conductivity by doping. The current of the doped NW changed from about −75 to 75 nA as the voltage V was varied from −1 to 1 V, and the resistivity drops to 12 Ωcm. For thin films, doping of cations of higher valence state than Zn (Zn^{2+}) into ZnO, such as In, Ga, and Ni, leads to an increase in the electrical conductivity.[2] Referred to the pure undoped ZnO NW, the doped Ni enhances the conductivity probably due to the presence of trivalent Ni^{3+} cations. A Ni^{3+} cation would contribute a hole carrier.

Figure 3.9c shows PL spectra of ZnO NWs before and after doping. The UV emission peak centered at 389 nm for the Ni-doped ZnO NWs, which exhibits a red shift of 5 nm compared to the 383 nm observed for the undoped ZnO NWs. The red shift is likely due to the bending at band edge. This result is similar to the Ni-doped ZnO thin film.[179] The ion doping may result in a weaker UV emission peak. From Fig. 3.9, a weak broad band is observed at ~ 510 nm for both undoped and doped NWs. This feature is commonly observed for ZnO, which is attributed to oxygen deficiency.

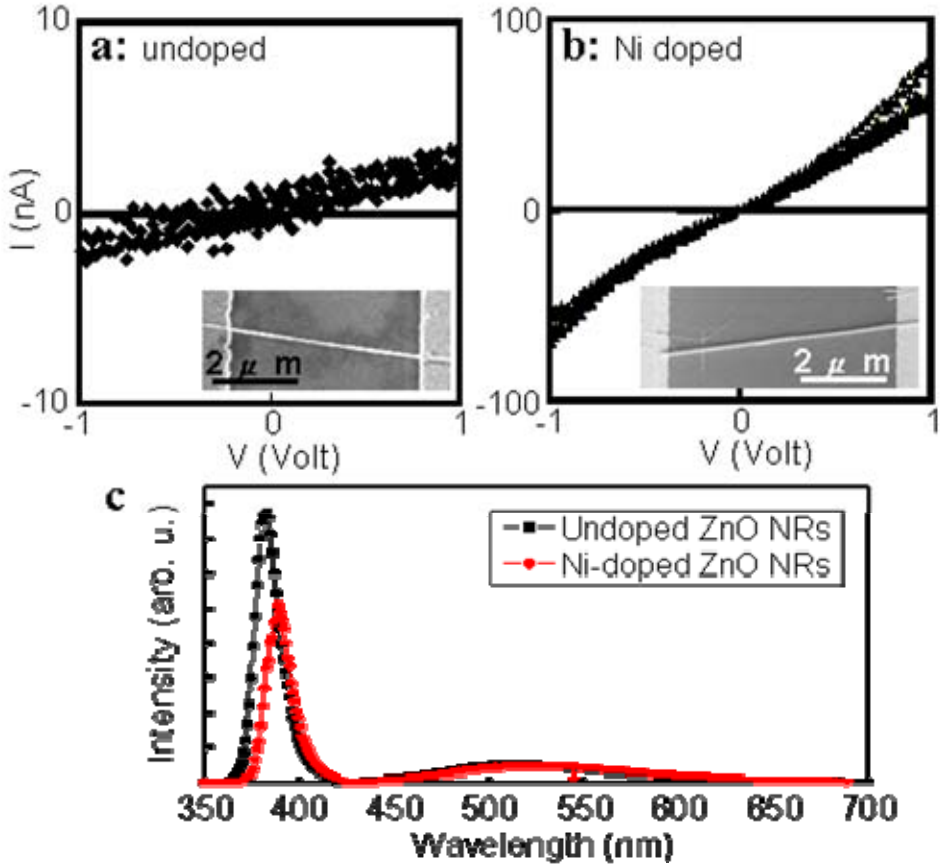

Fig. 3.9 I-V characteristics of an (a) undoped ZnO NW and (b) a Ni-doped NW measured by repeatedly scanning the bias from −1 to 1 V. (c) A comparison of the PL spectra for the undoped and Ni-doped ZnO NWs.

3.3.3 Conclusions

In summary, we show that by combining VLS growth and MEVVA doping, well-aligned Ni-doped ZnO NWs were obtained. After a proper annealing, the doped NWs have high crystallinity and little defects. The electrical conductivity was enhanced for over 30 times after doping. A red shift in PL peak of Ni-doped ZnO NWs was also observed. This research demonstrates a new approach for preparing aligned and doped NW arrays

that have much improved electrical performance, which could be important for fabricating arrays of sensors, transistors and photodetectors.

3.4 RuO_2 and RuO_2-TiO_2 Core-shelled Nanowire Transport Properties

For the core-shelled structures, extensive research has been performed for systems such as Ge/Si,[180] GaN/AlN/AlGaN,[181] Ta_2O_5/SiO_2, Fe_3O_4/MgO,[182]. The Ge/Si core-shelled NW, for example, is a high performance field-effect transistor due to the reduced carrier scattering. For the GaN/AlN/AlGaN core-shelled NW exhibits a high electron mobility. For Ta_2O_5/SiO_2 core-shelled structure, the confinement of propagation for light along axial can effectively reduce the energy loss owing to the different reflective index between Ta_2O_5 and SiO_2. Recently, the RuO_2 NWs have been synthesized using pure Ru as metal target under different flux ratio of O_2/Ar in a reactive sputtering system. Also, core-shelled TiO_2 and RuO_2 structure was achieved by reactive sputtering, in the present study, we mainly focus on the investigation of physical properties of the RuO_2 NWs. For the RuO_2- TiO_2 core-shelled structure synthesized by reactive sputtering, the detailed epitaxial relationship and electronics structures are investigated.[183]

3.4.1 Nanowire Growth and Crystal Structure

Figure 3.10(a) shows an SEM image of RuO_2 NWs synthesized by reactive sputtering approach at synthesis temperature of 450 ℃ for 3 h, indicating the high density and uniform RuO_2 NWs with the length to be more than several microns. In addition, most of the RuO_2 NWs have a square cross-section, as shown in inset of Fig. 3.10 (a). The corresponding XRD spectrum, as shown in Fig 3.10 (b), confirms the phase of NW is of RuO_2 with lattice constants of a = 0.45 nm and c = 0.31 nm. After deposition of TiO_2 thin layer via reactive sputtering deposition system, as shown in Fig. 3.10 (c), the morphology of these NWs still remains, but the sizes increase. The corresponding XRD spectrum of the NWsis is shown in Fig. 3.10 (d). It is hard to distinguish the individual peaks originated from both the RuO_2 and TiO_2 owing to the fact that the lattice mismatch between RuO_2 and TiO_2 is less than 2-5 %. The undistinguishable peaks from XRD results may indicate that the core and shell have an epitaxial relationship. TEM analysis is required to reveal the details.

Figure 3.11(a) shows TEM image of a RuO_2 NW with a diameter of 105 nm. The corresponding diffraction pattern with [110] zone axis is shown in the inset in Fig. 3.11 (b), indicating the [001] growth direction (c-axis). From the high resolution TEM image, as shown in Fig. 3.11 (b), two d values of 0.32 and 0.31 nm, which are consistent to the $(1\bar{1}0)$ and (001) planes can be found, respectively. In addition, average diameter of RuO_2 NW are found about 110 nm by examining a lot of RuO_2 NWs via TEM image.

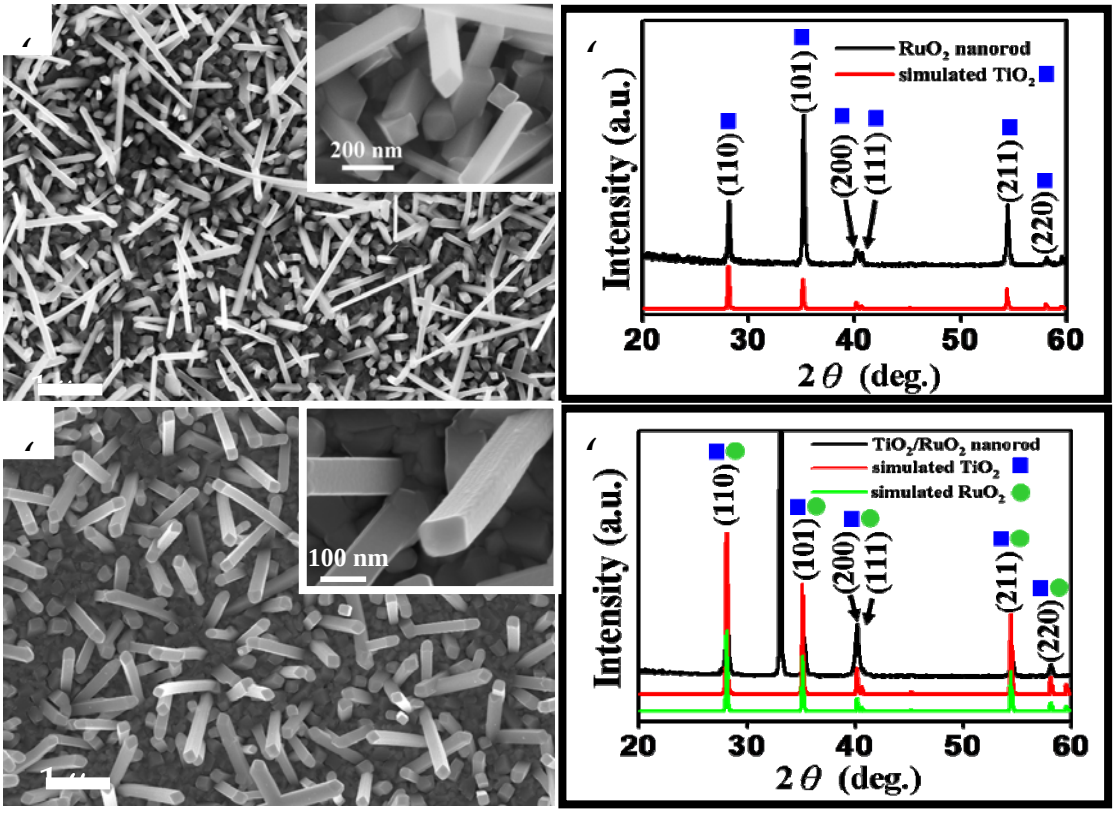

Fig. 3.10 a) SEM image of RuO_2 NWs synthesized by reactive sputtering at 450 °C for 3 h. The inset shows a magnified SEM image of RuO_2 NWs. b) XRD spectrum of the RuO_2 NWs. The marked spectrum shows the simulated result. c) SEM image of the RuO_2/TiO_2 core/shell structure. The inset shows the corresponding magnified SEM image. d) XRD spectrum of the RuO_2/TiO_2 core/shell structure. The marked spectra represent the simulated results.

A TEM image of a RuO_2 NW core-shelled with TiO_2 layer is shown in Fig. 2(c), where two different image contrasts can be distinctly found. Figure 3.11 (d) shows a high resolution TEM image taken from the interface region between TiO_2 and RuO_2, and the inset in Fig. 3.11 (d) shows the corresponding diffraction pattern. The epitaxial relationship between TiO_2 and RuO_2 is $(110)_{TiO2} \,||\, (110)_{RuO2}$ and $[1\bar{1}0]_{TiO2} \,||\, [1\bar{1}0]_{RuO2}$, However, some mismatch dislocations can be found at the interface of TiO_2 and RuO_2 by selecting the symmetric $\pm(1\bar{1}0)$ diffraction beams using Fourier filtering. Three edge dislocations are created very close to each other within $(1\bar{1}0)$ planes

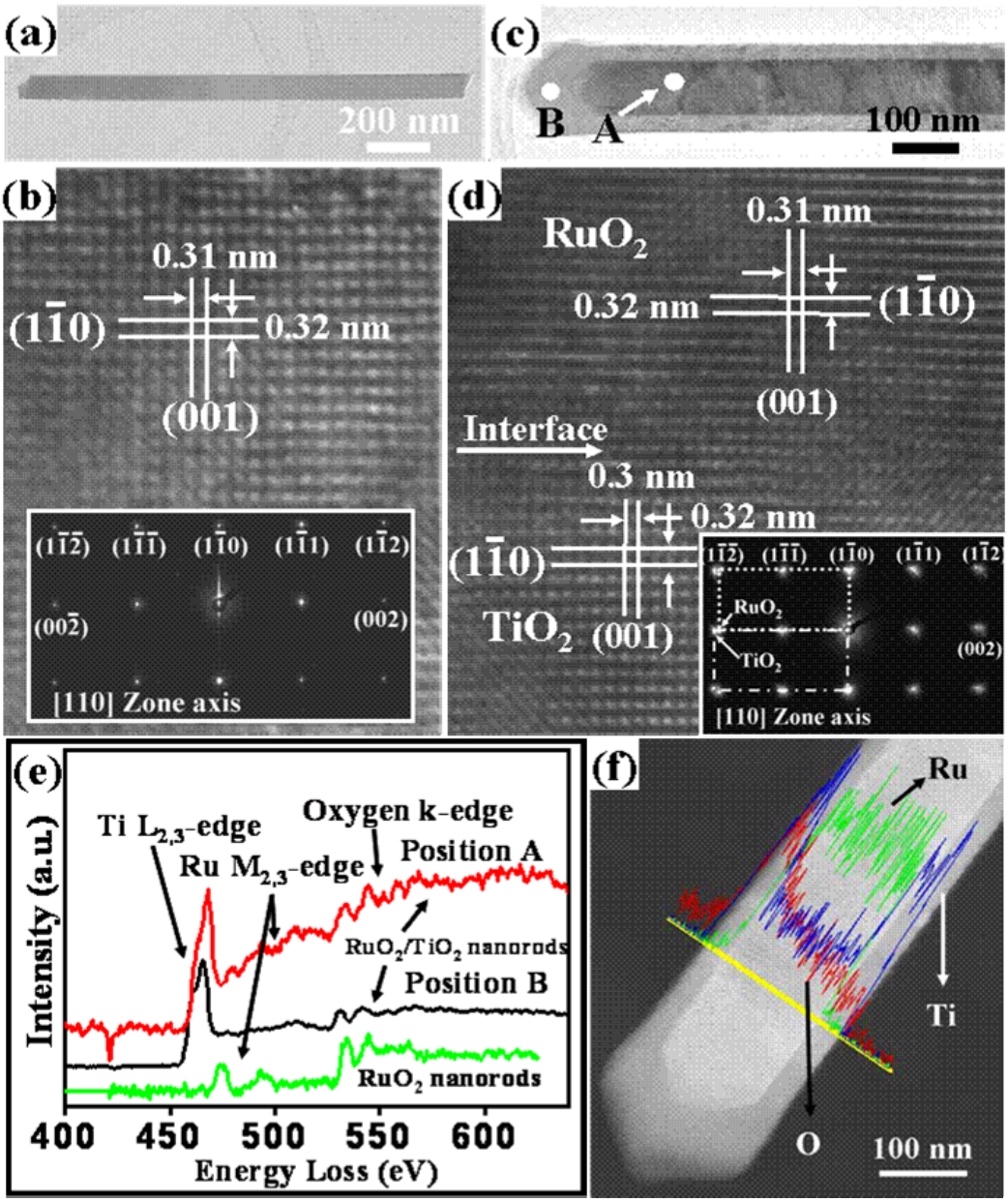

Fig. 3.11 a) TEM image of a RuO_2 NW with a diameter of 105 nm. b) The corresponding high-resolution TEM image. Two *d*-spacings of 0.32 and 0.31 nm are identified, which is consistent with the (11¯0) and (001) planes, respectively. The inset shows the diffraction pattern with [110] zone axis, indicating that the growth direction of RuO2 is along [001]. c) TEM image of a RuO_2/TiO_2 core/shell structure with a diameter of 160 nm. d) HRTEM image of the RuO_2/TiO_2 core/shell structure taken from the interface between TiO_2 and RuO_2. The corresponding *d*-spacings and planes are indexed and identified. The inset shows the diffraction pattern of which the two matrixes deviated from TiO_2 and RuO_2 are displayed. e) EELS spectrum for the Ti L-edge and O K-edge ELNEFS of the RuO_2/TiO_2 core/shell structure recorded from two points, labeled A and B for the RuO_2 core and the TiO_2 shell, respectively. The bottom EELS spectrum was acquired from a RuO2 NWas reference. f) The corresponding HAADF image of a RuO_2/TiO_2 core/shell structure. The distribution of Ru, Ti, and O are shown.

owing to the 5% lattice mismatch. The average diameter of the RuO_2- TiO_2 core-shelled NWs is 160-170 nm.

The electronic and chemical structures of the NW were examined by EELS, which is sensitive to the unoccupied valance band. All of the raw data acquired by EELS have been calibrated in an energy scale by the zero loss peak and deconvoluted by the low loss region to reduce the multiple-scatting effect. Figure 3.11 (e) shows the EELS spectra recorded from selected positions, labeled as A and B for the RuO_2- TiO_2 core-shelled structure in Fig. 3.11 (c). For a comparison purpose, the EELS spectrum shown at the bottom in Fig. 3.11 (e) was taken from a RuO_2 NW without TiO_2 coating. For the EELS from the TiO_2 shell (position B), Ti $L_{2,3}$ edge and Oxygen K-edge energy loss near edge fine structure (ELNES) are evidently found. In the spectrum acquired from position A, the M-edge of Ru is present. The EELS result indicates the presence of the core-shell structure. This confirmed by a line-scan chemical mapping across the NW. Figure 3.11 (f) shows the high-angle annular dark-field (HAADF) image for this TiO_2/RuO_2 core-shelled structure with the corresponding EDS line scan. The different image contrast and different element distribution across the whole NW confirm the core-shelled structure.

3.4.2 Electric Transport Properties

RuO_2 NWs may be a potential candidate as interconnect. For the I-V characteristic, all the NWs are aligned between two Au electrodes via

dielectrophoresis technique and Pt is deposited as the top electrode to make the perfect contact by focus ion beam (FIB) microscopy. A LabView program was used to control the I-V testing process. Although, the work function of RuO_2 (4.87 eV) is smaller than that of Pt (5.6 eV), a linear curve found in I-V cure, as shown in Fig. 3.12(a). This is likely to be the result of the metallic behavior of RuO_2 NW. By examining several different I-V curve of RuO_2 NW, the resistance is found at the range of 0.4-1.2 kΩ at room temperature. In addition, the resistivity of these RuO_2 NWs are measured to be 215-640 μΩ-cm by taking the diameters and lengths of these RuO_2 NWs into account as provided by SEM observation, which is consistent to the reported resistivity of 40-482 μΩ-cm for RuO_2 thin film.

The results of durability and reliability test of the RuO_2 NW were obtained by performing I-V measurements under a high applied voltage, as shown in Fig. 3.12(b). The NW can endure a current of up to 3.3 mA before failure, corresponding to a current density of 4×10^7 Acm^{-2}. The failure point occurs in the middle of the NW, as shown in inset of Fig. 3.12(b). The possible reason of failure is attributed to self-heating, which is consistent to NiSi, FeSi, $TaSi_2$ metallic NWs. In comparon to other metallic nanowries, such as NiSi NWs (3×10^8 Acm^{-2}), CNT (10^9 Acm^{-2}), $TaSi_2$ (3×10^8 Acm^{-2}), FeSi (1.6×10^7 Acm^{-2}) and Pd NWs (2×10^6 Acm^{-2}), the current density carried by RuO_2 NW is reasonably good. It is possible to use it as interconnects.

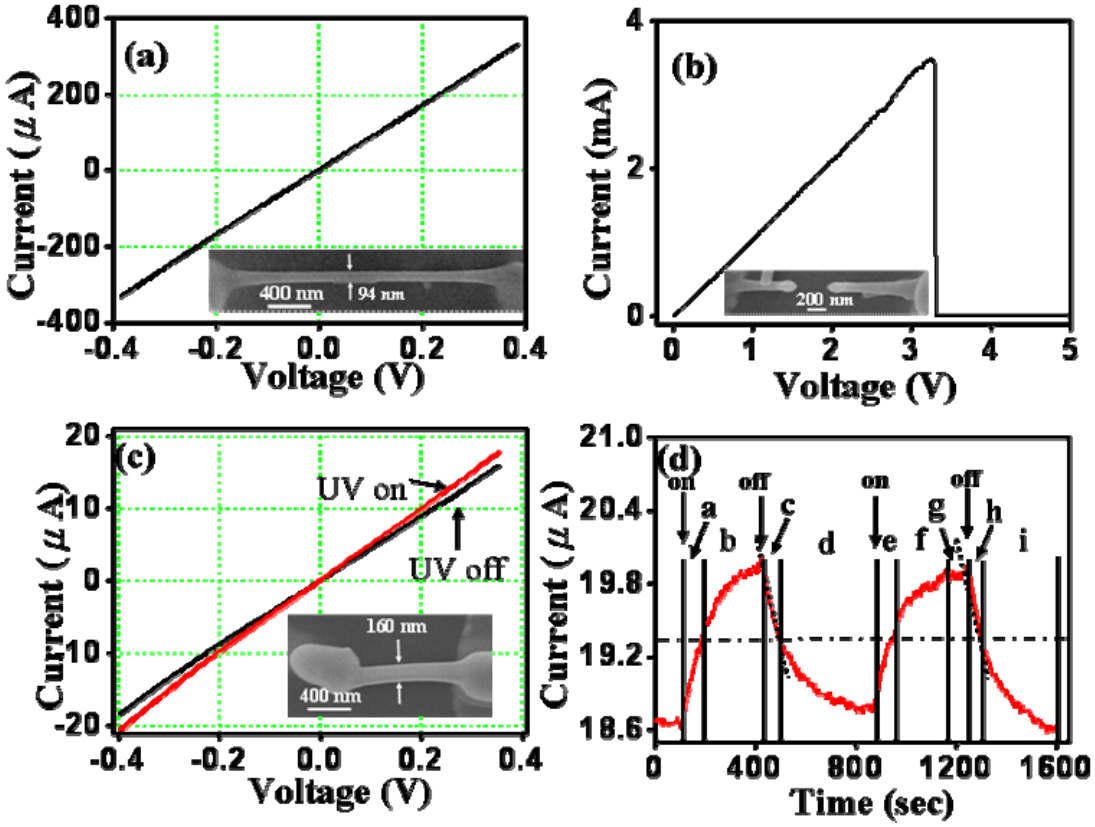

Fig. 3.12 a) *I–V* curve for a RuO_2 NW at room temperature. b) The *I–V* curve recorded at a high applied voltage. c) The *I–V* curve for RuO_2/TiO_2 core/shell structure with and without UV illumination. d) The current as a function of the UV illumination time.

3.4.3 Photoconductivity

TiO_2 has been extensively studied on its photo-catalyst behavior because it can catalytically decompose volatile compounds under UV light. It is well known that the thinner NWs may further enhance the sensitivity of the devices owing to increased surface-to-volume ratio. Here, we investigate the photoconductivity of the RuO_2-TiO_2 core-shelled structure under the UV illustration of 256 nm (4.9 eV), which is strong to excite the electron-hole pair near band edge. For the photoconductivity measurements, all the devices are excited by UV light with the wavelength of 256 nm. For contact issue, the

contact metal we used in this present was Pt with a work function of 5.6 eV that is smaller than that of TiO_2 (7.3 eV), so that the contact between Pt electrode and TiO_2 was ohmic. The corresponding I-V curve without UV illustration via two-terminal probes measurements, as shown in Fig. 3.12(c), demonstrates a linear behavior, confirming the ohmic contact feature. Inset in Fig. 3.12(c) shows the SEM image of RuO_2-TiO_2 core-shelled structure with the diameter of 160 nm and length of 1.5 μm. As a result, the effective resistively at room temperature for the NW is calculated to be ~ 0.044 Ω-cm, which is much smaller than that of pure TiO_2 thin film (2 MΩ-cm), The resistivity is decreased to 0.032 Ω-cm after UV light has been turned on for 8 min. In addition, the I-V curve as a function of UV illustration time is shown in Fig. 3.12(d), where the externally applied voltage along the NW was fixed at 0.4 V and individual response time for UV on/off is tabulated in table 2. The current of TiO_2/RuO_2 core-shelled structure was fast increased from 18.5 μA to 19.4 μA within 88 sec (area a) and then increased slowly to get saturated current of 20 μA within 219 sec (area b) during the first illustration of UV light. After the UV light was tuned off, the current drastically decreased from 20 μA to 19.4 μA within 52 sec (area c) and then decreased very slowly to original value (dark current) within 385 sec (area d). The second time illustration of UV light was done so as to confirm the previous results. The current fastly increased from 18.5 μA to 19.4 μA within 87 sec (area e) and started to reach the saturated value of 20 μA within 222 sec (area f) after the second UV light was

turned on. Noting that the UV light was kept on for 101 sec (area g) so that a plateau at maximum current of 20 μA was maintained. After the second UV light was off, the current dropped fast from 20 μA to 19.4 μA within 47 sec (area h) and returned to its original value (dark current) within 350 sec (area i). In general, TiO_2 can be considered as an N-type semiconductor, which is caused by the oxygen deficiencies. However, the surface absorption of water molecules can terminate the oxygen deficiencies (vacancies) on the surface of TiO_2 in a form of polar water molecules by physisorption process and followed by chemisorption process to form hydroxyl bonding (OH-), which retards the transport of electrons inside the TiO_2 if the nanowrie is exposed to atmosphere.[184] In addition, the oxygen molecules can absorb the electrons and terminate the oxygen vacancies as well.[185] Both water and oxygen molecules can form the space charge region (SCR), namely, depletion region to influence the conductance that make the conduction and valance bands near the surface of TiO_2 shell to be bent upward.[186] Once the electron-hole pairs are generated by UV light near the band edge of TiO_2, the photo-generated electron-hole pairs will proceed in two possible distinct processes: removal of absorbed oxygen species (O2, O^{2-}, and O_2^-) and water species (H_2O, OH^-) in SCR (depletion region). and increasing net carrier density to enhance the conductance.

Noting that current in decay rate (52 sec for first illustration and 47 sec for second illustration) is faster than that in increased rate (88 sec for first

illustration and 87 sec for second illustration). It is due to the fact that the water and oxygen molecules are very fast to absorb and accumulate to surface via physisorption and chemisorption because of the larger surface to volume ratio, resulting in drastic drop in conductance as the UV light is begun to turn off. This fast absorption can be confirmed at PL spectra where the highest intensity of peaks at 426 nm (2.9 eV) are resulted from the shallow traps (F, F^{+}, and F^{++}) caused by absorption of oxygen atoms on the surface. Once the oxygen defect sites on surface of TiO_2 shell is gradually decreased, the extra molecules have to diffuse much dipper into the TiO_2 shell to find the available oxygen defected sites and capture more electrons.[187] As a result, this diffusion behavior of absorbant will become the dominant reaction processes to slows down the whole absorption processes. This is why the decay of the current via absorption is fast at first and then become very slower (385 and 340 sec after first and second UV illustrations are off).

On the other hand, noting that the surface barrier caused by absorption can be suppressed when the nanowires is smaller than a critical diameter, resulting in causing less band upward on the surface.[188] Consequently, it can be expected that SCR should be created within the whole TiO_2 shell to decrease the surface barrier height (less band upward on the surface) caused by absorption of foreign molecules due to the fact that the average thickness of TiO_2 shell is about 25 nm. It can enhance the probability of recombination between photo-generated electron-hole pairs and foreign absorbed molecules

to increase the conductance when the UV light is on. Once the most of molecules are totally removed, probability for absorption via physisorption and chemisorption by extra foreign molecules on the surface of TiO_2 will be gradually increased because reaction between clear surface and foreign molecules begins more favorable. It means that the behavior desorbed by photo-generated electron-hole pairs and absorbed by foreign molecules needs to be balanced, resulting in the slowly saturated currents at the latter I-V characteristic before the saturated current is reached when the UV light is on.[187] However, other parameters, such as different intensity of UV light, energy of UV light (different wavelength of UV light), ambient gas, measured temperature, different thickness of TiO_2 shell will influence photocurrent characteristic as well. The more details regarding these parameters are needed more time to figure out in the future. Hence, we only demonstrate the advanced application of TiO_2/RuO_2 core-shelled structure on photoconductivity.

3.4.4 Summary

In conclusion, we have investigated the microstrucutre and electronic structure of RuO_2 NWs and RuO_2- TiO_2 core-shelled NWs using high resolution TEM and EELS. The TiO_2 layer is epitaxially grown on the surface of RuO_2 NW and the two exhibit the same crystal orientation. The elastic modulus of the RuO_2 NW was measured to be 113-390 GPa using AFM. The

elastic modulus of the RuO_2-TiO_2 core-shelled NWs can be understood using an effective medium model. The PL analysis of the RuO_2-TiO_2 core-shelled structure indicates its potential for applications in opto-electonics. For RuO_2 NW, the resistance at room temperature was found to be 0.4-1.2 kΩ with a resistivity of 215-640 μΩ-cm. In addition, the maximum current density before breaking down was measured to be 4×10^7 Acm^{-2}. Furthermore, the photoconductivity of the RuO_2-TiO_2 core-shelled structure under UV light has been studied. Our research indicates that the RuO_2 based NWs and relevants are a good candidates for interconnects and optoelectronics.

3.5 Electric Transport of $NH_4V_3O_8$ Nanobelts

Vanadium oxide and their derivated compounds have attracted much attention due to their outstanding structural flexibility combined with chemical and physical properties,[189] and also because of potential applications in areas such as catalysts,[190] high-energy lithium batteries,[191] chemical sensors, electrical and optical devices.[192, 193] Recently, various methods have been developed to synthesize the nanobelt materials of vanadium oxide[194] and their derivated compounds.[195] However, only limited kinds of single-crystal vanadates with 1-D nanostructures are obtained until now, and the synthesis of new-type nanobelts remains challenging. Herein, we report the synthesis, electrical transport measurements and conduction mechanism study of a novel nanostructure: $NH_4V_3O_8$ single crystalline nanobelts. This is likely to be

the first report on the electrical transport measurements on individual nanobelt of multiple vanadate and a propose about their conduction mechanism.[196]

3.5.1 Experimental Process

In a typical synthesis procedure, ammonium metavanadate (1.50 g) was dissolved in distilled water (90 ml) to form a light yellow clear solution. Hydrochloric acid was added dropwise to the ammonium metavanadate solution until the final pH of the solution was about 1.5 under stirring. A clear orange solution was formed and then transferred into a 100-mL Teflon-lined autoclave with a stainless-steel shell, which was maintained at 180℃ for 36 hours and then cooled to room temperature. The final yellow precipitate was collected and washed with distilled water three times to remove other residues and then dried in air at 80℃ for 8 hours.

Figures 3.13 a-c show low magnification SEM image, EDS spectrum and high magnification SEM image of $NH_4V_3O_8$ single crystalline nanobelts, respectively, and reveal that the resulting products is composed mainly of belt-like nanostructures with well-defined facets. As shown by the arrowheads, the rectangular ends of the belt-like materials can be seen clearly. The width and thickness of the nanobelts are in the range of 80-180 and 50-100 nm, respectively, with typical lengths up to tens of micrometers. Energy

dispersive X-ray spectroscoy (EDS) further confirms the presence of N, V and O (H cannot be detected by EDS).

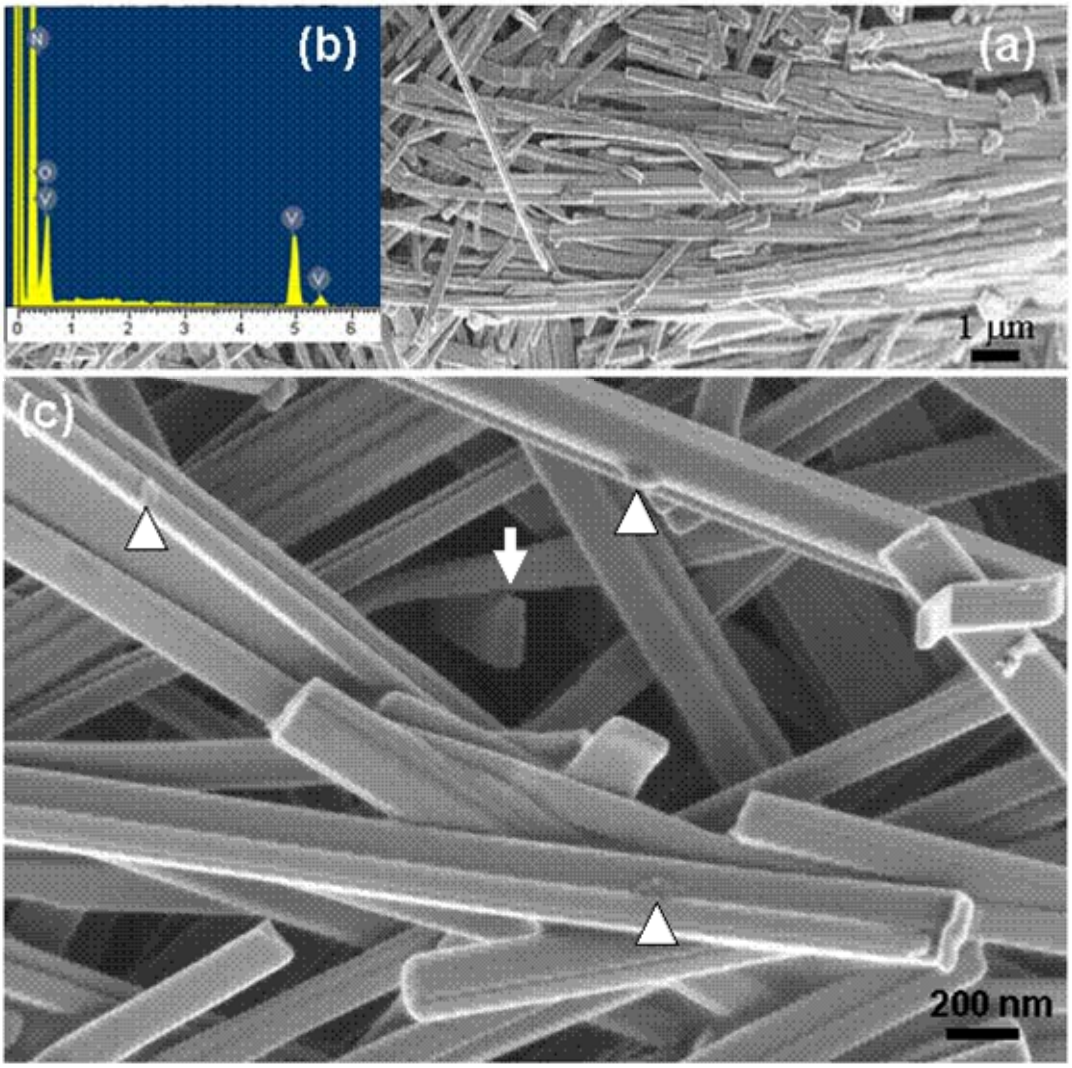

Fig. 3.13 Low magnification SEM image (a), EDS spectrum (b) and high magnification SEM image (c) of $NH_4V_3O_8$ nanobelts. In (b), the arrowheads indicate the rectangular ends of the nanobelts, the circles mark the bent or twinned nanobelts and the triangles show some bulk and surface defects.

The basic reaction we employed for the synthesis of the $NH_4V_3O_8$ nanobelts can be formulated as follows:

$$6NH_4VO_3+4H^+ \rightarrow (NH_4)_2V_6O_{16}+4NH_4^++2H_2O \quad (3.2)$$

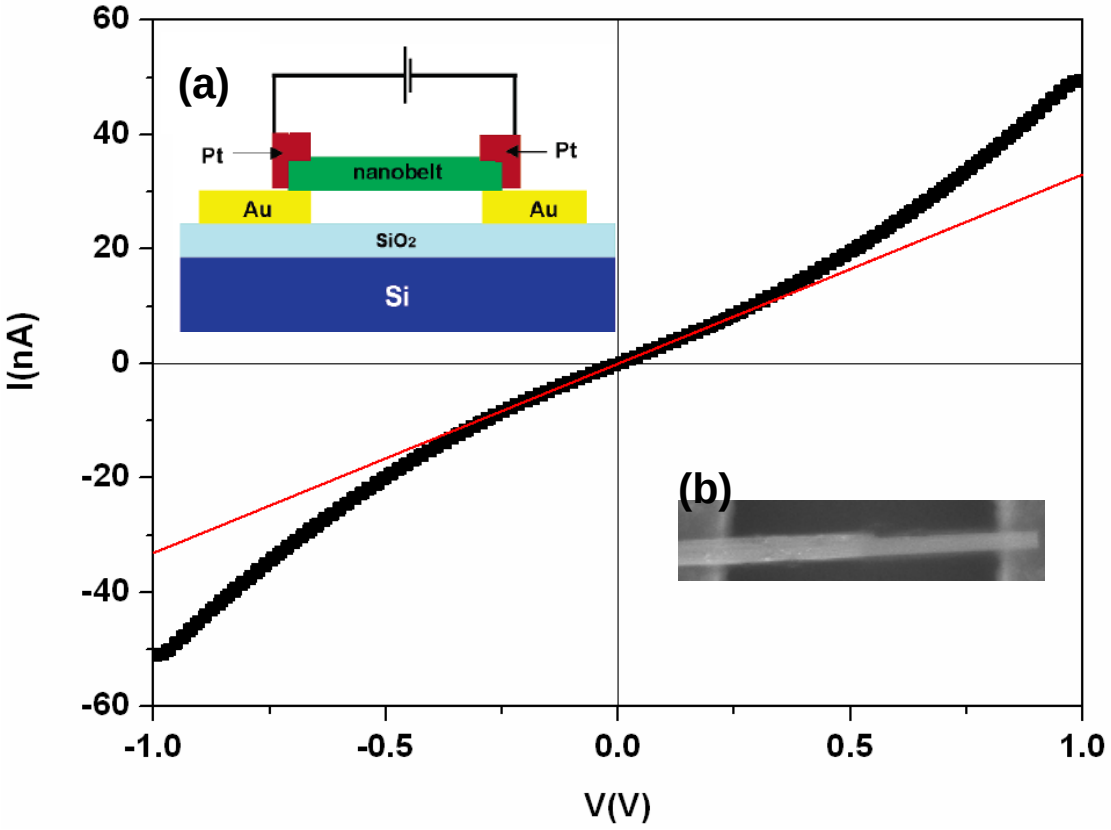

Fig 3.14 I-V curve of individual nanobelt. The inset A and B show schematic view and the SEM image of the individual nanobelt electrode, respectively.

In this process, ammonium metavanadate in aqueous solution forms NH_4^+ and VO_3^-. As the temperature increases, metavanadate groups start to agglutinate into VO_4 tetrahedra chains, in which the tetrahedral are connected by sharing corners. When the reaction proceeds to a certain extent, the tetrahedral chains coalesce to form VO_5 pyramid sheets bridged by H_2O between vanadium ions, in which pyramids are connected at corners or edges, and NH_4^+ inserts between VO_5 pyramid sheets, resulting in the formation of $(NH_4)_2V_6O_{16}\cdot 1.5H_2O$ nanobelts. Owing to the existence of NH_4^+ between VO_5 pyramid sheets, the nanobelts are expected to have good electrical conductivity so that they may be used as nanosensors.

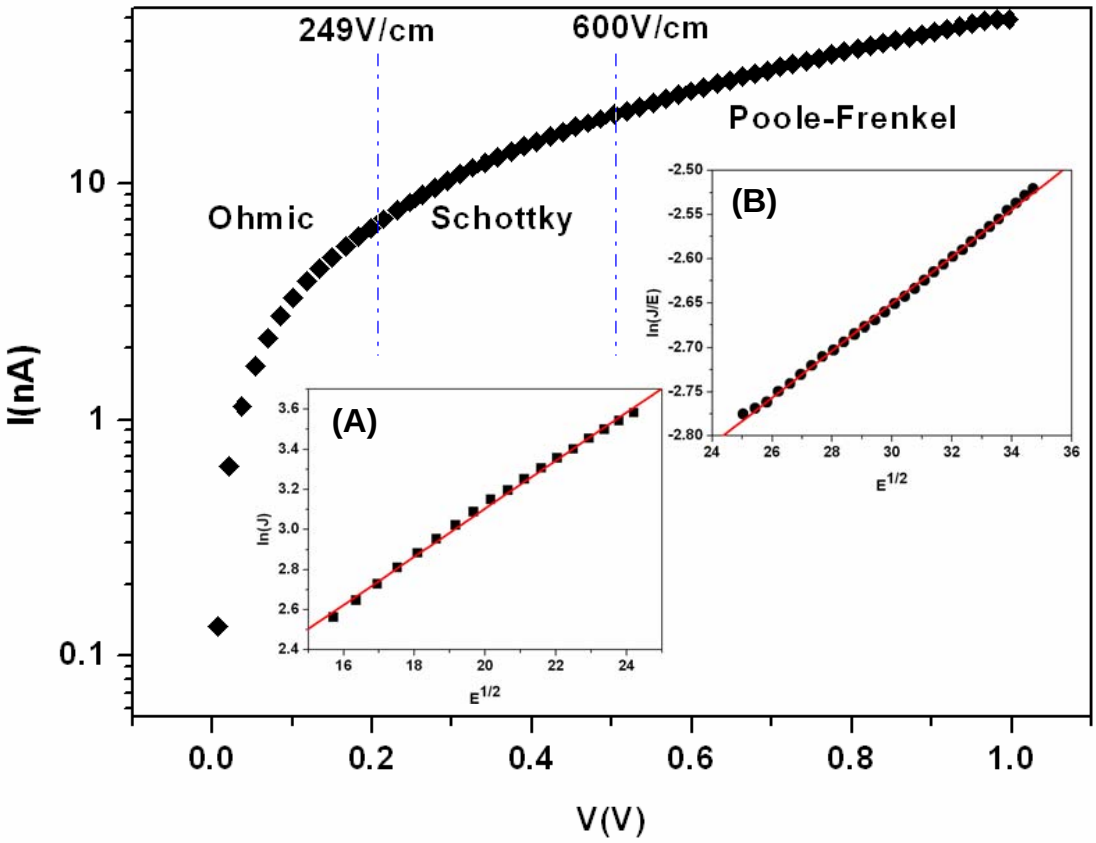

Fig 3.15 The positive part of the I-V characteristics of the transversal system, rebuild as a function of log (I). Inset A and B show the experimental plot of ln(J) versus $E^{1/2}$ at the electric field between 249 and 600 V/cm, and the experimental plot of ln(J/E) versus $E^{1/2}$ at the electric field more than 600 V/cm.

We have built the contacts using e-beam lithiography for measuring the electrical transport along a single nanobelt. The I-V curve of a single $NH_4V_3O_8$ nanobelt at room temperature is shown in Figure 3.14. Schematic view and the SEM image of the individual nanobelt electrode are shown in the inset A and B of Figure 3.14, respectively. With a contact resistance of about 10 MΩ, the effective length and cross-section of the sample is approximately 8×10^{-4} cm and 500×100 nm^2, respectively, so we can deduce the conductivity value of ~0.2 S/cm, and this value can range from 0.1 to 1 S/cm, depending on the samples.

Notably, the $NH_4V_3O_8$ nanobelt sample exhibits nonlinear, symmetric current/voltage (I/V) characteristics. In order further study the electrical conduction mechanism, we have simulated the I-V curve. It is found that the obtained characteristic is symmetrical and behaves linearly for electrical field lower than 249V/cm. This behavior may be explained by the ohmic mechanism of conductivity in the low electrical field (<249 V/cm). A further increase in the applied voltage results in an exponential behavior in the current mechanism. Since the thickness of the nanobelt is more than 50 nm, the tunnel current can be ignored. Figure 3.15 presents the positive part of the I-V characteristics of the transversal system, rebuilt as a function of log (I). The aim of this plot is to analyze the conduction mechanism in higher fields (enlarged voltages). The logarithm of the current density is plotted against the square root of electric field [ln(J) versus $E^{1/2}$] as shown in the inset A of Figure 3.15. The straight-line nature obtained at a medium electric field between 249 and 600 V/cm implies the Schottky emission. The Schottky current density is expressed as follows:

$$\ln J = \frac{\beta_{SE}}{kT}\sqrt{E} + \left[\ln(AT^2) - \frac{q\phi}{kT}\right] \tag{3.3}$$

where A is a constant, ϕ is the Schottky barrier height, q is the electronic charge, k is Boltzmann's constant and E is the electric field. The constant β_{SE} is given by

$$\beta_{SE} = \sqrt{\frac{q^3}{4\pi\varepsilon_0\varepsilon_r}} \tag{3.4}$$

where ε_r is the dielectric constant, ε_0 is the permittivity of the free space. The dielectric constant obtained from the slope (ε_r =132.1) is consistent with that obtained from the C–V technique (ε_r =131.6).[197]

Interestingly, with the increase of electrical field, the experimental data fit well to the Poole-Frenkel mechanism. Unlike the Schottky mechanism, defined by thermo-electron emission of the free charge carriers, the Poole-Frenkel transport is defined by emission from structural defects in energetic traps. A straight line (see the inset B in Figure 3.15) is obtained at a high electric field (>600 V/cm) in the experimental plot of ln(J/E) versus $E^{1/2}$. This suggests that the leakage current is dominated by the P-F conduction mechanism at a relatively high electric field. The expression for the P-F current density is as follows:[198]

$$\ln\left(\frac{J}{E}\right) = \frac{\beta_{\mathrm{PF}}}{\xi kT}\sqrt{E} + \left(\ln C - \frac{q\phi}{\xi kT}\right) \qquad (3.5)$$

where $q\phi$ is the ionization potential in eV, which is the amount of energy required for the trapped electron to overcome the influence of the trapping centre when no field is applied, $\beta_{\mathrm{PF}}\sqrt{E}$ is the amount by which the trap barrier height is reduced by the applied electric field E, C is a proportionality constant and k is the Boltzmann constant. The coefficient ξ is introduced in equation (3.5) for taking into account the influence of the trapping or acceptor centres ($1 < \xi < 2$). [23] When $\xi = 1$, the conduction mechanism is termed as normal P-F effect, whereas it is termed the P-F effect with compensation or

the modified P-F effect when ξ = 2. In this case, the semiconductor contains a non-negligible number of carrier traps. The P-F constant, β_{PF}, is given by

$$\beta_{PF} = \sqrt{\frac{q^3}{4\pi\varepsilon_0\varepsilon_r}} \quad (3.6)$$

where ε_0 is the permittivity of the free space and ε_r is the dynamic dielectric constant. The dielectric constant (ε_r =129.3) obtained from the slope of the straight line in the Poole–Frenkel plot also corresponds to that obtained from the *C*–*V* technique.[197] The $NH_4V_3O_8$ nanobelts are found to have some bulk and surface defects, as shown by triangle in Figure 3b. Therefore, the Poole-Frenkel emission in this case is the preferable mechanism that agrees with the results described in the reference.[199]

3.5.2 Conclusions

In summary, we have demonstrated a facile environmentally friendly route to synthesize pure $NH_4V_3O_8$ single crystal nanobelts at a large scale by hydrothermal treatment of aqueous solutions of NH_4VO_3 under acid condition. Such nanobelts grow along the direction of [010]. The widths, thicknesses, and lengths of the nanobelts are in the range of 80-180 nm, 50-100 nm, and tens of micrometers, respectively. The conductivity of one individual $NH_4V_3O_8$ nanobelt is estimated to be 0.1~1 S/cm at room temperature with a dielectric constant of ~130. Based on small polaron hopping, the dominant conduction mechanism is due to ohmic mechanism at low electric field below 249 V/cm, due to Schottky emission at medium electric field between 249 and

600 V/cm and due to the Poole–Frenkel emission mechanism at high field above 600 V/cm. It is anticipated that the novel $NH_4V_3O_8$ single crystalline nanobelts with high conductivity may have unique applications in nanoelectrodes or nanosensors.

3.6 Summary

Electrical transport properties study of nanobelts and nanowires is of great importance for nanobelts and nanowires characterization, electrical signal based device applications, and the investigation of unusual transport phenomena arising from one-dimensional quantum effects. Important factors that determine the transport properties of nanobelts include contact properties, material composition, surface conditions, and crystallinity. In previous section, transport properties of different nanowires are demonstrated and discussed. Detailed analysis reveals the intrinsic transport phenomena that are critical in the device application. Schottky diode, nonlinear transport properties, and Ni doping effects are investigated.

CHAPTER 4

FUNCTIONALIZATION STUDY OF ZnO NANOWIRES

To further improve the device performance and extent their potential applications, ZnO NWs are surface functionalized by different molecular species and polymers. Surface modification and functionalization are one of the widely used methods to enhance the electric transport properties of different 1D nanostructures, which is also adapted to the ZnO nanowire based devices here.[200-204] Due to the special physical and chemical properties of the attached chemical species, these surface coated ZnO NBs demonstrates unique and interesting properties in many applications.

In practical applications, most sensing devices require control of interfacial properties, e.g., the gas sensors need the surface of nanostructures to be highly sensitive to selective adsorption. For biomedical application, there are more requirements on the materials such as biocompatibility for specific application environment, bioinert ability that allows the materials to survive in biofluid environment, etc. The interfacial properties can range from straightforward adhesion between different materials, to direct modification of surface functional group of one material by another at an interface.[28, 64, 205-214]

As mentioned previously, physical attachment and chemical adsorption are two basis mechanisms for surface functionalization. In this chapter,

based on the physical adsorption in terms of electrostatic force and Van der Waals force, we investigated the possibility of polar surfaces of ZnO nanostructures to be selectively functionalized, the biocompatibility of ZnO nanostructures in several biological buffers, and also protein attachment on ZnO nanostructures surface.

4.1 Molecular Surface Functionalization

The self-assembled thin molecular-layer has demonstrated the effectiveness in modifying surface physics and properties of metal and metal oxide materials. It acts as a functional group in different nanowire based devices for chemical and biological sensing.[215] In this section, we explored a novel approach of using self-assembled thin monomolecular-layer on surface for improving the electrical and optoelectronic performances of NWs and NBs. A few kinds of molecules were tested and their performances were compared. With the molecular coated ZnO NBs, the contact properties and the carrier mobility were greatly enhanced. More importantly, the optical and gas sensing performance of these small organic molecule functionalized ZnO were also greatly enhanced. These processes have demonstrated an easy and effective method for improving the performance of the NW/NB-based devices.[216]

4.1.1 Functionalization of ZnO Nanobelts

Our study has been focused on ZnO NBs synthesized by a vapor-solid process. Various types of carboxylic acids self-assembled molecules with different terminal groups (such as stearic acid, lysine, dodecanedioic acid, mercapto-acetic acid and perfluorotetradecanoic acid) were used to treat the ZnO NBs. The chemical structures of the acids are shown in Figure 4.1a.

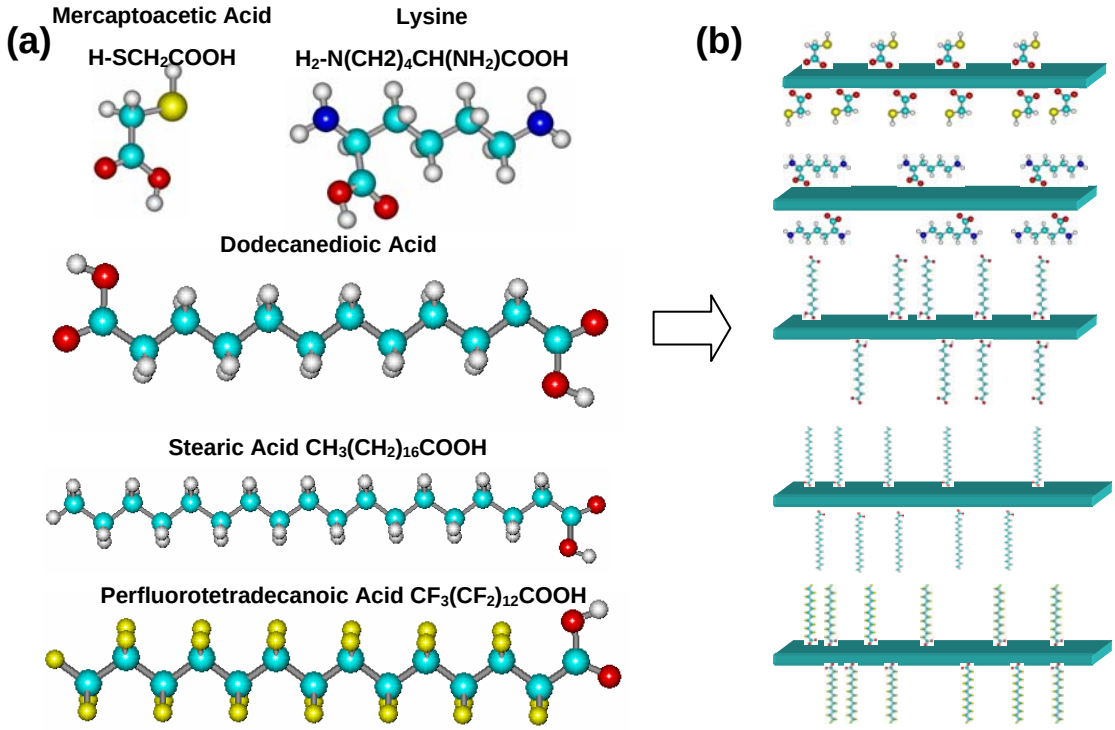

Fig. 4.1 (a) Molecular structures of the five molecules used for surface functionalization. (b) Schematic models of the molecule functionalized ZnO NBs.

The functionalization was achieved by grafting the –COOH group onto the surface of ZnO, and the surface properties of ZnO were tailored with different functional groups. The molecular solutions were prepared by dissolving the acids into an ethanol solution with a concentration of 5 mM. Then a small piece of ZnO NB samples was immersed into the solution. After

treating the samples at room temperature for 24 hours, the ZnO NBs samples were removed from the solution and rinsed with ethanol in order to remove excess un-reacted molecules. After drying the ZnO NBs, the contact angle of a deionized (DI) water droplet on a film made of NBs was measured by a goniometer (Rame-Hart Co.). Table 4.1 shows the results of the contact angle measurement of the treated samples.

Table 4.1. Contact angles of ZnO NBs film after acid treatment

Samples	Average contact angle
Stearic acid	112°
Lysine	56°
Dodecanedioic acid	58°
Mercapto-acetic acid	52°
Perfluorotetradecanoic acid	115°

As can be seen from the Table, lysine, dodecanedioic acid, mercapto-acetic acid treated substrates showed low contact angles (more hydrophilic), while stearic acid and perfluorotetradecanoic acid treated surfaces showed high contact angles (more hydrophobic). The difference indicates the successful coating of the thin layers of molecules on ZnO NBs as shown in Figure 4.1b. For lysine, dodecanedioic acid, mercapto-acetic acid, the hydrophilic terminal groups (-NH_2, -COOH and –SH) contributed to the reduced contact angles. On the other hand, stearic acid and perfluorotetradecanoic acid possess hydrophobic terminal groups (-CH_3, -F), which lead to the high contact angle.

These molecules modified ZnO substrates changed their surface energies and physical properties that could have a profound influence in their sensing properties.

4.1.2 Increased Electric Conductivity

Single NB based transport measurement was carried out using the functionalized NB by a special handling process to eliminate surface contamination and/or damage to the passivation layer. The electrode pattern was designed to have a few parallel electrodes separated by 5 to 20 μm. The molecular functionalized ZnO NBs were transferred onto the prefabricated electrodes by touching the NB sample with the electrodes. We can easily make a sample with only a single ZnO NB lying across two electrodes by this process. The as-fabricated devices showed very good electric transport performance, as shown in figure 4.2a. The black curve is the I-V characteristics of a ZnO NB functionalized with a monolayer of $HOOC(CH_2)_{10}COOH$ (dodecanedioic acid). The green curve is the I-V characteristics of an untreated NB, which is magnified by a factor of $5x10^5$ to bring to the same scale for comparison purpose. Figure 4.2b shows the conductivity measured for NBs coated with different end-group molecules. In our experiments, 30 samples for each group of devices were tested. More than 90% of the functionalized NB based devices were conducting and all of the untreated NB

based samples showed poor conductivity. The NB samples used for the

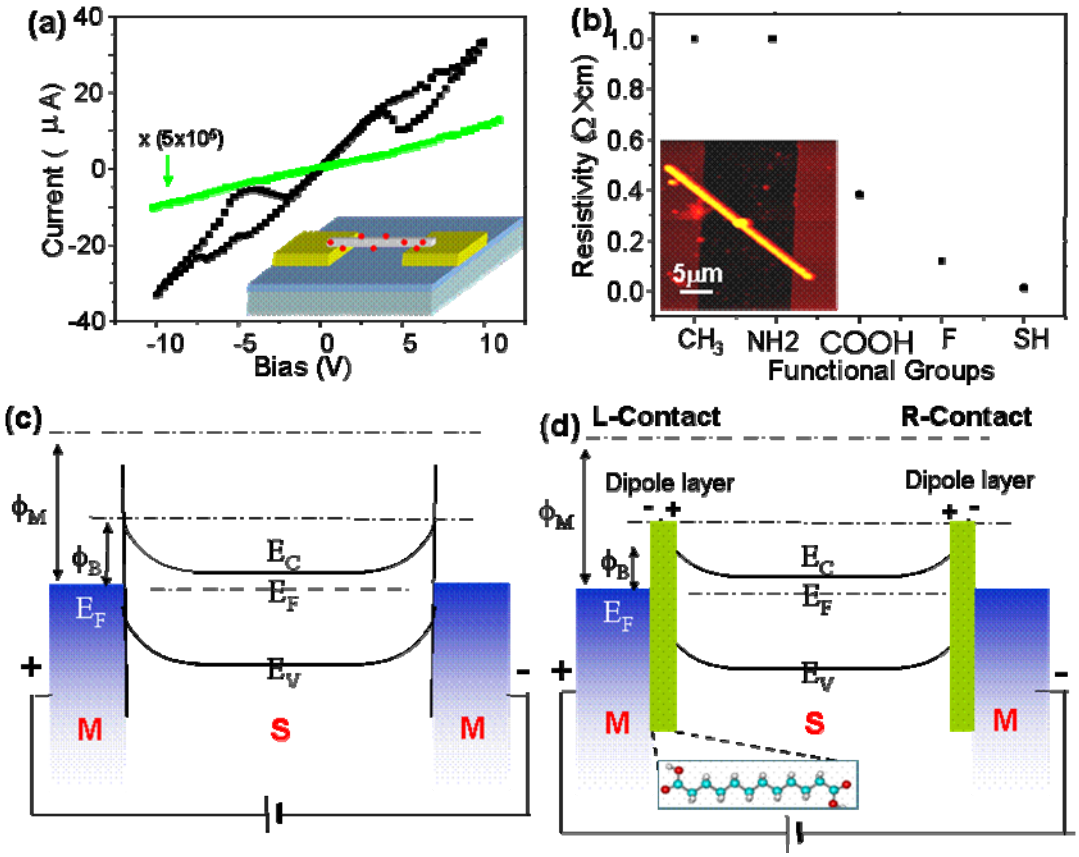

Fig. 4.2 (a) IV characteristics of a ZnO NB functionalized with the self-assemble thin molecule layer, $HOOC(CH_2)_{10}COOH$ (black line), and a untreated ZnO NB sample (green line). The current of the untreated NB is magnified by $5x10^5$ time for comparison purpose. Note: no Pt was deposited at the contacts so that the measured current for the untreated NB is low. The inset is a schematic view of the nanobelt device. (b) Resistivity of the NBs coated with different molecules. The lower inset image is an AFM image of a coated NB lying across two electrodes. (c) Energy-level diagram of metal/semiconductor/metal interfaces, ϕ_M is the work function of the metal. There is an energy barrier ϕ_B between the metal contact and the untreated NB. (d) Energy-level diagram of Au electrode and a ZnO NB with a thin molecular layer between. The molecules form an interface dipole layer, which helps to decrease the energy barrier between the NB and Au.

device fabrication were taken from the same type of sample with dry and clean surface so that the results can be directly compared with each other; the only difference is the layer of molecules functionalized on the surface. As shown in figure 4.2a, the current flowing through the molecular coated NB is around 10^6 times larger than the untreated NB. Figure 4.2b shows the

conductivity for NBs coated with different end-group molecules, indicating a large difference for different molecular treated ZnO surfaces.

The increased conductivity may be explained from the band structure at the contacts. Fig. 4.2c shows the band structure of the NB at the left-hand-contact (L-contact) and right-hand-contact (R-contact) along a single NB without the coating of a molecular layer at the surface. The contact between Au and ZnO is a Schottky contact of height Φ_B. When a monolayer molecules are introduced at the interface, as shown in Fig. 4.2d, it effectively reduces the barrier height due to the introduction of molecular states between the bandgap. The molecular layer may form a dipole at the interface.[23] When a positive voltage is applied from the left- to right-hand side, the L-contact is a metal-semiconductor (M-S) contact and it is a forward biased Schottky, thus its resistance is very low. At the R-contact, although the S-M contact is a reversely biased Schottky barrier, the dipole layer not only reduces the barrier height but also mediates the transport of electrons (for n-type semiconductor such as ZnO) from the metal contact to semiconductor, which effectively reduces the contact resistance, resulting in a drastic increase in conductance. In fact, a good contact was very easy to establish for the molecular coated ZnO NB, so the conductivity is very high for the treated NBs.

As shown in figure 4.2b, the resistivity of the functionalized NBs with different SAM molecules ranges from 0.1 Ω-cm. to 1 Ω-cm for the contacts made simply through a dry transfer, which is one order of magnitude lower

than that of the as-synthesized ZnO NBs, which were made in Ohmic contact with the electrodes through several layers of metal deposition using e-beam lithography.[169] The great enhancement in conductivity is attributed to the coating molecular layer that forms a highly ordered two-dimensional passivation layer on the surface of ZnO NB, which prevents the oxygen in atmosphere from combining with the point vacancies at the surface. In fact, a combination of a vacancy with an oxygen reduces the carrier density in the NB, thus, lowering the conductivity. Also, after bonding with ZnO NB, the reaction group, carboxyl -COOH changed to $-COO^-$, which is an electron donor and can provide an electron to the NB, consequently, increasing the carrier density, e.g. the conductivity.

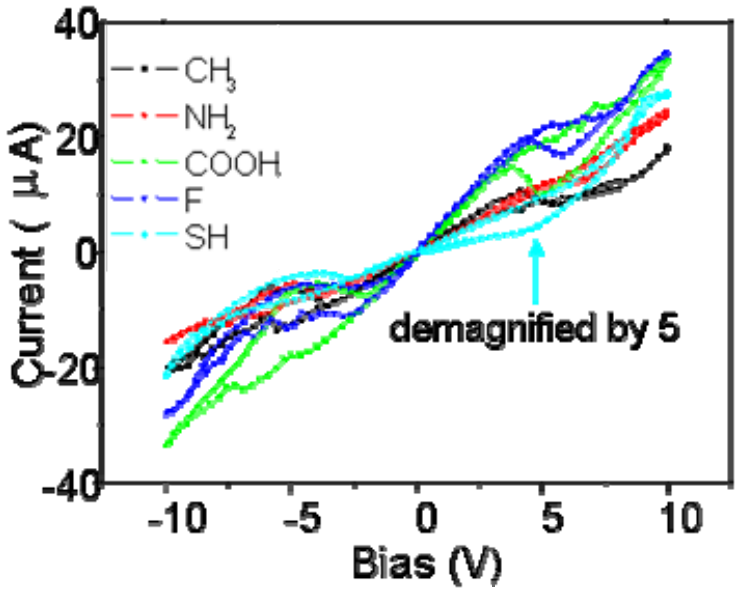

Fig. 4.3 Typical IV characteristics of the molecular functionalized ZnO NBs with different end-group molecules, which shows a typical negative differential resistance effect at room temperature. The current for the NB with molecule functionalization layer, $HOOC(CH_2)_{10}COOH$ (blue line), was demagnified by 5 times for comparison purpose.

For the IV characteristics of the ZnO NBs functionalized with different end-group molecules, negative differential resistance (NDR) was observed, as shown in figured 4.3. 80% of the SAM coated NBs, disregard the type of the end-groups, displayed a NDR behavior. The peak to valley ratios in the positive bias IV curves at room temperature range from 1.56 (dicarboxylic acids, $HOOC(CH_2)_{10}COOH$, green line) to 1.08 (lysine, $H_2N(CH_2)_4CH(NH_2)COOH$, red line). In the literature, several models have been proposed to explain the origin of the NSR.[9, 217] From previous study on the mechanism of the NDR[15] in molecular carrier transport, the high current peak is associated with the delocalization of the lowest unoccupied molecular orbital. Under the bias at around 4 V, the charge distribution in SAM molecules was disturbed due to a voltage-induced redox reaction. We suspect that the carrier transport of our SAM functionalized ZnO NBs were also affected by the electronic delocalization. At the bias of 4 V, the bias voltage induced a voltage-induced redox reaction, thus, the unoccupied molecular orbital in the SAM acted as a transition state to facilitate the electron-hole excitation in the ZnO NB, possibly resulting in the NDR effect.

4.1.3 Enhanced Photoconductivity

To further test the performance of these functionalized ZnO NB samples and explore their potential applications, we compared the current response under UV light expose for a SAM ($HOOC(CH_2)_{10}COOH$) coated ZnO NB and

an untreated NB. The contacts for the untreated ZnO NB and Au electrodes were deposited with Pt by Focus Ion beam system. The purpose of this process is to eliminate the huge contact resistance of untreated ZnO NB and Au electrodes and get an intrinsic photoresponse of untreated NB. Note the NBs used for Fig. 4.2 were not deposited with Pt so that the native NB (green curve) has a much lower current. The UV light source used in the experiment is a high intensity UV lamp with a wavelength of 365 nm. The light intensity at the sample surface was 8,900 mW/cm^2. Both the SAMs coated NB and the untreated NB showed an on/off state corresponding to the expose of the UV light, as shown in figure 4.4. Figure 4.4a is the UV response of the SAM functionalized NB. The current flowing through the SAM coated NB increased from 35 to 55 μA upon the exposure of the UV light a 57.1% enhancement. For the untreated ZnO NB, the current increased from 2.06 to 2.51 μA, a 22% enhancement. The photoresponse of the ZnO NBs to the UV light was enhanced by around 3 times after the functionalization of the ZnO NBs by a coating layer of $HOOC(CH_2)_{10}COOH$, which is an effective and feasible way of enhancing the optical response of NBs for UV detection. The absorption spectrum of a typical organic molecule, which has a similar structure as that of the molecules used in our experiment, has a strong peak at the wavelength of around 380 to 400 nm. This means that electrons in the molecules of SAM were excited to a higher energy state under the exposure of UV light, which left an unoccupied molecular orbital at an energy level that

falls within the band gap of ZnO. At the same time, the carriers inside the ZnO NB was also excited under the exposure of the UV light.[167] The unoccupied molecular orbital acted as a transition state for the electron in the valance band of ZnO to transit to the conduction band of ZnO, resulting in a higher efficiency of separating the electron-hole pair and the increased photocurrent efficiency.

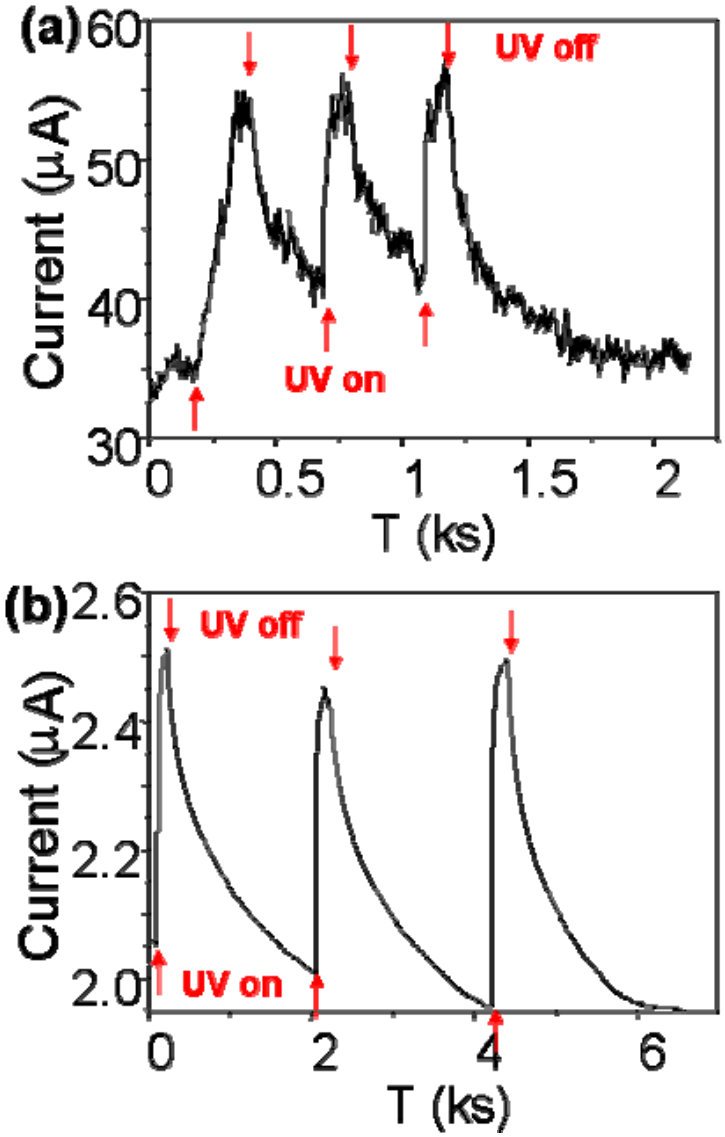

Fig. 4.4 Photocurrent of (a) $HOOC(CH_2)_{10}COOH$ functionalized ZnO NB and (b) untreated ZnO NB when subject to UV light illumination, received under identical measurement conditions. Note: Pt was deposited at the contacts to reduce the contact resistance.

4.1.4 High Gas Sensitivity

The SAM also enhances the sensitivity of the NB for gas sensors. For oxygen gas with a concentration of 154 ppm, the responses of the treated and untreated ZnO NBs are shown in figure 4.5. When the oxygen gas was tuned on, the current flowing through the $HOOC(CH_2)_{10}COOH$ coated NB decreased from 14 to 8 μA, which is a 43% drop (figure 4.5a). For the untreated ZnO NB, the electrode was deposited with Pt on the contacts for reducing the contact resistance and enhance gas sensing by the NB. The current flowing through the device decreased from 9.7 to 7.0 μA, a 28% drop (figure 4.5b). It is apparent that the gas sensing response of the ZnO NBs were enhanced by the functionalization of the $HOOC(CH_2)_{10}COOH$. The working temperature of the gas sensor in our experiment was 300 ^{o}C. At this temperature, the molecules had been debonded from ZnO NB and partially/fully decomposed. Due to bonding reaction of the carboxyl -COOH group with the ZnO NBs during the functionalization process, there are extra oxygen vacancies being created at the surface of ZnO NBs by functionalization. As such, more oxygen gas can combine with these surface defects after debonding the molecules, the conductance change in the treated NB is more significant comparing to the untreated NB. This is probably why the treated ZnO NB has higher sensitivity.

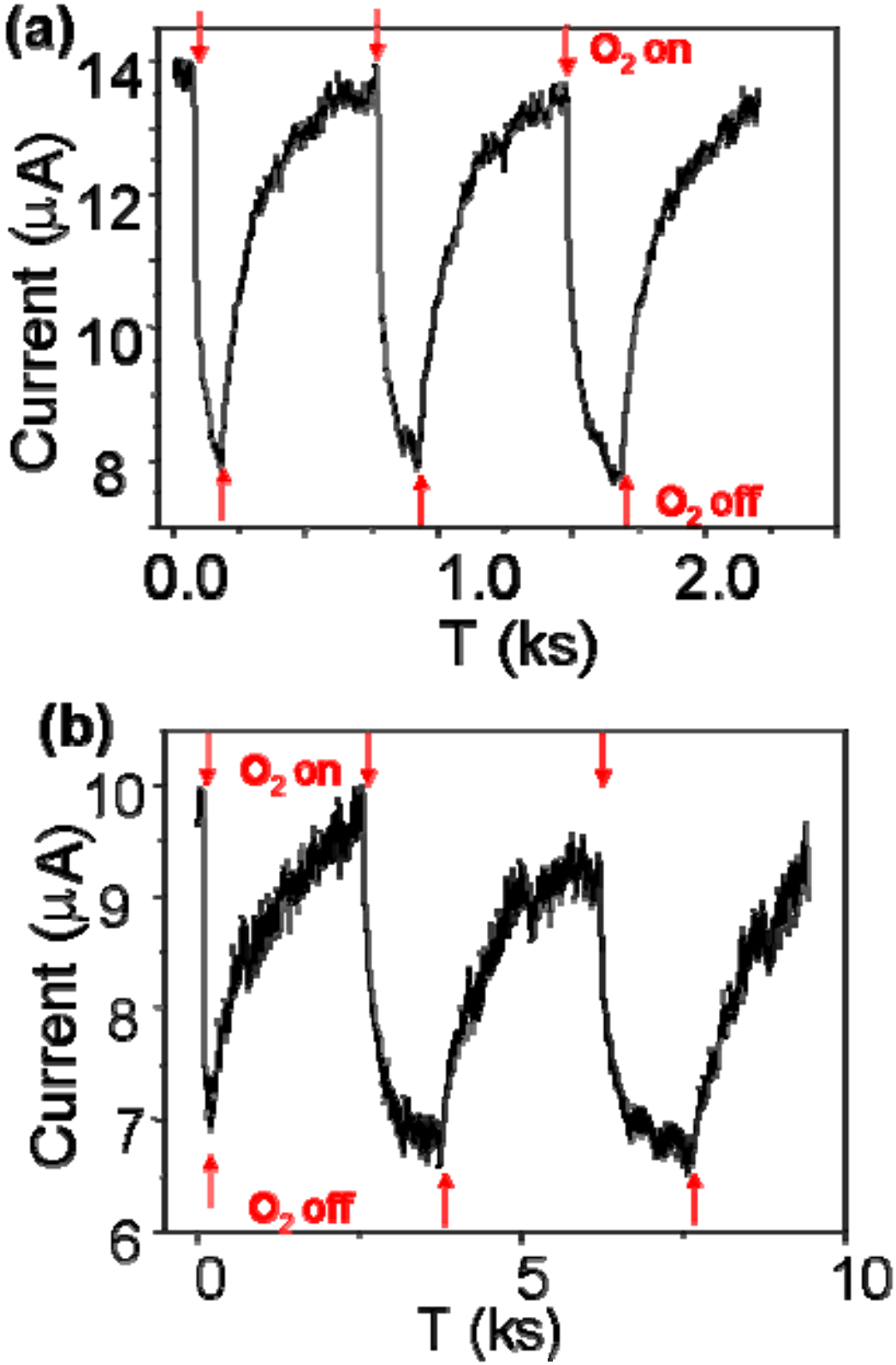

Fig. 4.5 Gas sensing properties of (a) $HOOC(CH_2)_{10}COOH$ functionalized ZnO NB and (b) untreated ZnO NB in responding to O_2 of 154 ppm in concentration. Note: Pt was deposited at the contacts to reduce the contact resistance.

4.1.5 Increased Bio-stability

Our previous study has shown that ZnO nanowires are soluble in biofluids.[218] The biodegradability is very beneficial for some applications. For nanodevices, we wish to increase the life time and bio-stability of the material so that it can achieve some designed purposes. In this section, we demonstrate that the coating molecules can protect the ZnO NBs in the buffer solution to substantially extend its lifetime.

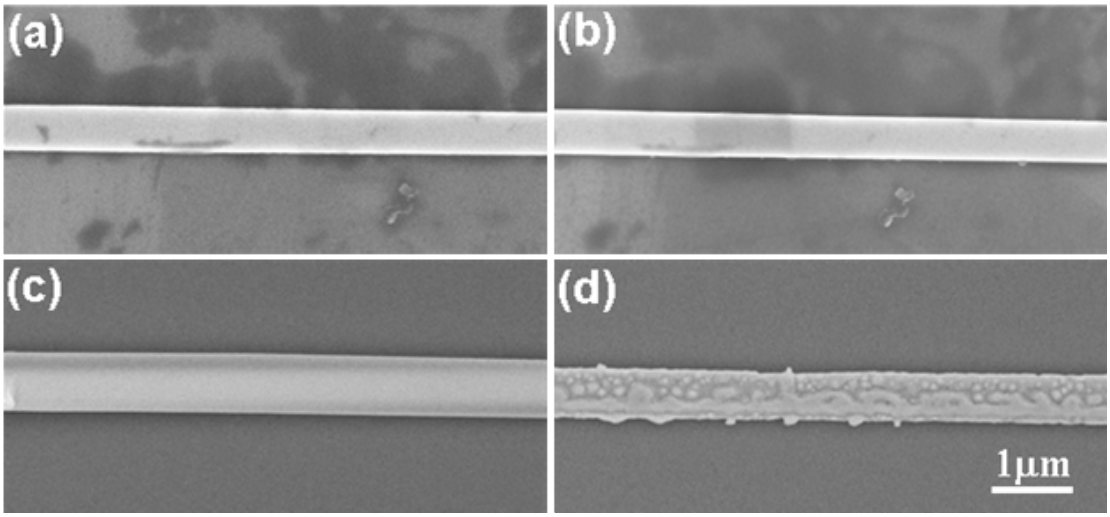

Fig. 4.6 SEM images of the same NB coated with $HOOC(CH_2)_{10}COOH$ (a) before and (b) after immersing into the buffer solution for 15 min. SEM images of an untreated NB (c) before and (d) after immersing into the buffer solution for 15mins.

To test the solubility of the SAM coated ZnO NBs and the uncoated ZnO NBs, a buffer solution with PH 7.0 (Fisher Scientific SB107-500) was used as the testing reagent. By dispersing the NBs in the solution for a fixed time, then we examine the "etching" result of the surface through SEM. Figure 4.6a is an SEM image of a $HOOC(CH_2)_{10}COOH$ coated NB before immersing into the buffer solution. Figure 4.6b is a SEM image of the same ZnO NB after 15 minutes etching in the buffer solution. The NB retained the same

morphology before and after the buffer solution treatment. Figures 4.6c and d are the SEM images of an untreated ZnO NB before and after the buffer solution treatment for 15 min. As can be seen in the images, the untreated NB was greatly etched by the buffer solution. The resistance to surface etching might come from the dense and well aligned molecules protecting the surface of ZnO NBs. With the coating of molecules on the surface, the surface chemical and physical properties were changed according to the contact angle measurement. This experiment shows a possible way to increase the stability of ZnO NBs in a bio-solution.

In conclusion, we have demonstrated that, by functionalizing the surfaces of a nanobelt/nanowire with a self-assembled thin molecular layer, their electrical and optoelectronic performances are greatly enhanced. The coating molecular layer has effectively decreased the contact resistance between a NB and the Au electrode, resulting in a change of a Schottky contact into an Ohmic contact. Furthermore, the photoconductivity and gas sensing response of the NBs have been dramatically increased. Lastly, the functionalized molecules greatly reduces the dissolution rate of ZnO NBs in biofluid, as such, it effectively extends the NW devices life time for biomedical applications. Our study on the molecular functionalized NWs presents a simple and cost-effective method for improving the performance of oxide nanowire/nanobelt based devices.

4.2 Giant UV Response by Polymer Functionalization

In this section, we demonstrate that the UV response of a ZnO NB based sensor has been enhanced by close to five orders of magnitude after functionalizing its surface with a polymer that has a high UV absorption ability. This giant enhancement in photoconductance is attributed to the energy levels introduced by the polymer lying in the corresponding band gap and in the conduction band of ZnO, which served as a "hopping" state and increased the excitation probability of an electron to the conduction band. This exciting discovery will greatly impact the applications of ZnO NWs/NBs for UV detection.[219]

4.2.1 Surface Functionalization and UV Response

The devices based on ZnO NB were fabricated by aligning a ZnO NB across two metal electrodes. The device fabrication was achieved using e-beam lithography and focused ion beam (FIB) microscopy.[170] Surface functionalization is one of the widely used methods to enhance the electric transport properties of different 1D nanostructures.[11] Due to the special physical and chemical properties of the attached chemical species, devices based on ZnO NWs/NBs demonstrate unique and interesting properties.[202] In this paper, a layer-by-layer self-assembly method was used for manipulating and functionalizing polymers onto the surface of ZnO NBs. In general, since

the functional polymers used for UV sensing was negatively charged, a positively charged polymer, poly(diallyldimethylammonium chloride) (PDADMAC), was chosen to assist the electrostatic assembly of the negatively charged polymer. Surface charge of ZnO NBs is negative in aquatic solution according to Zeta potential measurement. Prior to surface coating, the ZnO NBs used in the devices were cleaned with oxygen plasma to remove surface chemical residuals and other contaminants before testing or polymer functionalization. For a bare ZnO NB, PDADMAC was first adsorbed onto its surface by electrostatic attraction force between the negative surface charges of ZnO and positive charges of PDADMAC. Then, the ZnO NB was immersed in an anionically charged polymer solution of choice, which was adsorbed on the ZnO NB due to the electrostatic force from the cationically charged PDADMAC molecules.

Different kinds of polymers with different UV absorption abilities and wavelengths were used in the experiment to test their effects on enhancing UV response of the ZnO NB, including polystyrene sulfate (PSS), poly(styrene-co-maleic acid) (PS-co-MAc), anionically charged poly(N-isopropylacrylamide) (PNIPAM), carboxymethylcellulose (CMC). For the layered coating, these polymers are all negatively charged or modified to possess negative charges. A scanning electron microscopy (SEM) image of

these functionalized ZnO NBs is shown in the inset of Fig. 4.7b. The blur

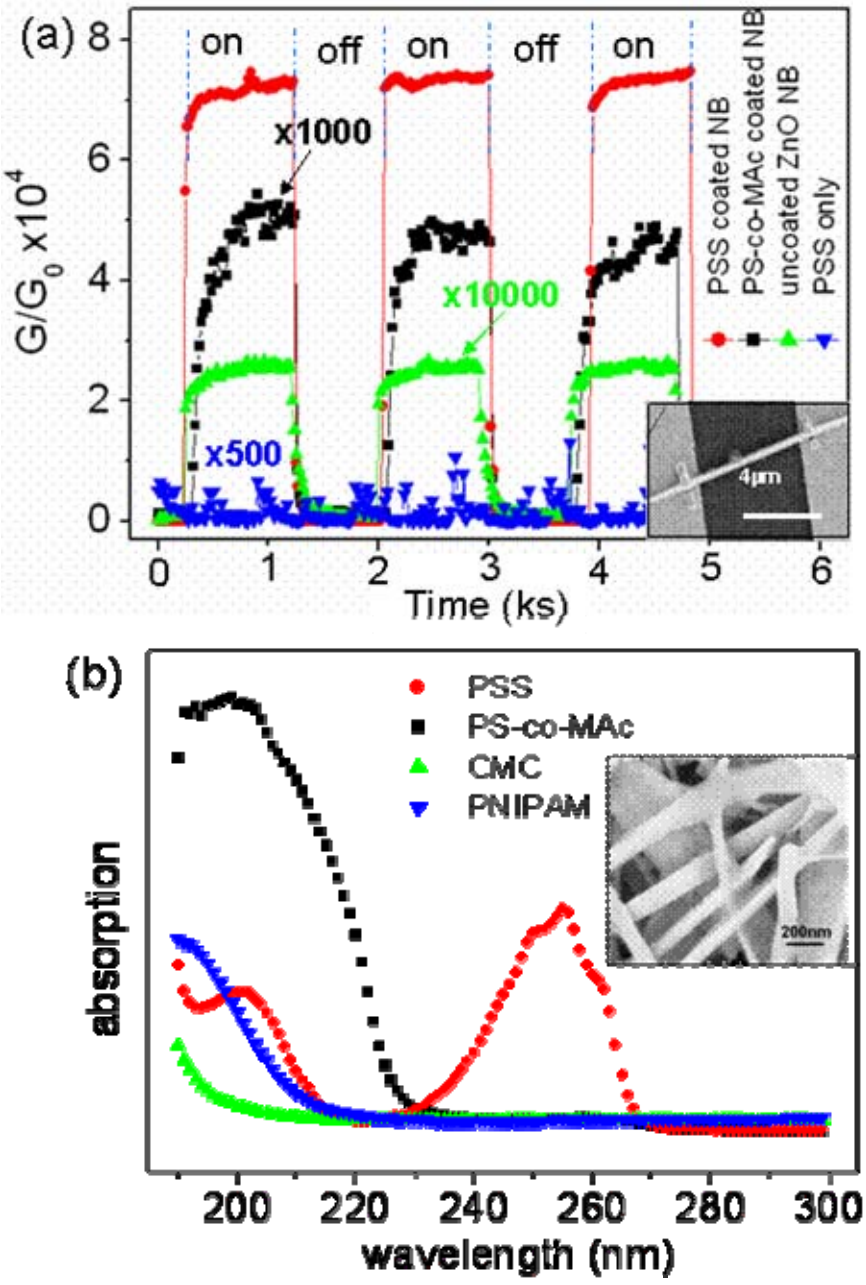

Fig. 4.7 (a) Normalized conductance responses of a single functionalized ZnO NB device (see inset) upon UV illumination being tuned on and off: bare ZnO NB without coating (green line, magnified by 10,000), PS-co-MAc coated ZnO NB (dark line, magnified by 1,000), PSS coated ZnO NB (red line), PSS polymer only (blue line, magnified by 500). Inset is an SEM image of a typical device. The applied voltage remained at 1 V for all of the measurements. (b) UV absorption spectra of PSS (red line), PS-co-MAc (dark line), PNIPAM (blue line), CMC (green line). Inset is an SEM image of a polymer coated ZnO NB sample.

edge of NBs in the figure indicates successful coating of polymers onto the NBs. IV characteristics of the polymer functionalized ZnO NB base devices were tested to investigate their electric transport under UV illumination. Fig. 4.7a is the photoconductance response of the single NB devices fabricated using ZnO NBs functionalized with different polymers, and the data are plotted for the ratio of the conductance measured when the UV was on (G) and off (G_0). The UV source used in the experiment had a wavelength distribution around 280 nm. The conductance of un-coated ZnO NB devices (green line) increased for 2.8 times upon UV illumination. The conductance of the PS-co-MAc coated NB (dark line) increased for 50 times upon UV illumination. The conductance for PNIPAM and CMC coated ZnO NBs was increased by 100 and 15 times, respectively (Fig. 4.9). Surprisingly, the photoconductance of the PSS coated ZnO NB (red line) increases by 75,000 times when UV was on. This is a sharp contrast to other three polymers coated ZnO NBs. It should be noted that dry PSS polymer itself is non-conductive and showed almost no-response to UV illumination (blue line), thus, its own cannot contribute to the huge increase in conductance. This phenomenon shows that the huge increase in conductance for PSS coated NB must be a coupling effect between the polymer and ZnO. This study shows the distinct effect of different polymers on the photoconductance of ZnO NB.

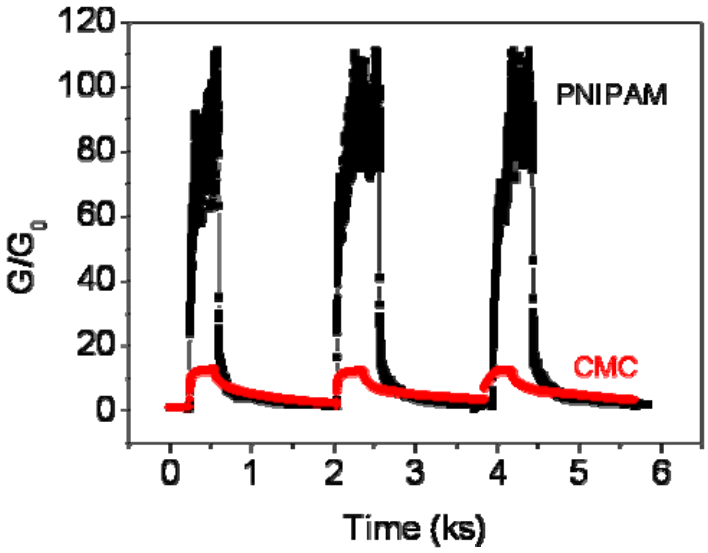

Fig. 4.8 Normalized conductance responses of a single functionalized ZnO NB device upon UV illumination being turned on and off: ZnO NB coated with PNIPAM (dark line) and ZnO NB coated with CMC (red line).

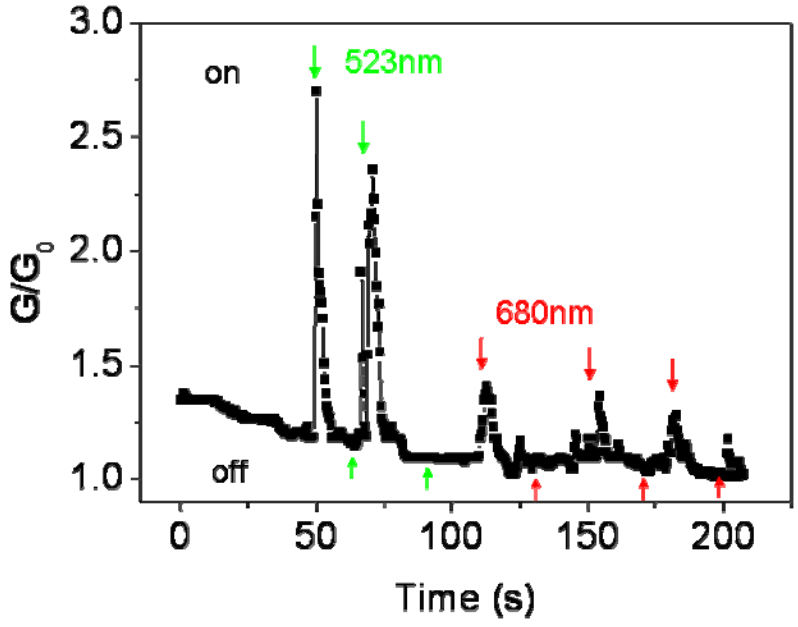

Fig. 4.9 Normalized conductance responses of a single PSS functionalized ZnO NB device upon illumination being turned on and off by different wavelength: Green arrows indicate response upon illumination of 523nm light source; Red arrows indicate 680nm light source.

From our measurement data, coating of polymers normally increases the UV response of ZnO NB by 10 – 100 times. However, the UV response of PSS coated NB has a much larger magnitude. To explore the reason for this distinct performance, we have measured the UV absorption spectra of the four polymers used in our study. As shown in Fig. 4.7b, PS-co-MAc MA, PNIPAM, and CMC show a UV absorption peak at wavelengths around 190-200 nm. The UV absorption decreased sharply with increasing of incident wavelength. In the 280 nm wavelength range as provided by the UV source in our experiments, the three polymers show little absorption. However, as for the UV absorption spectrum of PSS, there are two absorption peaks. One is around the wavelengths of 190 nm, and the other peak is at the wavelength of around 260 nm, matching well to the excitation wavelength of the UV source. The data suggest that the large absorbance of the PSS to the UV is likely responsible for the observed huge increase in photoconductance. PSS coated ZnO NB showed little response to exposure of light source with 523nm and 680nm wavelength (see supplementary material Fig. 4.9), which further proved our result.

4.2.2 Mechanism for UV Response Enhance

Soci et al. have proposed that the high sensitivity UV detection of ZnO NW was due to the presence of oxygen-related hole-trapping states at the NW surface.[144] This process can also be applied to explain our observation. The

first layer of coated polymer is cationically charged PDADMAC. The free electrons might be trapped by the positively charged sites at the surface. Upon UV illumination, these immobilized electrons can trap the photon-generated holes, and thus reduces the electron-hole recombination rates in ZnO NB and increases the carrier lifetime. This mechanism accounts for the enhanced UV response for ZnO NB coated with PS-co-Mac, PNIPAM, and CMC.

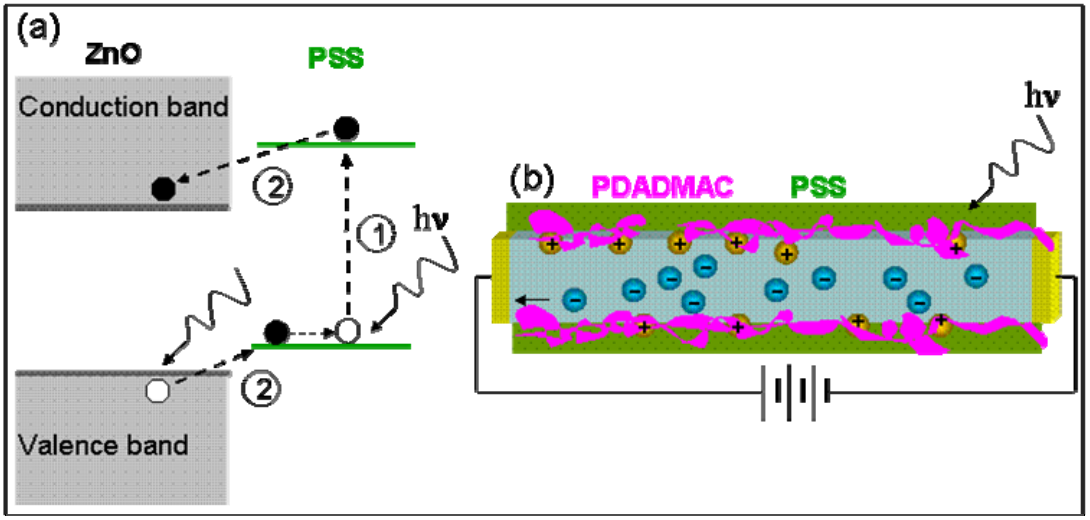

Fig. 4.10 (a) Schematic illustration of the electron-hole generation process with facilitation of transition states from the molecular energy states in PSS. (b) Schematically illustration of photon induced carrier transportation process in a ZnO NB by UV illumination.

The above mechanism may not be sufficient to account for the huge increase in photoresponse of the PSS coated NBs. From Fig. 4.7b, the UV absorption spectrum of PSS has a peak at around 260 nm, which is coincident close to the applied UV source wavelength. We proposed that this absorption peak and the related molecular energy states in PSS play a significant role for enhancing the photon response. Although the first layer of ZnO NB surface is

covered by PDADMAC, it is well known that the monolayer adsorption usually cannot reach 100% coverage. Therefore, the remaining surface could be covered by the next adsorbed layer of PSS, as shown in Fig. 4.8b. We now consider the area that PSS is directly interfacing with ZnO. Under UV light, an electron in PSS is excited from the ground state energy state to an exited energy state due to high absorption, which creates an unoccupied energy state (step (1)). If the ground energy state of the PSS is at the level within the bandgap of ZnO, it is possible that the electron in the valence band of ZnO NB is likely to be excited to the ground state of PSS, which subsequently transit to the conduction band of ZnO (step (2)). This "hopping" process may largely enhance the transition probability of the valence electrons in ZnO to its conduction band, resulting in a largely increase electron-hole pairs (Fig. 4.8a). The role played by PSS is to serve as a hopping-state or bridge for the electron transfer. As discussed above, the as generated holes are trapped at the NB surface by the PDADMAC, while the electrons are transported through the NB core, (Fig. 4.8b). Therefore, the conjunction of electron-hole pair generation in ZnO with the assistance of PSS and surface hole trapping effect by PDADMAC may largely prevent the electron-hole recombination, resulting in a huge increase in the photoconductance of PSS coated ZnO NB.

In conclusion, by coating ZnO NB using a polymer that exhibits a large UV absorption peak, the UV induced photoconductance increases by five orders of magnitude. This huge increase in photoconductance is suggested

due to an electron-hole generation process as assisted by the energy states in the polymer. Therefore, with coating UV sensitive polymers, the UV response of ZnO NB was greatly enhanced. This study sets the foundation for increasing the sensitivity of UV detectors based on ZnO. The result suggests that, by selecting polymers with different wavelengths of UV absorption, UV detectors with a large range of wavelengths and super-high sensitivity can be fabricated using arrays of ZnO NWs and NBs functionalized using different polymers. This discovery can have outstanding applications in photonics and optoelectronics.

4.3 Polymer Functionalized Piezoelectric-FET

Most recently, a new research direction termed of nanopiezotronics has been coined based on the piezoelectric-semiconducting coupled properties of ZnO NWs and NBs for fabricating novel and unique electronic components.[115, 220] The first application of nanopiezotronics is the piezoelectric nanogenerator based on ZnO NWs,[135] which demonstrates a unique approach of converting nano-scale mechanical energy into electric energy and harvesting energy from the environment for self-powered nanosystems.[93] Piezoelectric field-effect transistors (PE-FET) and diodes that operate based on the coupling effect of piezoelectric and semiconducting properties of ZnO have been developed. In this section, we report a first demonstration of humidity/chemical sensor

based on PE-FET . The devices were based on a single-side coated ZnO NB functionalized with multi-layers of polymers. Upon exposure of high humidity vapors, the polymers swell and produce an asymmetric strain across the ZnO NB. In returns, the deformation of ZnO NB produces a piezoelectric field across the NB, which serves as the gate for controlling the flow of current along the NB. This is the working principle of the polymer functionalized PE-FET. Also, the polymer functionalized PE-FET has been proved to work as a chemical sensor for detecting phase transition of the coated polymer.[160]

4.3.1 Polymer Functionalization

Polymers for functionalization of NB are anionically charged polyN-isopropylacrylamide (PNIPAM) and poly(diallyldimethylammonium chloride) (PDADMAC). PNIPAM is the most well known temperature sensitive polymer in aqueous solution, which exhibits a lower critical solution temperature (LCST) of around 32 ^{o}C.[221] Gels of PNIPAM show significant hydration-dehydration transitions in aqueous solution in response to relatively small temperature change, which results in significant volume change. The volume change ratio of a cross-linked PNIPAM can reach as high as a factor of 100.[222] PDADMAC is a cationic water soluble polymer widely used for charge neutralization in industry, and is a common cationic polymer used in layer-by-layer self-assembly. In order to introduce charge groups in

the polymer chain, acrylic acid sodium salt was copolymerized with NIPAM monomer at a molar ratio of 1:9. The preparation of anionic PNIPAM followed existing literature with some modifications.[223] A typical procedure for synthesizing anionic PNIPAM used as a polycation is as follows. A 250 ml three-neck round-bottom flask equipped with a mechanical stirrer and a condenser was filled with 100 mL of DI water, 1.0 g of NIPAM, 0.69 g of acrylic acid sodium salt, and 0.034 g of initiator KPS (~2 wt% based on the monomer). The solution was flushed with nitrogen flow for 30 min and heated to 60 ^{o}C. After the temperature reached equilibrium, the polymerization was carried out under a nitrogen atmosphere for 5 h.

In the experiments, our devices were fabricated with a single ZnO NB bridging across two Au electrodes with the aid of photolithography and E-beam lithography system, which is described in previous work. During the layer-by-layer assembly experiment, ZnO was first immersed in a dilute PDADMAC solution at pH of 8. Zeta potential measurement indicated that the zeta potential of the ZnO NB in water at pH value of 7.5 is -21 mV, which means that the surface of ZnO NB was negatively charged. Due to the anionic nature of the ZnO NB in water, the cationically charged PDADMAC molecules were then absorbed on the ZnO surface. This ZnO NB coated with positively charged polymers on the surface was immersed in an anionically charged PNIPAM solution. By repeating this process alternatively, multi-layers of polymer with controlled layer numbers can be assembled on

the ZnO NB surface. This multi-layer functionalization process is schematically shown in figure 4.11b, in which the green dots represent the cationic charged PDADMAC and the orange dots represent the anionically charged PNIPAM. Also, ZnO NBs incorporated in the device were closely attached to the substrate surface (with a distance less than ~70 nm), so the polymer molecules (the radius of gyration in water, R_g, is 160 nm determined by SLS) will mainly adsorb only on the upper side surface to form a multilayer polymers on the ZnO NB, which is also illustrated in the plots of figure 4.11c. The SEM image inset in figure 4.11c is an actual polymer functionalized device fabricated with this electrostatic self-assembly method.

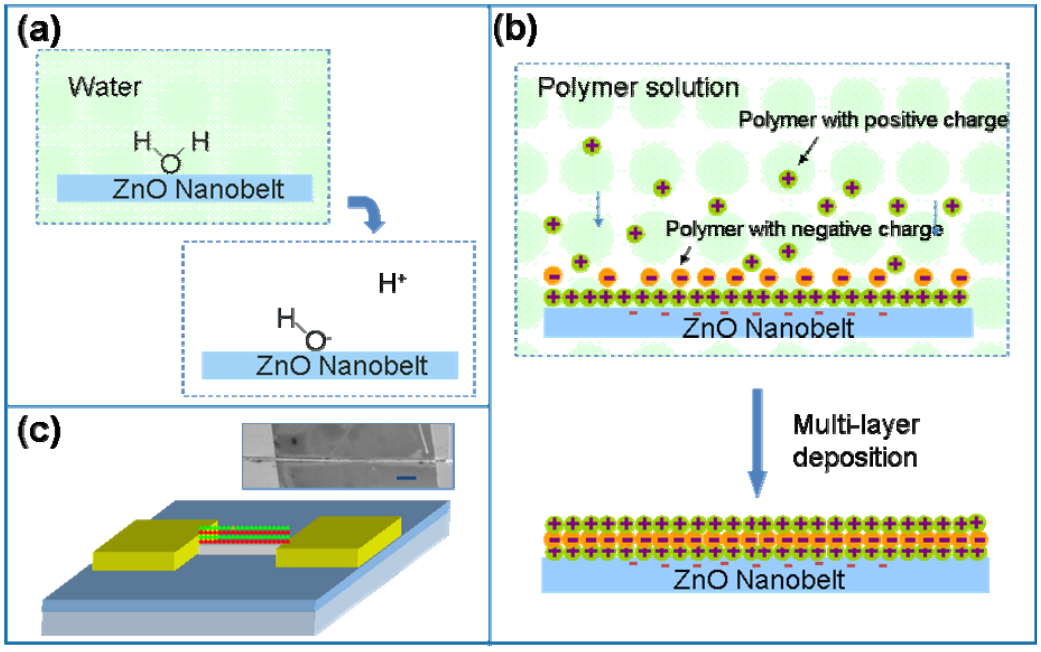

Fig. 4.11 Schematically illustration of the layer-by-layer electrostatic self-assembling process. a) Schematically illustration of ionization of H_2O molecules on the surface of ZnO NB, which results in negatively charged ZnO NBs in aqueous solutions. b) Schematically illustration of multi-layer deposition of different polymers onto the surface on ZnO NB surface upon electrostatic attraction of the charges on polymers. The green dots represent positively charged PDADMAC. The orange dots represent the negatively charged PNIPAM. c) Schematically illustration of the polymer functionalized device. Inset SEM image is an actual polymer functionalized device.

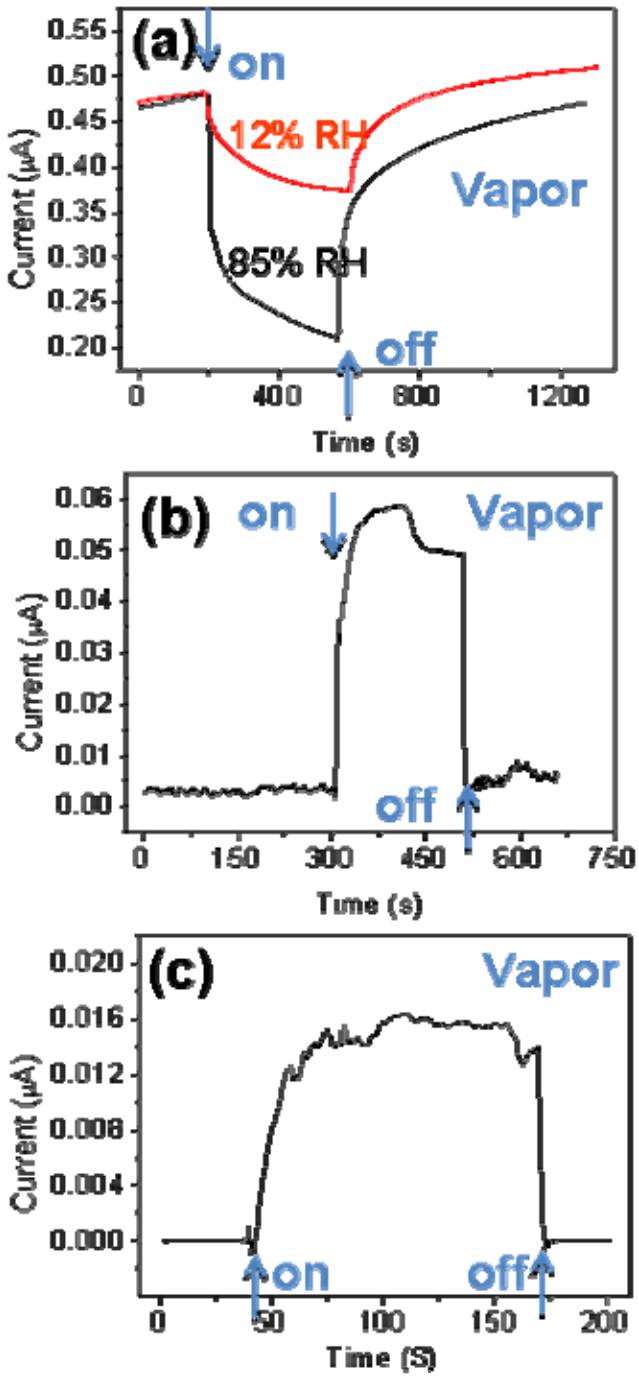

Fig. 4.12 a) IV responses of the PNIPAM polymer functionalized devices upon exposure to 85% (black curve) and 12% (red curve) relative humidity. b) Current response of an uncoated ZnO NB upon exposure to 85% relative humidity. c) Current response of multi-layer polymers upon 85% relative humidity vapor on and off. In contrast to (a), the current increases in the cases of both (b) and (c).

IV characteristics of these polymer functionalized ZnO NB base devices were tested to investigate their electric transport performance. These devices

are further fabricated using focused ion beam (FIB) microscopy to deposit Pt to secure the contacts before polymer functionalization. They displayed significant decrease in conductivity upon exposure of 85% Relative Humidity (RH) water vapor. Figure 4.12a is IV characteristics of PNIPAM functionalized samples upon exposure to 85% RH water vapor (black line) and 12% RH water vapor (red curve). The current flowing through the device decreased from 0.48 μA to 0.22 μA when the 85% RH water vapor was turned on and decrease from 0.48 μA to 0.38 μA when the 12% RH water vapor was turned on. After turning the water vapor off, the current gradually increased back to the original value. This current response to vapor on and off state can be repeated for many cycles and the detection limit could be very accurate according to the strong and steady response to the 12% RH water vapor in the experiment.

To explore the origin of the reduced current upon vapor exposure, we carried out a series of experiments based on different functional materials on the devices. First, the current response of an uncoated ZnO NB was examined. As shown in figure 4.12b, the current flowing through the uncoated ZnO NB increased from 0.005 μA to 0.055 μA upon 85% water vapor exposure. We suspect that upon vapor exposure, pre-absorption oxygen that caused the conductivity decreased of the NB was replaced by the physisoption or hydrogen bonding, which resulted in an increase of the conductivity. This mechanism accounts for the current increase for uncoated

ZnO NB. Similar current increase was observed when the conducting channel contains only multi-layers of polymers (figure 4.12c), which is contrary to the response of polymer coated NB. Upon exposure of water vapor, the ion mobility in the dehydrated multiple PNIPAM/PDADMAC polymer layers increased, which result in current increase. Current responses of the multi-layer polymers without ZnO NB or with ZnO NB only but without polymer are opposite to the response of polymer functionalized ZnO NBs. These experiments proved that neither ZnO NB nor multi-layer polymers could produce the decreased current response upon exposing to vapor. Therefore, we suspect that the decreased current response must come from the coupling effect of the coating polymer layers and the ZnO NBs.

It is believed that the reduced conductivity may come from a similar piezoelectric-semiconducting coupling properties of a bent ZnO NB, as reported previously . The polymers used in our experiments, PNIPAM, and PDADMAC, are all very sensitive to the environment humidity changes. According to the reference, the surface functionalization introduces surface strain on the NB. As shown in figure 4.13a, these polymers are closely packed before vapor exposure. Upon exposure of water vapor, these polymers will undergo a hydration process by absorbing a large amount of H_2O molecules from water vapor. As a result, the volumes of these polymers are increased in a significant ratio.

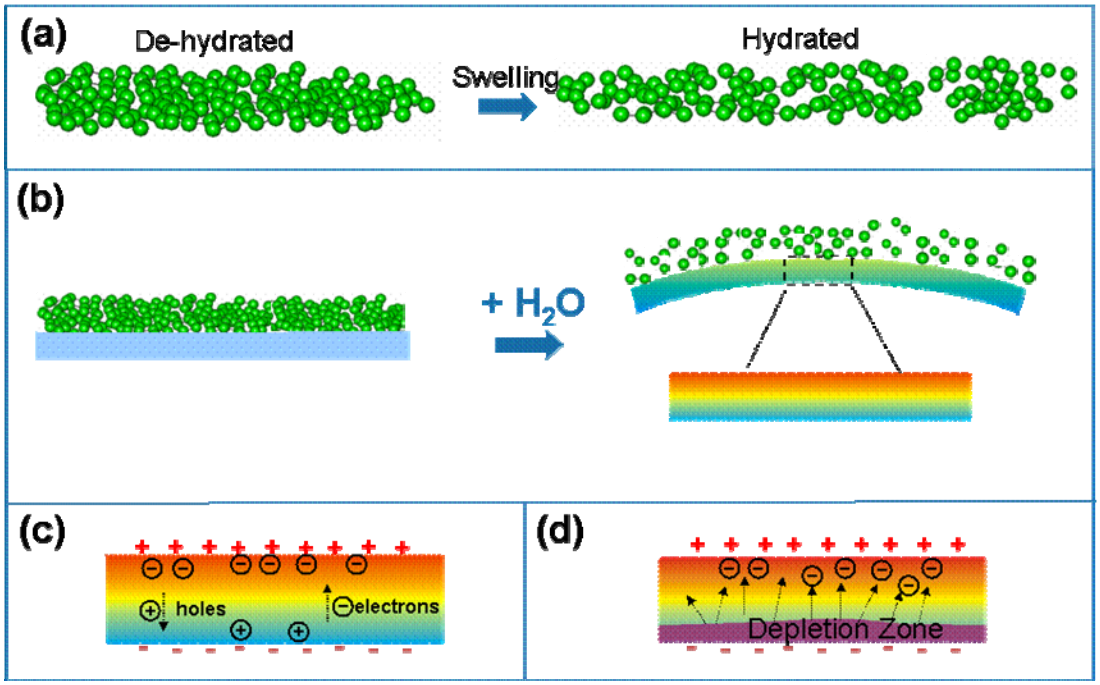

Fig. 4.13 Schematically illustration of mechanisms of polymer functionalized piezoelectric field effect transistor (PE-FET). a) The volume of the polymers increases significantly upon hydration. b) Schematically illustration of ZnO NB deformation upon polymer swelling and the consequent generated piezoelectric fields across the ZnO NB. The inner and outer surface of ZnO NB are negatively and positively charged respectively. c) Free electrons are trapped by the positive charged surface. d) A depletion region is formed by the repelling force of the negative charged surface.

Because the polymers were coated only at one side of the ZnO NB, the swelling of polymers then generated an asymmetric tensile stress at the contact surface with ZnO NB. Consequently, ZnO NB was bent under this asymmetric force, resulting in an asymmetric strain across the thickness of the NB. As demonstrated in our recent work, a bent ZnO NB could produce a piezoelectric potential across the NB due to the strain-induced piezoelectric effect. With the stretch and compression effect of a deformed ZnO NB, a positively charged and a negatively charged surface were produced at the outer and inner bending surface of a ZnO NB. Consequently, a piezoelectric

field was built across the ZnO NB. This is schematically illustrated in figure 4.13b. These ionic charges are immobile on ZnO NB surface without releasing the strain. With the electric force imposed by this electric field E_{PZ}, some free electrons in the n-type ZnO NB may move towards the positive charged surface and then be trapped at the surface. This trapping effect lowers the available carrier densities in ZnO NBs, which result in a decrease in conductivity. On the other hand, the negative charged surface of ZnO NBs acted as a back gate which repels free electrons away from the surface under the electrostatic effect. Therefore, a depletion region was formed in space close the negative charged surface. This reduces the size of the conducting channel in the ZnO NB. This also accounts for the decrease in conductivity of the bent ZnO NB. These two mechanisms are schematically presented in figures 4.13c and d, which together may be responsible for the observed decrease in conductivity. The depletion region formed by the negative charged surface and the consequent gating effect on the conduction channel in ZnO NB is analogous to the case of applying a gate voltage across a ZnO NB in a typical FET, e.g., piezoelectric field effect transistor (PE-FET). In our experiment, bending of the ZnO NB comes from the swelling of polymers, which is a result of chemical process. When the sample was dehydrated in the dry air, the strain was released and the ZnO NB return to it original shape.

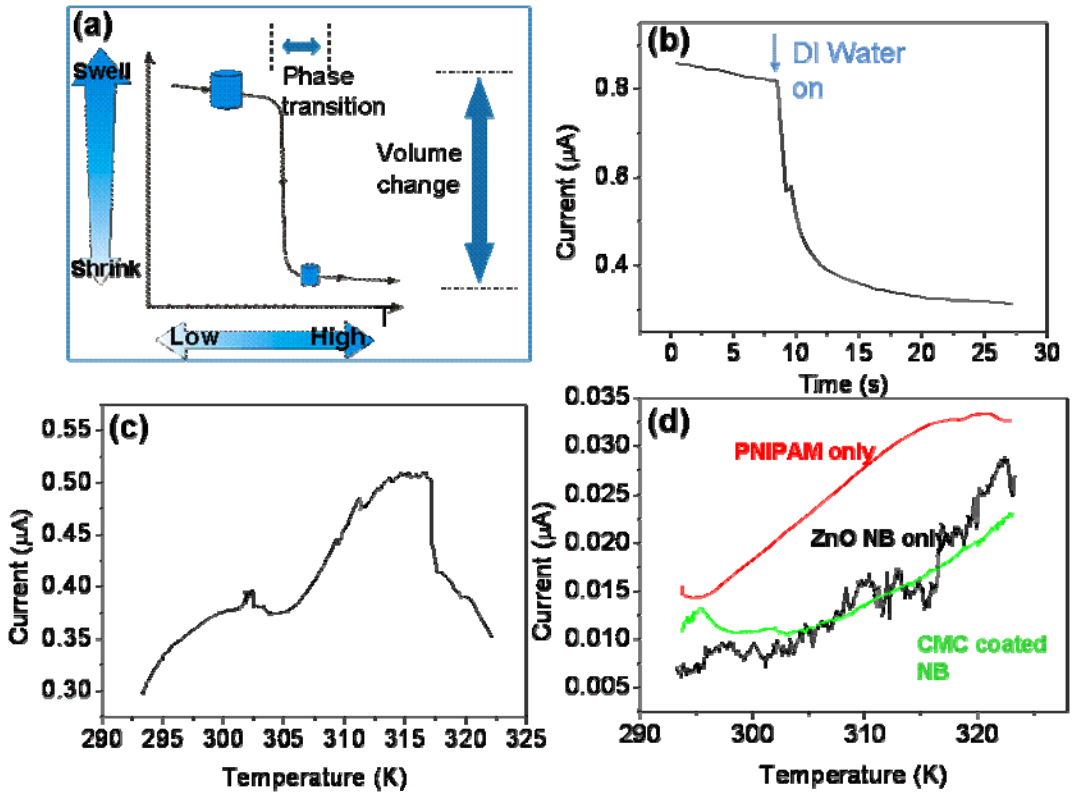

Fig. 4.14 a) Schematically illustration of the phase transition and the corresponding volume changes. b) Current response of PNIPAM functionalized ZnO NB upon exposure of DI water. c) Current response of the same devices with temperature increase in aquatic solution d) Current response of uncoated ZnO NB (black curve), PNIPAM polymer (red curve), and CMC polymer coated ZnO NB (green curve) upon temperature increase in the temperature range of 293 to 323 K.

The principle of the humidity sensor relies on the deformation produced by the coating polymer. A similar process can be used to detect the phase transition of a polymer, which normally accompanies with volume change. By monitoring the current changes flowing through the functionalized ZnO NB, we recorded in-situ phase transition of PNIPAM in aqueous solutions with the increase of temperature. As mentioned before, PNIPAM has a lower critical solution temperature (LCST) of around 32 °C (305K). When being exposed to aqueous solution at temperature lower than 305K, PNIPAM gels

hydrate to form an expanded gel structure on NB surface. In contrast to low temperature, PNIPAM dehydrates at temperatures above 32 ^{o}C. This hydration and dehydration phase transition process results in a significant change in the polymer volume as schematically illustrated in figure 4.14a. As a result, the polymer produces high tress on ZnO NB at low temperature when it absorbs water moisture. However, this stress will be released at high temperature due to the dehydration of the polymer hydrogel. Therefore, it is expected that conductivity of PNIPAM modified ZnO NB should show a temperature reversible responsibility at the PNIPAM's LCST of ~305K.

The polymer functionalized PE-FET based chemical sensor is shown in figure 4.14. Figure 4.14b is an in-situ current response of the same NB upon exposure to DI water. The transport current decreased from 0.8 μA to 0.3 μA when DI water was applied on the device, which was a result of the polymer swelling. By applying DI water on the polymer functionalized PE-FET, we then precisely controlled the temperature to increase from 293 K to 323 K. The in-situ current signal with the increase of temperature for a PNIPAM modified PE-FET is displayed in figure 4.14c. DI water was applied on the device during the temperature increase process. We suspect that the abrupt change of the curve slope at the temperature of around 305 K reflects the phase transition of PNIPAM. To prove this hypothesis, the current response of different targets in aqueous solution with respect to temperature increase

was tested. As shown in figure 4.14d, in the temperature range of around 293 to 323 K, an increase in temperature results in a quasi-linear increase in current magnitude. This is the case for all the tested samples, including uncoated ZnO NB (blue curve), pure PNIPAM polymer (red curve), and CMC (Carboxyl Methyl Cellulose, a polymer without the LCST phase transition effect at the temperature range tested in this study) coated ZnO NB (green curve), which shows that none of them will generate an abrupt current changes as observed in figure 4.14c. We can then conclude that the current signal change is a result of the stress release due to the phase transition of the PNIPAM polymer in aqueous solution with temperature increase. A tentative explanation to this effect is that, at the temperature range of 293 to 305 K, the current slowly increased due to the higher carrier mobility at higher temperature. At the temperature range of 305 to 315 K, the current underwent a faster increase. This might result from polymer contraction during the phase transition of PNIPAM in aqueous at this temperature range. As discussed before, when temperature increases, the volume of PNIPAM will significantly contract due to dehydration effect of the phase transition. Contraction of polymers released the strain applied on the ZnO NB. The deformation of ZnO NB was then released. Consequently, the piezoelectric field across the ZnO NB became smaller, so are the surface charged densities and the depletion region. This results in the increase of ZnO NB conductivity. At the temperature above 315 K, phase transition and

dehydration of PNIPAM were completed, so increase in temperature results in further hydration of PNIPAM and PDADMAC, which increase bending degree of ZnO NB, and consequently, decrease in the current magnitude. According to this, the current change provides in-situ information about the phase transition of the polymer. The primary working principle of this kind of chemical sensor is to convert the chemical changes in the structure to measurable electric signals.

4.3.2 Summary

In conclusion, we have fabricated PE-FET with the functionalization of different polymers on ZnO NBs. The electric transport across the device can be control by chemical properties of the coating polymers. When the devices were exposed to high humidity water vapor, coating polymers swell and consequently caused the bending of ZnO NB. Deformation of ZnO NB resulted in current decrease due to a coupling effect piezoelectricity and semiconducting properties. In the polymer functionalized PE-FET, the chemical energies changes were reflected on the electric signals, which is different from previous devices engineered with mechanical energies. This is a brand-new way in fabrication of nanopiezotronic devices and might bring a broad future of potential applications. Here, in this section, we also demonstrated the possible application of use this polymer functionalized PE-FET as a chemical sensor to monitor the phase transition of PNIPAM upon

temperature increase in aqueous solution. With the increase of better polymer functionalization control and device fabrication, we believe this polymer functionalized PE-FET might bring another way to produce energy and collect energy from environments.

4.4 Summary

Surface functionalization has been proven to be an efficient method to improve device performance of ZnO nanobelts in different aspects. So far, we have explored the surface modification and functionalization of ZnO nanostructures by molecules and polymers. From the results, it has been shown that ZnO nanobelts could be modified by surface chemical bonding and electrostatic self-assembly methods. Both methods are successfull in adjusting the surface chemical and physical properties of ZnO nanobelts and improving their transport, sensing and biological properties.

CHAPTER 5

FUTURE WORK RECOMMENDATIONS

Surface functionalization has been proven to be an efficient method to improve device performance of ZnO nanobelts in different aspects, such as transport property improvement, Gas sensing and UV sensing improvement. It is a very exciting opportunity to further develop current nano-devices for better device performance and from scientific models to commercialized products with this proved functionalization method. Moreover, besides facilitating the device fabrication, the functionalization process can also induce enhanced properties and new applications, such as bio-sensing and nanopiezoelectronics. Some novel applications have been described in previous chapters, such as the chemical sensor based on polymer functionalized PE-FET. More sophisticated devices can also been realized the device fabrication method and functionalization method in this dissertation. Although the work is still in blueprint or initiation stage, it is necessary to be pointed out as promising targets of future research. Starting from the chemical sensor and basic nanopiezotronics, more advanced cantilever based biosensors and other advanced nanopiezotronics are considered to be the achievable goals in near future.

5.1 **Piezoelectric and Piezoresistive Cantilevers as Chemical and Biological Sensors**

Cantilever transducer is a recently developed technique for chemical and biological sensing. It provides a promising, extremely sensitive platform for real-time, in situ, low cost detection of different physical, chemical, and biological properties. Because of its advantages in ultra-fast, dynamic response, compact size, high sensitivity and increased reliability, cantilever sensor is recognized as a promising candidate for the next generation of chemical and biological sensor.

Basically, a cantilever sensor is composed of a cantilever and a real-time read out system. By coating with a functional layer, the cantilever is bended when exposing to other chemical and biological species, due to the change in surface stress in the absorption process. Functionality of these cantilever sensors is based on detection of the deformation of the cantilever. Common detection methods include optical, piezoelectric, piezoresistive, capacitance and electron tunneling detection techniques.

Currently, most of the cantilever sensors are made with microelectro-mechanical systems (MEMS) by typical mask and etching process. Typical size of the functional part, cantilever, is around tens of micrometers in width. This relatively large size limits the sensitivity of these sensors. In this disclosure, we report two modified devices based on similar functionalities with extremely high sensitivity and selectivity. The basic idea

of the newly designed devices is to incorporated nanosize structures, ZnO nanowires/nanobelts and carbon nanotubes, as the functional cantilevers. The large surface to volume ratio of ZnO nanowires and carbon nanotubes greatly enhanced the sensitivity of the cantilever sensor. Also, the significant piezoelectricity of ZnO nanowires and piezo-resistivity of carbon nanotubes provide a precise and stable signal for the read-out system, which, at the same time, enhance the sensitivity of cantilever sensors.

(1) Piezoelectric cantilever based on ZnO nanowires/nanobelts

ZnO is a wide band-gap (3.37 eV) compound semiconductor and has strong piezoelectric and pyroelectric properties. These special characteristics make ZnO make a very promising candidate in applications of optoelectronics, mechanical actuators, and piezoelectric sensors. Here, we report a sensitive cantilever sensor utilizing the piezoelectric effect of ZnO nanowires.

By combination of e-beam lithography and sputtering (or other functionalization techniques), ZnO nanowires can be coated with a functional layer on selective area, as shown in figure 5.1. The as-functionalized ZnO nanowire is then incorporated into a detection system (figure 5.2) with the help of a nano-manipulation tool in focus ion beam system. The functionalized layer on ZnO will selectively bind with specific chemical and biological species when being exposed to chemical gas or physiological fluids. These binding ligands will change the surface stress due to changes in Gibbs

free energy associated with adsorption processes. Consequently, the ZnO nanowire cantilever is bended with asymmetric in surface stresses. Due to the large surface to volume ration, this deformation is very big compared to the MEMS cantilever even in a dilute bio-species environment. And also, due to the lack of central symmetry in wurtzite structure, the deflection of ZnO nanowire (with one side fixed) causes one side surface to be stretched and opposite side surface compressed. Positive potential V^+ ($V \propto Z_m$, Z_m is the bending displacement the ZnO) and negative potential V^- are produced in the stretched and compressed side surfaces respectively, due to the piezoelectric effect.

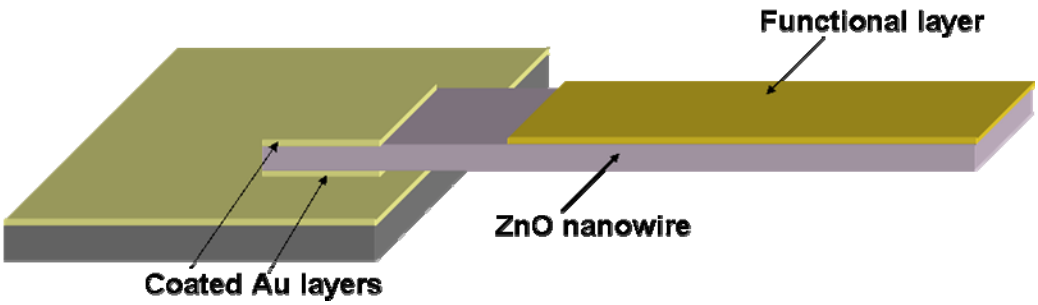

Fig. 5.1 A ZnO nanowire with a functional layer on the upper front surface and two coated Au layers at the end as contact electrodes

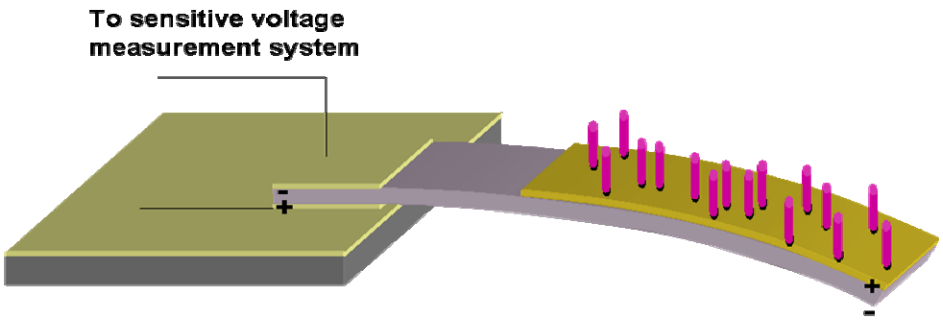

Fig. 5.2 ZnO nanowire is deformed due to the changes in surface stress when binding with biological species. Consequently, a potential difference is produced in the upper and bottom surface of the ZnO nanowire

This significant bias voltage due to piezoelectric effect on ZnO nanowire deformation provides a relatively convenient and much more precise way to measure the adsorbed chemical and biological species identity and qualities.

(2) Piezoresistive cantilever based on carbon nanotubes

The conductance of a carbon nanotube changes dramatically during bending due to the formation of defects and changes in band gap and conduction channels. By incorporating a carbon nanotube onto a common MEMS cantilever sensor, we can measure conductance changes of the carbon nanotube to monitor bending of the cantilever.

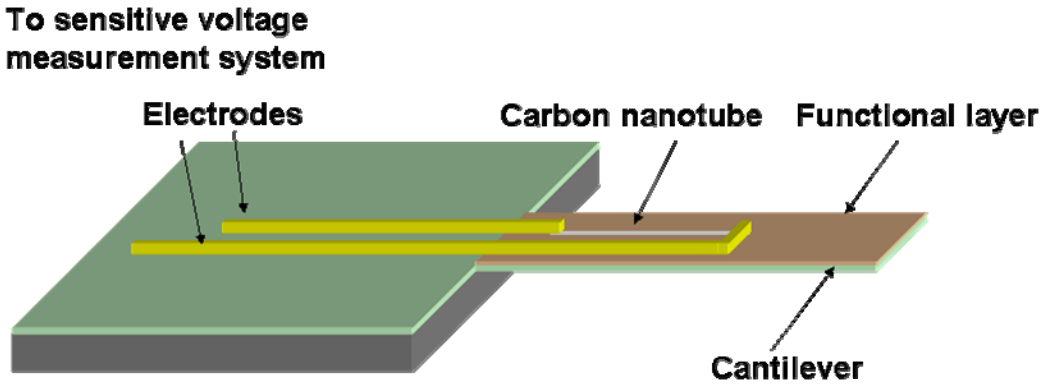

Fig. 5.3 Schematic view of a cantilever sensor based on a carbon nanotube. The carbon nanotube is placed on a cantilever, with both ends connected to two different electrodes. The bending of the cantilever can be monitored with the conductance change in the carbon nanotube.

A schematic view of such a carbon nanotube based cantilever sensor is shown in figure 5.3. A carbon nanotube is placed on a single side coated cantilever along the longitudinal direction. Two electrodes are fabricated

through e-beam lithography over both ends of the carbon nanotube. They are used to measure the conductance change in the carbon nanotube.

When the cantilever binds with biological species on the functionalized layer, it is bended due to the surface stress change. The carbon nanotube is also bended. Thus, by measuring this conductance change due to bending, we can extract the precise information of the adsorbed species.

5.2 Piezoeletronic Cantilever of ZnO Nanobelt as Hearing Aid

One out of ten people suffers from hearing loss worldwide, constructively and sensorineurally. People are affected by this in a way from mild impairment to profound deafness, both for children and adults. Nowadays, hearing aid devices offer people with hearing loss a significant way to improve the quality of their life. Typically, there are two categories of hearing loss, conductive hearing loss and sensorineural hearing loss (SNHL). For a conductive hearing loss, sound is not properly transmitted through the ear due to some conductive loss. An amplifier is all to restore normal hearing, which impose slight challenge for the hearing aid device fabrication. However, only 5% of the people suffering hearing loss are in this category. For a SNHL, it is normally caused by the damage to inner hair cells, outer hair cells, which cause a cochlear malfunction. Traditional way to help people with SNHL is to use digital signal processing for pre-processing of the sound

signals. However, this device has it apparent drawbacks such as relatively large size, high power consumption. Here, we proposed a brilliant mechanism which merges the miniature of nanowire structure and the piezoelectricity of ZnO. In the device, we mimic the mechanism of how a hair cell works, which potentially can be applied as an advanced category of hearing aid device option.

The hair cells in a human ear serve as a receptor for all the auditory signals. Basically, each hair cell acts as a biological strain gauge. The vibration of the auditory signals applied a mechanical force on the hair cell, which opens the ion conducting channel in the cell membrane. These ions flowing through the channel result in an influx of current, which changes the potential of the membrane. The potential change affects the rate of release from the hair cell of a synaptic transmitter. Consequently, a pattern of action potentials which encodes all the feature of the stimulus, i.e. auditory signals, such as intensity, time course and frequency, will be transmit to the brain via an afferent nerve fiber contacting the basolateral surface of the hair cell. This is basically how a hair cell works.

Most recently, a new research direction termed of nanopiezotronics has been coined based on the piezoelectric-coupled properties of ZnO NWs and NBs for fabricating novel and unique electronic components. The first application of nanopiezotronics is the piezoelectric nanogenerator based on

ZnO NWs, which demonstrates a unique approach of converting nano-scale mechanical energy into electric energy and an exciting technology for harvesting energy from the environment for self-powered nanosystems. Theoretical calculation proves that when a one end fastened ZnO NB vibrates, it will generate a strong electric signal at the fastened bottom end of the NB, which is shown in the figure 5.4. The vibration a ZnO NB can be tuned by the outer signal strength and frequency. Also, the morphology of the ZnO NB such as length, thickness can affects the resonance frequency of a NB. Therefore, by detecting the electric signal generated from the NB vibration, we can then mimic the ion current influx in the hair cell and membrane, which can work as a potential mechanism for the design of hearing aid. The advantage of a hearing aid lies in several aspects: First, with the electric signal generated from the NB vibration triggered by the auditory signal, it is a self power device, which eliminate the burden requirement of the power source; Second, with the small and adjustable size of ZnO NB, we can easily incorporate them into the human cochlear system without affecting other functional hair cells in the ear; Third, ZnO is biocompatible material, which is a good candidate for biomedical application.

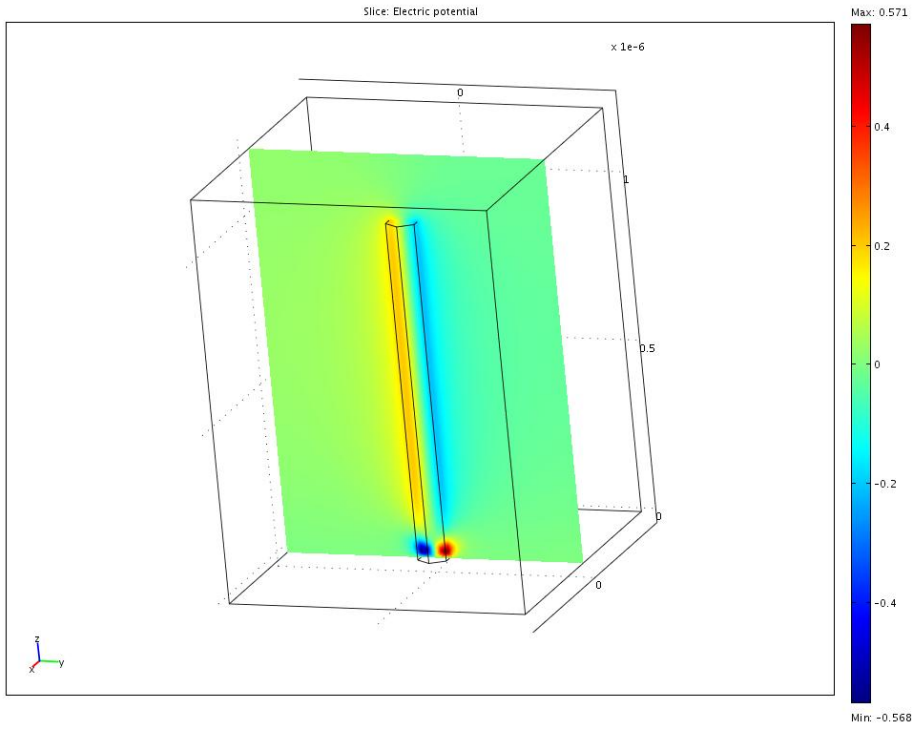

Fig 5.4 Theoretical calculation of piezoelectricity induced nanowires potential distribution.

Experimental Design

First, we propose to study the detail electric signal generated from a single ZnO NB. As shown in the schematically design of our device (figure 5.5), a ZnO NB is carefully place on a substrate with part of the NB stretches outside the substrate and suspends in the atmosphere environment. The NB is then secured on the substrate with two metal pads cover on a side surface of the ZnO NB. By detecting the electric signal generated at the root of the NB, this device mimics the working function of a human hair cell.

Secondly, by varying the NB under testing, such as changing NB with different length and different thickness, the resonance frequency of a NB is

different. We can then extract different response signal strength and find the optical device configuration for amplify the detected auditory signal.

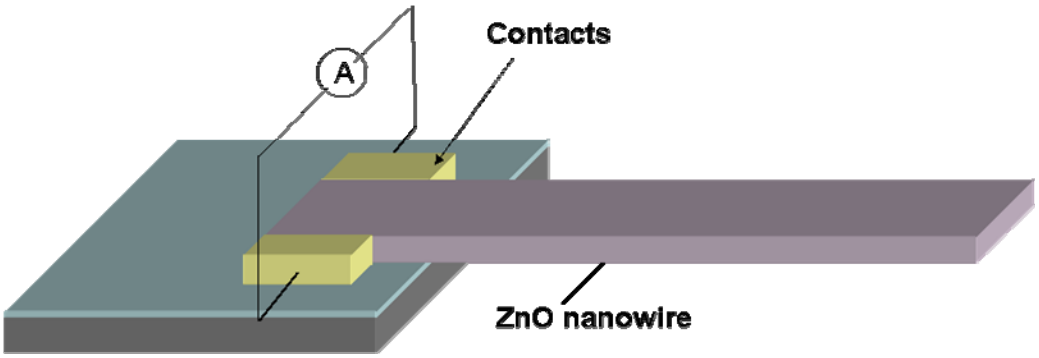

Fig. 5.5 Circuit setup and measurement for a sing ZnO nanowire as hearing Aid.

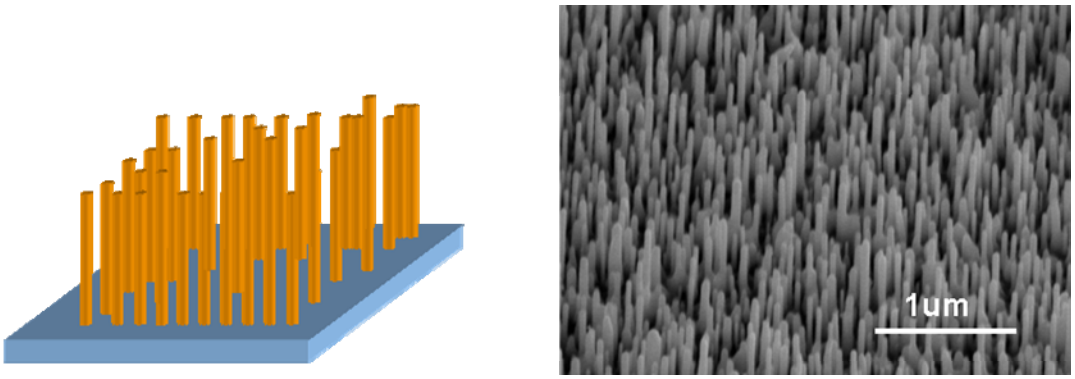

Fig 5.6 Schematic illustration of aligned ZnO nanowire arrays as template for hearing aid.

Thirdly, aligned ZnO NB/NW arrays are a perfect bionic mimic of the arrays of hair cells in the human air. With the high density of the NBs/NWs in a small area, the signal can be greatly magnified from the group vibration of the wires. (figure 5.6)

CHAPTER 6

CONCLUSION

ZnO is a promising material for the applications in nanotechnology and biotechnology. Due to its significant advantages in optical properties, piezoelectricity, and biology applications, it has been extensively studied for decades and has been demonstrated to possess supreme performance in many aspects. A large number of prototype nanodevices based on ZnO nanowires (NWs) and nanobelts (NBs) with unique and supreme properties have been realized. Some of them are believed to be a milestone and might bring a breakthrough in large extend in nanotechnology, such as the high efficient nanogenerators, low threshold single laser, high photo gain UV detector, and etc..

Due to its significance in potential applications, it is essential to understand the intrinsic transport properties of ZnO NW and explore efficient methods to further improve the performance of ZnO NW based devices and make them more applicable in future nanodevice systems. This is the primary aim of my research. To be more specific, research objects covered in the thesis are : 1) Investigating the intrinsic transport properties of ZnO NW, the semiconductor-metal contact interface properties, and the surface state effects. With further understanding the basic transport mechanisms and physics, we can get better control of the device stability and enhance the

device performance accordingly. 2) Studying the effect of surface functionalization in improving ZnO NW transport properties and modifying surface physical and chemical activities and exploring the performance advance of functionalized ZnO NWs in different devices. 3) Developing ZnO NB based nanopiezotronic devices by polymer surface coating, which provides another option for nanopiezotronics in energy conversion.

Following is a list of research achievements that have significant scientific and technical application impacts discussed in this thesis.

First, high performance rectifying diodes based on single ZnO NB were fabricated by dielectrophoresis. The ideality factor of the diode is ~3, and on/off current ratio is as high as 2000. The performance of the single NB diode makes it practically applicable. The formation of the Schottky diodes is investigated and suggested due to the asymmetric contacts formed in the dielectrophoresis aligning process. This study provides a simple way to fabricate high performance rectifying diodes. Moreover, detail analysis of the semiconductor and metal interfaces give insights for optimizing future device fabrication methods.

Second, by functionalizing the surfaces of ZnO NBs with a thin self-assembled molecular layer, the electrical and optoelectronic performances of a single NB based device are drastically improved. For a single NB based device, due to energy band tuning and surface modification, the conductance was enhanced by six orders of magnitude upon functionalization; Coating

molecule layer has changed a Schottky contact into an Ohmic contact without sophisticated deposition of multilayered metals. A functionalized NB showed negative differential resistance and exhibited huge improved photoconductivity and gas sensing response. The functionalized SAM also greatly reduced the etching rate of the ZnO NBs by buffer solution, largely extended their life time for biomedical applications. In this study, surface functionalization of ZnO NW was demonstrated to be an effective way to improve its transport and chemical activity properties in a significant extend.

Third, a novel approach to fabricate a nanopiezotronic device is investigated by combining the idea of surface functionalization and the piezoelectric-semiconducting coupling effect to explore the potential improvement of nanopiezotronics. A humidity/chemical sensor based PE-FET by surface functionalization is first demonstrated. The devices were based on a single-side coated ZnO NB functionalized with multi-layers of polymers. Upon exposure of high humidity vapors, the polymers swell and produce an asymmetric strain across the ZnO NB. In returns, the deformation of ZnO NB produces a piezoelectric field across the NB, which serves as the gate for controlling the flow of current along the NB. This is the working principle of the polymer functionalized PE-FET. Also, the polymer functionalized PE-FET has been proved to work as a chemical sensor for detecting phase transition of the coated polymer by the strain effect induced

from the polymer swelling and contract as a result of the phase transition. This work adds a new component to the family of nanopiezotronics.

In the polymer functionalized PE-FET, the chemical energies changes were reflected on the electric signals, which is different from previous devices engineered with mechanical energies. It converts chemical energies to electrical energy and provides a novel insight for nanosystems energy harvesting. This is a brand-new way in fabrication of nanopiezotronic devices and might bring a broad future of potential applications.

REFERENCES:

1. Alivisatos, A. P.; Harris, A. L.; Steigerwald, N. J.; Brus, L. E. *J. Chem. Phys.* **1988,** 89, 4001.

2. Alivisatos, A. P. *Science* **1996,** 271, 933.

3. Ashoori, R. C. *Nature* **1996,** 379, (6564), 413-419.

4. Beenakker, C. W. J.; Vanhouten, H. *Solid State Physics-Advances in Research and Applications* **1991,** 44, 1-228.

5. Bezryadin, A.; Verschueren, A. R. M.; Tans, S. J.; Dekker, C. *Physical Review Letters* **1998,** 80, (18), 4036-4039.

6. Bockrath, M.; Cobden, D. H.; McEuen, P. L.; Chopra, N. G.; Zettl, A.; Thess, A.; Smalley, R. E. *Science* **1997,** 275, (5308), 1922-1925.

7. Bonard, J. M.; Salvetat, J. P.; Stockli, T.; de Heer, W. A.; Forro, L.; Chatelain, A. *Applied Physics Letters* **1998,** 73, (7), 918-920.

8. Britton, C. L.; Jones, R. L.; Oden, P. I.; Hu, Z.; Warmack, R. J.; Smith, S. F.; Bryan, W. L.; Rochelle, J. M. *Ultramicroscopy* **2000,** 82, (1-4), 17-21.

9. Chen, J.; Reed, M. A.; Rawlett, A. M.; Tour, J. M. *Science* **1999,** 286, (5444), 1550-1552.

10. Chan, W. C. W.; Nie, S. M. *Science* **1998,** 281, (5385), 2016-2018.

11. Cobden, D. H.; Bockrath, M.; McEuen, P. L.; Rinzler, A. G.; Smalley, R. E. *Physical Review Letters* **1998,** 81, (3), 681-684.

12. CostaKramer, J. L.; Garcia, N.; GarciaMochales, P.; Serena, P. A.; Marques, M. I.; Correia, A. *Physical Review B* **1997,** 55, (8), 5416-5424.

13. Dean, K. A.; Chalamala, B. R. *Applied Physics Letters* **1999,** 75, (19), 3017-3019.

14. Diehl, M. R.; Yaliraki, S. N.; Beckman, R. A.; Barahona, M.; Heath, J. R. *Angewandte Chemie-International Edition* **2001,** 41, (2), 353-+.

15. Donhauser, Z. J.; Mantooth, B. A.; Kelly, K. F.; Bumm, L. A.; Monnell, J. D.; Stapleton, J. J.; Price, D. W.; Rawlett, A. M.; Allara, D. L.; Tour, J. M.; Weiss, P. S. *Science* **2001,** 292, (5525), 2303-2307.

16. Dresselhaus, M. S.; Dresselhaus, G.; Saito, R. *Phys. Rev. B* **1992,** 45, 6234-6242.

17. Fuhrer, M. S.; Cohen, M. L.; Zettl, A.; Crespi, V. *Solid State Communications* **1999,** 109, (2), 105-109.

18. Fuhrer, M. S.; Nygard, J.; Shih, L.; Forero, M.; Yoon, Y. G.; Mazzoni, M. S. C.; Choi, H. J.; Ihm, J.; Louie, S. G.; Zettl, A.; McEuen, P. L. *Science* **2000,** 288, (5465), 494-497.

19. Fujii, M.; Iwanaga, H.; Ichihara, M.; Takeuchi, S. *Journal of Crystal Growth* **1993,** 128, (1-4), 1095-1098.

20. Fujisawa, T.; Hirayama, Y.; Tarucha, S. *Applied Physics Letters* **1994,** 64, (17), 2250-2252.

21. Ginger, D. S.; Greenham, N. C. *Synth. Met.* **2001,** 124, 117-120.

22. Goldhaber-Gordon, D.; Shtrikman, H.; Mahalu, D.; Abusch-Magder, D.; Meirav, U.; Kastner, M. A. *Nature* **1998,** 391, (6663), 156-159.

23. Gores, J.; Goldhaber-Gordon, D.; Heemeyer, S.; Kastner, M. A.; Shtrikman, H.; Mahalu, D.; Meirav, U. *Physical Review B* **2000,** 62, (3), 2188-2194.

24. Gu, Q.; Cheng, C. D.; Haynie, D. T. *Nanotechnology* **2005,** 16, (8), 1358-1363.

25. Baselt, D. R.; Lee, G. U.; Hansen, K. M.; Chrisey, L. A.; Colton, R. J. *Proceedings of the Ieee* **1997,** 85, (4), 672-680.

26. Bjork, M. T.; Ohlsson, B. J.; Sass, T.; Persson, A. I.; Thelander, C.; Magnusson, M. H.; Deppert, K.; Wallenberg, L. R.; Samuelson, L. *Applied Physics Letters* **2002,** 80, (6), 1058-1060.

27. Cui, Y.; Duan, X. F.; Hu, J. T.; Lieber, C. M. *Journal of Physical Chemistry B* **2000,** 104, (22), 5213-5216.

28. Cui, Y.; Lieber, C. M. *Science* **2001,** 291, 851-853.

29. Duan, X. F.; Huang, Y.; Agarwal, R.; Lieber, C. M. *Nature* **2003,** 421, (6920), 241-245.

30. Duan, X. F.; Huang, Y.; Cui, Y.; Wang, J. F.; Lieber, C. M. *Nature* **2001,** 409, (6816), 66-69.

31. Fritz, J.; Baller, M. K.; Lang, H. P.; Rothuizen, H.; Vettiger, P.; Meyer, E.; Guntherodt, H. J.; Gerber, C.; Gimzewski, J. K. *Science* **2000,** 288, (5464), 316-318.

32. Wang, D. W.; Chang, Y. L.; Wang, Q.; Cao, J.; Farmer, D. B.; Gordon, R. G.; Dai, H. J. *Journal of the American Chemical Society* **2004,** 126, (37), 11602-11611.

33. Salomon, A.; Arad-Yellin, R.; Shanzer, A.; Karton, A.; Cahen, D. *Journal of the American Chemical Society* **2004,** 126, (37), 11648-11657.

34. Hu, J.; Odom, T. W.; Lieber, C. M. *Acc. Chem. res.* **1999,** 32, 435-445.

35. Gammon, D. **2000,** 405, (6789), 899-900.

36. Lavrik, N. V.; Sepaniak, M. J.; Datskos, P. G. *Review of Scientific Instruments* **2004,** 75, (7), 2229-2253.

37. Nakayama, Y.; Pauzauskie, P. J.; Radenovic, A.; Onorato, R. M.; Saykally, R. J.; Liphardt, J.; Yang, P. D. *Nature* **2007,** 447, (7148), 1098-U8.

38. Rawlett, A. M.; Hopson, T. J.; Nagahara, L. A.; Tsui, R. K.; Ramachandran, G. K.; Lindsay, S. M. *Applied Physics Letters* **2002,** 81, (16), 3043-3045.

39. Wang, X. D.; Ding, Y.; Summers, C. J.; Wang, Z. L. *J. Phys. Chem. B* **2004,** 108, 8773-8777.

40. Arnold, M. S.; Avouris, P.; Pan, Z. W.; Wang, Z. L. *Journal of Physical Chemistry B* **2003,** 107, (3), 659-663.

41. Raja, T.; Agrawal, V. D.; Bushnell, M. L. In *A tutorial on the emerging nanotechnology devices*, VLSI Design, 2004. Proceedings. 17th International Conference on, 2004; 2004; pp 343-360.

42. Gao, X. H.; Yang, L. L.; Petros, J. A.; Marshal, F. F.; Simons, J. W.; Nie, S. M. *Current Opinion in Biotechnology* **2005,** 16, (1), 63-72.

43. Han, M. Y.; Gao, X. H.; Su, J. Z.; Nie, S. *Nature Biotechnology* **2001,** 19, (7), 631-635.

44. Terabe, K.; Hasegawa, T.; Nakayama, T.; Aono, M. *Nature* **2005,** 433, (7021), 47-50.

45. Weis, J.; Haug, R. J.; Vonklitzing, K.; Ploog, K. *Physical Review Letters* **1993,** 71, (24), 4019-4022.

46. Winkler, R. *Physical Review B* **2000,** 62, (7), 4245-4248.

47. M. F. Crommie; C. P. Lutz; D. M. Eigler. *Science* **1993,** 262, 218.

48. Liu, C.; Zapien, J. A.; Yao, Y.; Meng, X.; Lee, C. S.; Fan, S.; Lifshitz, Y.; Lee, S. T. *Adv. Mater.* **2003,** 15, 838-841.

49. Liu, K. I.; Chien, C. L.; Searson, P. C.; Yu-Zhang, K. *Applied Physics Letters* **1998,** 73, (15), 2222-2222.

50. Lyshevski, M. A. In *Biomimetics, nanobioinformatics and nanotechnology*, Nanotechnology, 2003. IEEE-NANO 2003. 2003 Third IEEE Conference on, 2003; 2003; pp 216-219 vol.2.

51. Mai, W. J.; Wang, Z. L. *Applied Physics Letters* **2006,** 89, (7), -.

52. Martel, R.; Schmidt, T.; Shea, H. R.; Hertel, T.; Avouris, P. *Applied Physics Letters* **1998,** 73, (17), 2447-2449.

53. Maslov, A. V.; Ning, C. Z. *Applied Physics Letters* **2003,** 83, (6), 1237-1239.

54. Nan, C. W.; Liu, G.; Lin, Y. H.; Chen, H. D. *Physical Review Letters* **2005,** 94, (19), -.

55. Ng, H. T.; Chen, B.; Li, J.; Han, J.; Meyyappan, M.; Wu, J.; Li, S. X.; Haller, E. E. *Appl. Phys. Lett.* **2003,** 82, (13), 2023-2025.

56. Nie, S. M.; Chiu, D. T.; Zare, R. N. *Science* **1994,** 266, (5187), 1018-1021.

57. Whang, D.; Jin, S.; Lieber, C. M. *Nano Letters* **2003,** 3, (7), 951-954.

58. Moore, G. E. *Proceedings of the Ieee* **1998,** 86, (1), 82-85.

59. Wang, L.; Hu, Y.; Li, Z.; Tang, J. C.; Wang, X. S. *Nanotechnology* **2002,** 13, (6), 714-719.

60. Mintmire, J. W.; Dunlap, B. I.; White, C. T. *Phys. Rev. Lett.* **1992,** 68, 631-634.

61. Iijima, S. *Nature* **1991,** 354, 56-58.

62. Iijima, S.; Ichihashi, T. *Nature* **1993,** 363, 603-605.

63. Morales, A. M.; Lieber, C. M. *Science* **1998,** 279, (5348), 208-211.

64. Gudiksen, M. S.; Lauhon, L. J.; Wang, J.; Smith, D. C.; Lieber, C. M. *Nature* **2002,** 415, (6872), 617-620.

65. Wang, X. D.; Gao, P. X.; Li, J.; Summers, C. J.; Wang, Z. L. *Adv. Mater.* **2002,** 14, 1732-1735.

66. Klein, D. L.; Roth, R.; Lim, A. K. L.; Alivisatos, A. P.; McEuen, P. L. *Nature* **1997,** 389, (6652), 699-701.

67. Park, H.; Lim, A. K. L.; Alivisatos, A. P.; Park, J.; McEuen, P. L. *Applied Physics Letters* **1999,** 75, (2), 301-303.

68. Cerrina, F.; Marrian, C. *Mrs Bulletin* **1996,** 21, (12), 56-62.

69. Gibson, J. M. *Physics Today* **1997,** 50, (10), 56-61.

70. Hong, S. H.; Zhu, J.; Mirkin, C. A. *Science* **1999,** 286, (5439), 523-525.

71. Murray, C. B.; Kagan, C. R.; Bawendi, M. G. *Annual Review of Materials Science* **2000,** 30, 545-610.

72. Siska, A.; Konya, Z.; Hernadi, K.; Kiricsi, I.; Kordas, K.; Vajtai, R. *Journal of Materials Research* **2000,** 15, (10), 2087-2090.

73. Roura, P.; Costa, J.; Morante, J. R.; Bertran, E. *Journal of Applied Physics* **1997,** 81, (7), 3290-3293.

74. Dai, Y.; Zhang, Y.; Wang, Z. L.; Solid State Commun. 2003, 629. *Solid State Commun.* **2003,** 126, 629-633.

75. Li, C.; Zhang, D. H.; Liu, X. L.; Han, S.; Tang, T.; Han, J.; Zhou, C. W. *Applied Physics Letters* **2003,** 82, (10), 1613-1615.

76. Wang, D. W.; Wang, Q.; Javey, A.; Tu, R.; Dai, H. J.; Kim, H.; McIntyre, P. C.; Krishnamohan, T.; Saraswat, K. C. *Applied Physics Letters* **2003,** 83, (12), 2432-2434.

77. Chen, Y. J.; Xue, X. Y.; Wang, Y. G.; Wang, T. H. *Applied Physics Letters* **2005,** 87, (23), -.

78. Li, J. Y.; Qiao, Z. Y.; Chen, X. L.; Chen, L.; Cao, Y. G.; He, M.; Li, H.; Cao, Z. M.; Zhang, Z. *Journal of Alloys and Compounds* **2000,** 306, (1-2), 300-302.

79. Wang, Z. L.; Kong, X. Y.; Ding, Y.; Gao, P. X.; Hughes, W. L.; Yang, R. S.; Zhang, Y. *Advanced Functional Materials* **2004,** 14, (10), 943-956.

80. Pan, Z. W.; Mahurin, S. M.; Dai, S.; Lowndes, D. H. *Nano Letters* **2005,** 5, (4), 723-727.

81. Wang, Z. L. *Advanced Materials* **2003,** 15, (5), 432-436.

82. Pan, Z. W.; Dai, Z. R.; Wang, Z. L. *Science* **2001,** 291, (5510), 1947-1949.

83. Gao, T.; Wang, T. H. *Chemical Communications* **2004**, (22), 2558-2559.

84. Kong, X. Y.; Ding, Y.; Yang, R.; Wang, Z. L. *Science* **2004,** 303, (5662), 1348-1351.

85. Zaric, S.; Ostojic, G. N.; Kono, J.; Shaver, J.; Moore, V. C.; Strano, M. S.; Hauge, R. H.; Smalley, R. E.; Wei, X. *Science* **2004,** 304, (5674), 1129-1131.

86. Gao, P. M.; Ding, Y.; Mai, W. J.; Hughes, W. L.; Lao, C. S.; Wang, Z. L. *Science* **2005,** 309, (5741), 1700-1704.

87. Kong, X. Y.; Wang, Z. L. *Nano Lett.* **2003,** 3, 1625-1631.

88. Yang, P. D.; Yan, H. Q.; Mao, S.; Russo, R.; Johnson, J.; Saykally, R.; Morris, N.; Pham, J.; He, R. R.; Choi, H. J. *Advanced Functional Materials* **2002,** 12, (5), 323-331.

89. Yan, H. Q.; Johnson, J.; Law, M.; He, R. R.; Knutsen, K.; McKinney, J. R.; Pham, J.; Saykally, R.; Yang, P. D. *Advanced Materials* **2003,** 15, (22), 1907-+.

90. Greene, L.; Law, M.; Tan, D. H.; Goldberger, J.; Yang, P. *Nano Lett* **2005,** 5, 1231.

91. Goldberger, J.; Sirbuly, D. J.; Law, M.; Yang, P. *Journal of Physical Chemistry B* **2005,** 109, (1), 9-14.

92. Lin, C. C.; Chen, H. P.; Chen, S. Y. *Chemical Physics Letters* **2005,** 404, (1-3), 30-34.

93. Vayssieres, L. *Advanced Materials* **2003,** 15, (5), 464-466.

94. Gao, P. X.; Wang, Z. L. *Applied Physics Letters* **2004,** 84, (15), 2883-2885.

95. Park, J. Y.; Yun, Y. S.; Hong, Y. S.; Oh, H.; Kim, J. J.; Kim, S. S. *Applied Physics Letters* **2005,** 87, (12), -.

96. Keem, K.; Kim, H.; Kim, G. T.; Lee, J. S.; Min, B.; Cho, K.; Sung, M. Y.; Kim, S. *Applied Physics Letters* **2004,** 84, (22), 4376-4378.

97. Min, B.; Lee, J. S.; Hwang, J. W.; Keem, K. H.; Kang, M. I.; Cho, K.; Sung, M. Y.; Kim, S.; Lee, M. S.; Park, S. O.; Moon, J. T. *Journal of Crystal Growth* **2003,** 252, (4), 565-569.

98. Moon, T. H.; Jeong, M. C.; Lee, W.; Myoung, J. M. *Applied Surface Science* **2005,** 240, (1-4), 280-285.

99. Tuzemen, S.; Xiong, G.; Wilkinson, J.; Mischuck, B.; Ucer, K. B.; Williams, R. T. *Physica B-Condensed Matter* **2001,** 308, 1197-1200.

100. Sheng, H.; Emanetoglu, N. W.; Muthukumar, S.; Yakshinskiy, B. V.; Feng, S.; Lu, Y. *Journal of Electronic Materials* **2003,** 32, (9), 935-938.

101. Jeong, M. C.; Oh, B. Y.; Lee, W.; Myoung, J. M. *Applied Physics Letters* **2005,** 86, (10), -.

102. Liu, C. H.; Yiu, W. C.; Au, F. C. K.; Ding, J. X.; Lee, C. S.; Lee, S. T. *Applied Physics Letters* **2003,** 83, (15), 3168-3170.

103. Wan, Q.; Li, Q. H.; Chen, Y. J.; Wang, T. H.; He, X. L.; Li, J. P.; Lin, C. L. *Applied Physics Letters* **2004,** 84, (18), 3654-3656.

104. Li, Q. H.; Wan, Q.; Liang, Y. X.; Wang, T. H. *Applied Physics Letters* **2004,** 84, (22), 4556-4558.

105. Liu, C. H.; Zapien, J. A.; Yao, Y.; Meng, X. M.; Lee, C. S.; Fan, S. S.; Lifshitz, Y.; Lee, S. T. *Advanced Materials* **2003,** 15, (10), 838-+.

106. Park, C. H.; Zhang, S. B.; Wei, S. H. *Physical Review B* **2002,** 66, (7), -.

107. Ryu, Y. R.; Lee, T. S.; Leem, J. H.; White, H. W. *Applied Physics Letters* **2003,** 83, (19), 4032-4034.

108. Ryu, Y. R.; Kim, W. J.; White, H. W. *Journal of Crystal Growth* **2000,** 219, (4), 419-422.

109. LaRoche, J. R.; Heo, Y. W.; Kang, B. S.; Tien, L. C.; Kwon, Y.; Norton, D. P.; Gila, B. P.; Ren, F.; Pearton, S. J. *Journal of Electronic Materials* **2005,** 34, (4), 404-408.

110. Heo, Y. W.; Tien, L. C.; Norton, D. P.; Kang, B. S.; Ren, F.; Gila, B. P.; Pearton, S. J. *Applied Physics Letters* **2004,** 85, (11), 2002-2004.

111. Ronning, C.; Gao, P. X.; Ding, Y.; Wang, Z. L.; Schwen, D. *Applied Physics Letters* **2004,** 84, (5), 783-785.

112. Aoki, T.; Hatanaka, Y.; Look, D. C. *Applied Physics Letters* **2000,** 76, (22), 3257-3258.

113. Ip, K.; Baik, K. H.; Heo, Y. W.; Norton, D. P.; Pearton, S. J.; LaRoche, J. R.; Luo, B.; Ren, F.; Zavada, J. M. *Journal of Vacuum Science & Technology B* **2003,** 21, (6), 2378-2381.

114. Kim, H. K.; Han, S. H.; Seong, T. Y.; Choi, W. K. *Applied Physics Letters* **2000,** 77, (11), 1647-1649.

115. Polyakov, A. Y.; Smirnov, N. B.; Kozhukhova, E. A.; Vdovin, V. I.; Ip, K.; Heo, Y. W.; Norton, D. P.; Pearton, S. J. *Applied Physics Letters* **2003,** 83, (8), 1575-1577.

116. Mosbacker, H. L.; Strzhemechny, Y. M.; White, B. D.; Smith, P. E.; Look, D. C.; Reynolds, D. C.; Litton, C. W.; Brillson, L. J. *Applied Physics Letters* **2005,** 87, (1), -.

117. Li, Q. H.; Wan, Q.; Wang, Y. G.; Wang, T. H. *Applied Physics Letters* **2005,** 86, (26), -.

118. Coppa, B. J.; Fulton, C. C.; Hartlieb, P. J.; Davis, R. F.; Rodriguez, B. J.; Shields, B. J.; Nemanich, R. J. *Journal of Applied Physics* **2004,** 95, (10), 5856-5864.

119. Coppa, B. J.; Davis, R. F.; Nemanich, R. J. *Applied Physics Letters* **2003,** 82, (3), 400-402.

120. Oh, D. C.; Kim, J. J.; Makino, H.; Hanada, T.; Cho, M. W.; Yao, T.; Ko, H. J. *Applied Physics Letters* **2005,** 86, (4), -.

121. Zhong, J.; Muthukumar, S.; Chen, Y.; Lu, Y.; Ng, H. M.; Jiang, W.; Garfunkel, E. L. *Applied Physics Letters* **2003,** 83, (16), 3401-3403.

122. Mao, S. X.; Zhao, M. H.; Wang, Z. L. *Applied Physics Letters* **2003,** 83, (5), 993-995.

123. Christman, J. A.; Woolcott, R. R.; Kingon, A. I.; Nemanich, R. J. *Applied Physics Letters* **1998,** 73, (26), 3851-3853.

124. Johnson, J. C.; Yan, H. Q.; Schaller, R. D.; Petersen, P. B.; Yang, P. D.; Saykally, R. J. *Nano Letters* **2002,** 2, (4), 279-283.

125. Liang, S.; Sheng, H.; Liu, Y.; Huo, Z.; Lu, Y.; Shen, H. *Journal of Crystal Growth* **2001,** 225, (2-4), 110-113.

126. Park, J. H.; Choi, H. J.; Choi, Y. J.; Sohn, S. H.; Park, J. G. *Journal of Materials Chemistry* **2004,** 14, (1), 35-36.

127. Kim, S. H.; Jeong, S. W.; Hwang, D. K.; Park, S. J.; Seong, T. Y. *Electrochemical and Solid State Letters* **2005,** 8, (8), G198-G200.

128. Harnack, O.; Pacholski, C.; Weller, H.; Yasuda, A.; Wessels, J. M. *Nano Letters* **2003,** 3, (8), 1097-1101.

129. Yang, H.; Li, Y.; Norton, D. P.; Pearton, S. J.; Jung, S.; Ren, F.; Boatner, L. A. *Applied Physics Letters* **2005,** 86, (17), -.

130. Chen, Z. Q.; Kawasuso, A.; Xu, Y.; Naramoto, H.; Yuan, X. L.; Sekiguchi, T.; Suzuki, R.; Ohdaira, T. *Journal of Applied Physics* **2005,** 97, (1), -.

131. Look, D. C.; Claftin, B. *Physica Status Solidi B-Basic Research* **2004,** 241, (3), 624-630.

132. Meng, X. Q.; Zhao, D. X.; Zhang, J. Y.; Shen, D. Z.; Lu, Y. M.; Dong, L.; Xiao, Z. Y.; Liu, Y. C.; Fan, X. W. *Chemical Physics Letters* **2005,** 413, (4-6), 450-453.

133. Kind, H.; Yan, H. Q.; Messer, B.; Law, M.; Yang, P. D. *Advanced Materials* **2002,** 14, (2), 158-+.

134. Kang, B. S.; Ren, F.; Heo, Y. W.; Tien, L. C.; Norton, D. P.; Pearton, S. J. *Applied Physics Letters* **2005,** 86, (11), -.

135. Wang, Z. L. *Mrs Bulletin* **2007,** 32, (2), 109-116.

136. Chang, P. C.; Fan, Z.; Chien, C. J.; Stichtenoth, D.; Ronning, C.; Lu, J. G. *Applied Physics Letters* **2006,** 89, (13), -.

137. Ozgur, U.; Alivov, Y. I.; Liu, C.; Teke, A.; Reshchikov, M. A.; Dogan, S.; Avrutin, V.; Cho, S. J.; Morkoc, H. *Journal of Applied Physics* **2005,** 98, (4), -.

138. Heo, Y. W.; Norton, D. P.; Tien, L. C.; Kwon, Y.; Kang, B. S.; Ren, F.; Pearton, S. J.; LaRoche, J. R. *Materials Science & Engineering R-Reports* **2004,** 47, (1-2), 1-47.

139. Park, W. I.; Kim, J. S.; Yi, G. C.; Bae, M. H.; Lee, H. J. *Applied Physics Letters* **2004,** 85, (21), 5052-5054.

140. Cha, S. N.; Jang, J. E.; Choi, Y.; Amaratunga, G. A. J.; Ho, G. W.; Welland, M. E.; Hasko, D. G.; Kang, D. J.; Kim, J. M. *Applied Physics Letters* **2006,** 89, (26), -.

141. Basak, D.; Amin, G.; Mallik, B.; Paul, G. K.; Sen, S. K. *Journal of Crystal Growth* **2003,** 256, (1-2), 73-77.

142. Leung, Y. H.; Djurisic, A. B.; Gao, J.; Xie, M. H.; Wei, Z. F.; Xu, S. J.; Chan, W. K. *Chemical Physics Letters* **2004,** 394, (4-6), 452-457.

143. Look, D. C. *Semiconductor Science and Technology* **2005,** 20, (4), S55-S61.

144. Soci, C.; Zhang, A.; Xiang, B.; Dayeh, S. A.; Aplin, D. P. R.; Park, J.; Bao, X. Y.; Lo, Y. H.; Wang, D. *Nano Letters* **2007,** 7, (4), 1003-1009.

145. Huang, M. H.; Mao, S.; Feick, H.; Yan, H.; Wu, Y.; Kind, H.; Weber, E.; Russo, R.; Yang, P. *Science* **2001,** 292, (8), 1897-1899.

146. Johnson, J. C.; Yan, H. Q.; Schaller, R. D.; Haber, L. H.; Saykally, R. J.; Yang, P. D. *Journal of Physical Chemistry B* **2001,** 105, (46), 11387-11390.

147. Park, W. I.; Yi, G. C. *Adv. Mater.* **2004,** 16, (1), 87-90.

148. Shibata, T.; Unno, K.; Makino, E.; Ito, Y.; Shimada, S. *Sensors and Actuators a-Physical* **2002,** 102, (1-2), 106-113.

149. Li, Q. H.; Liang, Y. X.; Wan, Q.; Wang, T. H. *Applied Physics Letters* **2004,** 85, (26), 6389-6391.

150. Feng, P.; Wan, Q.; Wang, T. H. *Applied Physics Letters* **2005,** 87, (21), -.

151. Wang, H. T.; Kang, B. S.; Ren, F.; Tien, L. C.; Sadik, P. W.; Norton, D. P.; Pearton, S. J.; Lin, J. *Applied Physics a-Materials Science & Processing* **2005,** 81, (6), 1117-1119.

152. Wang, X. D.; Zhou, J.; Lao, C. S.; Song, J. H.; Xu, N. S.; Wang, Z. L. *Advanced Materials* **2007,** 19, (12), 1627-+.

153. Zhou, J.; Lao, C. S.; Gao, P. X.; Mai, W. J.; Hughes, W. L.; Deng, S. Z.; Xu, N. S.; Wang, Z. L. *Solid State Communications* **2006,** 139, (5), 222-226.

154. Wang, Z. L. *Advanced Materials* **2007,** 19, (6), 889-892.

155. Wang, X. D.; Song, J. H.; Liu, J.; Wang, Z. L. *Science* **2007,** 316, (5821), 102-105.

156. Wang, X. D.; Zhou, J.; Song, J. H.; Liu, J.; Xu, N. S.; Wang, Z. L. *Nano Letters* **2006,** 6, (12), 2768-2772.

157. He, H.; Hsin, C. L.; Liu, J.; Chen, L. J.; Wang, Z. L. *Advanced Materials* **2007,** 19, (6), 781-+.

158. Gao, P. X.; Song, J. H.; Liu, J.; Wang, Z. L. *Advanced Materials* **2007,** 19, (1), 67-+.

159. Wang, Z. L.; Song, J. H. *Science* **2006,** 312, (5771), 242-246.

160. Lao, C. S.; Kuang, Q.; Wang, Z. L.; Park, M. C.; Deng, Y. L. *Applied Physical Letters* **2007,** 90, (2007), 262107.

161. Wang, X. D.; Liu, J.; Song, J. H.; Wang, Z. L. *Nano Letters* **2007,** 7, (8), 2475-2479.

162. Wang, Z. L.; Kong, X. Y.; Zuo, J. M. *Phys. Rev. Lett.* **2003,** 91, 185502.

163. Lao, C. S.; Gao, P. M.; Sen Yang, R.; Zhang, Y.; Dai, Y.; Wang, Z. L. *Chemical Physics Letters* **2006,** 417, (4-6), 358-362.

164. Dai, Y.; Zhang, Y.; Wang, Z. L. *Solid State Communications* **2003,** 126, (11), 629-633.

165. Gao, P. M.; Lao, C. S.; Hughes, W. L.; Wang, Z. L. *Chemical Physics Letters* **2005,** 408, (1-3), 174-178.

166. Gao, P. X.; Lao, C. S.; Ding, Y.; Wang, Z. L. *Advanced Functional Materials* **2006,** 16, (1), 53-62.

167. Stern, E.; Cheng, G.; Klemic, J. F.; Broomfield, E.; Turner-Evans, D.; Li, C.; Zhou, C.; Reed, M. A. *Journal of Vacuum Science & Technology B* **2006,** 24, (1), 231-236.

168. Nam, C. Y.; Kim, J. Y.; Fischer, J. E. *Applied Physics Letters* **2005,** 86, (19), -.

169. Heo, Y. W.; Tien, L. C.; Kwon, Y.; Norton, D. P.; Pearton, S. J.; Kang, B. S.; Ren, F. *Applied Physics Letters* **2004,** 85, (12), 2274-2276.

170. Lao, C. S.; Liu, J.; Gao, P. X.; Zhang, L. Y.; Davidovic, D.; Tummala, R.; Wang, Z. L. *Nano Letters* **2006,** 6, (2), 263-266.

171. Pan, Z. W.; Dai, Z. R.; Wang, Z. L. *Science* **2001,** 291, 1947-1949.

172. Ip, K.; Gila, B. P.; Onstine, A. H.; Lambers, E. S.; Heo, Y. W.; Baik, K. H.; Norton, D. P.; Pearton, S. J.; Kim, S.; LaRoche, J. R.; Ren, F. *Applied Physics Letters* **2004,** 84, (25), 5133-5135.

173. Choi, H. J.; Seong, H. K.; Chang, J.; Lee, K. I.; Park, Y. J.; Kim, J. J.; Lee, S. K.; He, R. R.; Kuykendall, T.; Yang, P. D. *Advanced Materials* **2005,** 17, (11), 1351-+.

174. He, H.; Lao, C. S.; Chen, L. J.; Davidovic, D.; Wang, Z. L. *Journal of the American Chemical Society* **2005,** 127, (47), 16376-16377.

175. Brown, I. G.; Gavin, J. E.; Macgill, R. A. *Applied Physics Letters* **1985,** 47, (4), 358-360.

176. Wagner, R. S.; Ellis, W. C. *Applied Physics Letters* **1964,** 4, (5), 89-&.

177. Wang, X. D.; Summers, C. J.; Wang, Z. L. *Nano Lett.* **2004,** 4, 423-426.

178. Monteiro, T.; Boemare, C.; Soares, M. J.; Rita, E.; Alves, E. *Journal of Applied Physics* **2003,** 93, (11), 8995-9000.

179. Qiu, D. J.; Wu, H. Z.; Feng, A. M.; Lao, Y. F.; Chen, N. B.; Xu, T. N. *Applied Surface Science* **2004,** 222, (1-4), 263-268.

180. Xiang, J.; Lu, W.; Hu, Y. J.; Wu, Y.; Yan, H.; Lieber, C. M. *Nature* **2006,** 441, (7092), 489-493.

181. Chueh, Y. L.; Ko, M. T.; Chou, L. J.; Chen, L. J.; Wu, C. S.; Chen, C. D. *Nano Letters* **2006,** 6, (8), 1637-1644.

182. Zhang, D. H.; Liu, Z. Q.; Han, S.; Li, C.; Lei, B.; Stewart, M. P.; Tour, J. M.; Zhou, C. W. *Nano Letters* **2004,** 4, (11), 2151-2155.

183. Chueh, Y. L.; Hsieh, C. H.; Chang, M. T.; Chou, L. J.; Lao, C. S.; Song, J. H.; Gan, J. Y.; Wang, Z. L. *Advanced Materials* **2007,** 19, (1), 143-+.

184. Feng, X. J.; Feng, L.; Jin, M. H.; Zhai, J.; Jiang, L.; Zhu, D. B. *Journal of the American Chemical Society* **2004,** 126, (1), 62-63.

185. Kim, S.; Maier, J. *Electrochemical and Solid State Letters* **2003,** 6, (11), J7-J9.

186. Pomoni, K.; Vomvas, A.; Trapalis, C. *Thin Solid Films* **2005,** 479, (1-2), 160-165.

187. Vanheusden, K.; Warren, W. L.; Seager, C. H.; Tallant, D. R.; Voigt, J. A.; Gnade, B. E. *Journal of Applied Physics* **1996,** 79, (10), 7983-7990.

188. Calarco, R.; Marso, M.; Richter, T.; Aykanat, A. I.; Meijers, R.; Hart, A. V.; Stoica, T.; Luth, H. *Nano Letters* **2005,** 5, (5), 981-984.

189. Chen, W.; Xu, Q.; Hu, Y. S.; Mai, L. Q.; Zhu, Q. Y. *Journal of Materials Chemistry* **2002,** 12, (6), 1926-1929.

190. Prosini, P. P.; Xia, Y. Y.; Fujieda, T.; Vellone, R.; Shikano, M.; Sakai, T. *Electrochimica Acta* **2001,** 46, (17), 2623-2629.

191. Mai, L. Q.; Chen, W.; Xu, Q.; Peng, J. F.; Zhu, Q. Y. *Chemical Physics Letters* **2003,** 382, (3-4), 307-312.

192. Liu, J. F.; Wang, X.; Peng, Q.; Li, Y. D. *Advanced Materials* **2005,** 17, (6), 764-+.

193. Muster, J.; Kim, G. T.; Krstic, V.; Park, J. G.; Park, Y. W.; Roth, S.; Burghard, M. *Advanced Materials* **2000,** 12, (6), 420-+.

194. Liu, J. F.; Li, Q. H.; Wang, T. H.; Yu, D. P.; Li, Y. D. *Angewandte Chemie-International Edition* **2004,** 43, (38), 5048-5052.

195. Wu, X. C.; Tao, Y. R.; Dong, L.; Hong, J. M. *Journal of Materials Chemistry* **2004,** 14, (5), 901-904.

196. Mai, L. Q.; Lao, C. S.; Hu, B.; Zhou, J.; Qi, Y. Y.; Chen, W.; Gu, E. D.; Wang, Z. L. *Journal of Physical Chemistry B* **2006,** 110, (37), 18138-18141.

197. Chakraborty, S.; Bera, M. K.; Dalapati, G. K.; Paramanik, D.; Varma, S.; Bose, P. K.; Bhattacharya, S.; Maiti, C. K. *Semiconductor Science and Technology* **2006,** 21, (4), 467-472.

198. Chiu, F. C.; Wang, J. J.; Lee, J. Y.; Wu, S. C. *Journal of Applied Physics* **1997,** 81, (10), 6911-6915.

199. Golan, G.; Axelevitch, A.; Sigalov, B.; Gorenstein, B. *Journal of Optoelectronics and Advanced Materials* **2004,** 6, (1), 189-195.

200. Wang, C. J.; Cao, Q.; Ozel, T.; Gaur, A.; Rogers, J. A.; Shim, M. *Journal of the American Chemical Society* **2005,** 127, (32), 11460-11468.

201. Hirsch, A.; Vostrowsky, O. *Functional Molecular Nanostructures* **2005,** 245, 193-237.

202. Khrenov, V.; Klapper, M.; Koch, M.; Mullen, K. *Macromolecular Chemistry and Physics* **2005,** 206, (1), 95-101.

203. Yue, M.; Lin, H.; Dedrick, D. E.; Satyanarayana, S.; Majumdar, A.; Bedekar, A. S.; Jenkins, J. W.; Sundaram, S. *Journal of Microelectromechanical Systems* **2004,** 13, (2), 290-299.

204. Reiss, P.; Bleuse, J.; Pron, A. *Nano Letters* **2002,** 2, (7), 781-784.

205. Lieber, C. M. *MRS Bull.* **2003,** 28, 486-491.

206. Patolsky, F.; Lieber, C. M. *Materials Today* **2005,** 8, 20-28.

207. Hahm, J.; Lieber, C. M. *Nano Lett.* **2004,** 4, 51-54.

208. Cui, Y.; Wei, Q. Q.; Park, H. K.; Lieber, C. M. *Science* **2001,** 293, (5533), 1289-1292.

209. Huang, Y.; Duan, X. F.; Wei, Q. Q.; Lieber, C. M. *Science* **2001,** 291, (5504), 630-633.

210. Wu, Y.; Xiang, J.; Yang, C.; Lu, W.; Lieber, C. M. *Nature* **2004,** 430, (7000), 704-704.

211. Cui, Y.; Zhong, Z. H.; Wang, D. L.; Wang, W. U.; Lieber, C. M. *Nano Letters* **2003,** 3, (2), 149-152.

212. Patolsky, F.; Zheng, G. F.; Hayden, O.; Lakadamyali, M.; Zhuang, X. W.; Lieber, C. M. *Proceedings of the National Academy of Sciences of the United States of America* **2004,** 101, (39), 14017-14022.

213. Yang, C.; Zhong, Z. H.; Fang, Y.; Lieber, C. M. *Abstracts of Papers of the American Chemical Society* **2004,** 227, U1302-U1302.

214. Patolsky, F.; Timko, B. P.; Yu, G. H.; Fang, Y.; Greytak, A. B.; Zheng, G. F.; Lieber, C. M. *Science* **2006,** 313, (5790), 1100-1104.

215. Duan, X. F.; Huang, Y.; Lieber, C. M. *Nano Letters* **2002,** 2, (5), 487-490.

216. Lao, C. S.; Li, Y.; Wong, C. P.; Wang, Z. L. *Nano Letters* **2007,** 7, 1323.

217. Cornil, J.; Calbert, J. P.; Bredas, J. L. *Journal of the American Chemical Society* **2001,** 123, (6), 1250-1251.

218. Zhou, J.; Liu, J.; Yang, R. S.; Lao, C. S.; Gao, P. X.; Tummala, R.; Xu, N. S.; Wang, Z. L. *Small* **2006,** 2, (11), 1344-1347.

219. Lao, C. S.; Park, M. C.; Kuang, Q.; Deng, Y. L.; Wang, Z. L. *J. Am. Chem. Soc.* **2007,** Online.

220. Ip, K.; Heo, Y. W.; Baik, K. H.; Norton, D. P.; Pearton, S. J.; Kim, S.; LaRoche, J. R.; Ren, F. *Applied Physics Letters* **2004,** 84, (15), 2835-2837.

221. Schild, H. G. *Progress in Polymer Science* **1992,** 17, (2), 163-249.

222. Shi, S. H.; Liu, L. J. *Journal of Applied Polymer Science* **2006,** 102, (5), 4177-4184.

223. Sun, Q. Q.; Deng, Y. L. *Langmuir* **2005,** 21, (13), 5812-5816.